The Dissertation Committee for Adrian Marius Ambruș
certifies that this is the approved version of the following dissertation:

Modeling and Control of Managed Pressure Drilling Operations

Committee:

Eric van Oort, Supervisor

Benito Fernandez, Co-Supervisor

Raul Longoria

Ronald Barr

Behçet Açikmeşe

Pradeepkumar Ashok

Modeling and Control of Managed Pressure Drilling Operations

by

Adrian Marius Ambruș, B.S.M.E.; M.S.M.E.

DISSERTATION

Presented to the Faculty of the Graduate School of

The University of Texas at Austin

in Partial Fulfillment

of the Requirements

for the Degree of

DOCTOR OF PHILOSOPHY

THE UNIVERSITY OF TEXAS AT AUSTIN

May 2017

This dissertation is dedicated to my mother, Corina.

Acknowledgments

I would like to first thank my adviser, Prof. Dr. Eric van Oort, who provided the constant guidance, supervision and funding throughout my graduate studies. I am very grateful to have been mentored by Dr. van Oort, and to have learned from his vast experience in all areas of drilling engineering. Also, at the very top of my acknowledgments list I have to mention Dr. Pradeep Ashok, who provided valuable and frequent insight in the areas of drilling automation, data analytics and Bayesian modeling. Dr. Ashok also helped steer my overall research efforts from the very early days of my Ph.D.

Also, I am deeply thankful to Dr. Ali Karimi Vajargah and Dr. Ulf Jakob Aarsnes, both of whom offered extensive guidance on multi-phase flow modeling, and served as co-authors on many of the publications that form the core of this dissertation. Dr. Aarsnes helped with the development and preliminary validation of the Reduced Drift-flux model, and also with some of the control and estimation theory. Dr. Karimi is also thanked for securing the experimental data set used in this study, together with Prof. Babak Akbari from Louisiana State University.

I would also like to thank Prof. Dr. Benito Fernandez, who, as a co-supervisor throughout the candidacy process, offered additional feedback in the later part of my studies. Dr. Fernandez had a meaningful contribution

to my early studies as well, through the new concepts I have learned from his courses in Fault Diagnostics, Applied Intelligence for Engineers, and Nonlinear Control Systems. I would also like to mention Dr. Mitch Pryor, who provided valuable feedback early on in my Ph.D., and Prof. Dr. Behçet Açikmeşe, who assisted with the LMI theory used for control design in Chapter 4 of this dissertation. Prof. Dr. Ole Morten Aamo from NTNU is also thanked for the feedback on some of the publications co-authored as part of my studies.

I would also like to acknowledge Eric Cayeux, who facilitated a very rewarding research collaboration with the International Research Institute of Stavanger on a series of technical papers related to drilling automation and modeling. As part of this collaboration, I was able to travel to Stavanger, Norway and to experience their advanced research facilities first-hand.

The Rig Automation and Performance Improvement in Drilling (RAPID) sponsor companies are also thanked for the financial support and feedback offered during the last two years of my studies. Next on the list of thanks are all my colleagues in RAPID and the Drilling and Rig Automation Group. Among them I would like to mention Parham Pournazari, Zheren Ma, Runqi Han, and Roman Shor, all of whom were great collaborators, and were always available for a chat or a beer at the end of a long work day. Last but not least, I would like to express my gratitude to Tesse Smitherman, who assisted with administrative issues and travel arrangements.

Finally, I would like to thank my mother, Corina, and my family, for their loving support and encouragement.

Modeling and Control of Managed Pressure Drilling Operations

Publication No. _____

Adrian Marius Ambruș, Ph.D.
The University of Texas at Austin, 2017

Supervisor: Eric van Oort
Co-Supervisor: Benito Fernandez

The upstream oil and gas industry has witnessed a marked increase in the number of wells drilled in areas with elevated subsurface formation pressures and narrow drilling margins. Managed Pressure Drilling (MPD) techniques have been developed to deal with the challenge of narrow margin wells, offering great promise for improved rig safety and reduced non-productive time. Automation of MPD operations can ensure improved control over wellbore pressure profiles, and there are several commercial solutions currently available. However, these automation efforts seldom take into account the uncertainty and complex dynamics inherent in subsurface environments, and usually assume ideally functioning sensors and actuators, which is rarely the case in real-world drilling operations.

This dissertation describes a set of tools and methods that can form the basis for an automation framework for MPD systems, with specific focus on

the surface back-pressure technique of MPD. Model-based control algorithms with robust reference tracking, as well as methods for detecting system faults and handling modeling uncertainty, are integrated with a novel multi-phase hydraulics model. The control system and event detection modules are designed using physics-based representations of the drilling processes, as well as models relating uncertain variables in a probabilistic fashion. Validation on high-fidelity simulation models is conducted in order to ascertain the effectiveness of the developed methods.

Table of Contents

List of Tables

List of Figures

Chapter 1

Introduction

Drilling wells for oil and gas extraction from subsurface geological formations has been practiced for more than a century with tremendous impact on the global economy. As easily accessible hydrocarbon reserves are becoming increasingly scarcer, the focus of the upstream oil and gas industry has shifted to more challenging reservoirs, present in deep-water and high-pressure high-temperature (HPHT) environments, where the margin between success and failure is very narrow. One of the most notable examples of a failed operation is the 2010 Macondo / Deepwater Horizon accident, where an uncontrolled release of hydrocarbons and the subsequent explosion claimed the lives of 11 crew members and spilled almost 5 million barrels of oil into the Gulf of Mexico, causing extensive environmental damage (U.S. National Research Council, 2012). One of the factors that helped escalate this disaster was the crew's failure to ascertain trends in measured kick indicator parameters, which would have allowed timely identification of a potential blow-out. The Macondo accident, which occurred at a time when drilling automation started gaining momentum, highlighted not only the necessity for increased regulation of operational practices and safeguards, but also the need for improved real-time decision and control systems for drilling operations.

Drilling automation can greatly improve safety and optimize drilling efficiency, but needs to be properly implemented. Measurements supplied to the control system are often noisy and uncertain and sensor failures are common in the harsh drilling environments. Poor sensor data quality not only affects the input to the control system, but can also produce false alarms on the rig site, which can put the drilling crew under unnecessary stress. Often times, a process fault may significantly alter the operating conditions for which the controller was tuned, rendering the closed-loop system unstable. Actuators can also degrade and fail, jeopardizing control performance and requiring the operator to shut-down the system until remedial action is taken. These events not only pose safety hazards, but also lead to significant down time, which can have significant economic implications, particularly on offshore rigs where the daily operation cost can be as high as \$1-\$1.5 million (Cheremisinoff and Davletshin, 2010).

This dissertation introduces a model-based methodology for automating Managed Pressure Drilling (MPD) used on oil and gas wells, with considerations for robust control, fault detection and accommodation of uncertain, time-varying processes. The following sections will provide a basic overview of drilling, together with the challenges associated with narrow drilling margins (in the context of pressure management) which have led to the development of MPD technology. Next, the chapter will give a technical background on MPD, followed by a presentation of the key aspects that need to be addressed in MPD automation. Subsequently, the research objectives will be defined,

and an outline of this dissertation will be provided.

1.1 Overview of MPD

1.1.1 Background

Modern-day equipment used in the upstream oil and gas industry involves a long, slender steel pipe ("drillstring") ending in a bottom-hole assembly (BHA). The BHA contains a drill bit with multiple cutters, and heavier pieces of pipe called "drill collars" for applying weight on bit (WOB). As the bit rotates, the rock beneath it fails in shear or compression, extending the well deeper into the formation. Bit rotation is typically achieved from surface, using a top drive, although the more antiquated kelly and rotary table are still present on some rigs. When drilling wells deviated from vertical, downhole positive displacement motors are used to rotate the bit without rotation from surface, a technique called "slide drilling". As the well depth increases, more stands of pipe are added to the drillstring (the process of adding a stand to the drillstring is commonly known as "making a connection"). After a section of the well is drilled, the drillstring is pulled out of the borehole using the "draw works", a large motor-powered spool running wire rope for hoisting or lowering drill pipe. Next, a larger diameter steel pipe called "casing" is run into the hole and the space between the outer casing wall and the formation is cemented to provide an effective seal against formation fluids. An essential component of the drilling process is the "drilling mud", a viscous fluid with non-Newtonian rheological properties. The drilling mud is pumped from the

rig floor through the standpipe, then into the drillstring, and all the way down to the bit. It exits the bit through small-diameter bit nozzles, and then flows back to the surface through the "annulus" formed by the drillstring outer wall and the surrounding formation (or casing string).

The drilling mud serves multiple functions (van Oort, 2013):

- provide a primary barrier against formation fluids, by maintaining sufficient hydrostatic and circulating pressure (or equivalent circulating density (ECD));
- prevent the wellbore wall from collapse due to shear, compressive or tensile failure;
- circulate drill cuttings from the bit to the surface solids processing equipment;
- provide cooling and lubrication to the bit;
- reduce the friction between the drillstring and the wellbore wall;
- create a low-permeability filter cake around the wellbore wall, which aids in sealing porous and permeable formations to minimize formation damage;
- provide a physical channel for transmission of information between surface and downhole equipment (and vice versa), through mud-pulse telemetry;

- assist in the collection and interpretation of data from logging tools used in evaluating petrophysical properties of the drilled formations.

If at any point the bottom-hole pressure (BHP) falls below the formation pore pressure, an influx ("kick") of hydrocarbons and other fluids contained in the formation will occur. When the kick is not contained, it can travel up the annulus at high flow rates and pressures, resulting in a "blow-out" which can have disastrous consequences for the safety of the rig crew and of the environment. As soon as an influx is detected, the typical response is to shut-in the well by closing the blow-out preventers (BOP) located at the wellhead, then circulate the influx through a choke manifold in a controlled fashion and displace the mud to a heavier one that will restore static over-balance. The actions described are commonly categorized as "well control" procedures, and can take on several flavors, based on the operational method. The most common ones are the "Driller's Method" and the "Wait and Weight" (W&W) method, although the "volumetric" , "concurrent", "bullheading" or "dynamic kill" methods are sometimes employed, based on the complexity of the well control situation (van Oort, 2013).

The BHP also needs to stay above the collapse pressure, in order to prevent compressive (shear) failure at the wellbore wall, which may result in pack-off or stuck pipe scenarios, or at the very least, over-gauge hole sections. There are cases when it is desired to drill underbalanced with respect to the pore pressure (i.e. BHP between collapse and pore pressure), effectively producing hydrocarbons while drilling the well. The underbalanced drilling

(UBD) technique requires additional equipment on the outlet side for handling the hydrocarbon flow, and on the inlet side, for injecting foaming agents and gas in order to reduce the drilling mud hydrostatic head. Focus in the remainder of this document will be on overbalanced drilling conditions.

In addition to maintaining overbalance with respect to the formation pore pressure and collapse pressure, it is also required for the static and circulating mud density to not exceed the fracture gradient, above which fractures are initiated, resulting in mud being lost to the formation. Sustained lost circulation can lead to significant reduction in the hydrostatic head, which may lead to underground blow-out situations. In extended-reach (i.e. wells with a horizontal extent of more than twice the vertical depth), deepwater wells, or wells drilled in depleted hydrocarbon reservoirs, the window between pore pressure/collapse pressure gradient and fracture gradient (also known as the "drilling margin") can become extremely narrow (see Figure 1.1 for a graphical depiction). In such wells, very accurate mud system planning and casing point selection is required to negotiate the narrow pressure window successfully. The mud density (commonly referred to as "mud weight") has to fall within this window at all times. Even when ECD values while drilling lie within reasonable margins of the mud window limits, during pipe movement in and out of the well ("tripping"), "swab" or "surge" pressures can draw the effective mud weight above or below those limits. For instance, a "swab" kick may be taken while the pipe is being tripped out of the well, for instance, when changing the bit or BHA. Once pipe movement is halted, the downhole pressure may again

reach overbalance, but the well may need to be shut in to allow safe removal of the kick. The kick tolerance (the maximum gas volume which can be safely circulated without fracturing the formation) may be lower than 10 bbl in wells with narrow drilling margins (Karimi Vajargah et al., 2014). In light of these problems, the MPD technology has been developed to facilitate safe drilling in the most challenging pressure window environments.

The International Association of Drilling Contractors (IADC) defines MPD as "an adaptive drilling process used to more precisely control the annular pressure profile throughout the wellbore" with the declared objectives "to ascertain the downhole pressure environment limits and to manage the annular hydraulic pressure profile accordingly" (Malloy et al., 2009). Several varieties of MPD have been developed and commercialized, the majority over the past decade. These include the Surface Back-pressure technique (also known as Constant Bottom-Hole Pressure (CBHP)), Continuous Circulation Systems, Dual Gradient Drilling with Mud Cap methods (floating and pressurized), Mechanical Lifting Devices (Mud Lift, EC-Drill) etc. (van Oort, 2013). This work will primarily focus on the CBHP technique, but the methodologies developed herein may be extended to the other embodiments of MPD.

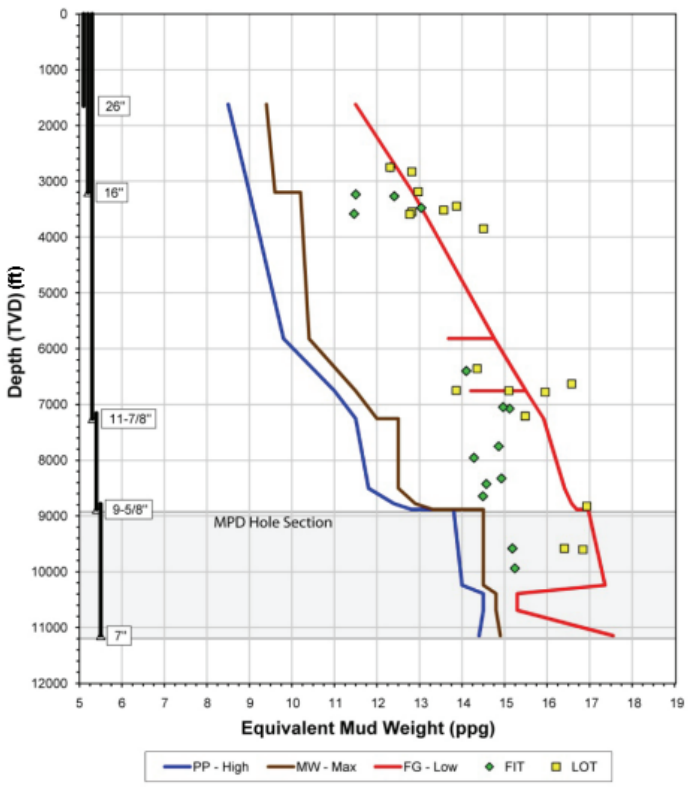

Figure 1.1: Pore pressure (PP) and fracture gradient curves (FG) versus true vertical depth (TVD) from a deepwater Gulf of Mexico well (from Fredericks et al. (2011)). Markers indicate formation integrity tests (FIT) and leak-off tests (LOT) used for fracture gradient estimation. The drilling margin at 10,500 ft is less than 1 lbm/gal (ppg) in this example.

1.1.2 Equipment Used in CBHP MPD

CBHP MPD requires specialized equipment in addition to the components used in conventional drilling operations. Figure 1.2 presents a flow schematic for a state-of-the-art automated MPD system, the Dynamic Annular Pressure Control (DAPC) system. The main components of the MPD

system include the Rotating Control Head (also known as Rotating Control Device (RCD)), along with a specialized choke manifold and a back-pressure pump. These elements are illustrated in further detail in Figure 1.3.

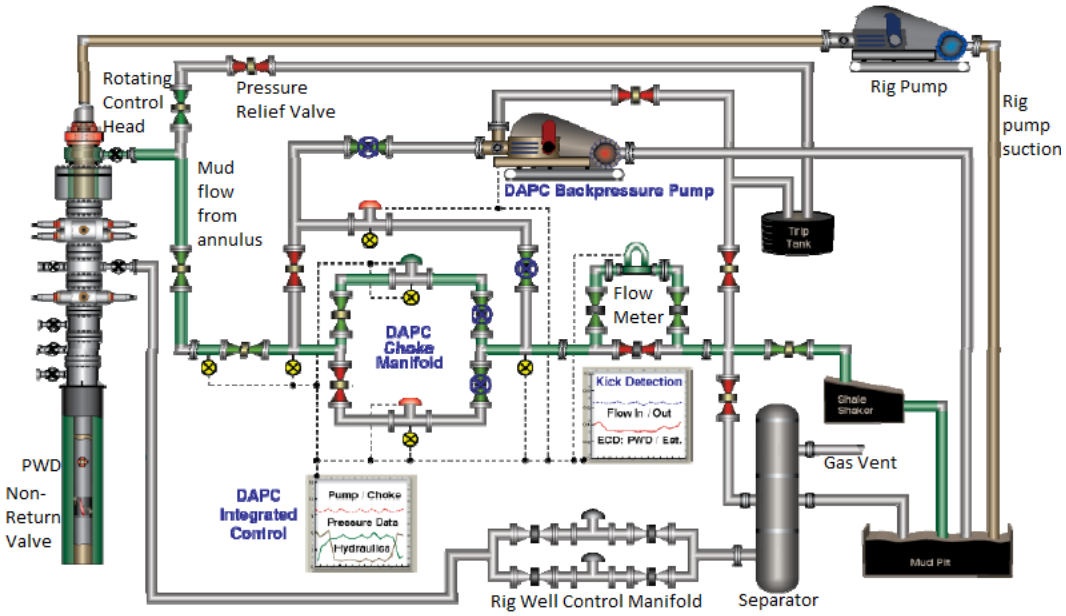

Figure 1.2: Flow schematic for the DAPC MPD Control System (from Chustz et al. (2008)). The mud flow path is indicated in green. The mud returns from the annulus through the choke manifold. The redundant chokes have an adjustable valve opening which changes the amount of back-pressure applied to the flow. A back-pressure pump provides flow through the choke manifold when the main rig pumps are turned off. A non-return valve prevents backflow in the drillstring. The chokes and back-pressure pump may be automatically operated from an integrated control module connected to a hydraulics model and Pressure While Drilling (PWD) sensors.

(a) RCD (b) Choke manifold (c) Back-pressure pump

Figure 1.3: Depictions of MPD equipment (from Saeed et al. (2012)).

The RCD is mounted on top of the blow-out preventer stack and creates a dynamic seal of the annular space, which results in a closed hydraulic system (Saeed et al., 2012). The return flow is diverted through the MPD choke manifold, which can be manually operated or automatically controlled. Two or three chokes are typically installed in parallel to provide redundancy in case of failure. In the most basic form of MPD, a specially trained operator adjusts the choke opening to trap or release back-pressure in order to maintain constant pressure at a selected pivot point, which is the point where the difference between the limits determined by the pore/collapse and fracture pressure gradient is the smallest. This pivot point is typically located at the bottom of the well for a converging pressure window or at the casing shoe for a diverging one (van Oort, 2013). The trapped pressure approach is commonly performed during drilling connections, where the main rig pump rate is gradually stepped down while the choke opening is reduced (Medley et al., 2008). Conversely, when restarting the pumps, the trapped pressure is released by opening the choke. The inclusion of a back-pressure pump upstream of the

choke allows for continuous flow through the choke when the main pump is disconnected, such as during a connection procedure. Alternately, a rig pump diverter system can be used to redirect the flow from the standpipe manifold to the choke line, thus reducing the complexity caused by introducing an additional pump (Saeed et al., 2012). Furthermore, circulation of mud into the drillstring during connections can be maintained using a Continuous Circulation System (Calderoni et al., 2006) or Continuous Circulation Valve (Torsvoll et al., 2006).

Of equal importance to the success of the operation are the sensors used to monitor the essential rig parameters during MPD. The wellhead pressure sensor responsible for measuring the pressure upstream of the choke is of paramount importance for automation of back-pressure MPD. Redundant combinations of sensors (typically three), mounted at the wellhead, provide contingency in case one of them fails (Saeed et al., 2012). Additional pressure sensors are mounted downstream of the choke, on the standpipe (which measures the total circulating pressure in the hydraulic system) and at the bottom of the well. The choke skid is also instrumented with sensors for measuring the choke position, fluid temperature and flow rate. The latter is preferably obtained from a Coriolis meter, which also characterizes the fluid density. Coriolis meters are used less frequently on the inlet side of the hydraulic system, where pump stroke counters have to this day been the standard for determining circulation rates. Counting pump strokes is an indirect and often unreliable measurement technique. Other sensors used on a drilling rig

(both MPD and conventional) include rotary RPM, hook load, torque and block height sensors, which can be used to infer other real-time drilling parameters, such as bit depth, weight-on-bit, and rate of penetration. Downhole sensors are also available in some cases, with the most important one, for MPD purposes, being downhole pressure. Downhole instrumentation also includes temperature sensors, accelerometers for monitoring vibration and borehole inclination, magnetometers, formation evaluation tools (Gamma ray, resistivity, sonic logging etc.), and strain gauges for measuring weight on bit, torque on bit and bending moments. These sensors are typically located right above the bit, or above the downhole motor, and reside in specialized subs.

1.1.3 Operational Challenges

Several important items need to be addressed when designing control systems for CBHP MPD. Wells drilled with MPD are typically characterized by narrow pressure margins, and thus pressure control needs to be precise, with little room for error. The bandwidth of the physical system varies with scale, which can go from shallow wells to Extended Reach Drilling (ERD) wells, with total depths in excess of 30,000 ft (Gradishar et al., 2014). As the well measured depth increases, so does travel time for a pressure wave generated at the surface (standpipe or choke) to reach the bottom of the well, which complicates pressure control. Based on a 1000 m/s (3000 ft/s) sonic velocity in an oil-based drilling fluid (Kaasa et al., 2012), a 10-km ERD well would take about 20 seconds for a pressure wave to travel from the choke line all the way

down the annulus and back up to the standpipe, and thus the choke controller needs to be able to perform very fine changes to avoid excessive pressure fluctuation and potential instability. This situation is further complicated when gas is present in the well, as the compressibility of a gas-liquid mixture tends to be significantly higher than that of the pure liquid, even at low gas volumes (Kaasa et al., 2012). This makes pressure control during a gas kick even more challenging, particularly when dissolved gas breaks out of the drilling mud, and the resulting free gas rapidly expands as it reaches the surface.

The control bandwidth is further limited by the choke closing and opening time, and also by the flow rate through the choke. The controller needs to handle both high and low flow rates, such as the slow circulation rates used in well control. During pump staging and connections, an additional backpressure pump or flow diverters are needed to maintain the desired BHP. In such cases, precise coordination between pump and choke control modules is crucial to achieve the desired pressure response with minimal overshoot or undershoot. In addition, the controller needs to handle external disturbances, such as hoisting and lowering of the drillstring, or heave motion on floating off-shore rigs. A robust control system needs to accommodate various contingency scenarios and non-ideal operating conditions, starting with kicks and loss of drilling fluid, and continuing with plugged or washed out choke valves or bit nozzles, pump degradation and failure, leaks in the drillstring, annulus pack-offs due to cuttings accumulation, borehole enlargement, etc. (Figure 1.4).

In addition to process faults, data quality is another important aspect to account for in an MPD control system, as closing the loop with bad data can lead to hazardous situations. Sensor and actuator redundancy can alleviate some of these problems, but cost and space constraints on a drilling rig often limit the amount of physical redundancy available. Even with properly functioning sensors, data acquisition and telemetry rates may not be fast enough to enable the desired pressure control, particularly when downhole measurements are used for feedback.

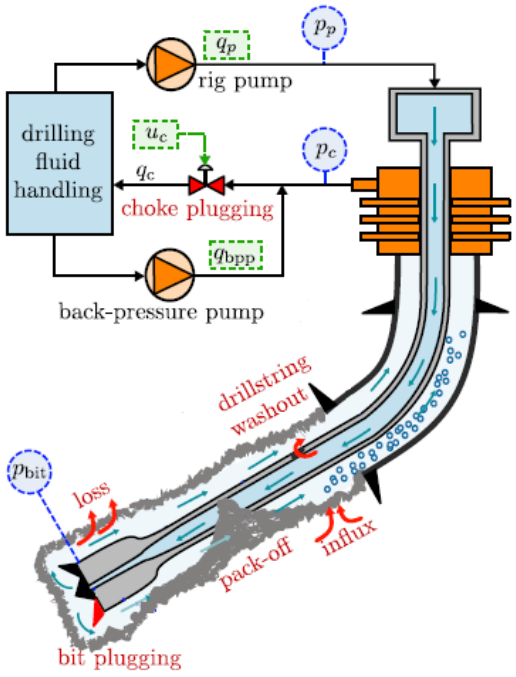

Figure 1.4: Illustration of common faults (shown in red) in MPD operations (from Willersrud et al. (2013)). A plugged choke may occur due to cuttings or solid particles in the drilling mud. The solid particles may also plug the drill bit nozzles. A leak in the drillstring ("washout") can create an additional flow path from the drillstring to the annulus. Finally, cutting beds may form in the annular section causing a flow restriction or a "pack-off".

Another important challenge lies in the ability to model the physics of the drilling process with sufficient accuracy for the task at hand. For MPD, and well control in general, the hydraulic domain is the most critical, and precise control of wellbore pressure can be quite a difficult task. Hydraulic models can be fairly complex, requiring large computational power and a vast number of inputs. When real-time operation is required, such as for low-level control or set point generation, some of that complexity needs to be traded off to allow faster computation. Simpler models often misrepresent transient and spatial effects, particularly in ERD wells. Multi-phase flow is much more complex to model than single-phase (liquid only) flow, and is often not amenable to model-based control design. However, using a controller designed with a single-phase model during a multi-phase scenario, such as gas kick handling, may often generate erroneous control actions or set points. The degree to which the models can represent uncertainty is also a desirable quality, since many well parameters are uncertain or unknown.

The amount of tuning and calibration required by a model, and how often calibration needs to be performed, are also critical selection criteria when evaluating a hydraulic model. For instance, in deep HPHT wells, down-hole pressure and temperatures vary greatly from surface conditions, and the drilling fluid properties, measured at surface, need to be re-calibrated at the downhole conditions at regular depth intervals. Other properties, such as gel strength, are time-dependent, while mud density can vary with both space and time (e.g. after a long period without mud circulation, density may experience

variations across the wellbore due to differential settling of weighting material, known as "barite sag"). The ability to quickly update model parameters in response to unforeseen events and faults also needs to be considered, especially if these parameters are featured in the control law.

1.2 Research Objectives

This dissertation aims to address some of the shortcomings of currently available MPD control systems, particularly their reliance on over-simplified process models and lack of considerations for process uncertainty and unplanned events. To tackle this problem, the work presented here introduces a fast and easy to implement numerical model for multi-phase hydraulics, which can be used to develop advanced control and estimation algorithms catered to MPD operations. The novel modeling approach starts with the multi-phase mass and momentum conservation equations and derives a simplified model consisting of a set of coupled partial and ordinary differential equations.

A second objective is to explore robust automated choke control algorithms for MPD. Several advanced control techniques, including feedback linearization, LQG control, and gain scheduled controllers developed using convex optimization techniques are investigated and applied to the problem of pressure regulation in back-pressure MPD scenarios. The design process includes robustness considerations and attempts to quantify the modeling and approximation errors for a wide range of operating points and two-phase conditions. The control design also includes algorithms to handle kick and lost

circulation events, where the goal changes from keeping a constant pressure target to minimizing losses or influx in the well.

The final objective of this dissertation is to develop a methodology for automated event detection in MPD, which can handle uncertain and potentially noisy sensor data, and to demonstrate the detection capabilities in a series of simulations with induced faults. A Bayesian network model of MPD hydraulics is developed for this purpose. Once a fault is detected, the model also requires adjustment of certain parameters to capture the new system conditions. For this purpose, several parameter estimation algorithms are developed for quantifying influx and lost circulation rates, evaluating formation pore and fracture pressures, and also for monitoring hydraulics parameters such as pump efficiency and choke valve area. The control algorithms require permanent communication with the event detection and parameter estimation modules, such that the control inputs can be updated to handle both ideal and degrading system conditions.

1.3 Dissertation Outline

The dissertation is structured as follows:

- **Chapter 2** presents a detailed literature review of back-pressure MPD control systems, citing both industry and academic approaches. It also presents a broad survey of modeling, estimation and event detection techniques used in MPD applications. Finally, it highlights issues per-

taining to sensor data quality with a focus on how they relate to MPD systems.

- **Chapter 3** is focused on hydraulics modeling for MPD. It starts by surveying the existing modeling techniques for both single- and multi-phase flow, and gives the mathematical formulation for the various models. It then proceeds with the development of a simplified transient model based on a reduced Drift-Flux model. The model is validated using a high-fidelity hydraulics simulator and experimental data. A large portion of this work has been published in several conferences and journals (Ambrus et al. (2015a), Aarsnes et al. (2016b) and Ambrus et al. (2016)).

- **Chapter 4** elaborates the development and testing, through simulation scenarios, of choke control algorithms for back-pressure MPD. The techniques used include feedback linearization, LQG control, and gain scheduled controllers designed using Linear Matrix Inequalities (LMI) techniques. A part of this chapter, specifically the general control structure and application of LMI methods for robust choke control design has been published in the Journal of Process Control (Aarsnes et al., 2016a), and the work there has been extended by implementing an adaptive control gain computed using the simplified model detailed in Chapter 3.

- **Chapter 5** builds upon the control algorithms described in Chapter 4 by adding event detection and observers for parameter estimation, including pore and fracture pressure estimation during kick and lost circulation

events. First, the theory behind each of the methods is detailed, and then the complete system is evaluated in a series of simulated test cases representative of events that need to be handled by an MPD system. A large part of the work in this chapter has been published in a conference paper (Ambrus et al., 2017), and some of the estimation algorithms described have been featured in additional publications (Ambrus et al. (2016), Aarsnes et al. (2015)).

- **Chapter 6** presents the highlights and contributions of this dissertation and suggests recommendations for further work on this topic.

- **Appendix A** lists the key symbols, abbreviations and acronyms used in this dissertation.

- **Appendix B** details the numerical scheme for implementation of the hydraulics model.

- **Appendix C** details the frictional pressure calculations used in the hydraulics model.

- **Appendix D** shows a detailed derivation of the LMI formulation in Chapter 4.

- **Appendix E** lists the publications authored or co-authored as part of this doctoral study.

- **Appendix F** contains paper SPE/IADC 173164-MS (Ambrus et al., 2015b) by the author of this dissertation. This paper proposes a more

general framework for designing control algorithms for various drilling automation tasks, some of which extends beyond the scope of this dissertation. As it contains aspects which are also relevant to MPD control, it is included here for reference.

Chapter 2

Literature Review

The following sections review the state-of-the-art in MPD control systems, modeling and estimation techniques used for MPD control design, as well as issues pertaining to drilling rig data quality and event detection in an MPD context. These are followed by a critical summary of the literature findings.

2.1 MPD Control Systems

Over the past decade, the CBHP MPD technique was developed into several commercial systems that were successfully deployed in the field. The most notable ones are Micro-Flux Control (Santos et al., 2003) (Leuchtenberg, 2008) and DAPC (van Riet et al., 2003) (van Riet, 2005). The former relies on detecting influxes and fluid losses from differential flow rate measurement and manipulating the choke opening to mitigate those influxes and losses by adding or reducing back-pressure. The Micro-Flux system also enables real-time estimation of fracture and pore pressure, if downhole pressure measurements are available (Rostami et al., 2015). The DAPC method, on the other hand, contains a feedback loop that allows regulation of downhole pressure throughout

the operation, with automatic adjustment of choke opening as well as flow from a back-pressure pump (van Riet et al., 2003). The typical implementation of DAPC relies on a PID controller which requires extensive tuning by the operator, sometimes taking up to several hours, and re-tuning needs to be performed when the operating conditions change (Reitsma and Couturier, 2012). Nevertheless, successful field implementation of the system was reported for several offshore projects (Roes et al., 2006) (Chustz et al., 2007) (Fredericks et al., 2010). Another commercial system using separate valves on the standpipe, return line and a bypass line, diverting flow from the standpipe to the annulus, was devised to allow a constant BHP to be maintained in the event of a drill string connection, without requiring a back-pressure pump (Lovorn et al., 2012). A linear PID controller was also used in conjuction with a Continuous Circulation System in high pressure/high temperature wells in the North Sea (Iversen et al., 2006) (Bjørkevoll et al., 2008) (Syltoy et al., 2008), enabling development of fields which were inaccessible with conventional drilling methods due to the very narrow pore pressure / fracture margins. Figure 2.1 shows the layout of a typical MPD control system. A hydraulics model calculates a choke pressure set point based on a desired downhole pressure, and the choke and/or pump rate are automatically adjusted to track the set point. In other operating modes, the control goal is to track a choke pressure or choke position set point calculated without consideration for downhole conditions (Saeed et al., 2012).

As MPD started gaining increased acceptance in the oil and gas indus-

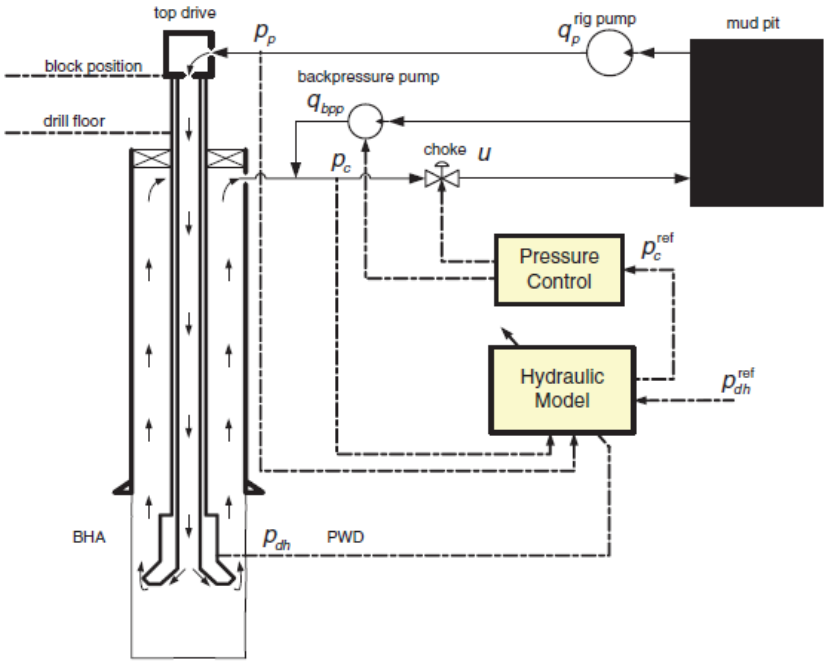

Figure 2.1: Control system block diagram of an automated MPD system (from Kaasa et al. (2012)). The main control variable is the choke position (u), while the rig pump rate (q_p) and back-pressure pump rate (q_{bpp}) can be treated as known disturbances for control design. Measurements of pump pressure (p_p), choke pressure (p_c), and downhole pressure (p_{dh}), together with a downhole pressure set point (p_{dh}^{ref}) are supplied to a real-time hydraulics model. This model calculates the choke pressure set point (p_c^{ref}) for the feedback controller.

try, a set of guidelines and specifications were outlined by operator companies to ensure proper performance of the system. The MPD control system was required to maintain downhole pressure within 5 bars (70 psi) of the setpoint at all times, and have a closed loop response time of no more than 30 seconds (Godhavn, 2010). Recommendations were also given for the choke actuation, with the choke being capable of closing within 10-30 seconds, and its actual opening has to be within 0.1% of the command value at steady-state. Addi-

tionally, the controller should have a minimum phase margin of 45° to avoid instability caused by slow choke dynamics and measurement delays (Godhavn and Knudsen, 2010). The system should be able to handle various operational modes (drilling, pump start-ups and shut-downs, drillstring connections, pipe tripping), as well as critical situations, such as influxes from the formation, mud losses, rig power failures and plugged choke instances (Godhavn, 2010). Additionally, on floating rigs, the system has to compensate for pressure fluctuations induced by the vertical motion of the drillstring due to heave (Landet et al., 2012b).

While the industry continues to rely predominantly on simple PID solutions, several researchers in the past years have investigated more advanced control methodologies for CBHP MPD. Godhavn (2010) developed a gain scheduled PID controller to increase robustness with respect to different operating conditions. Godhavn et al. (2011) present a control law derived using feedback linearization which accommodates the process non-linearity introduced by the choke. This set-up involves computing a reference choke flow rate using feedback from the measured and desired choke pressure, and then using these to compute the choke actuation required to achieve that flow rate. The resulting controller was implemented on a test drilling rig and the authors reported that it performed better than a conventional PID scheme. Significant research has also been invested in adaptive and Model-Predictive Control (MPC) solutions. Most of these controllers were only tested using simulation models and thus their real-world performance has yet to be inves-

tigated. Zhou et al. (2008) present an adaptive output feedback controller which is used to track the reference BHP. Lyapunov analysis is used to prove asymptotic stability of the closed loop system. $\mathcal{L}_1$ adaptive control is used by Li et al. (2011), allowing tracking of BHP with robust performance bounds in the presence of uncertain parameters and unmodeled dynamics. An adaptive controller designed using the backstepping method is used for choke pressure tracking in Hauge et al. (2012b). This particular control design is selected in order to accommodate unmeasured disturbances as well as actuator dynamics. Stakvik et al. (2016) use an adaptive model-based choke control scheme where the bulk modulus of the drilling fluid is updated based on real-time pressure and flow measurements.

MPC is employed by several authors (Breyholtz et al., 2010b) (Breyholtz et al., 2010a) (Siahaan et al., 2014) (Pixton et al., 2014) (Eaton et al., 2015) with application to drilling, connections and tripping operations. Breyholtz et al. (2010b) propose a multi-level framework for MPD control systems, consisting of an optimization level, a supervisory level based on linear MPC and a feedback control level with gain scheduled PI controllers. The manipulated variables include choke opening, main pump and back-pressure pump rates and drillstring axial velocity. The MPC serves to provide reference values to the inner control layer with the objective of regulating BHP and hook position, the latter being essential to reducing swab and surge pressures during pipe tripping. While the optimization level is not presented in sufficient detail, the authors propose that a rolling horizon approach can be used there,

with the primary goal of optimizing net present value of the operation. Ultimately, it is claimed that this multi-level control architecture can outperform multiple decentralized controllers (Breyholtz et al., 2010b). Aside from MPC and adaptive control, other methods investigated in recent years include Linear Quadratic Gaussian (LQG) Control (Aarsnes et al., 2012), $\mathcal{H}_\infty$ Control (Yilmaz et al., 2013), Fuzzy Logic Control (Yilmaz et al., 2011) and boundary control for stabilization of an infinite-dimensional hyperbolic system (Aamo, 2013).

On the topic of kick handling in MPD, Carlsen et al. (2008) use an Internal Model Controller to coordinate choke opening and pump rate. The result is a dynamic shut-in procedure which is shown in simulations to be more effective than a conventional shut-in, such as Driller's Method. This approach is further investigated in Carlsen et al. (2013), where Internal Model Control is evaluated against PI control and MPC for the task of maintaining constant BHP while the kick is circulated out of the well. Zhou et al. (2011) implement a switched control scheme for kick attenuation. During normal drilling conditions, the controller relies on a feedback term from the downhole pressure and feedforward term for the flow rate disturbance, whereas during the kick, it switches to a feedforward, pure flow controller. Hauge et al. (2012a) use a pure flow controller in conjunction with feedback linearization of the choke dynamics. Since it does not take pressure into account, this controller has to be switched off once the influx is attenuated, in order to avoid drift in the downhole pressure. A multivariable controller capable of controlling BHP

as well as Rate of Penetration (ROP) was developed by Shishavan et al. (2014). The approach therein uses Nonlinear Model Predictive Control to coordinate choke opening, pump rate, surface rotation rate and WOB. When a kick is detected, the pressure controller switches from downhole pressure setpoint to choke pressure setpoint and adjusts the manipulated variables until the kick is attenuated. The authors claim that adding the surface rotation as a manipulated variable has the effect of attenuating the kick faster by providing additional annular friction.

2.2 Modeling and Estimation for Control Design

All MPD control systems discussed in the previous section were developed using transient hydraulic models. Advanced multi-phase flow models consisting of nonlinear partial differential equations are available in the oil and gas industry (Bendiksen et al., 1991) (Petersen et al., 2008) (Cayeux and Daireaux, 2013), but using these models directly for control system design is not practical due to their mathematical complexity and slow run times. One possible solution is to use such models for generating step response simulations in order to capture the flow and pressure dynamics. By stepping choke opening and pump rate, one may construct transfer functions relating these to back-pressure and BHP, while computing time constants and delay times to characterize the system response. This approach is used in several of the aforementioned control designs, particularly in those involving MPC (Breyholtz et al., 2010b) (Breyholtz et al., 2010a) (Siahaan et al., 2014) (Carlsen

et al., 2008) (Carlsen et al., 2013).

A popular approach for MPD control design is the use of low-order lumped models, the most frequently cited one being the model developed by Kaasa et al. (2012). This model essentially represents a discretization of the continuity and Navier-Stokes equations for two separate control volumes modeling flow inside the drillstring and annulus, respectively. This results in a system of three first-order ordinary differential equations, with pump pressure, choke pressure and flow rate at the bit as the states. The model depends on several time-varying uncertain parameters, such as the fluid bulk modulus, the density of the fluid in the annulus and the hydraulic friction factor. These typically depend on the downhole temperature and pressure profiles, and can be substantially altered when gas is present in the well. The parameter with the highest impact is the bulk modulus, which characterizes the pressure transients in the well (Kaasa et al., 2012). As a result, these parameters need to be calibrated on-line from the available measurements. Experimental validation of the model was conducted on data from MPD tests performed in a North Sea well (Stamnes, 2011). The Kaasa et al. model is used predominantly by the adaptive control designs (Zhou et al., 2008) (Zhou et al., 2011) (Li et al., 2011) (Hauge et al., 2012a) (Hauge et al., 2012b), and also by the controllers proposed in (Godhavn et al., 2011),(Yilmaz et al., 2013) and (Shishavan et al., 2014).

Other researchers have investigated higher-order lumped models obtained by discretizing the drillstring and annulus into multiple control vol-

umes. This approach has the advantage of capturing high-frequency pressure transients, which is particularly important for the heave problem, where a simple model like the one proposed by Kaasa was found to be insufficient for designing a controller with good disturbance rejection properties (Landet, 2011). The higher order model developed by Landet (2011) matched pressure data collected from a test rig much better than the Kaasa model. The work by Landet also investigated issues related to non-ideal choke behavior, such as rate limitations, stiction and dead bands, which introduce additional non-linearities to the model. An alternative to lumped models is using an infinite-dimensional hydraulic transmission line model which captures the pressure wave propagation in a more realistic way. The standard equations for a hydraulic transmission line are derived from the mass, momentum and energy conservation relations for axial, laminar fluid flow (Goodson and Leonard, 1972). The resulting system of partial differential equations (PDE) can be expressed in Laplace transform notation using the characteristic impedance and propagation operator. Hydraulic transmission lines have been applied to modeling of MPD operations in the work of several authors (Landet et al., 2012a) (Mahdianfar et al., 2012) (Aamo, 2013) (Aarsnes et al., 2012). The frequency response of the transmission line model was also used to evaluate the error generated by finite order discretization of the pressure dynamics with variable number of control volumes (Aarsnes et al., 2012). This error becomes more significant as the number of control volumes is reduced or when the length of individual control volumes increases.

The models described above contain unmeasured states and uncertain parameters which need to be estimated in real-time, such as fluid friction factors, mud density, and bulk modulus. In response, researchers on the MPD control problem have also devoted significant time to designing efficient estimation techniques. For the low-order model developed by Kaasa et al., nonlinear adaptive observers were designed to estimate the friction factor and density together with flow rate and pressure at the bit (Stamnes et al., 2008) (Stamnes et al., 2011). Recursive Least Squares was used for bulk modulus estimation (Kaasa et al., 2012). Gravdal et al. (2005) et al. used an Unscented Kalman Filter for calibration of drillstring and annulus friction factors. Pixton et al. (2014) implemented a Moving Horizon Estimator for calibrating the annulus friction factor and density. Aamo (2013) used a backstepping transformation to design an infinite-dimensional observer for estimating the states of a transmission line hydraulic model. Other researchers used neural network models to predict unmeasured parameters (Nybø, 2009) (Pool et al., 2013).

The problem of estimating reservoir parameters during kick handling is also tackled from different angles. Zhou et al. (2011) use adaptive observers to estimate reservoir flow rate and pore pressure. The estimation is shown to be accurate until gas expansion in the annulus becomes significant. An adaptive observer is also used by Hauge et al. (2012a) for estimating the influx rate in addition to the location along the wellbore where the influx occured. In a follow-up publication, the same authors use an infinite-dimensional boundary observer designed using backstepping transformations applied to a linear

hyperbolic PDE system (Hauge et al., 2013). This observer is applied to a transmission line model of the drilling hydraulics in order to estimate influxes or lost circulation occuring at the bottom of the well. Gravdal et al. (2010) use the surface back-pressure build-up curve resulting from a shut-in procedure together with wired drill pipe[1] measurements to estimate pore pressure. When the back-pressure curve becomes linear, this is an indication that pressure equilibrium has been reached in the influx zone. The measured downhole pressure can then be used as the new pore pressure estimate. Application of this algorithm requires the well to be completely shut-in, and thus timely kick detection is important to avoid fracturing the formation with excessive shut-in pressures. Research has also been done on modeling gas expansion dynamics following a kick incident. An ordinary differential equation model of the gas percolation is developed from first principles by Hauge et al. (2012c). The gas bubble is assumed to have a triangular distribution profile. An Unscented Kalman Filter together with wired drill pipe pressure and temperature measurements are used to estimate the gas distribution parameters, gas bubble rise velocity and mass of gas in the annulus. The validity of this model holds from the time the influx is taken up to when the gas bubble reaches the choke.

2.3 Drilling Rig Sensor Data Quality

An aspect that cannot be neglected for a drilling automation task is the quality of measurements that are fed to the controllers and estimators.

[1]Details on the wired drill pipe technology will be given in a later section.

Common data quality issues encountered on drilling rigs include calibration errors, data gaps, outliers, inconsistent units, drifting and noisy sensor readings (Mathis and Thonhauser, 2007) (Arnaout et al., 2013). If these data are also fed to a system for detecting process faults, such as influxes from the formation, false alarms or missed detection situations may arise. Frequent false alarms may cause significant non-productive time on the rig and distract the drilling team from other potential hazards, eventually diminishing their trust in the alarm system (Nybø et al., 2008) (Nybø et al., 2012). Remedial measures such as filling data gaps by interpolation, removing outliers by median filtering and verifying that parameters lie within physical limits can be automated by a data quality control module (Mathis and Thonhauser, 2007). Models need to be calibrated and continuously updated to reflect changes in drilling parameters (Nybø and Sui, 2014). Discrepancies between models and measurements can be overcome by combining physical models with artificial intelligence in order to reduce false alarms and provide better data quality control (Nybø et al., 2008).

The data quality problem may not arise from the sensors used, but from the data acquisition process itself. One such problem is when a sensor reading is updated faster than the acquisition system can process. Citing an example from Arnaout et al. (2013), the measurement of traveling block position[2] may drift when pulling the block too fast. This will affect the computed axial

[2]The traveling block is a component of the rig hoisting system. Its position is typically measured with an encoder mounted on the draw works drum

drillstring velocity, which is used in ROP calculations, and also for predicting swab and surge pressure while tripping. In other cases, the sensor resolution might be insufficient to feed new measurements to the control system in a timely manner. For instance, the pump rate measured from stroke counters needs a full revolution for a new value to be recorded. Thus, when starting the pump at low speeds, it may take up to 30 seconds for a non-zero pump rate to be recorded (Cayeux et al., 2013). As a result of this delayed measurement, the choke may open too late, causing an undesired pressure spike (Gravdal et al., 2014). Alternately, the rotational speed of the pump motor may be used to infer the pump strokes per minute. In the absence of an encoder on the pump motor shaft, the drive command value may be used, but this might not reflect the actual speed, since the mud pump motor is typically controlled in open-loop mode (Cayeux et al., 2013). Furthermore, in order to be used in the hydraulic model, the pump stroke rate must be converted to volumetric flow rate. This requires information on the pump liner dimensions and volumetric efficiency; failure to update this information will lead to an erroneous flow rate input to the control system (Cayeux et al., 2013).

Transmission of downhole sensor data is another important factor affecting the proper functioning of MPD systems. Mud pulse telemetry is the most common technique used, where pressure pulses encrypting data from downhole tools are detected on surface by standpipe pressure sensors (Pixton et al., 2014). Transmission rates with mud pulse telemetry are limited to 2-48 bits per second (Craig et al., 2013). In long, extended reach wells,

the bandwidth of mud pulse telemetry degrades significantly and use of highly compressible fluid systems such as Synthetic/Oil-Based Muds further increases the transmission delays (Gravdal et al., 2014). These delays, in combination with low sampling rates, can result in significant degradation of the control performance for BHP regulation. Additionally, mud-pulsing does not work below a certain circulation rate or when aerated or foam mud systems are used.

A solution to these problems is the use of Wired Drill Pipe (WDP), a technology developed in recent years, allowing bi-directional data transfer of information across the drillstring at rates up to 57,600 bits per second (Craig et al., 2013). The physical components of WDP include coaxial cables connecting the pin and box end of each pipe joint, with induction coils at both ends of the connection and electronic elements preventing signal degradation (Craig et al., 2013). The WDP network can function with any fluid type, including foam muds, the only requirement being that a continuous connection exists between the surface and downhole environment. In addition to providing increased bandwidth in data transmission, the WDP set-up allows placement of multiple sensors across the drillstring, with direct implications for MPD, where it is advantageous to have annular pressure and temperature measurements at various points along the well (Pixton et al., 2014). Having these distributed sensors allows enhanced capabilities for real-time model calibration and detection of influxes or mud losses, wellbore restrictions or enlargements (Cayeux et al., 2013). Usage of WDP together with MPD systems allowed for signif-

icant risk reduction and rig time savings in several operations, some of them in severely depleted reservoirs (Pixton et al., 2014).

2.4 Drilling Event and State Recognition

For a control system to effectively function in a variety of operating conditions, a software module is necessary to automatically identify drilling-related problems (hereafter referred to as "events"), as well as normal rig states (e.g. drilling, tripping pipe, making a connection). Several event and rig state detection systems have been proposed over the years, some of them implemented as commercial solutions. This section will highlight some of these solutions, particularly the ones that are relevant to MPD systems; as such, the focus will be on detection of hydraulics and well control-related problems.

Several authors employed deterministic approaches to event and state detection. Niedermayr et al. (2004) developed a system for recognizing well control events and rig states based on trends in measured parameters and heuristics. Different algorithms for kick detection were proposed based on the well operational state, all of them requiring calibration and tuning before being used in a real-time setting. Saeed et al. (2011) used a similar approach where they identified parameter signatures from sensor data and compared them to pre-defined event signatures. The system would alert the operator whenever an exact or partial match occurred. Karimi Vajargah et al. (2014) presented a methodology for kick detection based on flow rate measurements, pit gain, pump pressure as well as WDP annular pressure readings. This methodology

is capable of determining the influx size as well as its type (gas or liquid).

Other research involved probabilistic techniques, allowing for event and state detection in the presence of uncertain information. Hargreaves et al. (2001) designed a kick detection system using Bayesian model matching of fluid out-flow rates. This system had the capability to adjust its sensitivity based on the measurement noise, thus reducing the occurrence of false alarms. Field testing of the system was conducted in a number of different drilling environments and promising results were reported, such as the ability to detect a 0.2 bbl kick on a fixed rig, and a 3 bbl influx on a semi-submersible in the presence of heave. Aldred et al. (2008) presented an extension of this work which resulted in an event detection software package capable of recognizing kicks as well as lost circulation and drillstring washouts. Probabilistic methods have also been used for rig state detection, for example by Dunlop et al. (2006) who proposed Kalman Filters and particle filters to automate this task. Other methods investigated for automatic rig state determination include polynomial basis functions fitted to time series data (Arnaout et al., 2012), clustering algorithms (Nybø and Sui, 2014) and Artificial Immune Systems (Serapiao et al., 2007).

Drilling problem identification was also attacked using fault detection and isolation techniques. Willersrud et al. (2013) used a low-order dynamic hydraulics model, a bank of adaptive observers, and generalized likelihood ratio decision functions for diagnosis of faults such as bit plugging, pack-offs and drillstring washouts. The methods were tested on a medium scale flow

loop, showing the capability to identify different faults fairly accurately. Nybø (2009) presented a generalized observer scheme with structured residuals, used to distinguish between normal and faulty behavior in a drilling system. The observer scheme used a grey-box model consisting of a hydraulics simulator and a Recurrent Neural Network for predicting flow rate and mud tank volume.

2.5 Conclusions

Since its introduction more than a decade ago, MPD has matured as a technology, enabling safe well construction in demanding environments. The state-of-the-art in control systems available for MPD shows significant promise for improving rig safety and reducing non-productive time. Commercially available systems such as Micro-Flux, DAPC and their variations have been successfully tested in land and offshore operations. Enhancement of these systems with high-fidelity multi-phase hydraulic models, continuous circulation devices and WDP telemetry have extended the operational capabilities of MPD control systems.

In spite of the promising developments in MPD automation, the current systems are not yet fully autonomous, in the sense that they can not perform a complete drilling routine without operator input. In reality, these systems can be described as providing "supervised automation" at best (Saeed et al., 2012). The existing literature on MPD control systems typically focuses on low-level isolated automation tasks, such as regulating choke pressure or BHP to a desired set point. Few authors have addressed coordination of multiple

automation tasks (Shishavan et al., 2014) (Siahaan et al., 2014) (Carlsen et al., 2008) or multi-layered architectures (Breyholtz et al., 2010b), but the scope of their work would still fall under the "supervised automation" category. Integration of hierarchical control structures with autonomous decision making would be the next step in MPD systems. The framework, however, needs to be cast in a way to gain the operator's trust, offering situational awareness, facile visualization and troubleshooting.

A control problem which demands more thorough investigation is influx handling in MPD operations, particularly when the influx contains gas. Most choke control designs available in the industry are conducted for single-phase flow and consequently do not capture the distributed two-phase flow dynamics inherent during a gas kick event. This leads to degraded performance of the control algorithms and, in some cases, to unstable controllers which must be shut down by the operator (Reitsma and Couturier, 2012). Once gas enters the well, the fluid compressibility changes, causing slower system response and delays in pressure transmission. Thus, robust controllers need to be designed to cover varying quantities of gas present in the well while being able to seamlessly handle the resulting changes in the plant dynamics. In this respect, augmenting the single-phase models typically used for control design with terms accounting for gas expansion is necessary in order to reduce the modeling uncertainty.

Last but not least, a robust MPD control system needs to include provisions for fault detection, isolation and accommodation. Most researchers

have developed real-time event detection systems as a stand-alone application, rather than in the context of a full control architecture or decision support system. Furthermore, most available event detection systems are typically focused on process dysfunctions only, without giving consideration to sensor or actuator faults. An effective detection system must be able to isolate sensor, actuator and process faults using the uncertain information inherent to the drilling environment. A data quality module is also necessary to flag erroneous data while reducing the number of false alarms resulting from improperly calibrated or degrading sensors.

Chapter 3

Development of a Simplified Transient Model for Multi-Phase Hydraulics Modeling

This chapter will present the state-of-the-art in terms of hydraulics modeling for single- and multi-phase scenarios, and then will introduce a new simplified transient model ("reduced Drift-Flux model") for handling two-phase flow in MPD[1,2,3]. A detailed derivation of the new model is presented in Chapter 3.2, followed by validation using high-fidelity simulator software, as well as with an experimental data set (Chapter 3.3). The chapter concludes with a discussion of how the model can be applied to MPD control systems, and more broadly, to automated well control (Chapter 3.4).

[1]Chapter 3.2 is based on the paper: Ulf Jakob F. Aarsnes, Adrian Ambrus, Florent Di Meglio, Ali Karimi Vajargah, Ole Morten Aamo, and Eric van Oort. "A simplified two-phase flow model using a quasi-equilibrium momentum balance". International Journal of Multiphase Flow, Volume 83, July 2016, Pages 77-85. The dissertation author contributed to the model development (in collaboration with Ulf Jakob Aarsnes).

[2]Chapter 3.3 is based on the paper: Adrian Ambrus, Ulf Jakob F. Aarsnes, Ali Karimi Vajargah, Babak Akbari, Eric van Oort, and Ole Morten Aamo. "Real-time estimation of reservoir influx rate and pore pressure using a simplified transient two-phase flow model". Journal of Natural Gas Science and Engineering, Volume 32, May 2016, Pages 439-452. The dissertation author contributed to the model verification using experimental data and multi-phase hydraulics modeling software.

[3]Chapter 3.4 is featured in the paper: Adrian Ambrus, Ulf Jakob F. Aarsnes, Ali Karimi Vajargah, Babak Akbari and Eric van Oort. "A Simplified Transient Multi-Phase Model for Automated Well Control Applications". International Petroleum Technology Conference, December 2015. The dissertation author contributed to the model development, experimental validation, and discussion of applications.

3.1 Background

3.1.1 Single-Phase Modeling

Several modeling approaches exist for modeling flow of liquid in pipelines, ranging from steady-state pressure drop correlations, to partial differential equations governing the mass, momentum and energy balances. The mass conservation for one-dimensional flow can be expressed as (Kaasa et al., 2012):

$$\frac{\partial \rho}{\partial t} + \frac{\partial (\rho v)}{\partial x} = 0 \tag{3.1}$$

where ρ is the fluid density, and v the fluid velocity. Taking the cross-sectional flow area $A(x)$ as piecewise constant, and assuming incompressible flow, the mass balance becomes:

$$\frac{\partial p}{\partial t} + \frac{\beta}{A}\frac{\partial q}{\partial x} = 0 \tag{3.2}$$

where q is the volumetric flow rate of the fluid, the bulk modulus β, relates to the speed of sound in the liquid (c_L), as $\beta = \rho c_L^2$. Next, the momentum balance, derived from the one-dimensional Navier-Stokes equation, is:

$$\rho\frac{\partial v}{\partial t} + \rho v\frac{\partial v}{\partial x} + \frac{\partial p}{\partial x} = -\frac{\partial \tau_w}{\partial x} - \rho g cos(\theta) \tag{3.3}$$

which for incompressible flow ($\frac{\partial v}{\partial x} = 0$), becomes:

$$\frac{\rho}{A}\frac{\partial q}{\partial t} + \frac{\partial p}{\partial x} = -\frac{\partial \tau_w}{\partial x} - \rho g cos(\theta) \tag{3.4}$$

where τ_w represents the shear stress at the pipe wall, g is gravitational acceleration, and θ is the well inclination angle measured from vertical. If we write

the frictional term $\frac{\partial \tau_w}{\partial x} = \frac{k}{A} q$ (where k is a frequency-independent friction factor), and neglect the steady-state hydrostatic component, $\rho g cos(\theta)$, (i.e. we are only interested in perturbed dynamics), we can rewrite the momentum balance as:

$$\rho \frac{\partial q}{\partial t} + A \frac{\partial p}{\partial x} = -kq \tag{3.5}$$

Eq. (3.5), together with Eq.(3.2), form the model for a two-port hydraulic transmission line with losses, which can be expressed, more conveniently for analysis, in Laplace domain as (Goodson and Leonard, 1972):

$$\begin{bmatrix} P_1 \\ Q_1 \end{bmatrix} (s) = \begin{bmatrix} \cosh \Gamma & Z_c \sinh \Gamma \\ \frac{1}{Z_c} \sinh \Gamma & \cosh \Gamma \end{bmatrix} \begin{bmatrix} P_2 \\ Q_2 \end{bmatrix} (s), \tag{3.6}$$

where $P_1(s), Q_1(s)$ and $P_2(s), Q_2(s)$ are the Laplace transforms of pressure and flow rate at the inlet and outlet, respectively, and s is the Laplace variable. The propagation operator Γ and characteristic line impedance Z_c are given as (Goodson and Leonard, 1972):

$$\Gamma(s) = \frac{sL}{c_L} \sqrt{1 + \frac{k}{s}}, \quad Z_c(s) = \frac{\rho c_L}{A} \sqrt{1 + \frac{k}{s}}, \tag{3.7}$$

where L is the length of the transmission line (i.e. total depth of the well, in our case). In equivalent form, the two-port hydraulic transmission line relations can be written as:

$$\begin{bmatrix} P_1 \\ P_2 \end{bmatrix} (s) = Z_c \begin{bmatrix} \frac{\cosh \Gamma}{\sinh \Gamma} & -\frac{1}{\sinh \Gamma} \\ \frac{1}{\sinh \Gamma} & -\frac{\cosh \Gamma}{\sinh \Gamma} \end{bmatrix} \begin{bmatrix} Q_1 \\ Q_2 \end{bmatrix} (s), \tag{3.8}$$

Alternately, a lumped approximation of the pressure-flow dynamics can be used, which splits the well into N control volumes of equal length $l = L/N$:

$$\dot{p}_j = \frac{\beta_j}{A_j l}(q_{j-1} - q_j), \qquad j = 1, \ldots, N \tag{3.9}$$

$$\dot{q}_j = \frac{A_j}{l\rho_j}(p_j - p_{j+1}) - kq_j - \rho_j lgcos\theta, \qquad j = 1, \ldots, N-1 \tag{3.10}$$

$$q_0 = q_p, \qquad q_N = q_c. \tag{3.11}$$

A simple lumped model with two control volumes (one for the inside of the drillstring, and the other one for the annulus section), is (Kaasa et al., 2012):

$$\dot{p}_p = \frac{\beta}{V_d}(q_p - q_{bit}), \tag{3.12}$$

$$\dot{q}_{bit} = \frac{1}{\int_0^L \frac{\rho}{A}\mathrm{d}x}(p_p - p_{bit} - p_c - \int_0^L \Big(\frac{\partial \tau_w}{\partial x} - \rho gcos\theta\Big)\mathrm{d}x), \tag{3.13}$$

$$\dot{p}_c = \frac{\beta}{V_a}(q_{bit} - q_c), \tag{3.14}$$

where V_d and V_a are the volumes of fluid in the drillstring and annulus, respectively, p_p is pump pressure (or standpipe pressure (SPP)), q_p is pump rate, q_{bit} is flow rate through the bit, $q_c = C_v Z \frac{\sqrt{p_c - p_0}}{\sqrt{\rho}}$ is flow rate through the choke and $p_{bit} = \frac{\rho q_{bit}^2}{2A_b^2 C_d^2}$ is pressure drop through the drill bit. In the relation for choke flow rate, C_v is a coefficient related to the choke area, Z is the choke opening, p_c is the surface back-pressure, or casing / well head pressure (WHP), and p_0 is choke downstream pressure. In the bit pressure drop equation, A_b is the total area of the bit nozzles, and C_d is the bit discharge coefficient.

3.1.2 Multi-Phase Modeling

Well control is a very complex process due to transient multi-phase flow behavior. The earliest modeling efforts relied on empirical correlations based on experimental data collected at different liquid and gas velocities (Eaton et al. (1967), Orkiszewski (1967), Beggs and Brill (1973), Mukherjee and Brill (1983)). More accurate are the so-called "mechanistic" models, which rely on first principles laws of mass, momentum and energy conservation. Compared to correlation-based models, mechanistic models are valid over a broader range of velocities and fluid types (Yuan and Zhou, 2009), and are better at capturing transient effects. The simplest mechanistic models for gas kick simulations are the so-called "single bubble" models, which assume that the gas occupies the entire annulus cross-section over a certain length. While these models are very simple to derive and implement, they tend to over-predict annular pressures, especially for small and medium kick sizes (Nickens, 1987).

A general mechanistic two (multi)-phase flow problem is typically formulated by using a two (or multi)-fluid model or a Drift-Flux Model (DFM). In the two-fluid model, each phase is considered separately; hence, the model is formulated in terms of two sets of conservation equations governing the balance of mass and momentum, for each phase, together with a mixture energy balance (Bendiksen et al., 1991). The liquid and gas mass conservation for

one-dimensional two-phase flow can be written as:

$$\frac{\partial(\alpha_L\rho_L)}{\partial t} + \frac{1}{A}\frac{\partial(A\alpha_L\rho_L v_L)}{\partial x} = \Gamma_L \tag{3.15}$$

$$\frac{\partial(\alpha_G\rho_G)}{\partial t} + \frac{1}{A}\frac{\partial(A\alpha_G\rho_G v_G)}{\partial x} = \Gamma_G \tag{3.16}$$

where α_L and α_G are liquid and gas volume fractions, satisfying $\alpha_L + \alpha_G = 1$. ρ_L and ρ_G are liquid and gas density, v_L and v_G are liquid and gas velocity, and Γ_L and Γ_G are liquid and gas mass flow source terms per unit volume. The momentum conservation for liquid and gas yields:

$$\frac{\partial(\alpha_L\rho_L v_L)}{\partial t} + \frac{1}{A}\frac{\partial[A(\alpha_L\rho_L v_L^2 + \alpha_L P)]}{\partial x} - F_i \tag{3.17}$$

$$= -\rho_L g cos(\theta) - \frac{f_L}{8A}\rho_L v_L^2 S_L + \frac{f_i}{8A}\rho_L v_\infty^2 S_i \tag{3.18}$$

$$\frac{\partial(\alpha_G\rho_G v_G)}{\partial t} + \frac{1}{A}\frac{\partial[A(\alpha_G\rho_G v_G^2 + \alpha_G P)]}{\partial x} + F_i \tag{3.19}$$

$$= -\rho_G g cos(\theta) - \frac{f_G}{8A}\rho_G v_G^2 S_G - \frac{f_i}{8A}\rho_G v_\infty^2 S_i \tag{3.20}$$

where $P(x)$ is the pressure along the well, f_i, f_G and f_L are friction coefficients for the interface, gas and liquid phases, S_i, S_G and S_L represent the interfacial, gas, and liquid phase wetted perimeters, v_∞ is the slip velocity (i.e. relative velocity between gas and liquid phases), and F_i is the interphase shear force.

Finally, the mixture energy equation is:

$$\frac{\partial\Big[\alpha_L\rho_L\Big(E_L + \frac{v_L^2}{2} + gh\Big) + \alpha_G\rho_G\Big(E_G + \frac{v_G^2}{2} + gh\Big)\Big]}{\partial t} \tag{3.21}$$

$$+ \frac{\partial\Big[\alpha_L\rho_L v_L\Big(H_L + \frac{v_L^2}{2} + gh\Big) + \alpha_G\rho_G v_G\Big(H_G + \frac{v_G^2}{2} + gh\Big)\Big]}{\partial x} = -H_S - U_H \tag{3.22}$$

$$\tag{3.23}$$

where h is true vertical depth, E_G and E_L are gas and liquid internal energy, H_G and H_L are gas and liquid enthalpies, H_S is enthalpy from mass sources and U_H is heat transfer per unit volume. The introduction of two momentum equations in a formulation presents considerable difficulties because of the associated mathematical complications, uncertainties in specifying interfacial interaction terms between two phases, and also numerical instabilities (Ishii, 1977). The two-fluid formulation with separate momentum balance equations is simplified by using a combined momentum conservation equation and also a closure (slip) relation in the DFM (Evje and Fjelde (2002), Gavrilyuk and Fabre (1996)):

$$\frac{\partial(\alpha_L\rho_L v_L + \alpha_G\rho_G v_G)}{\partial t} + \frac{1}{A}\frac{\partial[A(P + \alpha_G\rho_G v_G^2 + \alpha_L\rho_L v_L^2)]}{\partial x} = -\rho_m g\cos\theta(x) - \frac{2f\rho_m v_m|v_m|}{D} \tag{3.24}$$

$$v_G = C_0 v_m + v_\infty \tag{3.25}$$

In the relations above, ρ_m is the mixture density, v_m is the mixture velocity, D is the wellbore diameter, and C_0 is the slip law profile parameter, which is related to the gas concentration and velocity profile (Shi et al., 2005). The DFM is most frequently used in the literature for multi-phase flow modeling in drilling (Nickens (1987), Podio and Yang (1986), Rommetveit and Vefring (1991), Petersen et al. (2008), Udegbunam et al. (2014)). Model-based estimation and control techniques for distributed systems such as the two-fluid model and the DFM require using either high-order numerical schemes or sophisticated emerging techniques which operate on the partial differential equations

directly (Di Meglio and Aarsnes, 2015). However, such techniques remain too unwieldy, or have yet to mature to the degree required for practical industry application. Consequently, attempts to further simplify two-phase flow models have been made by several researchers. The homogeneous model assumes no slip between phases and uses averaged bulk fluid properties to simplify the mass balance into a single equation for the fluid mixture (Shirdel and Sepehrnoori, 2012). Hauge et al. (2012c) proposed a second-order ODE model together with algebraic relations to model the gas bubble distribution along the well. A first-order PDE model was introduced by Taitel et al. (1989), while a second-order PDE model was proposed by Masella et al. (1998) and employed by Choi et al. (2013). Such models, called No Pressure Wave models or Reduced DFMs, receive their justification from the fact that for many applications we are more interested in the slow gas propagation dynamics than the fast pressure transients. Furthermore, since the validity of the full DFM representation of fast pressure dynamics is questionable, the case can be made for the pressure wave dynamics to be discarded (Linga et al., 2015). However, discarding the pressure dynamics results in discrete jumps in pressure responses to changing boundary conditions, which makes the model unsuitable for applications where pressure dynamics are important, such as in MPD. This problem can be overcome by adding a first-order ODE representation of the pressure dynamics, similar to the one used in the lumped single-phase case, but with some additional terms.

Figure 3.1 highlights the existing multi-phase modeling techniques, or-

dered in terms of complexity. The reduced DFM proposed in this chapter fits in the mid-range of complexity, computational cost, and usability, while preserving the multi-phase behavior. The simple structure of the model, as will be shown in the following sections, facilitates its numerical implementation, and yields a run time several orders of magnitude faster than the full DFM and Two-Fluid models.

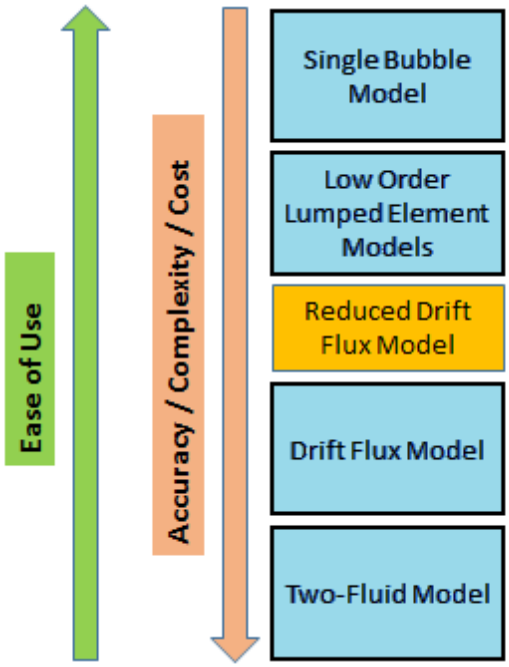

Figure 3.1: Comparison of multi-phase hydraulics modeling techniques. The single bubble model and low-order lumped models are easy to implement but tend to over-simplify the multi-phase effects. The Drift-Flux and Two-Fluid models represent the physics with a higher degree of accuracy but are computationally expensive. The proposed Reduced Drift-Flux model aims to achieve a balance between the run time and implementation advantages of low-order models and the accuracy of the more advanced multi-phase models.

3.2 Development of the Reduced Drift-Flux Model

3.2.1 Modeling Assumptions and Simplifications

The following assumptions and simplifications are made for the reduced DFM derivation:

1. A steady-state, linear temperature profile is assumed throughout the wellbore. Temperature transients can be neglected as long as temperature boundary conditions do not show significant changes with time (Aarsnes et al., 2016c).

2. The density of the liquid phase is constant in space and time. In practice, this will not be the case, as liquid density is increased with pressure and reduced with increasing temperature, but for the sake of our model, we will assume these variations to be negligible.

3. Distributed pressure transients are neglected. This assumption is justified by the fact that void wave propagation is typically several orders of magnitude slower than pressure wave propagation in drilling fluids (Masella et al., 1998).

4. When computing the frictional pressure drop, a uniform velocity for the gas-liquid mixture is used.

5. When computing the gas and liquid velocities, the pressure transient terms are neglected.

3.2.2 Derivation of Reduced DFM

The derivation starts from the classical two-phase DFM formulation where we assume that the flow area $A(x)$ is piecewise constant, and neglect, for now, any mass source terms and mass transfer (Gavrilyuk and Fabre, 1996):

$$\frac{\partial(\alpha_L \rho_L)}{\partial t} + \frac{\partial(\alpha_L \rho_L v_L)}{\partial x} = 0 \tag{3.26}$$

$$\frac{\partial(\alpha_G \rho_G)}{\partial t} + \frac{\partial(\alpha_G \rho_G v_G)}{\partial x} = 0 \tag{3.27}$$

$$\frac{\partial(\alpha_L \rho_L v_L + \alpha_G \rho_G v_G)}{\partial t} + \frac{\partial(P + \alpha_G \rho_G v_G^2 + \alpha_L \rho_L v_L^2)}{\partial x} = S \tag{3.28}$$

where

$$S = -\rho_m g \cos\theta - \frac{2 f \rho_m v_m |v_m|}{D} \tag{3.29}$$

$$\alpha_L + \alpha_G = 1 \tag{3.30}$$

$$P = \rho_G Z_G R_G T \tag{3.31}$$

$$\rho_m = \alpha_G \rho_G + \alpha_L \rho_L \tag{3.32}$$

$$v_m = \alpha_G v_G + \alpha_L v_L \tag{3.33}$$

In Eq. 3.31, Z_G is the gas compressibility factor, R_G is the ideal gas constant, and $T(x)$ is the temperature (assumed to vary linearly with depth, as indicated above). Recall the slip law:

$$v_G = \frac{v_m}{1 - \alpha_L^*} + v_\infty \tag{3.34}$$

where ${\alpha_L}^* \in [0, 1)$ and $v_\infty \geq 0$ are constant parameters. For convenience in the derivations, we used the notation:

$$\alpha_L^* \equiv \frac{C_0 - 1}{C_0}. \tag{3.35}$$

The derivation starts with the following relation, derived from the slip law:

$$\alpha_L v_L = (\alpha_L - \alpha_L^*) v_G - (1 - \alpha_L^*) v_\infty. \tag{3.36}$$

From (3.26) we have, with the assumption of constant ρ_L:

$$\frac{\partial \alpha_L}{\partial t} + \frac{\partial (\alpha_L - \alpha_L^*) v_G}{\partial x} = 0 \tag{3.37}$$

$$\implies \frac{\partial \alpha_L}{\partial t} + \frac{\partial \alpha_L}{\partial x} v_G + (\alpha_L - \alpha_L^*) \frac{\partial v_G}{\partial x} = 0 \tag{3.38}$$

$$\implies \frac{\partial \alpha_G}{\partial t} + v_G \frac{\partial \alpha_G}{\partial x} = (\alpha_L - \alpha_L^*) \frac{\partial v_G}{\partial x} \tag{3.39}$$

where the term on the right-hand side of (3.39) is due to gas expansion. From (3.27) we have:

$$\frac{\partial v_G}{\partial x} = -\frac{1}{\alpha_G \rho_G} \left[\frac{\partial (\alpha_G \rho_G)}{\partial t} + v_G \frac{\partial (\alpha_G \rho_G)}{\partial x} \right] \tag{3.40}$$

$$\frac{\partial v_G}{\partial x} = -\frac{1}{\alpha_G \rho_G} \left[\rho_G \frac{\partial \alpha_G}{\partial t} + \alpha_G \frac{\partial \rho_G}{\partial t} + v_G \left(\rho_G \frac{\partial \alpha_G}{\partial x} + \alpha_G \frac{\partial \rho_G}{\partial x} \right) \right] \tag{3.41}$$

Inserting (3.41) into (3.39), we get:

$$\begin{aligned} &\frac{\partial \alpha_G}{\partial t} \left(1 + \frac{\alpha_L - \alpha_L^*}{\alpha_G} \right) + v_G \frac{\partial \alpha_G}{\partial x} \left(1 + \frac{\alpha_L - \alpha_L^*}{\alpha_G} \right) \\ &= -\frac{\alpha_L - \alpha_L^*}{\rho_G} \left(\frac{\partial \rho_G}{\partial t} + v_G \frac{\partial \rho_G}{\partial x} \right). \end{aligned} \tag{3.42}$$

Thus, defining the local gas expansion term E_G:

$$E_G \equiv -\frac{\alpha_G (\alpha_L - \alpha_L^*)}{(1 - \alpha_L^*) \rho_G} \left(\frac{\partial \rho_G}{\partial t} + v_G \frac{\partial \rho_G}{\partial x} \right), \tag{3.43}$$

we have:

$$\frac{\partial \alpha_G}{\partial t} + v_G \frac{\partial \alpha_G}{\partial x} = E_G, \tag{3.44}$$

i.e. the gas expansion is a source term in the void fraction transport equation.

The boundary condition for Eq. 3.44, defined at the bottom of the well ($x = 0$), is given as:

$$\alpha_G(x{=}0, t) = \frac{q_G}{A v_G(x{=}0, t)}, \tag{3.45}$$

$$v_G(x{=}0, t) = C_0 \frac{q_G + q_L}{A} + v_\infty. \tag{3.46}$$

The velocity gradient can now be written as:

$$\frac{\partial v_G}{\partial x} = -\frac{1}{\alpha_G \rho_G} \left(\rho_G E_G + \alpha_G \frac{\partial \rho_G}{\partial t} + v_G \alpha_G \frac{\partial \rho_G}{\partial x} \right) \tag{3.47}$$

$$\frac{\partial v_G}{\partial x} = -\frac{1}{\alpha_G \rho_G} \left[\rho_G E_G - \frac{\rho_G (1 - \alpha_L^*)}{\alpha_L - \alpha_L^*} E_G \right] \tag{3.48}$$

$$\frac{\partial v_G}{\partial x} = \frac{E_G}{\alpha_L - \alpha_L^*} \tag{3.49}$$

Next, we use a lumped expression for the pressure dynamics obtained by assuming the pressure dynamics to be uniform in x, effectively relaxing the fast pressure characteristics of (3.26)–(3.28):

$$\frac{dp_c}{dt} = \frac{\beta_L}{V_a} \left(q_L + q_G + T_{E_G} - q_c \right), \tag{3.50}$$

with the variables q_L, q_G representing the liquid, respectively gas, volumetric flow rate entering at the bottom of the well, β_L the bulk modulus of the liquid

phase, and T_{E_G} the integral of the gas velocity gradient over the length of the well:

$$T_{E_G} = \int_0^L A \frac{\partial v_G}{\partial x} \mathrm{d}x. \tag{3.51}$$

The distributed pressure is obtained from (3.28), assuming quasi-steady state and neglecting the convective term $\frac{\partial(\alpha_G \rho_G v_G^2 + \alpha_L \rho_L v_L^2)}{\partial x}$:

$$P(x) = p_c - \int_x^L S(\xi) \mathrm{d}\xi. \tag{3.52}$$

This expression is dependent on v_m which, in turn, is a function of $E_G(P)$, and $\rho_G(P)$. To avoid the implicit dependency of the right-hand side of Eq. 3.52 on the pressure P, we need to use a simplification, for instance by assuming v_m uniform in space, and also by making the mixture density ρ_m independent of pressure, for the purpose of this calculation. One possible approximation is:

$$S(x) \approx -\bar{\rho}_m(x) \left[g \cos\theta(x) + \frac{2 f (q_G + q_L)|q_G + q_L|}{A^2 D} \right], \tag{3.53}$$

$$\bar{\rho}_m = \rho_L \alpha_L(x) + \bar{\rho}_G \alpha_G(x), \tag{3.54}$$

where $\bar{\rho_G}$ denotes that a mean approximate gas density is used, and the mixture velocity is approximated as $(q_G + q_L)/A$. With these approximations, the source term S becomes explicit in the state α_G and the exogenous variables q_L, q_G. The friction factor f in Eq. 3.54 is calculated using the yield-power law (YPL) fluid correlations, detailed in Appendix C.

Next, we derive a relationship between the derivatives of gas density and pressure, so that we can more conveniently express E_G in terms of P and

its derivatives, rather than ρ_G. We use the following relation, which holds true for an isentropic process (Moon et al., 2011):

$$\Big(\frac{\partial \rho_G}{\partial P}\Big)_s \equiv \frac{1}{c_G^2} = \frac{\rho_G}{\gamma\Big[1+\frac{\rho_G}{Z_G}\Big(\frac{\partial Z_G}{\partial \rho_G}\Big)_T\Big]P}. \tag{3.55}$$

where c_G is the speed of sound in gas and γ is the adiabatic gas constant. From the real gas law, we have:

$$\Big(\frac{\partial Z_G}{\partial \rho_G}\Big)_T = \Big(\frac{\partial Z_G}{\partial P}\Big)_T R_G T\Big[Z_G + \rho_G\Big(\frac{\partial Z_G}{\partial \rho_G}\Big)_T\Big] \tag{3.56}$$

which gives:

$$\frac{\partial \rho_G}{\rho_G} = \frac{\partial P}{\bar{\gamma} P} \tag{3.57}$$

with

$$\bar{\gamma} \equiv \gamma\Big[1-\rho_G R_G T\Big(\frac{\partial Z_G}{\partial P}\Big)_T\Big]^{-1} \tag{3.58}$$

Now we can write:

$$E_G = -\frac{\alpha_G(\alpha_L-\alpha_L^*)}{(1-\alpha_L^*)\bar{\gamma}P}\left(\frac{\partial P}{\partial t}+v_G\frac{\partial P}{\partial x}\right), \tag{3.59}$$

$$\frac{\partial P(x,t)}{\partial x} = S(x) \tag{3.60}$$

$$\frac{\partial P(x,t)}{\partial t} \approx \frac{dp_c}{dt} = \frac{\beta_L}{V_a}\left(q_L+q_G+T_{E_G}-q_c\right), \tag{3.61}$$

and

$$\frac{\partial v_G}{\partial x} = -\frac{C_0\alpha_G}{P\bar{\gamma}}v_G S, \tag{3.62}$$

$$v_G(x) = v_G(x=0,t)\exp\Big[-\int_0^x \frac{C_0\alpha_G(\xi)}{P(\xi)\bar{\gamma}(\xi)}S(\xi)\mathrm{d}\xi\Big]. \tag{3.63}$$

Note that in the calculation of $v_G(x)$ we simplified the velocity gradient expression (Eq. 3.49) by neglecting the pressure transient $\frac{\partial P}{\partial t}$, in order to allow for an analytical expression. This assumption may cause transient errors during large pressure changes, for instance due to gas expansion when it reaches the surface. For the calculation of T_{E_G}, we will include the pressure transient term, as follows:

$$\begin{aligned} T_{E_G} &= -\frac{1}{\alpha_L - \alpha_L^*} \int_0^L A \frac{\alpha_G(\alpha_L - \alpha_L^*)}{(1-\alpha_L^*)\bar{\gamma}P} \left(\frac{\partial P}{\partial t} + v_G \frac{\partial P}{\partial x} \right) \mathrm{d}x \\ &= -\int_0^L A \frac{\alpha_G}{(1-\alpha_L^*)\bar{\gamma}P} \mathrm{d}x \frac{dp_c}{dt} - \int_0^L A \frac{\alpha_G}{(1-\alpha_L^*)\bar{\gamma}P} v_G S(x) \mathrm{d}x. \end{aligned} \tag{3.64}$$

Equivalently, we can write:

$$T_{E_G} = -\int_0^L A \frac{C_0 \alpha_G}{\bar{\gamma}P} \left(\frac{dp_c}{dt} + v_G \frac{\partial P}{\partial x} \right) \mathrm{d}x, \tag{3.65}$$

T_{E_G} can be split into two terms, one of them impacting the effective bulk modulus $\bar{\beta}$, and the other one accounting for the gas expansion when propagating through the negative pressure gradient. We will denote this second term as T_{ex}. Inserting Eq. (3.64) into the pressure dynamics (3.50), we obtain:

$$\frac{dp_c}{dt} = \frac{\beta_L}{V_a} \left(q_L + q_G - q_c - \int_0^L \frac{C_0 \alpha_G}{\bar{\gamma}P} v_G S(x) A \mathrm{d}x - \int_0^L \frac{C_0 \alpha_G}{\bar{\gamma}P} A \mathrm{d}x \frac{dp_c}{dt} \right), \tag{3.66}$$

Moving the terms containing $\frac{dp_c}{dt}$ on the left-hand side of Eq. 3.66, we get:

$$\frac{dp_c}{dt} \left(1 + \frac{\beta_L}{V_a} \int_0^L \frac{C_0 \alpha_G}{\bar{\gamma}P} A \mathrm{d}x \right) = \frac{\beta_L}{V_a} \big(q_L + q_G - q_c + T_{ex} \big), \tag{3.67}$$

$$T_{ex} \equiv -\int_0^L \frac{C_0 \alpha_G}{\bar{\gamma}P} v_G S(x) A \mathrm{d}x, \tag{3.68}$$

which finally allows us to write:

$$\frac{dp_c}{dt} = \frac{\bar{\beta}}{V_a}\big(q_L + q_G - q_c + T_{ex}\big), \tag{3.69}$$

$$\bar{\beta} \equiv \frac{\beta_L}{1 + \frac{\beta_L}{V_a}\int_0^L \frac{C_0 \alpha_G}{\bar{\gamma} P} A \mathrm{d}x}, \tag{3.70}$$

where we have defined the effective bulk modulus $\bar{\beta}$, and effective gas expansion T_{ex}. Through Eq. 3.70, the model handles the mud compressibility in the presence of gas. This model is generally applicable for water-based (WBM), oil-based (OBM) and synthetic-based muds (SBM), which vary in compressibility (Ahmed, 2006).

3.2.3 Reduced DFM With Mass Source Terms

We start again from the mass balance equations:

$$\frac{\partial(\alpha_L \rho_L)}{\partial t} + \frac{\partial(\alpha_L \rho_L v_L)}{\partial x} = \Gamma_L \tag{3.71}$$

$$\frac{\partial(\alpha_G \rho_G)}{\partial t} + \frac{\partial(\alpha_G \rho_G v_G)}{\partial x} = \Gamma_G \tag{3.72}$$

where Γ_L, Γ_G are liquid and gas source terms, respectively. From (3.71) we have:

$$\frac{\partial \alpha_L}{\partial t} + \frac{\partial(\alpha_L - \alpha_L^*) v_G}{\partial x} = \frac{\Gamma_L}{\rho_L} \tag{3.73}$$

$$\implies \frac{\partial \alpha_G}{\partial t} + v_G \frac{\partial \alpha_G}{\partial x} = (\alpha_L - \alpha_L^*)\frac{\partial v_G}{\partial x} - \frac{\Gamma_L}{\rho_L} \tag{3.74}$$

From (3.72) we now get:

$$\begin{aligned}\frac{\partial v_G}{\partial x} =& \frac{\Gamma_G}{\alpha_G \rho_G} - \frac{1}{\alpha_G \rho_G}\left[\frac{\partial(\alpha_G \rho_G)}{\partial t} + v_G \frac{\partial(\alpha_G \rho_G)}{\partial x}\right] \\ =& \frac{\Gamma_G}{\alpha_G \rho_G} - \frac{1}{\rho_G}\left(\frac{\partial \rho_G}{\partial t} + v_G \frac{\partial \rho_G}{\partial x}\right) - \frac{1}{\alpha_G}\left(\frac{\partial \alpha_G}{\partial t} + v_G \frac{\partial \alpha_G}{\partial x}\right)\end{aligned} \tag{3.75}$$

Inserting (3.75) into (3.74), using the definition for the local gas expansion term E_G:

$$\frac{\partial \alpha_G}{\partial t} + v_G \frac{\partial \alpha_G}{\partial x} = E_G + \frac{1}{1-\alpha_L^*}\left[(\alpha_L - \alpha_L^*)\frac{\Gamma_G}{\rho_G} - \alpha_G \frac{\Gamma_L}{\rho_L}\right] \tag{3.76}$$

Defining the dimensionless source terms Γ_G^*, Γ_L^* as:

$$\Gamma_G^* \equiv \frac{\alpha_L - \alpha_L^*}{(1-\alpha_L^*)\rho_G}\Gamma_G, \quad \Gamma_L^* \equiv \frac{\alpha_G}{(1-\alpha_L^*)\rho_L}\Gamma_L, \tag{3.77}$$

we have:

$$\frac{\partial \alpha_G}{\partial t} + v_G \frac{\partial \alpha_G}{\partial x} = E_G + \Gamma_G^* - \Gamma_L^*. \tag{3.78}$$

The velocity gradient is obtained by combining (3.74) and (3.78):

$$\begin{aligned} \frac{\partial v_G}{\partial x} =& \frac{E_G + \Gamma_G^* - \Gamma_L^* + \Gamma_L/\rho_L}{\alpha_L - \alpha_L^*} \\ =& \frac{E_G + \Gamma_G^*}{\alpha_L - \alpha_L^*} + \frac{1}{1-\alpha_L^*}\frac{\Gamma_L}{\rho_L}. \end{aligned} \tag{3.79}$$

In implementation the singularity at $\alpha_L = \alpha_L^*$ should be avoided, hence the following form is more convenient:

$$\frac{\partial v_G}{\partial x} = C_0\Big(- \frac{\alpha_G v_G}{P\bar{\gamma}} S + \frac{c_G^2}{P\bar{\gamma}}\Gamma_G + \frac{1}{\rho_L}\Gamma_L\Big), \tag{3.80}$$

Consequently, by defining the integral:

$$I_v(x) = \int_0^x \frac{C_0 \alpha_G(\xi)}{P(\xi)\bar{\gamma}(\xi)} S(\xi) \mathrm{d}\xi, \tag{3.81}$$

we write the distributed velocity as:

$$v_G(x) = e^{-I_v(x)}\left[v_{G0} + C_0 \int_0^x \left(\frac{c_G^2(\zeta)}{P(\zeta)\bar{\gamma}(\zeta)}\Gamma_G(\zeta) + \frac{\Gamma_L(\zeta)}{\rho_L}\right) e^{I_v(\zeta)} \mathrm{d}\zeta\right], \tag{3.82}$$

and the gas expansion term becomes:

$$T_{ex} = \int_0^L AC_0\Big(- \frac{\alpha_G}{\bar{\gamma}P} v_G S(x) + \frac{c_G^2}{P\bar{\gamma}}\Gamma_G + \frac{\Gamma_L}{\rho_L}\Big)\mathrm{d}x. \tag{3.83}$$

3.2.4 Reduced DFM with Interphase Mass Transfer

The formulation presented thus far neglected the effect of mass transfer between phases. This is a reasonable assumption when WBM is used, for which the effects of formation gas dissolution and generally negligible (Karimi Vajargah, 2013). However, for OBM or SBM, this is no longer the case, and the model needs to account for mass transfer. To include solubility effects to the two-phase mass balance, we can write (Shirdel and Sepehrnoori, 2012):

$$\frac{\partial[\alpha_L(\rho_L - \rho_G^*)]}{\partial t} + \frac{\partial[\alpha_L(\rho_L - \rho_G^*)v_L]}{\partial x} = \Gamma_L \tag{3.84}$$

$$\frac{\partial(\alpha_G\rho_G + \alpha_L\rho_G^*)}{\partial t} + \frac{\partial(\alpha_G\rho_G v_G + \alpha_L\rho_G^* v_L)}{\partial x} = \Gamma_G \tag{3.85}$$

where ρ_G^* is the equivalent density of dissolved gas.

There is now an additional unknown, ρ_G^*, that needs to be solved for, while the number of equations and closure relations has remained the same. Thus we need to break down the problem into two separate cases. The first one is defined at those wellbore locations where only dissolved gas exists, in other words the amount of gas is below the saturation threshold, which is a function of factors such as pressure, temperature, the oil/water ratio of the drilling mud. The second one applies to locations where free gas starts to break out of the solution, once the saturation threshold is exceeded. We will define the threshold as $\rho_{G,sat}^* \equiv \rho_{G,sc}\frac{R_s(P,T)}{B_o(P,T)}$, where $\rho_{G,sc}$ is gas density at standard conditions, R_s is the gas solubility in the oil phase, and B_o is the oil formation volume factor. R_s and B_o vary with pressure and temperature and

can be found from pressure-volume-temperature (PVT) correlations (O'Bryan and Bourgoyne Jr, 1990),(Monteiro et al., 2010).

3.2.4.1 Case 1: Dissolved gas only

If only dissolved gas exists in a control volume (i.e. $\rho_G^*(x,t) < \rho_{G,sat}^*(x,t)$), we can simplify Eqs. (3.84)-(3.85) by setting $\alpha_G = 0$ and $\alpha_L = 1$, which gives:

$$\frac{\partial(\rho_L - \rho_G^*)}{\partial t} + \frac{\partial[(\rho_L - \rho_G^*)v_L]}{\partial x} = \Gamma_L \tag{3.86}$$

$$\frac{\partial(\rho_G^*)}{\partial t} + \frac{\partial(\rho_G^* v_L)}{\partial x} = \Gamma_G \tag{3.87}$$

or, equivalently:

$$\frac{\partial(\rho_L - \rho_G^*)}{\partial t} + (\rho_L - \rho_G^*)\frac{\partial v_L}{\partial x} + v_L\frac{\partial(\rho_L - \rho_G^*)}{\partial x} = \Gamma_L \tag{3.88}$$

$$\frac{\partial \rho_G^*}{\partial t} + \rho_G^*\frac{\partial v_L}{\partial x} + v_L\frac{\partial \rho_G^*}{\partial x} = \Gamma_G. \tag{3.89}$$

By adding Eqs.(3.88)-(3.89) together, we have:

$$\frac{\partial \rho_L}{\partial t} + \frac{\partial(\rho_L v_L)}{\partial x} = \Gamma_L + \Gamma_G \tag{3.90}$$

from which we derive:

$$\frac{\partial v_L}{\partial x} = \frac{1}{\rho_L}\Big(\Gamma_L + \Gamma_G - \frac{\partial \rho_L}{\partial t} - v_L\frac{\partial \rho_L}{\partial x}\Big). \tag{3.91}$$

Substituting (3.91) into (3.89), we get:

$$\frac{\partial \rho_G^*}{\partial t} + v_L\frac{\partial \rho_G^*}{\partial x} = \Gamma_G - \frac{\rho_G^*}{\rho_L}\Big(\Gamma_L + \Gamma_G - \frac{\partial \rho_L}{\partial t} - v_L\frac{\partial \rho_L}{\partial x}\Big). \tag{3.92}$$

If we assume constant ρ_L, we obtain a simplified transport equation for ρ_G^*:

$$\frac{\partial \rho_G^*}{\partial t} + v_L\frac{\partial \rho_G^*}{\partial x} = \Gamma_G - \frac{\rho_G^*}{\rho_L}\Big(\Gamma_L + \Gamma_G\Big). \tag{3.93}$$

We can also find an analytical expression for the liquid velocity profile:

$$v_L(x) = e^{-I_{v_L}(x)}\Big[v_L(0) + \int_0^x \frac{\Gamma_L(\xi) + \Gamma_G(\xi)}{\rho_L(\xi)} e^{I_{v_L}(\xi)} \mathrm{d}\xi\Big] \tag{3.94}$$

with $I_{v_L}(x) = \int_0^x \frac{\partial \rho_L / \partial \xi}{\rho_L(\xi)} \mathrm{d}\xi$ or, for constant ρ_L:

$$v_L(x) = v_L(0) + \int_0^x \frac{\Gamma_L(\xi) + \Gamma_G(\xi)}{\rho_L} \mathrm{d}\xi. \tag{3.95}$$

The boundary conditions are given by:

$$\rho_G^*(x=0,t) = \frac{\rho_L q_L q_G}{q_L + q_G}; v_L(x=0,t) = \frac{q_L}{A}. \tag{3.96}$$

3.2.4.2 Case 2: Dissolved and free gas

If the mud becomes saturated with gas ($\rho_G^*(x,t) = \rho_{G,sat}^*(x,t)$), we have $\alpha_G(x) > 0$. After some algebra, we can write the equations (3.84)-(3.85) as:

$$\frac{\partial(\alpha_L \rho_L)}{\partial t} + \frac{\partial(\alpha_L \rho_L v_L)}{\partial x} = \Gamma_L + \Gamma_D \tag{3.97}$$

$$\frac{\partial(\alpha_G \rho_G)}{\partial t} + \frac{\partial(\alpha_G \rho_G v_G)}{\partial x} = \Gamma_G - \Gamma_D \tag{3.98}$$

where we define the mass transfer term:

$$\begin{aligned}\Gamma_D \equiv & \frac{\partial(\alpha_L \rho_{G,sat}^*)}{\partial t} + \frac{\partial(\alpha_L \rho_{G,sat}^* v_L)}{\partial x} \\ &= \alpha_L \frac{\partial \rho_{G,sat}^*}{\partial t} + \alpha_L v_L \frac{\partial \rho_{G,sat}^*}{\partial x} + \rho_{G,sat}^* \Big[\frac{\partial \alpha_L}{\partial t} + \frac{\partial(\alpha_L v_L)}{\partial x}\Big]\end{aligned} \tag{3.99}$$

From (3.97) with constant ρ_L, we have:

$$\frac{\partial \alpha_L}{\partial t} + \frac{\partial(\alpha_L v_L)}{\partial x} = \frac{\Gamma_L + \Gamma_D}{\rho_L} \tag{3.100}$$

$$\implies \Gamma_D = \alpha_L \Big(\frac{\partial \rho_{G,sat}^*}{\partial t} + v_L \frac{\partial \rho_{G,sat}^*}{\partial x}\Big) + \frac{\rho_{G,sat}^* (\Gamma_L + \Gamma_D)}{\rho_L} \tag{3.101}$$

After bringing Γ_D on the left-hand side of (3.101), we have:

$$\Gamma_D = \frac{\rho_L}{\rho_L - \rho^*_{G,sat}}\Big[\alpha_L\Big(\frac{\partial \rho^*_{G,sat}}{\partial t} + v_L\frac{\partial \rho^*_{G,sat}}{\partial x}\Big) + \frac{\rho^*_{G,sat}\Gamma_L}{\rho_L}\Big] \tag{3.102}$$

The derivatives of $\rho^*_{G,sat}$ can be calculated using the chain rule:

$$\begin{aligned}\frac{\partial \rho^*_{G,sat}}{\partial t} &= \frac{\partial \rho^*_{G,sat}}{\partial P}\frac{\partial P}{\partial t} + \frac{\partial \rho^*_{G,sat}}{\partial T}\frac{\partial T}{\partial t} \\ &= \rho_{G,sc}\frac{\Big(\frac{\partial R_S}{\partial P}\frac{\partial P}{\partial t} + \frac{\partial R_S}{\partial T}\frac{\partial T}{\partial t}\Big)B_O - R_S\Big(\frac{\partial B_O}{\partial P}\frac{\partial P}{\partial t} + \frac{\partial B_O}{\partial T}\frac{\partial T}{\partial t}\Big)}{B_O^2}\end{aligned} \tag{3.103}$$

$$\begin{aligned}\frac{\partial \rho^*_{G,sat}}{\partial x} &= \frac{\partial \rho^*_{G,sat}}{\partial P}\frac{\partial P}{\partial x} + \frac{\partial \rho^*_{G,sat}}{\partial T}\frac{\partial T}{\partial x} \\ &= \rho_{G,sc}\frac{\Big(\frac{\partial R_S}{\partial P}\frac{\partial P}{\partial x} + \frac{\partial R_S}{\partial T}\frac{\partial T}{\partial x}\Big)B_O - R_S\Big(\frac{\partial B_O}{\partial P}\frac{\partial P}{\partial x} + \frac{\partial B_O}{\partial T}\frac{\partial T}{\partial x}\Big)}{B_O^2}\end{aligned} \tag{3.104}$$

The transport equation, velocity formula and gas expansion term in the pressure dynamics (T_{ex}) can be easily adapted by making $\Gamma_L \rightarrow \Gamma_L + \Gamma_D$ and $\Gamma_G \rightarrow \Gamma_G - \Gamma_D$ in (3.76),(3.82) and (3.83), which gives:

$$\frac{\partial \alpha_G}{\partial t} + v_G\frac{\partial \alpha_G}{\partial x} = E_G + \frac{1}{1-\alpha_L^*}\left[(\alpha_L - \alpha_L^*)\frac{\Gamma_G - \Gamma_D}{\rho_G} - \alpha_G\frac{\Gamma_L + \Gamma_D}{\rho_L}\right] \tag{3.105}$$

$$v_G(x) = e^{-I_v(x)}\left[v_{G0} + C_0\int_0^x\left(\frac{c_G^2(\Gamma_G - \Gamma_D)}{P\bar{\gamma}} + \frac{\Gamma_L + \Gamma_D}{\rho_L}\right)e^{I_v(\zeta)}\mathrm{d}\zeta\right] \tag{3.106}$$

$$T_{ex} = \int_0^L AC_0\Big(-\frac{\alpha_G}{\bar{\gamma}P}v_G S(x) + \frac{c_G^2(\Gamma_G - \Gamma_D)}{P\bar{\gamma}} + \frac{\Gamma_L + \Gamma_D}{\rho_L}\Big)\mathrm{d}x. \tag{3.107}$$

3.2.5 Choke Model

The flow rate through the choke, q_c, entering the pressure dynamics relation (Eq. 3.50), can be modeled as a function of the choke size, choke

opening, mud density, and pressure drop through the choke. For two-phase (gas-liquid) flow, one approach is to assume mixed flow, where the fluids see the same choke opening. The other approach is stratified flow, where each of the two fluids sees a different opening as it passes through the choke (Fjalestad et al., 2010). Throughout this work, we will assume mixed flow, for which the following equation is used:

$$w_c = C_v Z \sqrt{\frac{p_c - p_0}{\frac{\chi_L}{\rho_L} + \frac{\chi_G}{Y^2 \rho_G}}} \tag{3.108}$$

where w_c is the total mass flow rate through the choke, χ_L is the liquid mass flow fraction, χ_G is the gas mass flow fraction, p_c is the surface back pressure, p_0 is the choke downstream pressure, C_v is a constant related to the choke area, Y is a gas expansion factor and Z is the choke opening. χ_L and χ_G can be computed as:

$$\chi_L = \frac{\alpha_L \rho_L v_L}{\alpha_L \rho_L v_L + \alpha_G \rho_G v_G}; \chi_G = 1 - \chi_L \tag{3.109}$$

For stratified flow, the choke model becomes:

$$w_c = C_v Z \frac{\sqrt{p_c - p_0}}{\frac{\chi_L}{\sqrt{\rho_L}} + \frac{\chi_G}{Y\sqrt{\rho_G}}} \tag{3.110}$$

To convert from mass flow rate w_c to volume flow rate q_c, we need to apply the relation

$$q_c = \frac{w_c \chi_L}{\rho_L} + \frac{w_c \chi_G}{\rho_G}, \tag{3.111}$$

where the first term represents the liquid flow rate, $q_{L,c}$, and the second term the gas flow rate through the choke, $q_{G,c}$.

3.3 Model Validation

The reduced DFM is validated using a high-fidelity drilling hydraulics simulator with multi-phase flow modeling capabilities developed at the University of Texas at Austin (Ma et al., 2016), and also using experimental data from a gas kick event simulated by injecting natural gas into an on-shore well used for test purposes. In each case, the relevant model outputs are compared: WHP, BHP, mud flow out rate, pit gain, and gas fractions.

The pit gain (i.e. increase in mud volume due to the kick and subsequent expansion), V_G, is calculated by integrating the difference between the flow out rate at the choke and the pump rate:

$$V_G = \int_0^t (q_c - q_p)\mathrm{d}t \tag{3.112}$$

3.3.1 Validation using a Multi-Phase Simulator

The scenario generated using the high-fidelity simulator is that of a 15,847 ft deviated on-shore well drilled with a CBHP MPD system. The well path is illustrated in Figure 3.2.

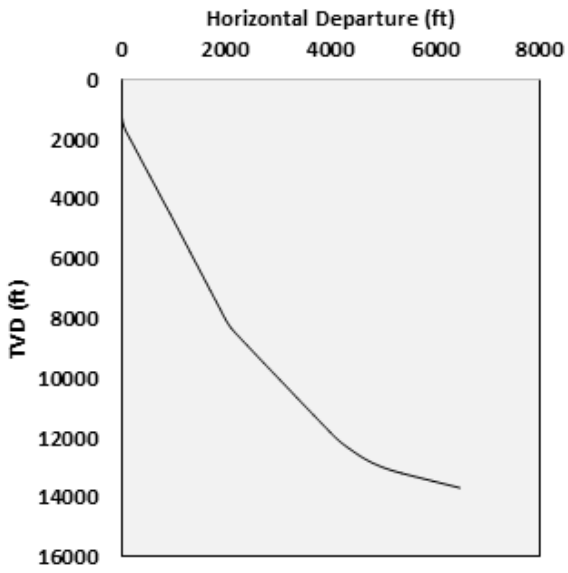

Figure 3.2: Wellbore path used in the simulation, given by horizontal departure versus true vertical depth (TVD). The trajectory begins to deviate from vertical after a depth of 2000 ft.

For the first case, a 10-ppg WBM with non-Newtonian rheology is circulated at a constant rate of 600 gpm. A natural gas reservoir (SG = 0.65) with a pore pressure of 7870 psi and a productivity index equal to 0.146 ft^3/min/psi is intersected at the bottom of the well. When the influx starts, the well is underbalanced by approximately 300 psi, which results in a 8-bbl kick taken over a period of 5 minutes. Choke opening is then decreased and the additional back-pressure returns the well to an overbalanced state. The choke opening is subsequently adjusted by a PI controller to maintain a target BHP of 8000 psi. Table 3.1 summarizes the parameters used in this simulation scenario.

Table 3.1: Input parameters for model validation using a high-fidelity simulator.

Parameter	*Value*	*Unit*
Well depth	15,847	ft
Casing shoe depth	13,000	ft
Casing inner diameter	9.76	in
Hole size	9.5	in
Drill pipe outer diameter	5	in
Drill pipe inner diameter	4.28	in
Drill collar outer diameter	6.5	in
Drill collar inner diameter	2.5	in
BHA length	1282	ft
Mud density	10	lbm/gal
Mud consistency index	20	cP
Mud power-law index	1	
Mud yield stress	10	lbs/(100ft^2)
Sound velocity in mud	3400	ft/s
Choke line ID	2	in
Nozzle total flow area	0.6	in^2
Surface temperature	60	°F
Bottom-hole temperature	135	°F

The Shi slip model (Shi et al., 2005) is used to compute the slip parameters C_0 and v_∞. The gas influx rate, along with the choke opening profile generated by the simulator, are entered as input to the reduced DFM (see Figure 3.3).

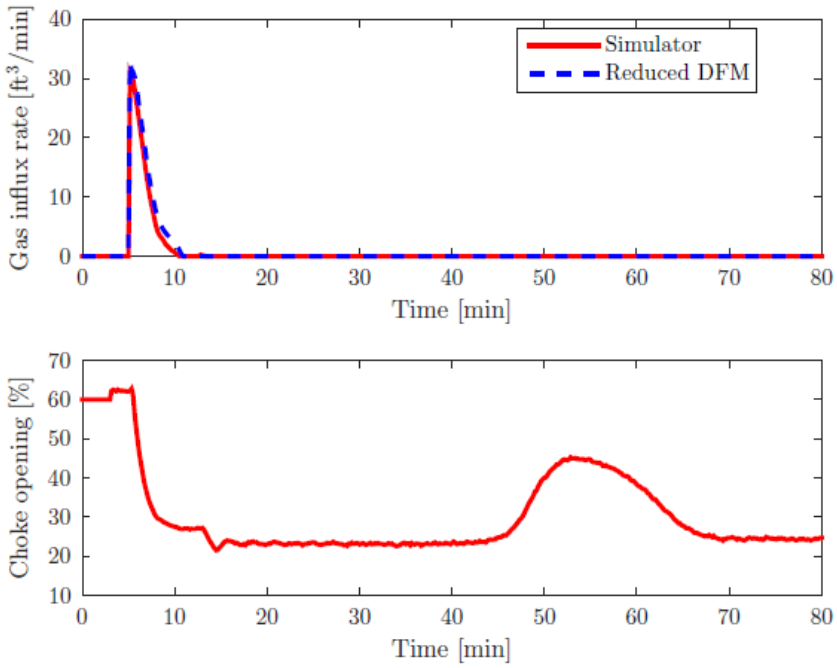

Figure 3.3: Influx rate (upper) and choke opening (lower) for a gas kick simulation in WBM. The influx commences at 5 minutes and ends at 10 minutes, after sufficient back-pressure has been added by closing the choke. Adjustment of the choke is done automatically by a PI controller. The increase in choke opening around 50 minutes coincides with the gas reaching the surface.

The gas volume fraction profiles in Figure 3.4 indicate very good agreement between the simulator gas profile and that obtained from the reduced DFM, which shows that the model is capable of preserving the two-phase behavior. The gas expansion is also obvious as the bubble migrates toward the top of the well, and it reaches a peak void fraction of 0.2 at the surface.

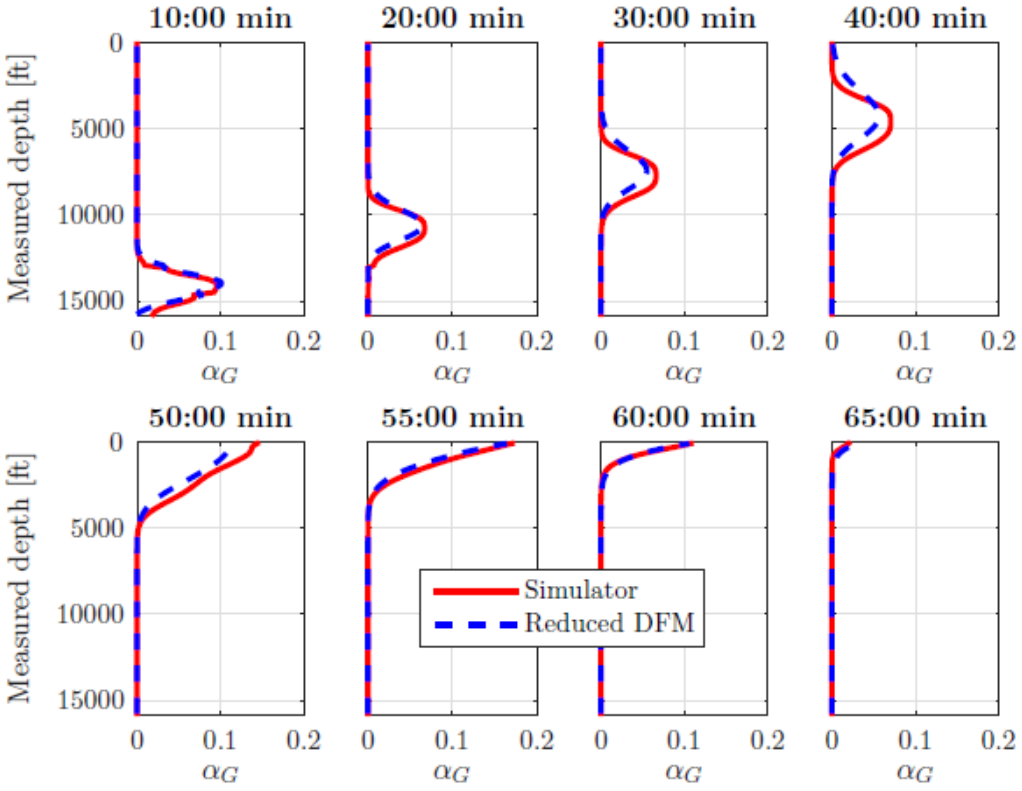

Figure 3.4: Evolution of free gas profile, as predicted by simulator and reduced DFM for a gas kick simulation in WBM. The simulator and reduced DFM profiles are in good agreement throughout the simulation.

As Figures 3.5a and 3.5b indicate, there is a reasonable agreement between the BHP and WHP, and also the flow out and pit gain computed by the model and those obtained from the high-fidelity simulator. The reduced DFM slightly under-predicts the peak WHP, and the maximum pit gain when gas hits the choke, but the overall trend is maintained. These errors can be attributed to uncertainty in the two-phase choke model, and in the calculation of the gas velocity (Eq. 3.82), which does not include the pressure transients.

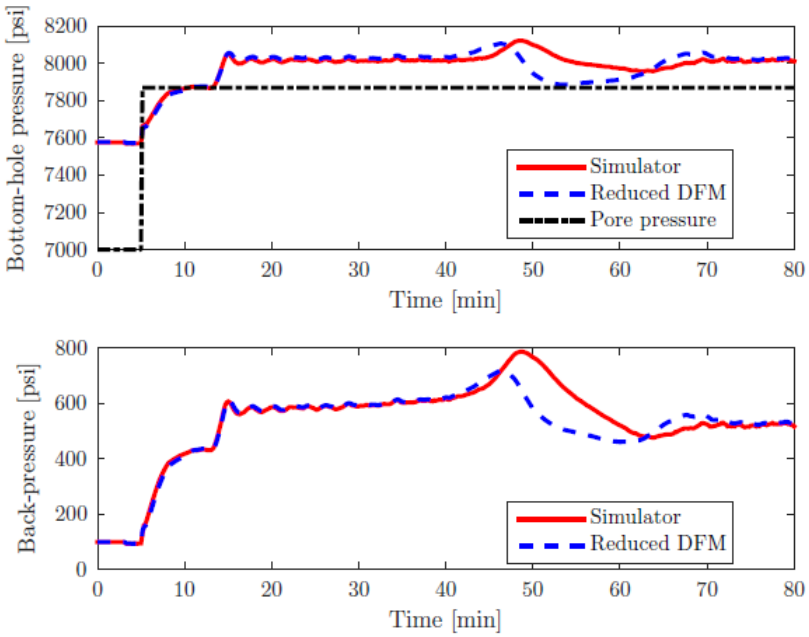

(a) BHP (upper) and WHP (lower).

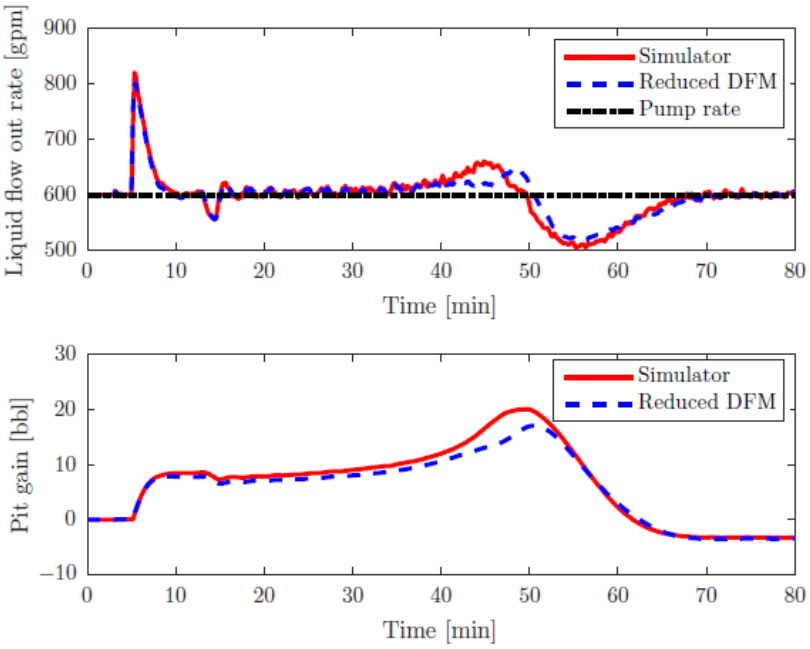

(b) Mud flow out rate (upper) and pit gain (lower).

Figure 3.5: Comparison of simulator results with the reduced DFM for a gas kick simulation in WBM.

Next, we will evaluate the reduced DFM on a scenario using an SBM with an oil/water ratio of 70/30, for the same well setup detailed in Table 3.1. All the other mud properties (density, rheology, sound speed) remain the same as the ones defined in the WBM case. Figure 3.6 shows the influx rate and choke opening used in the simulation.

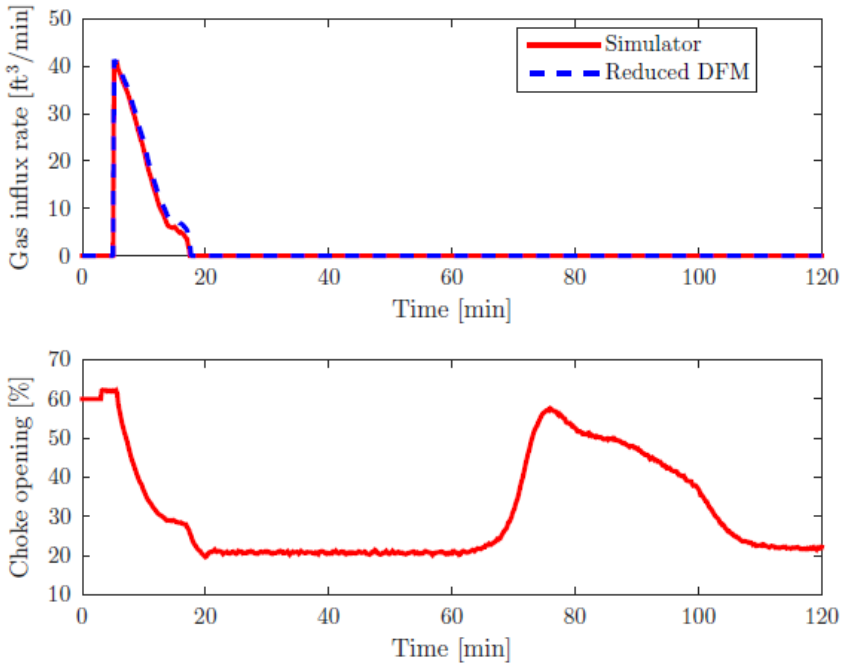

Figure 3.6: Influx rate (upper) and choke opening (lower) for a gas kick simulation in SBM. The influx commences at 5 minutes and ends at 18 minutes. The controller opens the choke as the gas reaches the surface.

Because the kick size is relatively small (7 bbl initial pit gain), all the influx is initially dissolved in the mud, as indicated by Figure 3.7. The gas remains dissolved until around 60 minutes, after which, due to the lower pressure encountered, a gas bubble starts breaking out; 10 minutes later, the

bubble reaches the surface. Throughout the simulation, the predicted dissolved gas and free gas distributions closely agree with the actual profiles generated by the multi-phase simulator (see Figures 3.7 and 3.8).

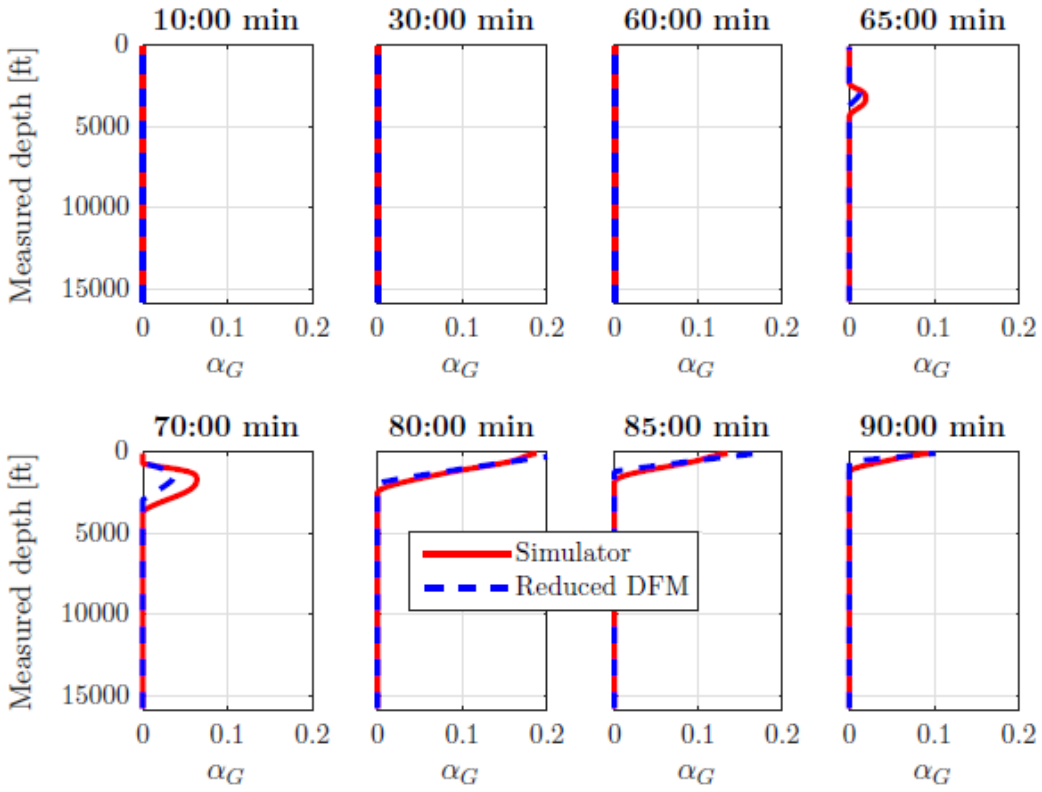

Figure 3.7: Evolution of free gas profile for a gas kick simulation in SBM. Gas breaks out of the mud at 65 minutes. The reduced DFM slightly under-predicts the initial amount of free gas, but after 80 minutes the reduced DFM predictions match the free gas profiles from the simulator.

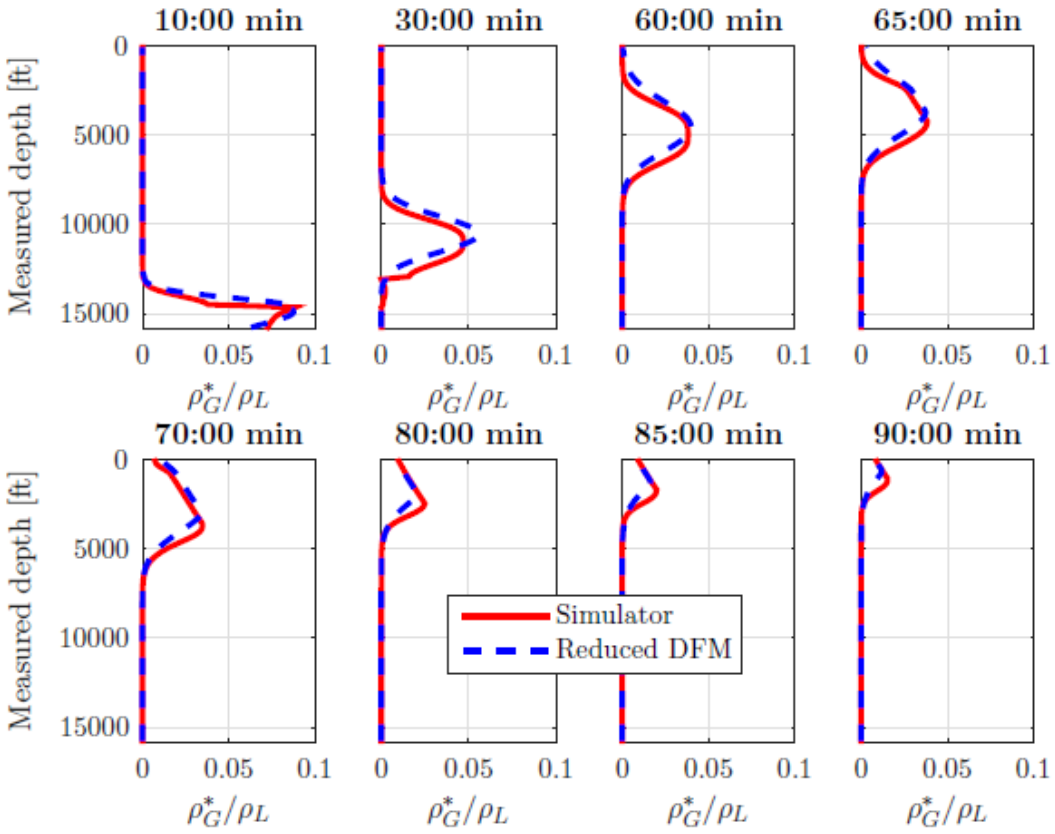

Figure 3.8: Evolution of dissolved gas profile for a gas kick simulation in SBM. The gas kick is initially fully dissolved in the mud. The simulator and reduced DFM profiles are in close agreement throughout the simulation.

As far as the other model outputs are concerned, Figure 3.9a shows the pressure trends, while Figure 3.9b shows the flow out and pit gain for this simulation. The pit gain and flow out show very good agreement with the simulator results, as do the back-pressure and BHP, with the exception of the interval between roughly 60 and 70 minutes. This corresponds to the interval between the gas breakout from the mud, and the bubble reaching the

surface, which is characterized by a rapid increase in surface back-pressure and pit gain. After this point, the free gas starts expanding rapidly, and the choke is opened to relieve the excessive back-pressure. As the back-pressure is reduced, the discrepancy between the model-predicted values and the actual ones becomes smaller.

The discrepancy between the pressure trends could be due to various factors, one of them being the amount of gas breaking out of the mud, which is strongly dependent on the pressure profile. As back-pressure is added, some of the free gas may re-dissolve into the mud, which in turn reduces the flow out, and the difference in flow is made up by an increase in pressure. One possible solution to avoid large discrepancies in pressure (which can be critical in narrow margin wells) is to use a low-pass filter when updating the saturation threshold (ρ_G^*). This will limit the amount of free gas that dissolves back into the solution at is sees a higher saturation threshold. Alternately, the measured back-pressure can be used to correct the model prediction through a state estimator. The latter would also potentially reduce the error in predicted back-pressure seen in the WBM case.

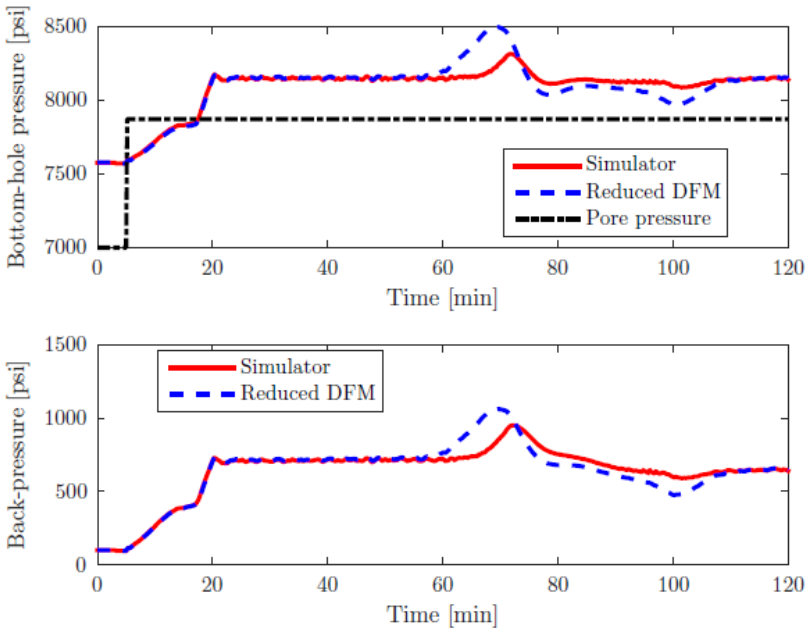

(a) BHP (upper) and WHP (lower).

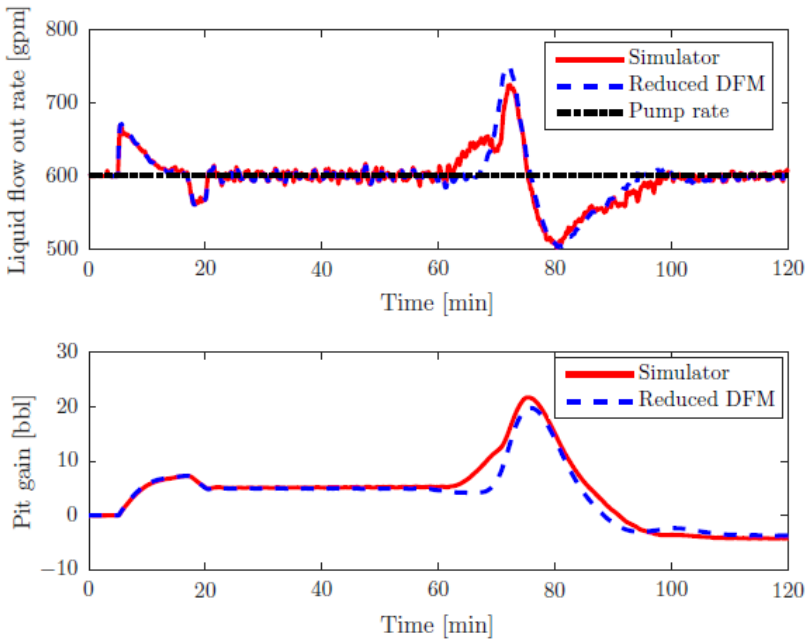

(b) Mud flow out rate (upper) and pit gain (lower).

Figure 3.9: Comparison of simulator results with the reduced DFM for a gas kick simulation in SBM.

3.3.2 Experimental Data

Next, the model was validated on an experimental data set obtained from a well control test conducted at Louisiana State University. The test setup, illustrated in Figure 3.10, was detailed by Chirinos et al. (2011). A 11-bbl gas kick was simulated by injecting natural gas inside the 1.25-in tubing while WBM was continuously pumped through the annulus formed by the 3.5-in drill pipe and the 1.25-in tubing, with returns taken through the annulus between the 9.625-in casing and the 3.5-in drill pipe.

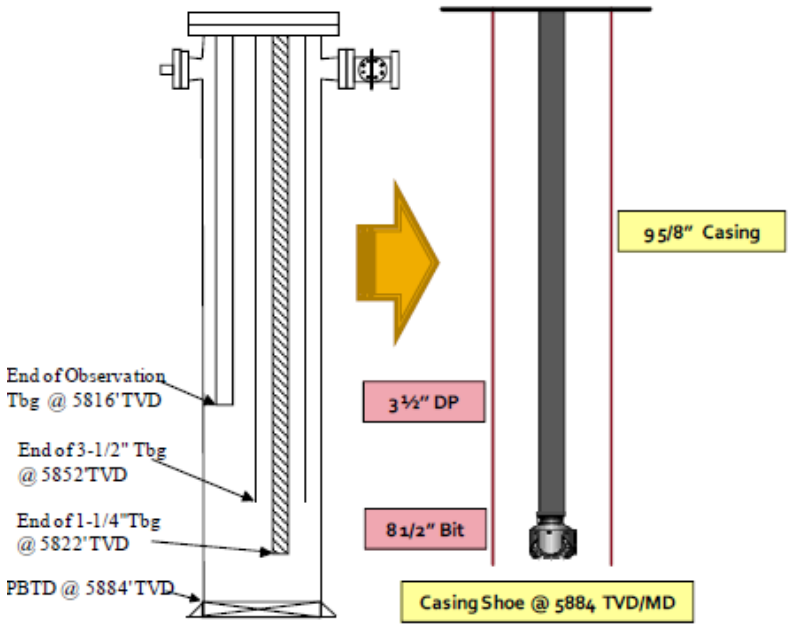

Figure 3.10: Louisiana State University well schematic (from Chirinos et al. (2011)). A 9.625-in casing string was used from the surface to the total depth of 5884 ft. Gas was injected through a 1.25-in tubing and mud was pumped through a 3.5-in drill pipe.

The mud circulation rate was varied from 90 to 150 gpm. A manually operated choke manifold was used to provide back-pressure, with the goal of keeping a constant SPP throughout the gas circulation. The mud circulation and gas injection rate recorded during the test were used as inputs to the model and are shown in Figure 3.11. Well geometry, mud properties and other model inputs are detailed in Table 3.2. Since there was no down-hole pressure measurement in the experimental setup, the BHP (p_{bh}) was inferred from the SPP and liquid flow rate according to the following (steady-state) equation (Guo and Liu, 2011):

$$p_{bh} = p_p + \rho_L g h - \frac{2 f \rho_L q_L^2}{A_d^2 D_d} L \tag{3.113}$$

where A_d, D_d are the drill pipe internal flow area and internal diameter, respectively, and h is the true vertical depth of the well.

Table 3.2: Input parameters for Louisiana State University well control test.

Parameter	*Value*	*Unit*
Well depth/casing depth	5884	ft
Casing size	9.625	in
Drill pipe outer diameter	3.5	in
Drill pipe inner diameter	2.6	in
Gas injection tubing diameter	1.25	in
Mud density	8.6	lbm/gal
Mud consistency index	8	cP
Mud power-law index	1	
Mud yield stress	2	lbs/(100ft^2)
Sound velocity in mud	4000	ft/s
Choke line ID	3.73	in
Surface temperature	93	°F
Bottom-hole temperature	140	°F

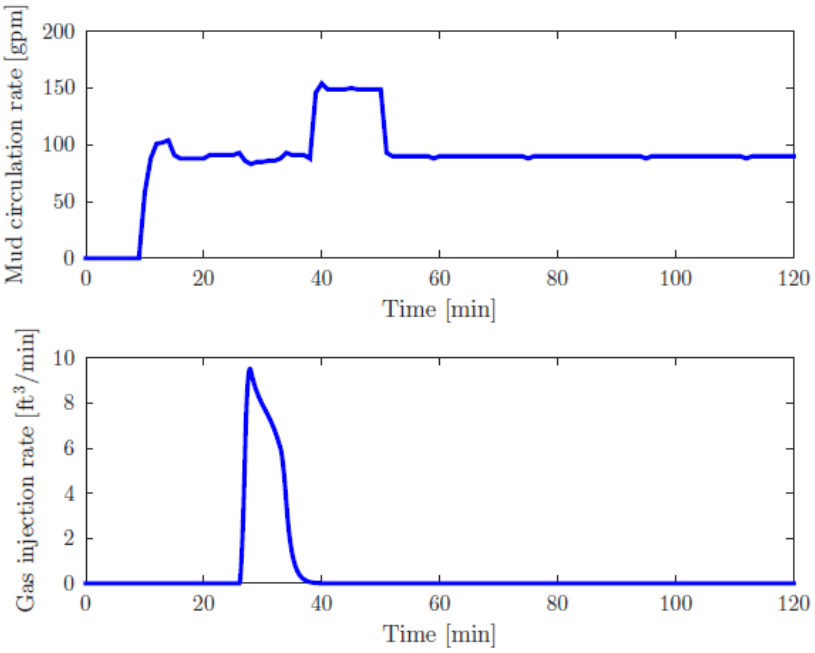

Figure 3.11: Mud circulation rate (upper) and gas injection rate (lower) from the well control test. The mud pumps were initially ramped to 90 gpm. Gas was injected between 26 and 38 minutes. After the injection, the pump rate was increased to 150 gpm and then reduced back to 90 gpm.

Simulation results show close match for pressures (Figure 3.12a) and reasonable agreement for the flow out and pit gain trends (Figure 3.12b) recorded from the experiment. In the case of flow out, the recorded data showed a sharp increase when gas reached the surface around 90 minutes, followed by a sudden drop at 100 minutes, after which there was no recorded data. The erratic behavior may be the result of the flow meter not having been properly calibrated for two-phase flow. The recorded pit gain displays good agreement in the overall trend throughout the gas circulation, except for a 1-bbl offset which could be due to possible mud losses or leaks.

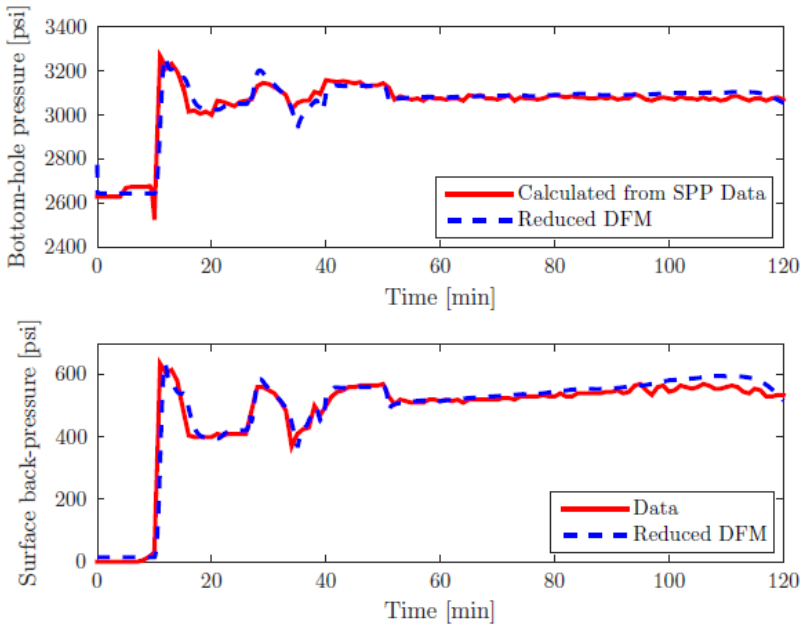

(a) BHP (upper) and WHP (lower).

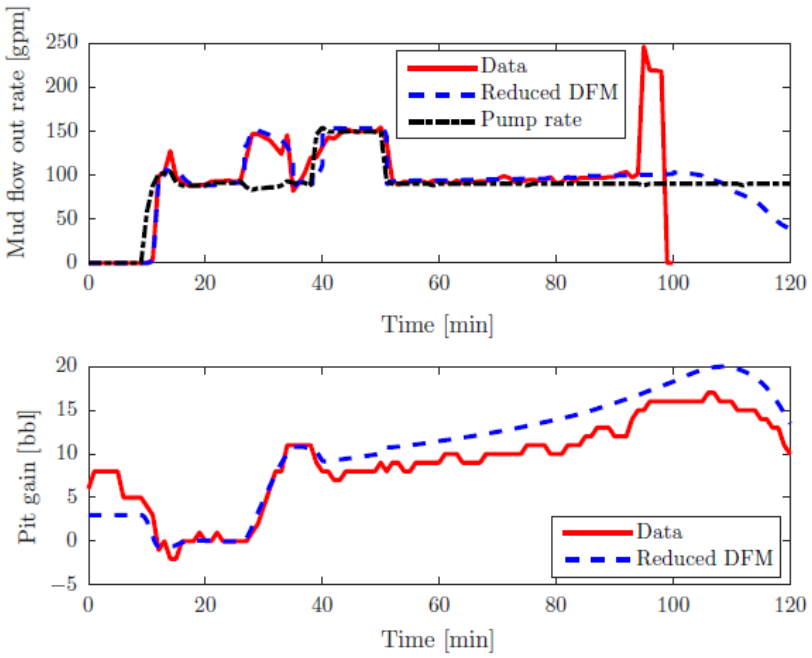

(b) Mud flow out rate (upper) and pit gain (lower).

Figure 3.12: Comparison of well control test data with the reduced DFM predictions.

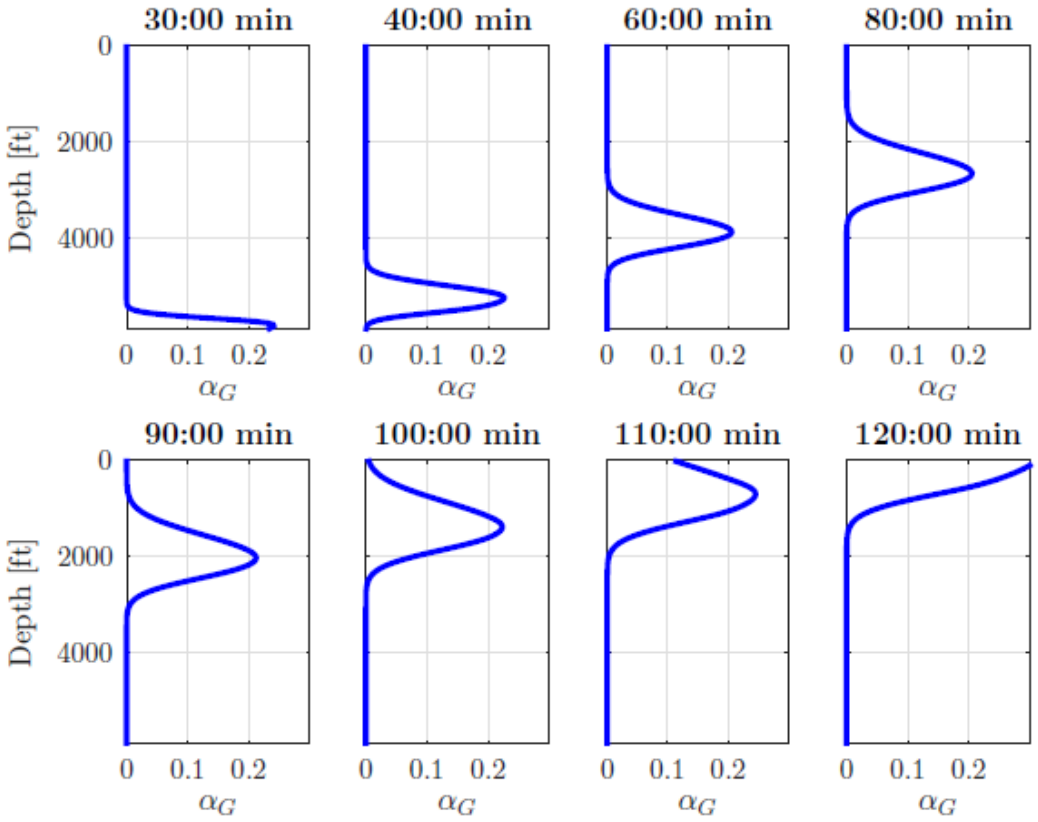

Figure 3.13: Gas volume fraction vs. depth, as predicted by reduced DFM. The gas fraction increases due to expansion as gas reaches the surface. The peak gas fraction was found to be in the range of 0.2-0.25 for most of the test.

Figure 3.13 shows the gas fraction distribution at various points in the simulations, starting from the onset of gas injection, to the point when gas starts exiting the well. The moment when gas reaches the surface roughly occurs 70 minutes after the gas injection into the well (100 minutes into the simulation). This is consistent with the time when the maximum pit gain was recorded. Note that throughout the gas circulation, the peak volume fraction was around 0.2, which largely corresponds to the bubble flow regime.

3.4 Discussion on Model Applications

One of the main advantages of the proposed model is the reduced computational time and cost, compared to state-of-the-art hydraulics simulators, such as the one used for its validation. The reduced DFM, implemented in MATLAB with 200 grid cells and a 0.5-second time step using an explicit scheme (detailed in Appendix B), required less than 10 minutes on a standard personal computer for a model scenario spanning more than 2 hours. The low run time is achieved without sacrificing complex modeling features, such as gas solubility, non-ideal gas behavior, or non-Newtonian fluid rheology. As such, the model is ideally suited for real-time decision making during kick incidents. The predicted annular pressure and gas rise velocity profiles can be used to select the best response in a conventional or MPD well control setting (Karimi Vajargah et al., 2014), and give recommendations on optimal set points and drilling parameters. The model predictions can also be used to determine allowable pressure ratings and gas handling capacities for surface equipment used on wells posing influx management challenges, such as deepwater and slim hole designs. The predictive capabilities can be further enhanced by encompassing uncertainty into the model formulation and its parameters, and propagate this uncertainty to the final outputs (Cayeux et al., 2016).

Another well-suited application of the model is in the design of automated control systems for influx handling. Most automated well control systems currently available in the industry rely on single-phase hydraulic models or steady-state "single bubble" calculations for computing set points. Such

models lead to over-estimating the change in choke opening required to keep the BHP constant as gas migrates towards the upper sections of the well, which may potentially trigger lost circulation incidents and even additional influxes. In the absence of a reliable model, automated choke control, commonly used in MPD systems, requires extensive tuning, often done manually by human operators. The presence of gas in the well may render previous tuning ineffective, leading to an unstable control system which needs to be shut down by the operator (Reitsma and Couturier, 2012).

The reduced DFM can also be used for estimating influx rates and certain reservoir parameters affecting the kick intensity, such as pore pressure and productivity index, from pressure and flow measurements recorded during a kick. For this purpose, the formulation needs to be augmented with a realistic reservoir inflow model (e.g. Wiggins et al. (1996)), and an on-line regression technique. Once the influx rate is estimated from top side measurements, it can be fed back to the model to obtain gas volume fractions and other model variables. Better knowledge of influx rates, pore pressure and reservoir productivity is of great importance not only for influx management and prevention, but also for designing MPD and underbalanced drilling operations. The following chapters will elaborate further on these and other applications.

Chapter 4

Robust Choke Control Design for Managed Pressure Drilling

This chapter will introduce several designs for automated choke control using a model-based approach, with considerations for disturbance rejection and uncertainty handling[1]. The non-linear choke model presents another challenge that needs to be addressed in the control design. For the kick handling problem we will design a switched controller capable of operating in two different modes: one mode for stopping flow from the formation, and another aimed at keeping a constant pressure target during the subsequent circulation phase. We will start with a feedback linearization approach for handling single-phase flow, and then augment the control design for multi-phase flow handling using the model developed in Chapter 3. For the pressure tracking problem, we will also explore a linear time-invariant representation (LTI) of the pressure dynamics. Using this representation, we will design a second-

[1]The work in Chapter 4.3 and a part of Chapter 4.2 have been presented in the journal publication: Ulf Jakob F. Aarsnes, Behçet Açikmeşe, Adrian Ambrus, Ole Morten Aamo. "Robust controller design for automated kick handling in managed pressure drilling". Journal of Process Control, Volume 47, November 2016, Pages 46-57. The author of this dissertation contributed to that work through theoretical analysis (in collaboration with Ulf Jakob Aarsnes and Behçet Açikmeşe), validation of simulation results, and surveying of the existing literature on control techniques for MPD systems.

order state feedback controller computed using the Linear Quadratic Gaussian (LQG) technique and another one based on Linear Matrix Inequalities (LMI), which we use for improving robustness to uncertainties in the plant model. The designs will be evaluated in simulations against standard PID controllers used in the industry. The testing includes single-phase and two-phase scenarios where a gas kick is mitigated. Also investigated are the effects of sensor data availability, sampling rates, measurement noise and delays on the control performance.

4.1 Feedback Linearization Controller

The goal of the control problem is to track a desired BHP to a predefined reference value, p_{bh}^{ref} (we will refer to this from here onward as the *pressure control mode*). We start by defining the BHP tracking error $e_p = p_{bh}^{ref} - p_{bh}$. To guarantee good tracking performance and eliminate steady-state error, we can try to achieve linear error dynamics of the form:

$$\dot{e}_p = k_p e_p + k_i \int e_p \mathrm{d}t. \tag{4.1}$$

where $k_p > 0, k_i > 0$ are proportional and integral gains. For a "regulator" control problem, we have a constant p_{bh}^{ref}, which results in $\dot{e}_p = \dot{p}_{bh}$. We would like to relate the change in p_{bh} to that in surface pressure p_c. If we neglect spatial pressure transients in the annulus, we may write:

$$p_{bh} = p_c + \int_0^L \frac{2f\rho_m v_m^2}{D}\mathrm{d}x + \int_0^L \rho_m g cos\theta \mathrm{d}x \tag{4.2}$$

For a constant pump rate, and no other source of flow into the well, we can assume that $\frac{\partial v_m}{\partial t} = 0$, and that the mud density ρ_m does not change in time, and also the length of the well is slowly changing, such that we may neglect the time derivatives of the second and third terms in Eq. 4.2. This leads to $\dot{p}_{bh}(t) \approx \dot{p}_c(t)$. Recall the reduced DFM pressure dynamics for the annular section, defined in Chapter 3:

$$\dot{p}_c = \frac{\bar{\beta}}{V_a}\big(q_p + q_{res} - q_c + T_{ex}\big), \tag{4.3}$$

where, q_{res} is the flow rate from the reservoir (i.e. during a kick). For single-phase choke flow, we have:

$$q_c = C_v Z \sqrt{\frac{p_c - p_0}{\rho_L}} \equiv \Psi(Z, p_c). \tag{4.4}$$

Since we do not have perfect knowledge of the reservoir, we will set $q_{res} = 0$, or use an observer to estimate it (this will be detailed in Chapter 5). A simple approach for dealing with the choke non-linearity defined in Eq. 4.4 is to use feedback linearization to eliminate the non-linearity. For instance, we can define a control law:

$$Z = \frac{\sqrt{\rho_L}}{C_v\sqrt{p_c - p_0}} u \equiv \Psi^{-1}(u, p_c) \tag{4.5}$$

where u is the control input. In the implementation of the feedback linearizing control law, the back-pressure p_c should be low-pass filtered to avoid measurement noise in the denominator. The block diagram for the plant with the feedback linearization controller is shown in Figure 4.1, where $C(s)$ is a linear

controller, G_1, G_2 represent the transfer functions relating q_c to p_{bh} and p_c, respectively, L_u is the transfer function for actuation dynamics, while L_{pc} and L_y represent measurement dynamics. A process disturbance w and measurement noise ν_c, ν_{bh} may also be included.

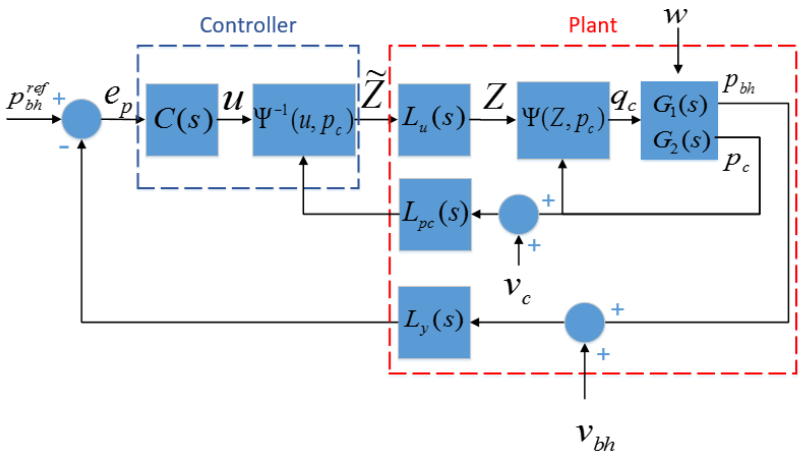

Figure 4.1: Block diagram for choke controller with feedback linearization. The controller consists of a linear term $C(s)$ and the feedback linearization law $\Psi^{-1}()$ which produces a choke position command $\tilde{Z}$. An inner feedback loop is created from the surface back-pressure p_c entering the feedback linearization. The plant includes the choke non-linearity $\Psi()$, together with actuation (L_u) and measurement dynamics (L_{pc}, L_y).

By applying linear perturbation analysis on the non-linear blocks Ψ and Ψ^{-1}, we can derive the open-loop transfer function from the input $\tilde{u} = u - \bar{u}$ to the output $\tilde{p}_{bh} = p_{bh} - \bar{p}_{bh}$, where $\bar{u}, \bar{p}_{bh}$ denote steady-state values:

$$G(s) = \frac{G_1(s)L_u(s)}{1 - \frac{\bar{u}G_2(s)[1-L_{pc}(s)]L_u(s)}{2(\bar{p}_c - p_0)}} \tag{4.6}$$

and $\bar{p}_c$ is the surface back-pressure at steady-state. For the ideal case of $L_u(s) = L_{pc}(s) = 1$ (no actuation or measurement dynamics), and for the first-

order transfer function $G_1(s) = -\frac{\bar{\beta}}{V_a s}$, we retrieve the first-order approximation

$$\dot{p}_{bh} = \frac{\bar{\beta}}{V_a}\big(q_p - u\big), \tag{4.7}$$

Note the pole at the origin in $G_1(s)$ which implies a marginally stable open-loop system.

In order to evaluate stability for the open-loop system defined in Eq. 4.6 over a wide range of frequencies, we will use the infinite-dimensional transfer functions $G_1(s) = -\frac{Z_c(s)}{\sinh \Gamma(s)}$, $G_2(s) = -Z_c(s)\frac{\cosh \Gamma(s)}{\sinh \Gamma(s)}$, with $\Gamma(s) = \frac{sL}{c_L}\sqrt{1 + \frac{k}{s}}$, $Z_c(s) = \frac{\rho c_L}{A}\sqrt{1 + \frac{k}{s}}$, together with the measurement dynamics $L_{pc}(s) = \frac{1}{20s+1}$ and the actuation dynamics $L_u(s) = \frac{1}{5s+1}$. Figure 4.2 shows the frequency response for different values of $\bar{p}_c$.

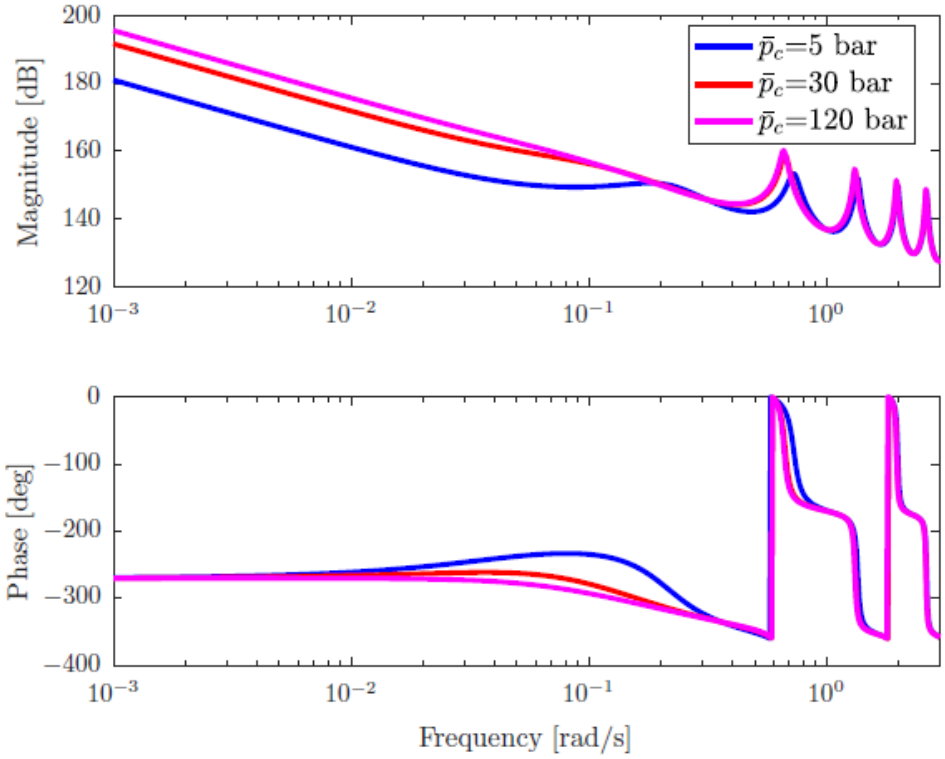

Figure 4.2: Frequency response of open-loop plant transfer function for feedback linearized system for different back-pressure operating points. The feedback linearization results in a large uncertainty in magnitude for frequencies below 0.1 rad/s.

It is noticed that the proposed feedback linearization introduces steady-state uncertainty in magnitude due to the unmodeled actuation and measurement dynamics entering the inner feedback loop. Also, due to the term $\frac{\bar{\beta}}{V_a}$ which can be on the order of $10^6 - 10^8$ Pa/m^3, this control law requires a high gain reduction to obtain a stable closed-loop system.

A feedback linearizing controller that will produce the error dynamics

in Eq. 4.1 can be designed as

$$u = -\frac{V_a}{\bar{\beta}}(k_p e_p + k_i \int e_p \mathrm{d}t) + q_p \tag{4.8}$$

$$\implies Z = \Big[-\frac{V_a}{\bar{\beta}}(k_p e_p + k_i \int e_p \mathrm{d}t) + q_p \Big] \frac{\sqrt{\rho_L}}{C_v \sqrt{p_c - p_0}} \tag{4.9}$$

For two-phase mixed flow through the choke, we have:

$$q_c = q_{L,c} + q_{G,c} = C_v Z \Big(\frac{\chi_L}{\rho_L} + \frac{\chi_G}{\rho_G} \Big) \sqrt{\frac{p_c - p_0}{\frac{\chi_L}{\rho_L} + \frac{\chi_G}{Y^2 \rho_G}}} \tag{4.10}$$

which entails a modification to the feedback linearization:

$$Z = \Big[\frac{V_a}{\bar{\beta}}(-k_p e_p - k_i \int e_p \mathrm{d}t) + q_p + T_{ex} - q_{G,c} \Big] \frac{\rho_L \sqrt{\frac{\chi_L}{\rho_L} + \frac{\chi_G}{Y^2 \rho_G}}}{\chi_L C_v \sqrt{p_c - p_0}} \tag{4.11}$$

where χ_L, χ_G are the liquid and gas mass fraction at the choke, respectively, $q_{G,c}$ is the volumetric gas flow rate at the choke and Y is a gas expansion factor in the choke model. We note that not all flow meters currently used in the industry are suitable for two-phase flow, and thus the gas flow rate together with the liquid and mass fractions may need to be estimated from other measurements (e.g., choke pressure, pit gain) or computed using a model, such as the one described in Chapter 3. Also the terms $\bar{\beta}$ and T_{ex} need to be computed from the model.

4.2 LQG Controller

To cast the problem in a formulation suitable for LQG design, we may either use feedback linearization, as in the previous section, or we may linearize the pressure dynamics around an operating point and model perturbations

from that operating point. In this section, we will proceed with the latter approach to derive a first-order approximated model. The approximation is based on the assumption that $\dot{p}_{bh}(t) \approx \dot{p}_c(t)$, i.e. we neglect the distributed pressure transients. Denoting the equilibrium states $\bar{q}_c = \bar{q}_{bit} = q_p$ and $\bar{p}_c, \bar{p}_{bh}$, we will use the perturbed variables:

$$\tilde{q}_c(t) = q_c(t) - \bar{q}, \qquad \tilde{q}_{bit}(t) = q_{bit}(t) - \bar{q}, \tag{4.12}$$

$$\tilde{p}_c(t) = p_c(t) - \bar{p}_c, \qquad \tilde{p}_{bh}(t) = p_{bh}(t) - \bar{p}_{bh}. \tag{4.13}$$

To close the loop around the pressure state, we need to linearize the choke model as well. To simplify notation, we introduce a static mapping between the control input u and the choke opening Z:

$$Z(u) = C_v^{-1}\Big(q_p \frac{\sqrt{\rho_L}}{\sqrt{u}}\Big), \tag{4.14}$$

where the mapping was chosen such that u corresponds to the steady state $\bar{p}_c - p_0$ for $q_{bit} = q_c = q_p$ and liquid-only flow (i.e. $\bar{u} = \bar{p}_c - p_0$), for which (4.4) becomes

$$q_c = q_p \frac{\sqrt{p_c - p_0}}{\sqrt{u}}. \tag{4.15}$$

The block diagram with the static choke mapping is illustrated in Figure 4.3.

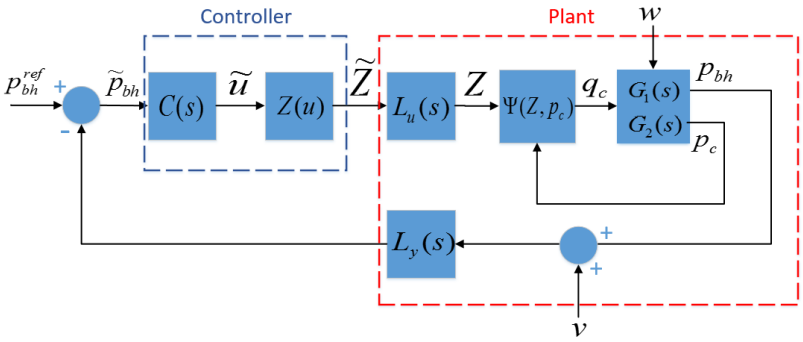

Figure 4.3: Block diagram for choke controller with static choke mapping. The plant structure is similar to the one shown in Figure 4.1 except for the elimination of feedback from p_c to the controller.

The choke equation (4.15) is linearized and evaluated at a given operating point. Using the perturbation variables, we obtain a relation of the form:

$$\tilde{q}_c = K_p \tilde{p}_c - K_u \tilde{u}. \tag{4.16}$$

where $\tilde{u} = u - \bar{u}$ and the linearization coefficients are defined as

$$K_p = \frac{q_p}{C_K} \frac{1}{2\sqrt{\bar{p}_c - p_0}\sqrt{\bar{u}}}, \tag{4.17}$$

$$K_u = \frac{q_p}{C_K} \frac{\sqrt{\bar{p}_c - p_0}}{2\bar{u}\sqrt{\bar{u}}}. \tag{4.18}$$

At the equilibrium point, we have $\bar{u} = \bar{p}_c - p_0$, and thus, $K_u = K_p$. The transfer function from $\tilde{u}$ to $\tilde{p}_{bh}$, is given by:

$$G(s) = -\frac{q_p L_u(s) G_1(s)}{2C_K \bar{u} - q_p L_u(s) G_2(s)} \tag{4.19}$$

Figure 4.4 shows the frequency response of the open-loop system.

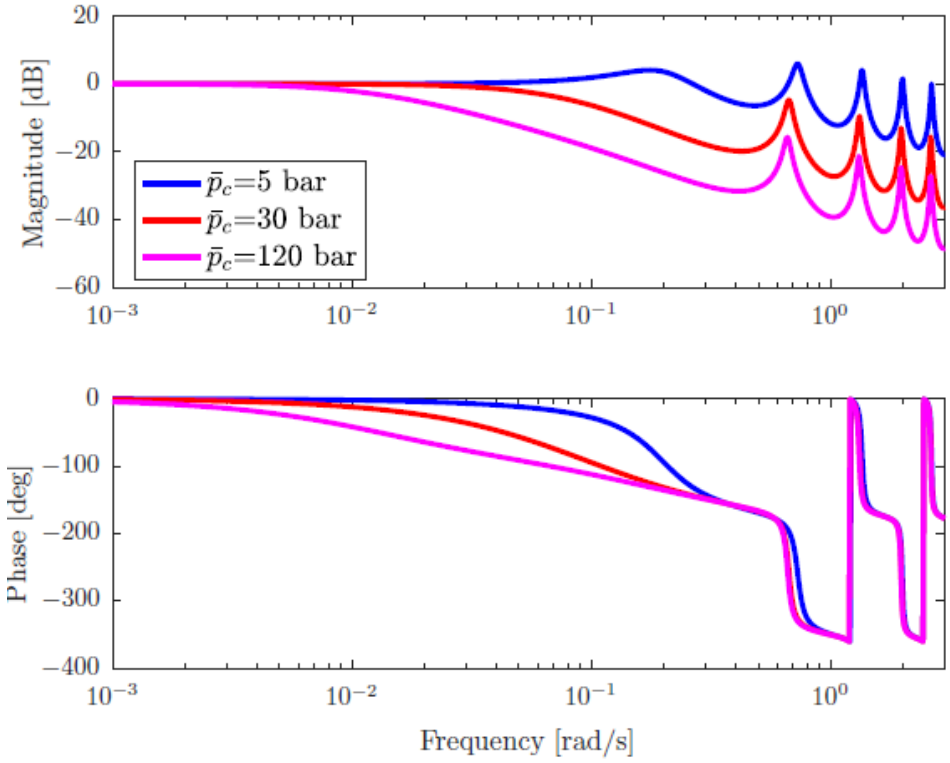

Figure 4.4: Frequency response of open-loop linearized system with static choke mapping for different back-pressure operating points. This structure introduces uncertainty in magnitude and phase above 0.01 rad/s, which needs to be accounted for in the control design.

Compared to the feedback linearized open-loop plant (Figure 4.2), the linearization with the static choke mapping eliminates the steady-state uncertainty, and significantly improves open-loop performance in the low frequency range. At frequencies above 0.05 rad/s, the magnitude variation with different back-pressure operating points starts to become notable, however this can be easily described with a multiplicative uncertainty, as will be shown in a later section. While the actuation dynamics are necessary in evaluating the actual

system performance, they will be discarded in the controller design. Furthermore, if we use the first-order approximation $G_1(s) = G_2(s) = -\frac{\bar{\beta}}{V_a s}$, we get the simplified transfer function:

$$G(s) = \frac{1}{\frac{2C_K V \bar{u}}{\bar{\beta} q_p} s + 1} \tag{4.20}$$

Re-casting Eq. 4.20 in time domain, we can write the first-order linearized perturbation dynamics as:

$$\dot{\tilde{p}}_{bh}(t) \approx \frac{1}{\tau(t)}\big(- \tilde{p}_{bh} + \tilde{u}\big) \tag{4.21}$$

$$\tau(t) = \frac{V_a}{K_p(t)\bar{\beta}(t)}, \quad K_p(t) = \frac{q_p}{2C_K(t)}\frac{1}{\bar{u}(t)}. \tag{4.22}$$

Several observations need to be made with regard to Eq. 4.22:

1. The time constant of the first-order plant, $\tau(t)$, is time-varying and changes with the operating point $\bar{u}$ and also with the bulk modulus $\bar{\beta}(t)$ which is a function of the mud density, and also of the gas content in the well. Figure 4.5 illustrates the range of $\tau(t)$ values for different gas kick volumes.

2. The variation $\tau(t)$ due to changes in the operating point can be calculated directly from Eq. 4.22.

3. The bulk modulus of the gas-liquid mixture can be estimated using the reduced DFM, as shown in Chapter 3, but for the design of the controller we will treat it as uncertain.

4. The high-frequency dynamics that were discarded to obtain the first-order plant also introduce uncertainty in the model. These high-frequency modes occur due to the pressure wave propagation and reflection, which result in a series of resonances and anti-resonances. Modeling this uncertainty will be addressed in a later section.

5. C_K is a factor arising from the linearization of the two-phase choke model, and it depends on the model used (e.g. mixed or stratified flow).

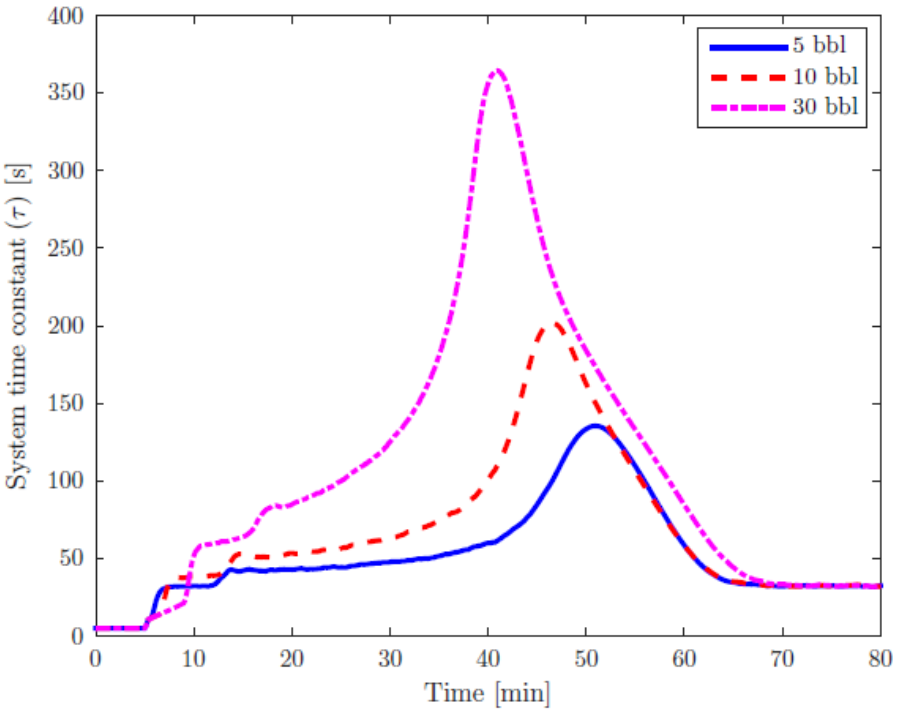

Figure 4.5: Evolution of first-order system time constant, $\tau(t)$, during a gas kick in WBM, for different kick detection volumes (in barrels). Higher kick volumes result in larger time constants. $\tau(t)$ may range from 2 seconds to 400 seconds during a large gas kick. The peak values correspond to gas arriving at the surface.

We will next proceed to design a LQG controller with integral action. Let I_e represent the integrated tracking error. We have the following augmented system:

$$\dot{\tilde{p}}_{bh} = \frac{1}{\tau(t)}\left(-\tilde{p}_{bh} + \tilde{u}\right) + w \tag{4.23}$$

$$\dot{I}_e = \tilde{p}_{bh}, \tag{4.24}$$

$$y = \tilde{p}_{bh} + v \tag{4.25}$$

where w and v represent the process and measurement noise, with $E(w^2) = \gamma_w$,$E(v^2) = \gamma_v$,$E(wv) = 0$. The LQG controller aims to minimize the quadratic cost:

$$J = \int_0^\infty (x^T Q x + u^T R u)\mathrm{d}t \tag{4.26}$$

where we select $Q = \begin{bmatrix} \rho_1 & 0 \\ 0 & \rho_2 \end{bmatrix}$ and $R = 1$ with $\rho_1, \rho_2 > 0$ tuning factors allowing the control design to trade off between the desired transient response and the control effort used. For the standard state space formulation $\dot{x} = Ax + Bu$, the optimal gains are found by solving the associated Riccati equation with the unknown matrix X (Anderson and Moore, 1990):

$$A^T X + XA - XBR^{-1}B^T X + Q = 0 \tag{4.27}$$

The controller gains are given by:

$$k_1 = \sqrt{\rho_1 + 2\sqrt{\rho_2}\tau + 1} - 1 \tag{4.28}$$

$$k_2 = \sqrt{\rho_2} \tag{4.29}$$

It should be noted that the expression for k_1 contains the time constant τ, which means that k_1 can be designed as a time-varying gain, $k_1(\tau(t))$, allowing for improved performance, if the variation in τ is known or estimated from the model. For the state estimator (Kalman Filter) associated with the LQG controller, the gain is given by:

$$L = \frac{\sqrt{\gamma_w \gamma_v \tau^2 + 1} - 1}{\gamma_v \tau} \tag{4.30}$$

The closed loop system is described by the following equations:

$$\dot{\mathbf{x}}_c = \begin{bmatrix} -\left(\frac{1+k_1}{\tau} + L\right) & -\frac{k_2}{\tau} \\ 0 & 0 \end{bmatrix} \mathbf{x}_c + \begin{bmatrix} L \\ 1 \end{bmatrix} \tilde{p}_{bh} \tag{4.31}$$

$$\tilde{u} = -\begin{bmatrix} k_1 & k_2 \end{bmatrix} \mathbf{x}_c \tag{4.32}$$

where $\mathbf{x}_c = \begin{bmatrix} \hat{p}_{bh} \\ I_e \end{bmatrix}$, $\hat{p}_{bh}$ being the filtered BHP perturbation. Once $\tilde{u}$ is computed, we can invert the static choke mapping to compute the choke position:

$$Z = \frac{1}{C_v} \frac{q_p \sqrt{\rho_L}}{\sqrt{\tilde{u} + \bar{u} - p_0}} \tag{4.33}$$

4.3 LMI-Based Control Design

4.3.1 Representing Model Uncertainty

In transfer function notation we can express Eq. 4.21 as $\tilde{p}_{bh} = P_n \tilde{u}$, where P_n represents the nominal first-order plant (i.e. without uncertainty). The uncertainty due to the discarded high-frequency dynamics will be represented as a multiplicative uncertainty, $\|\Delta(t)\| \leq 1$, with the weighting function $W(s) = \tau_\Delta s$, where τ_Δ represents the period at which the high-frequency pressure dynamics become significant. Due to the choice for the weighting function,

the uncertainty is applied in time domain to the derivative of the actuation, $\dot{\tilde{u}} = u_d$. This results in the uncertain plant given as:

$$\dot{\tilde{p}}_{bh} = \frac{1}{\tau(t)}\left(-\tilde{p}_{bh} + \tilde{u} + w + \tau_\Delta p\right), \tag{4.34}$$

$$p = \Delta(t)\dot{\tilde{u}}, \quad \|\Delta(t)\| \leq 1. \tag{4.35}$$

To determine an appropriate value for τ_Δ, we will compare the frequency response of the first-order nominal plant, P_n, with a high-order plant, P. For single-phase flow, we may use the transmission line model, described in Chapter 3.1.1:

$$\begin{bmatrix} P_{bh}(s) \\ P_c(s) \end{bmatrix} = Z_c(s) \begin{bmatrix} \frac{\cosh\Gamma(s)}{\sinh\Gamma(s)} & -\frac{1}{\sinh\Gamma(s)} \\ \frac{1}{\sinh\Gamma(s)} & -\frac{\cosh\Gamma(s)}{\sinh\Gamma(s)} \end{bmatrix} \begin{bmatrix} Q_{bit}(s) \\ Q_c(s) \end{bmatrix}, \tag{4.36}$$

where $P_{bh}(s)$, $P_c(s)$, $Q_{bit}(s)$, $Q_c(s)$ are the Laplace transforms of BHP, back-pressure, bit flow rate and choke flow rate. If we denote the transfer functions $G_1(s) = -Z_c(s)\frac{1}{\sinh\Gamma(s)}$, $G_2(s) = -Z_c(s)\frac{\cosh\Gamma(s)}{\sinh\Gamma(s)}$, this writes as:

$$\begin{bmatrix} P_{bh}(s) \\ P_c(s) \end{bmatrix} = \begin{bmatrix} -G_2(s) & G_1(s) \\ -G_1(s) & G_2(s) \end{bmatrix} \begin{bmatrix} Q_{bit}(s) \\ Q_c(s) \end{bmatrix}, \tag{4.37}$$

In perturbed dynamics form ($\tilde{q}_{bit} = 0$), we have

$$\begin{bmatrix} \tilde{P}_{bh}(s) \\ \tilde{P}_c(s) \end{bmatrix}(s) = \begin{bmatrix} \tilde{G}_1(s) \\ \tilde{G}_2(s) \end{bmatrix} \tilde{Q}_c(s) \tag{4.38}$$

For low frequencies ($s \to 0$), we have $\sinh\Gamma(s) \approx \Gamma(s), \cosh\Gamma(s) \approx 1$, which gives $\tilde{G}_1(s) = \tilde{G}_2(s) = -\frac{Z_c(s)}{\Gamma(s)} = -\frac{\beta_L}{V_a s}$, or equivalently, $\dot{\tilde{p}}_{bh}(t) = \dot{\tilde{p}}_c(t) = -\frac{\beta_L}{V_a}\tilde{q}_c(t)$. Using Eq. 4.16 we get the infinite-dimensional plant transfer function

$$P = \frac{-\tilde{G}_1 K_u}{1 - \tilde{G}_2 K_p}. \tag{4.39}$$

The nominal plant P_n can be compared with the infinite-dimensional plant P in frequency domain to observe the error due to high-frequency dynamics. The frequency response of P_n and P for different operating points $\bar{u}$ is shown in Figure 4.6.

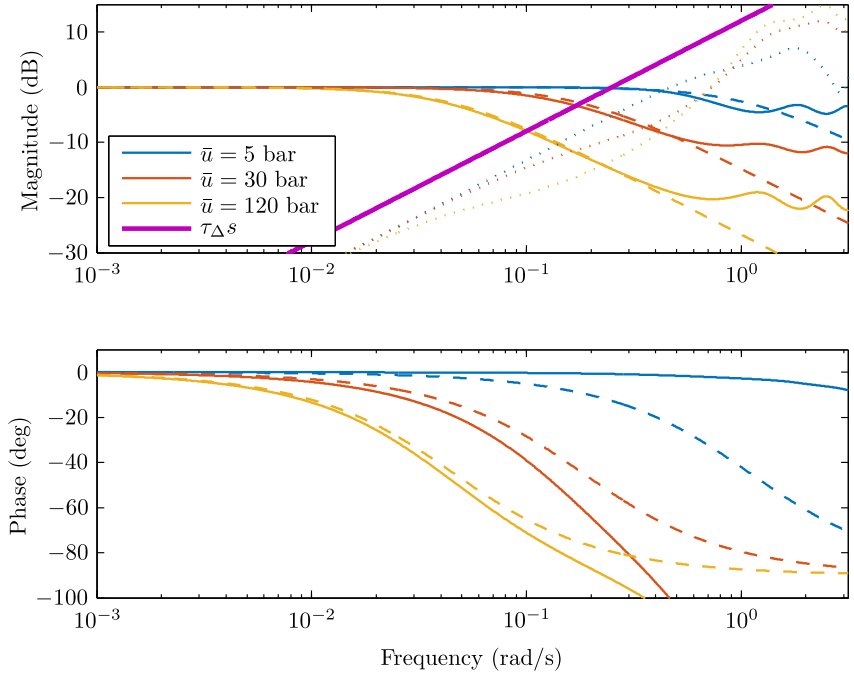

Figure 4.6: Comparison of infinite-dimensional plants P (–) and first-order approximations P_n (- -), with the relative error $\frac{P-P_n}{P_n}(\cdots)$ and error bound $\tau_\Delta s$ for different operating points $\bar{u}$ with no gas in the well. The error bound with $\tau_\Delta = 4$ seconds covers the relative error for the entire range of operating points.

For the two-phase case, it is not possible to derive an infinite-dimensional transfer function similar to Eq. 4.39, but instead we may derive a high-order LTI approximation and then proceed with the analysis as before to evaluate the high-frequency uncertainty. We will use the lumped model from Eqs. 3.9-

3.11, rewritten in terms of perturbation variables, such that the hydrostatic and pump flow terms vanish (assuming steady pump rate):

$$\dot{\tilde{p}}_j = \frac{\bar{\beta}_j}{A_j l}(\tilde{q}_{j-1} - \tilde{q}_j), \qquad j = 1, \ldots, N \tag{4.40}$$

$$\dot{\tilde{q}}_j = \frac{A_j}{l\bar{\rho}_j}(\tilde{p}_j - \tilde{p}_{j+1}) - k\tilde{q}_j, \qquad j = 1, \ldots, N-1 \tag{4.41}$$

$$\tilde{q}_0 = 0, \qquad \tilde{q}_N = \tilde{q}_c. \tag{4.42}$$

with

$$\bar{\beta}_j = \frac{\beta_L p(x_j)}{p(x_j)\big(1-\alpha_G(x_j)\big) + \beta_L \alpha_G(x_j)}, \tag{4.43}$$

where $p(x_j), \alpha_G(x_j)$ denote that the pressure and void fraction are averaged over control volume j, and β_L denotes the liquid bulk modulus. The effective density in control volume j is given as

$$\bar{\rho}_j = \rho_L(1-\alpha_G(x_j)) + \rho_G \alpha_G(x_j), \tag{4.44}$$

where ρ_L and ρ_G are liquid and gas densities, respectively. To illustrate the response of the lumped model in a kick scenario, an uncontrolled kick in a 3000-m (9842 ft) deep vertical well with a reservoir pore pressure of 421 bar (6100 psi) and a BHP of 415 bar (6019 psi) was simulated using an implementation of the full DFM (it was assumed that gas was not dissolved in the mud). The gas distribution at different instants following the start of the kick, shown in Figure 4.7, was used to calculate the $\bar{\beta}$ and $\bar{\rho}$ terms in Eqs. 4.40-4.42, and then to simulate the impulse response (from choke flow rate to BHP) based on the gas profiles at each instant. The gas fraction α_G is assumed to be time-invariant throughout each simulation, i.e. $\alpha_G(x,t) = \alpha_G(x)$.

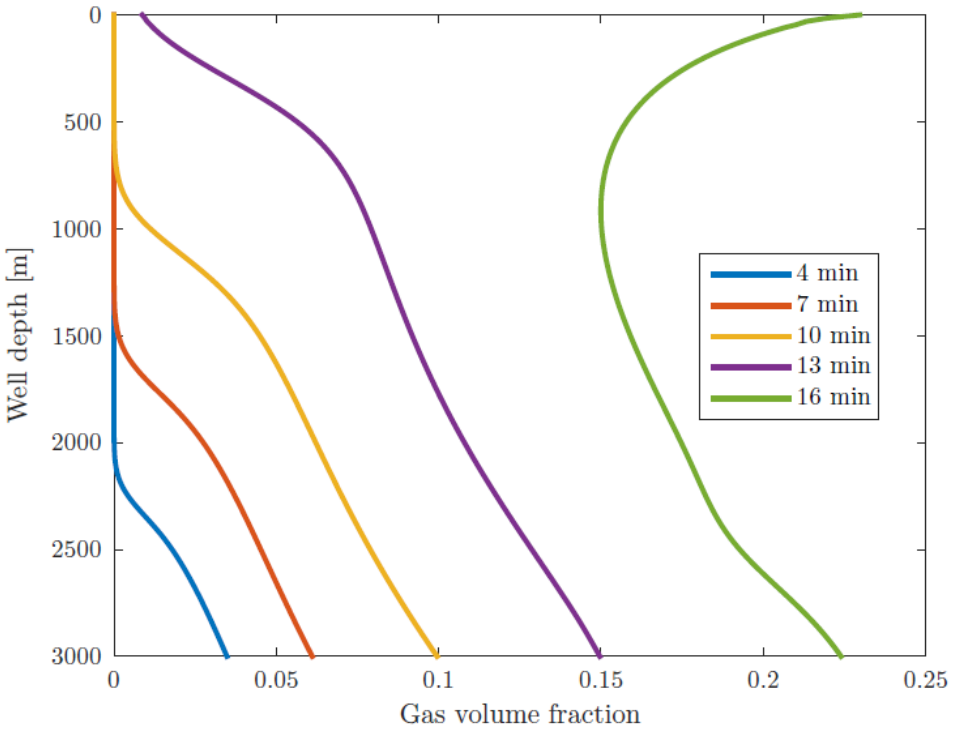

Figure 4.7: Gas volume fraction profiles at different times after an uncontrolled kick incident. The gas distributions together with Eqs. 4.40-4.44 are used to simulate the high-order plant model P with two-phase conditions.

Figure 4.8 shows the approximated impulse responses compared to the actual response from the full DFM. As more gas enters the well, the transients become slower, and the initial delay between the application of the impulse and the observed change in p_{bh} increases. For larger amounts of gas, the steady-state error between the lumped approximation and DFM also increases. $N = 50$ control volumes were used for the lumped approximation.

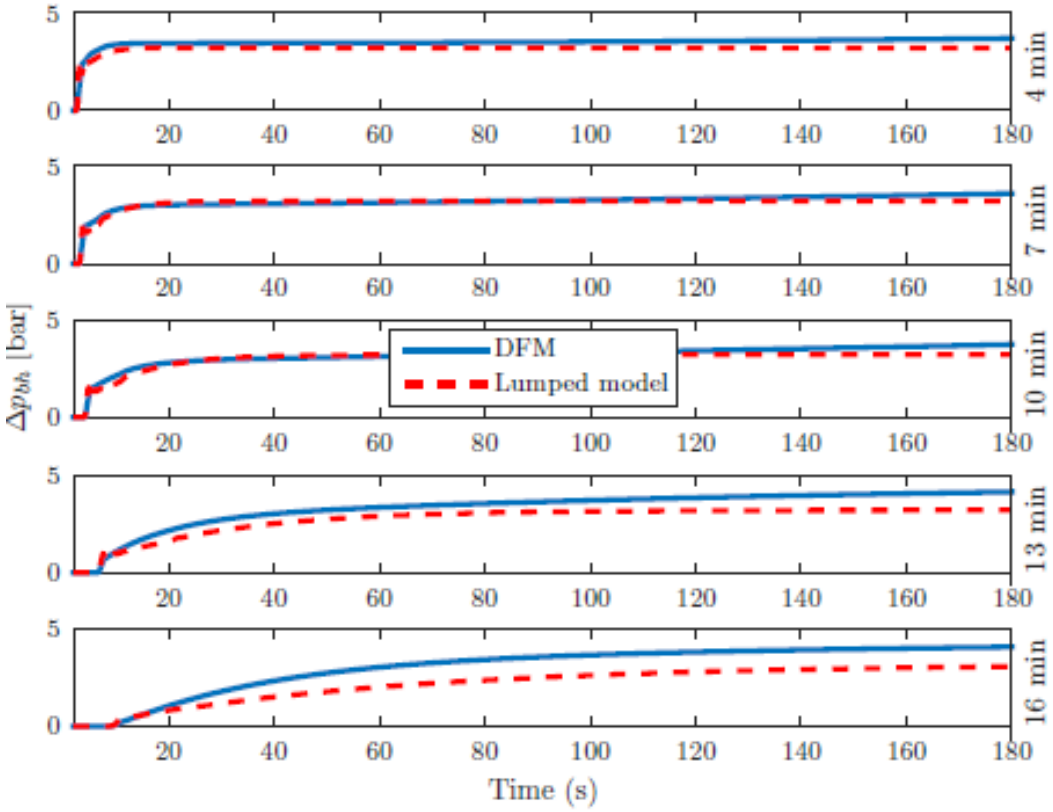

Figure 4.8: Impulse responses of the high-order lumped approximation with gas compared to the DFM simulation. Each response is generated by an impulse in flow rate q_c initiated at different time instants corresponding to the gas distributions in Figure 4.7. As more gas enters the well, the transients become slower, as indicated by the longer response times. Also, for larger amounts of gas, the steady-state error between the approximation and DFM increases.

Next, we compare the frequency response of the nominal plant P_n to the high-order lumped approximations of the two-phase dynamics in Figure 4.9. Here τ is dependent on both the gas profile $\alpha_G(x)$ and the operating point $\bar{u}$. We see that the constant $\tau_\Delta = 4$ seconds is sufficient to represent the

error caused by the high frequency dynamics, except for the cases with large amounts of gas. It can be reasoned that this error is due to the distributed pressure dynamics discarded by the first order approximation. The frequency at which the discarded dynamics become important is dependent on the gas profile, as the presence of gas lowers the pressure wave propagation speed in the drilling fluid.

The uncertainty in $\tau(t)$ can be represented through a lower and upper bound, $\underline{\tau}$ and $\overline{\tau}$, respectively. Also, we add integral action to the control to improve disturbance rejection, introducing an extra state, I_e, for the integrated error. The system is then written in state space form as:

$$\dot{\tilde{p}}_{bh} = \frac{1}{\tau(t)} \left(-\tilde{p}_{bh} + \tilde{u} + w + \tau_\Delta p \right), \quad \tau(t) \in [\underline{\tau}, \overline{\tau}] \tag{4.45}$$

$$\dot{\tilde{u}} = u_d \tag{4.46}$$

$$\dot{I}_e = \tilde{p}_{bh}, \tag{4.47}$$

where w is the disturbance, and p represents the uncertainty due to the high-frequency pressure dynamics:

$$q = u_d \tag{4.48}$$

$$p = \Delta(t) q, \quad |\Delta(t)| \leq 1. \tag{4.49}$$

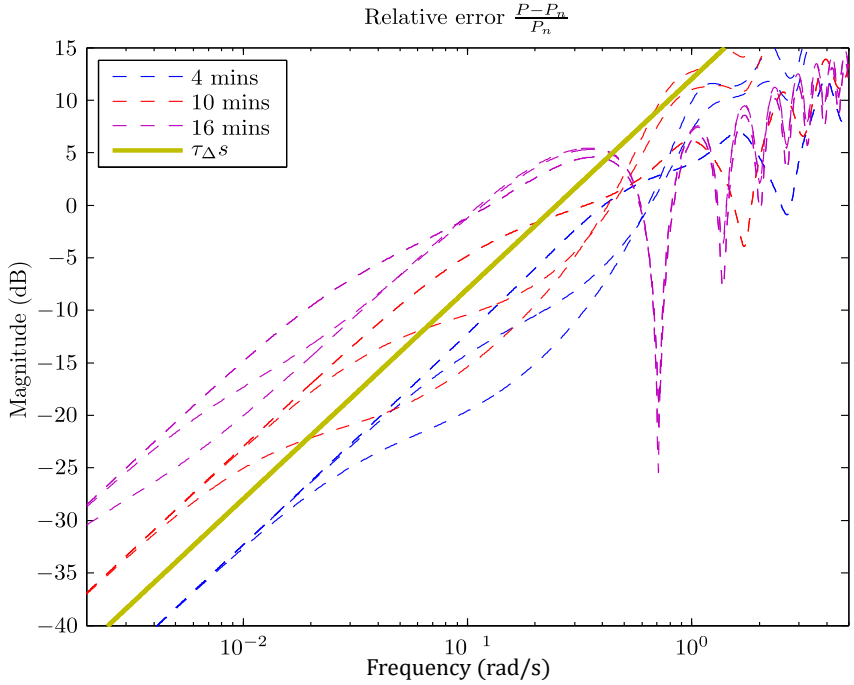

Figure 4.9: Relative error (dashed lines) between first-order nominal plant P_n and the high-order plant P for the gas distributions in Figure 4.7 and the range of operating points $\bar{u}$ covered in Figure 4.6. The error bound $\tau_\Delta s$ (solid line) with $\tau_\Delta = 4$ seconds covers the low-frequency error for small amounts of gas and also the error at high frequencies for the entire range of gas distributions and operating points. The low-frequency uncertainty due to the gas can be handled either with a higher τ_Δ or through bounds on $\tau(t)$.

4.3.2 Control Design

The control problem can be formulated as finding a state feedback gain, K, which minimizes the $\mathbf{L}_2$ gain from the disturbance to the integrated error, defined as (Boyd et al., 1994):

$$\gamma \equiv \sup_{\|w\|_2 \neq 0} \frac{\|I_e\|_2}{\|w\|_2}, \tag{4.50}$$

where $\|w\|_2 = (\int_0^\infty \|w(t)\|^2 \mathrm{d}t)^{\frac{1}{2}}; \|I_e(t)\|_2 = (\int_0^\infty \|I_e(t)\|^2 \mathrm{d}t)^{\frac{1}{2}}$. To solve this problem we will represent the system as a norm-bound Linear Differential Inclusion (LDI) (Boyd et al., 1994):

$$\dot{x} = A(t)x + B_u u + B_w(t)w + B_p(t)p, \tag{4.51}$$

$$q = C_q x + D_{qu} u + D_{qp} p, \tag{4.52}$$

$$z = C_z x \tag{4.53}$$

$$p = \Delta(t) q, \quad |\Delta(t)| \leq 1, \tag{4.54}$$

where $A(t)$ is the time-varying system matrix, and the actuation, disturbance and norm-bound uncertainty enter through the input vectors $B_u, B_w(t), B_p(t)$ respectively. With the bounds on $\tau(t) \in [\underline{\tau}, \overline{\tau}]$, and denoting $\tau_1 = \underline{\tau}, \tau_2 = \overline{\tau}$ the time-varying plant (4.51)–(4.54) can be described as an LDI, Ω, given by the convex hull (**Co**):

$$\Omega = \mathbf{Co}\left\{ \begin{bmatrix} A_1 & B_u & B_{w,1} & B_{p,1} \\ C_q & D_{qp} & D_{qu} & 0 \\ C_z & 0 & 0 & 0 \end{bmatrix}, \begin{bmatrix} A_2 & B_u & B_{w,2} & B_{p,2} \\ C_q & D_{qp} & D_{qu} & 0 \\ C_z & 0 & 0 & 0 \end{bmatrix} \right\}. \tag{4.55}$$

with

$$A_i = \begin{bmatrix} \frac{-1}{\tau_i} & \frac{1}{\tau_i} & 0 \\ 0 & 0 & 0 \\ 1 & 0 & 0 \end{bmatrix}, B_{w,i} = \begin{bmatrix} \frac{1}{\tau_i} \\ 0 \\ 0 \end{bmatrix}, B_{p,i} = \begin{bmatrix} \frac{\tau_\Delta}{\tau_i} \\ 0 \\ 0 \end{bmatrix}, \tag{4.56}$$

$i = 1, 2,$

$$B_u = \begin{bmatrix} 0 \\ 1 \\ 0 \end{bmatrix}, C_q = \begin{bmatrix} 0 \\ 0 \\ 0 \end{bmatrix}^T, C_z = \begin{bmatrix} 0 \\ 0 \\ 1 \end{bmatrix}^T, \tag{4.57}$$

and $D_{qp} = 0, D_{qu} = 1$. A state feedback controller that minimizes the $\mathbf{L}_2$ gain can be designed by solving the eigenvalue problem (Boyd et al., 1994) in the matrix variables Y, Q and scalars γ, μ (see Appendix D for detailed derivation):

$$\text{minimize} \quad \gamma \tag{4.58}$$

$$\text{subject to:} \quad Q > 0, \mu > 0 \tag{4.59}$$

$$\begin{bmatrix} \begin{pmatrix} A_i Q + Q A_i^T \\ +B_u Y + Y^T B_u^T \\ +B_{w,i} B_{w,i}^T + \mu B_{p,i} B_{p,i}^T \end{pmatrix} & QC_z^T & \mu B_{p,i} D_{qp}^T + QC_q^T + Y^T D_{qu}^T \\ C_z Q & -\gamma^2 I & 0 \\ \mu D_{qp} B_{p,i}^T + C_q Q + D_{qu} Y & 0 & -\mu(I - D_{qp} D_{qp}^T) \end{bmatrix} \leq 0, \tag{4.60}$$

$i = 1, 2.$

The solution of this problem is the feedback gain: $K = \begin{bmatrix} k_1 & k_2 & k_3 \end{bmatrix}^T = YQ^{-1}$. Because the formulation (4.58)–(4.60) assumes a positive feedback, the gains k_1, k_2, k_3 are all negative. In transfer function representation, the controller can be written as $\tilde{u} = C(s)\tilde{p}_{bh}$ with:

$$C(s) = \frac{k_1 s + k_3}{s(s - k_2)}. \tag{4.61}$$

which follows from the fact that:

$$u_d(t) = k_1 \tilde{p}_{bh}(t) + k_2 \tilde{u}(t) + k_3 \tilde{I}_e(t) \tag{4.62}$$

$$\implies s\tilde{u}(s) = k_1 \tilde{p}_{bh}(s) + k_2 \tilde{u}(s) + \frac{k_3}{s} \tilde{p}_{bh}(s) \tag{4.63}$$

The control performance can be further improved by making the gain dependent on $\tau(t)$, or an estimate of it. This approach leads to a time-varying

feedback law, which can be included in the LDI by augmenting the plant (4.51)–(4.54). For instance, we may introduce an additional proportional feedback gain, $k_\tau\big(\hat{\tau}(t)\big)$, dependent on the estimated time constant $\hat{\tau}$. This additional gain also enters in the norm-bound uncertainty, such that we have to modify the expression for q. The updated state space description becomes:

$$\dot{\tilde{p}}_{bh} = -\frac{1 + k_\tau\big(\hat{\tau}(t)\big)}{\tau(t)}\tilde{p}_{bh} + \frac{1}{\tau(t)}\left(\tilde{u} + w + \tau_\Delta p\right) \tag{4.64}$$

$$\dot{\tilde{u}} = u_d \tag{4.65}$$

$$\dot{I}_e = \tilde{p}_{bh}, \tag{4.66}$$

$$q = k_\tau\big(\hat{\tau}(t)\big)\frac{1 + k_\tau\big(\hat{\tau}(t)\big)}{\tau(t)}\tilde{p}_{bh} - \frac{k_\tau\big(\hat{\tau}(t)\big)}{\tau(t)}\tilde{u} + u_d - \frac{k_\tau\big(\hat{\tau}(t)\big)}{\tau(t)}\tau_\Delta p \tag{4.67}$$

$$p = \Delta(t)q, \quad |\Delta(t)| \leq 1. \tag{4.68}$$

For $k_\tau(\hat{\tau})$ we would like to design a simple, explicit control law that can improve performance. One approach is to use the optimal control gain from the first-order LQG formulation (no integral action):

$$k_\tau\big(\hat{\tau}(t)\big) = \sqrt{\rho\hat{\tau}(t) + 1} - 1, \tag{4.69}$$

where $\rho > 0$ is a tuning factor. The controller $C(s)$ is now found similarly to the static case, with the full controller given as:

$$\tilde{u} = (C(s) - k_\tau\big(\hat{\tau}(t)\big))\tilde{p}_{bh}. \tag{4.70}$$

With the time-varying feedback gain $k_\tau\big(\hat{\tau}(t)\big)$, the LDI is the same as the one

given by (4.55)–(4.57), except for the following changes:

$$A_i = \begin{bmatrix} -\frac{1+k_\tau(\hat{\tau}_i)}{\tau_i} & \frac{1}{\tau_i} & 0 \\ 0 & 0 & 0 \\ 1 & 0 & 0 \end{bmatrix}, \tag{4.71}$$

$$C_{q,i} = -k_\tau(\hat{\tau}_i) \begin{bmatrix} -\frac{1+k_\tau(\hat{\tau}_i)}{\tau_i} & \frac{1}{\tau_i} & 0 \end{bmatrix}, \tag{4.72}$$

$$D_{qp} = -k_\tau(\hat{\tau}_i)\frac{\tau_\Delta}{\tau}. \tag{4.73}$$

Because we introduced another uncertain variable in $\hat{\tau}$, we now need four edges to describe the polytope. Given the range for τ: $\tau \in [\underline{\tau}, \overline{\tau}]$ and an uncertainty bound given by r such that $\tau \in [\hat{\tau}r, \hat{\tau}/r]$, the polytope edges are given by:

$$\tau_1 = \underline{\tau}, \qquad \hat{\tau}_1 = \underline{\tau}/r, \tag{4.74}$$

$$\tau_2 = \underline{\tau}/r^2, \qquad \hat{\tau}_2 = \underline{\tau}/r, \tag{4.75}$$

$$\tau_3 = \overline{\tau}r^2, \qquad \hat{\tau}_3 = \overline{\tau}r, \tag{4.76}$$

$$\tau_4 = \overline{\tau}, \qquad \hat{\tau}_4 = \overline{\tau}r. \tag{4.77}$$

The closed loop performance (in terms of $\mathbf{L}_2$ gain) of the fixed gain controllers (i.e. with $k_\tau = 0$) for a range of $\overline{\tau}$ values and time-varying gain controllers for 10%, 30%, 50% and 70% uncertainty in the estimate of τ is shown in Figure 4.10. The lower bound $\underline{\tau}$ was fixed at 1.8 and $\rho = 0.08$ was used for the time-varying gain, which was found to give the best results. The higher $\mathbf{L}_2$ gain indicates that the performance degrades rapidly with increasing upper bound on $\tau(t)$. Compared to the fixed gain controllers, the time-varying designs yield notable increases in performance even with large uncertainties in τ. This is a desirable feature as τ may be difficult to precisely evaluate with gas present in the well, particularly when gas starts to rapidly expand.

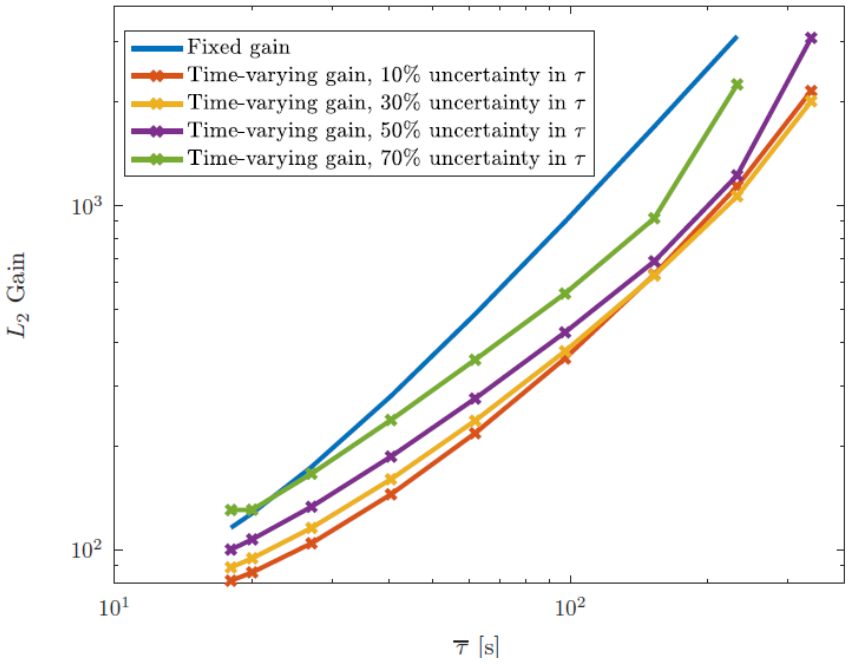

Figure 4.10: $\mathbf{L}_2$ gain of LMI-based controllers parametrized by the upper bound of τ. Adding the time-varying gain improves the disturbance rejection performance as indicated by a lower $\mathbf{L}_2$ gain from the disturbance to the tracking error. Increasing the upper bound on τ or the uncertainty in the estimate of τ improves controller robustness at the expense of lower performance.

4.4 Control Design for Kick and Loss Attenuation

When a kick (or lost circulation) event occurs, it is not sufficient to robustly control BHP to a constant set point, since this set point may be well below the actual pore pressure (or above the fracture pressure). Therefore, the control law needs to be adjusted to enable attenuation of the kick (or losses), as follows (assuming the feedback linearization design for single-phase

flow through the choke):

$$Z = (q_p + k(T_{ex}))\frac{\sqrt{\rho_L}}{C_v\sqrt{p_c - p_0}} \tag{4.78}$$

where $k(T_{ex})$ is a function of the gas expansion occurring in the well following a kick. Since T_{ex} is not exactly known, we will use an estimate, denoted $\hat{T}_{ex}$ (this may be calculated using the reduced DFM presented in Chapter 3). This control law constitutes the *flow control mode*. For lost circulation, we will set $k(T_{ex}) = 0$ since this term is not needed. To find a suitable expression for the control parameter $k(\hat{T}_{ex})$ for the problem of kick attenuation, we start by replacing Eq. 4.78 into Eq. 4.79, we have:

$$\dot{p}_c = \frac{\bar{\beta}}{V_a}\big(q_{res} + T_{ex} - k(\hat{T}_{ex})\big), \tag{4.79}$$

The influx flow rate q_{res} can be expressed using a simple, but qualitatively correct reservoir model:

$$q_{res} = \begin{cases} J\big(p_{res} - p_{bh}\big), & p_{bh} < p_{res} \\ 0, & p_{bh} > p_{res} \end{cases} \tag{4.80}$$

where J is a constant representing the production index of the reservoir and p_{res} is the reservoir pressure. In this formulation it was assumed that the reservoir is located at the bottom of the well. Rewriting Eq. 4.2, using a simplified relation for annular friction, and assuming a mean effective mud density (in terms of gas volume V_G) $\bar{\rho}_m = (1 - \frac{V_G}{V_a})\rho_L$, with $\dot{V}_G = q_{res} + T_{ex}$ we have:

$$p_{bh} = p_c + \frac{2f\bar{\rho}_m L(q_{res} + q_p)^2}{A^2 D} + \bar{\rho}_m \int_0^L g cos\theta \mathrm{d}x. \tag{4.81}$$

Taking the time derivative of the equation above, and substituting the dynamics of $\dot{p}_c$ yields:

$$\dot{p}_{bh} = \frac{\bar{\beta}}{V_a}\big(q_{res} + T_{ex} - k(\hat{T}_{ex})\big) + (1 - \frac{V_G}{V})\rho_L \frac{4fL(q_{res}+q_p)}{A^2 D}\dot{q}_{res} \tag{4.82}$$

$$- \frac{q_{res}+T_{ex}}{V_a}\rho_L\Big[\frac{2fL(q_{res}+q_p)^2}{A^2 D} + \int_0^L g cos\theta \mathrm{d}x\Big] \tag{4.83}$$

Using $\dot{q}_{res} = -J\dot{p}_{bh}$, Eq. 4.83 can be written as:

$$\dot{p}_{bh} = \frac{\bar{\beta}}{V_a\Big(1 + \frac{4fL\bar{\rho}_m(q_{res}+q_p)}{A^2 D}J\Big)}\Big[\big(q_{res}+T_{ex}\big)\Big(1 - \frac{\rho_L}{\bar{\beta}}\Big[\frac{2fL(q_{res}+q_p)^2}{A^2 D} \tag{4.84}$$

$$+ \int_0^L g cos\theta \mathrm{d}x\Big]\Big) - k(\hat{T}_{ex})\Big] \tag{4.85}$$

If we select:

$$k(\hat{T}_{ex}) = \hat{T}_{ex}\Big(1 - \frac{\rho_L}{\bar{\beta}}\Big[\frac{2fL(q_{res}+q_p)^2}{A^2 D} + \int_0^L g cos\theta \mathrm{d}x\Big]\Big) \tag{4.86}$$

we obtain:

$$\dot{p}_{bh} \approx \gamma(t)(q_{res} + T_{ex} - \hat{T}_{ex}) \tag{4.87}$$

where we have used the notation

$$\gamma(t) \equiv \frac{\bar{\beta}(t) - \rho_L\Big[\frac{2fL(q_{res}+q_p)^2}{A^2 D} + \int_0^L g cos\theta \mathrm{d}x\Big]}{V_a\Big[1 + \frac{4fL\bar{\rho}_m(q_{res}+q_p)}{A^2 D}J\Big]}. \tag{4.88}$$

It is noted that the second term in the numerator of γ represents the sum of the annular friction and hydrostatic pressure. Even for an extended reach well, this value can be several orders of magnitude below the drilling fluid bulk modulus, and thus $\gamma(t) > 0$.

Using the pressure draw-down $p_{dd} \equiv p_{res} - p_{bh}$ we obtain:

$$\dot{p}_{dd} \approx \begin{cases} -\gamma(t)\Big(Jp_{dd} + \tilde{T}_{ex}\Big), & p_{dd} > 0 \\ -\gamma(t)\tilde{T}_{ex}, & p_{dd} \leq 0, \end{cases} \tag{4.89}$$

with $\tilde{T}_{ex} = T_{ex} - \hat{T}_{ex}$. Hence, we can conclude that with the proposed control law, p_{dd} tends to 0 (i.e. $p_{bh} \to p_{res}$, or equivalently, $q_{res} \to 0$) if our estimate of the gas expansion T_{ex} is correct. In practice, we may not know the size of q_{res}, and thus an estimate of it will need to be used when computing the control gain (Eq. 4.86). Details on the q_{res} estimation will be provided in Chapter 5.

For the lost circulation case, we will assume dynamic mud losses, and use a linear model relating the rate of lost circulation to the difference between the circulating pressure and the formation fracture pressure, as:

$$q_{frac} = \begin{cases} k_{frac}\big(p(x_{loss}) - p_{frac}\big), & p(x_{loss}) > p_{frac} \\ 0, & p(x_{loss}) < p_{frac} \end{cases} \tag{4.90}$$

where x_{loss} indicates the depth where the loss zone occurs and $p(x_{loss})$ is the circulating pressure at that depth. A simplified annular pressure relation at the loss zone, assuming single-phase flow, can be written as:

$$p(x_{loss}) = p_c + \frac{2fx_{loss}\rho_L(q_p - q_{frac})^2}{A^2 D} + \rho_L \int_{L-x_{loss}}^{L} gcos\theta \mathrm{d}x. \tag{4.91}$$

Note that the hydrostatic pressure (last term in Eq. 4.91) does not change unless total losses occur ($q_{frac} \geq q_p$), which requires Mud Cap Drilling techniques (Pressurized or Floating). We will focus the derivation on the case with partial losses ($q_{frac} < q_p$), which can be handled by CBHP MPD. With that assumption, the time derivative of Eq. 4.91 gives:

$$\dot{p}(x_{loss}) = \frac{\bar{\beta}}{V_a}\big(q_p - q_{frac} - q_c\big) - \rho_L \frac{4fx_{loss}\rho_L(q_p - q_{frac})}{A^2 D}\dot{q}_{frac}. \tag{4.92}$$

If we apply the feedback linearizing control law:

$$Z = q_p \frac{\sqrt{\rho_L}}{C_v \sqrt{p_c - p_0}} \tag{4.93}$$

and apply the fracture model (Eq. 4.90) the pressure dynamics become:

$$\dot{p}(x_{loss}) = -\frac{\bar{\beta}}{V_a} q_{frac} - \frac{4 f x_{loss} \rho_L (q_p - q_{frac})}{A^2 D} k_{frac} \dot{p}(x_{loss}), \tag{4.94}$$

or, equivalently,

$$\frac{d}{dt}\Big(p(x_{loss}) - p_{frac}\Big) = -\frac{\bar{\beta} k_{frac}}{V_a\Big(1 + \frac{4 f x_{loss} \rho_L (q_p - q_{frac})}{A^2 D} k_{frac}\Big)}\big(p(x_{loss}) - p_{frac}\big) \tag{4.95}$$

which guarantees asymptotically stable dynamics with $p(x_{loss}) \to p_{frac} \implies q_{frac} \to 0$. Inspecting the denominator of the term in Eq. 4.95, it can be seen that the convergence rate slightly increases as q_{frac} is reduced. One important observation is that this loss attenuation algorithm does not require any knowledge of the loss rate or fracture pressure. The control performance during a lost circulation event will be demonstrated through a simulated scenario in Chapter 5.

Flow control is engaged as soon as a kick or lost circulation event is detected by the system (the detection logic will be detailed in Chapter 5). The flow controller acts until further influx or loss is no longer detectable by the system; at that point, the system switches back to pressure control.

4.5 Set Point Selection

For the pressure control mode, the tracking error, e_p, was defined as the instantaneous difference between the measured BHP and the set point.

However, if a downhole pressure sensor is not available, an alternative is to use the SPP for the kick circulation phase. One disadvantage to using SPP is that it is very sensitive to any changes in flow rate, and also to the presence of drill string leaks (washouts), plugged or washed out bit nozzles, or to a loss in pump efficiency. BHP measurements, on the other hand, can have a substantial lag and/or low sampling rates, depending on the telemetry method used. As a result, the control system may often face a situation where it will need to quickly update the pressure set point, and additional logic needs to be implemented to ensure a seamless transition. When a kick or lost circulation event is confirmed, the pressure set point needs to be updated to ensure that no further influx or loss occurs (unless drilling in naturally fractured formations where losses are inevitable but can be minimized). This is done by adding a safety margin above (for influx) or below (for loss) the measured or modeled downhole pressure, and using that as the new set point. Updating the set point should be done carefully, since sudden changes in the set point may cause the controller to overshoot. For this purpose, a low-pass filter with 30 second time constant is applied to the set point before, and this filtered value is used by the controller.

The constraints on the control inputs and outputs have to be taken into account when computing the set point for the pressure controller. Figure 4.11 illustrates an example solution space for an MPD operation where allowable pump rate (in strokes per minute) and back pressure combinations are shown after operational constraints are applied. Green regions represent allowable

parameter combinations, and the lower right plot is obtained by superposing the other three plots. In arriving at these constraints, a multitude of factors are considered, such as formation pressure information in relation to wellbore pressure/ECD (if known), choke characteristics, pressure ratings of RCD and marine risers (for off-shore wells), maximum pump pressures, flow rate requirements for hole cleaning and kick circulation, etc. These constraints need to be updated periodically to account for changes in operating conditions as drilling progresses.

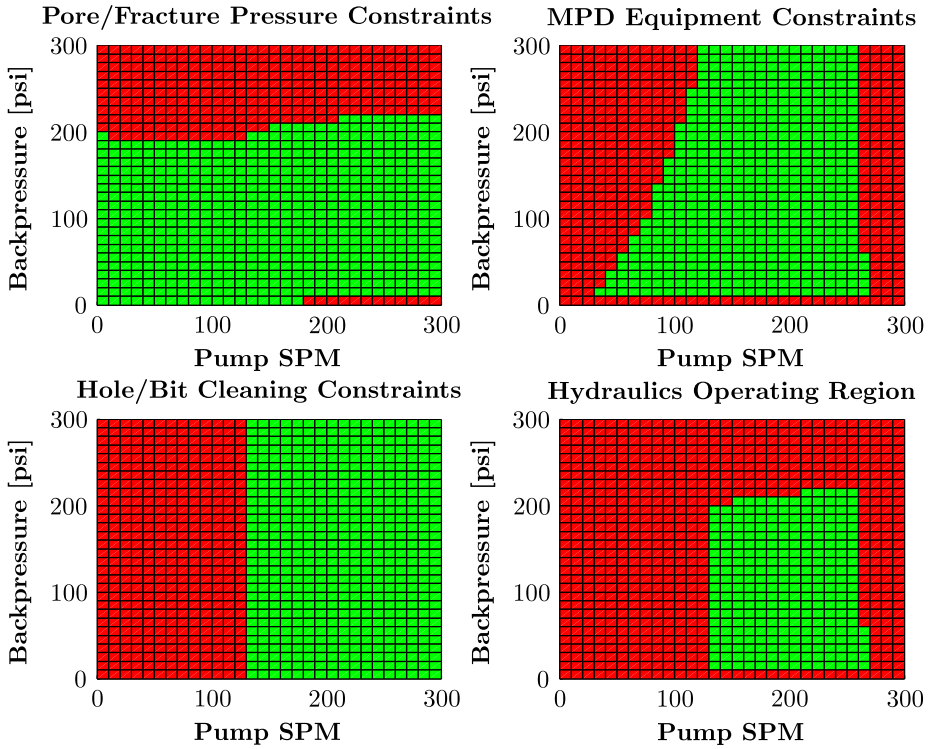

Figure 4.11: Sample constraints for set point selection for back-pressure MPD. Green regions represent allowable combinations of pump strokes per minute (SPM) and back-pressure. The lower right plot is obtained as a superposition of the three other plots.

A general methodology for incorporating process information and equipment specifications using probabilistic look-up tables is detailed by Ambrus et al. (2015b), included for reference in Appendix F. These constraints can be derived from information stored in the look-up tables, by combining individual tables and applying known information to reduce their dimensionality. Once the constraints are determined, a model-predictive controller may be used to generate the optimal set point vector for the MPD choke controller, by solving the constrained optimization problem:

$$\begin{aligned} &\underset{\mathbf{r}\in\mathcal{R}}{\text{minimize}}\ J(k) \text{ subject to} \\ &f_i(\mathbf{x},\mathbf{u},\mathbf{r}) = 0, i = 1,..,m \\ &g_j(\mathbf{x},\mathbf{u},\mathbf{r}) \leq 0, j = 1,..,n \end{aligned} \tag{4.96}$$

where $\mathbf{r} = \{r(k), r(k+1), ..., r(k+N-1)\}$, is the reference trajectory for a control horizon of length N, and $\mathcal{R}$ is the range of feasible set point values.

4.6 Evaluation of Control Designs

This section demonstrates the proposed control designs against a conventional PI controller regulating the choke position in response to pressure or flow rate error (based on the control mode), according to:

$$Z_{pc} = k_{p,p}(p_{bh} - p_{bh}^{ref}) + k_{i,p}\int (p_{bh} - p_{bh}^{ref})\mathrm{d}t \tag{4.97}$$

$$Z_{fc} = k_{p,f}(q_p - q_c) + k_{i,f}\int (q_p - q_c)\mathrm{d}t \tag{4.98}$$

The PI gains are selected as $k_{p,p} = 6\times10^{-8}, k_{i,p} = 10^{-9}, k_{p,f} = 2, k_{i,f} = 0.6$ based on pre-defined settings available in the multi-phase hydraulics software

used for this study (Ma et al., 2016). The feedback linearization controller uses $k_p = 0.04, k_i = 10^{-5}$ and a low-pass filter time constant of 20 s for the back-pressure measurement. The LQG controller uses the design factors $\rho_1 = 0.01, \rho_2 = 0.004, \gamma_Q = 10^9, \gamma_R = 10^{10}$. The values for γ_Q and γ_R were selected based on a pressure measurement noise covariance of 1 bar^2 (10^5 Pa)^2. Finally, for the LMI-based controller, we use $\overline{\tau} = 62$ with 50% uncertainty in τ and $\rho = 0.08$ for the time-varying gain. These particular gains were found to give the best results, in terms of robustness and performance, for the control strategies investigated.

We will also investigate the performance of LQG and LMI-based controllers with fixed values of τ and also with a gain-scheduled τ computed using Eq. 4.22, with the effective bulk modulus $\bar{\beta}(t)$ computed from the reduced DFM from Chapter 3. All time-based simulations in this section are conducted using the high-fidelity hydraulics simulator by Ma et al. (2016) for the well setup and parameters defined in Chapter 3.3.1.

4.6.1 Stability Margins for Pressure Tracking Controllers

During the control design process, evaluation of control performance and robustness is commonly achieved by simulating the system response over a wide range of input frequencies, and determining the stability margins associated with the frequency response. These margins can be inferred from the Bode plot of the loop transfer function, defined as the product of the plant (P) and controller (C) transfer functions. For each of the three pressure con-

trollers developed in this chapter (feedback linearization, LQG with integral action, and LMI-based control with time-varying gain), we evaluate the loop transfer function using plants represented by the high-order LTI model of the wellbore pressure dynamics given in Eqs. 4.40-4.42, evaluated at different back-pressure operating points, and with different amounts of gas (using the two-phase approximation given by Eq. 4.43).

Closed-loop stability of an LTI system can be defined in terms of gain and phase margins (Åström and Murray, 2010). The gain margin represents the amplification (in dB) in the open-loop gain that renders the closed-loop system unstable, and corresponds to the input frequency at which the phase crosses -180°. The phase margin is defined as the smallest amount of phase lag at which the closed-loop system becomes unstable, and is found at the gain cross-over frequency (i.e. where the magnitude curve crosses 0 dB). Another measure for characterizing stability is the delay margin, defined as the lowest amount of time delay in the system that leads to instability. The delay margin is computed from the phase margin divided by the gain cross-over frequency. For high-order systems with a number of resonant modes, multiple 0 dB or -180° crossings may exist, but the crossings which yield the lowest margins are the most critical to the control designer.

Figures 4.12-4.14 show the gain, phase and delay margins for a variety of operating points with different amounts of gas in the well. The feedback linearization design starts with very good margins in the absence of gas (gain margin > 15 dB, phase margin $> 85°$, and delay margin > 40 seconds), but the

margins degrade quickly as gas enters the well, and even become negative for large gas fractions, indicating that the closed-loop system becomes unstable.

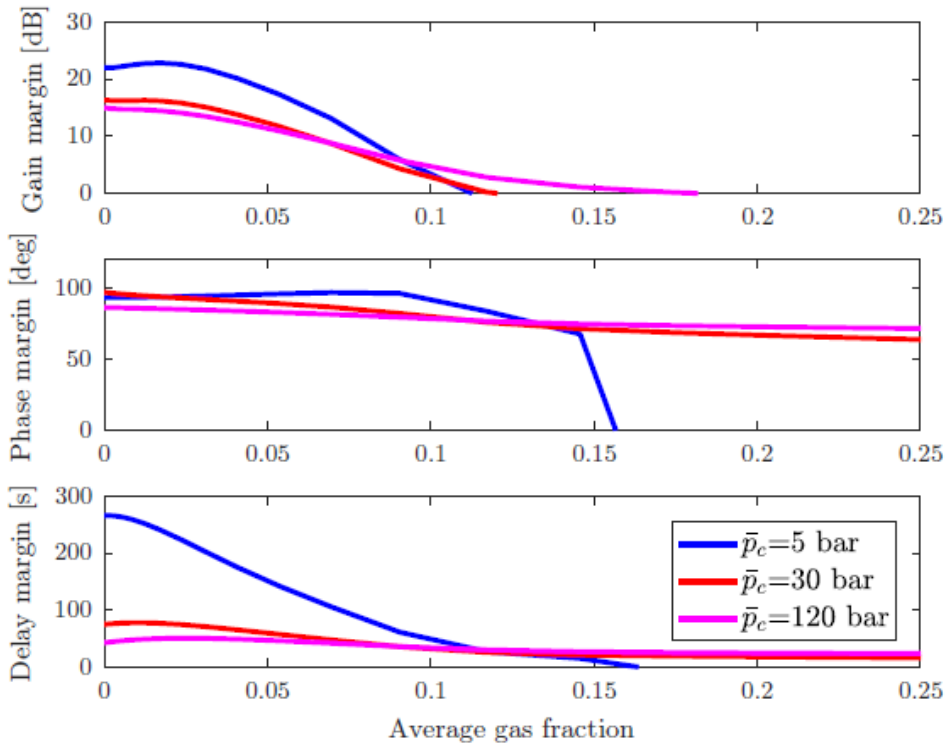

Figure 4.12: Stability margins for plant with feedback linearization controller as a function of back-pressure operating point and gas fraction. The margins degrade with increased gas fractions. Gain and phase margins below zero indicate an unstable closed-loop system.

The LQG controller yields fairly constant gain and phase margins as the gas amount increases, while delay margins actually improve as more gas enters the well. The phase margins for the larger back-pressure operating points are around 60°, which guarantee sufficient robustness. Finally, the LMI controller provides ample phase margins of more than 70°, and delay margins

exceeding 45 seconds, regardless of operating point and gas fraction.

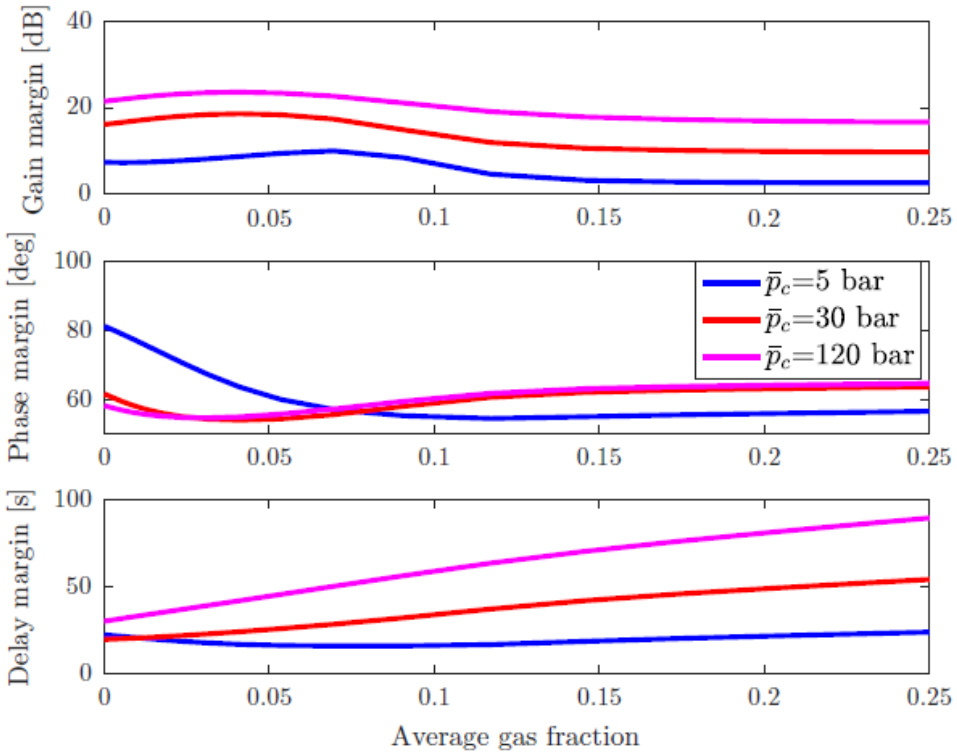

Figure 4.13: Stability margins for plant with LQG controller as a function of back-pressure operating point and gas fraction. The phase and delay margins at higher back-pressure operating points improve with increasing gas content, while gain margins slightly decrease. The system tends to be more stable at larger back-pressures.

It should be noted that the results shown in Figures 4.12-4.14 assume a steady-state gas distribution in the calculation of the plant transfer function. If the gas profile rapidly changes (such as when gas reaches the choke and starts to exit the well), the closed-loop stability margins may be actually lower than the ones calculated in this section. This will be confirmed through a series of

gas kick simulations later in this chapter.

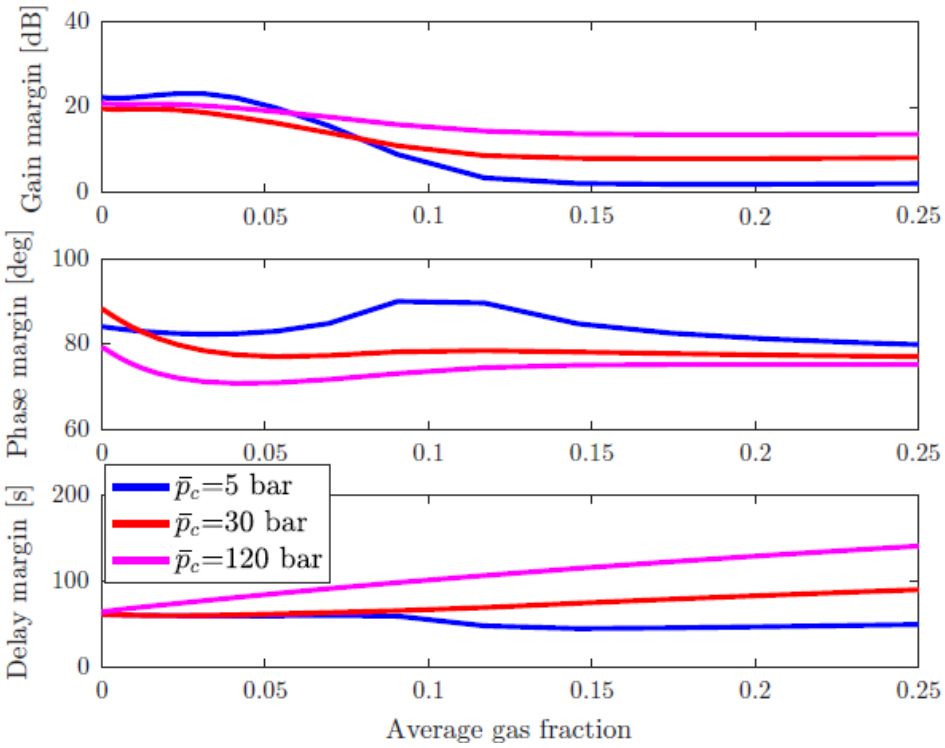

Figure 4.14: Stability margins for plant with LMI-based controller as a function of back-pressure operating point and gas fraction. The high gain and phase margins for a wide range of gas amounts and operating points indicate that the closed-loop system remains stable in the presence of large plant variations and time delays.

4.6.2 Single-Phase Tests

We will first test the controllers in a series of single-phase MPD simulations, where we will evaluate the robustness to different operating points, measurement delays, and data sampling rates. We will also simulate a series of step changes in pump rate to observe the response to measured distur-

bances. In all these scenarios, BHP data is assumed to be available, and the surface and downhole pressure measurements are injected with random noise with a standard deviation of 30 and 50 psi, respectively. The choke actuation dynamics are modeled as a low-pass filter with a time constant of 5 seconds.

To evaluate different back-pressure operating points, we will simulate a series of gradual step changes in the BHP set point. For the ideal case (no measurement delays, pressure sampled at 1 Hz), all controllers show smooth tracking for the different reference levels. Figure 4.15 shows the BHP response and choke actuation, while Figure 4.16 presents the back-pressure values and equivalent time constant τ. As the back-pressure increases, so does τ, which implies a slower system. For the case with BHP measurement delays, we see that a 15-second delay is sufficient to induce instability in the PI controller at the highest operating point (Figure 4.17), while a 30-second delay also results in an unstable response for the LQG design (Figure 4.18). It is noted that the LQG regains stability at the final operating point, as the system time constant increases. One potential design change to improve the robustness to delay (i.e. the delay margin) is to reduce the Kalman gain L, or the weighting factors ρ_1 and ρ_2 which are related to the controller aggressiveness. Finally, the effect of lower sampling rate for the BHP readings is shown in Figure 4.19. All controllers except for the PI remain stable even with the BHP sampled only every 30 seconds.

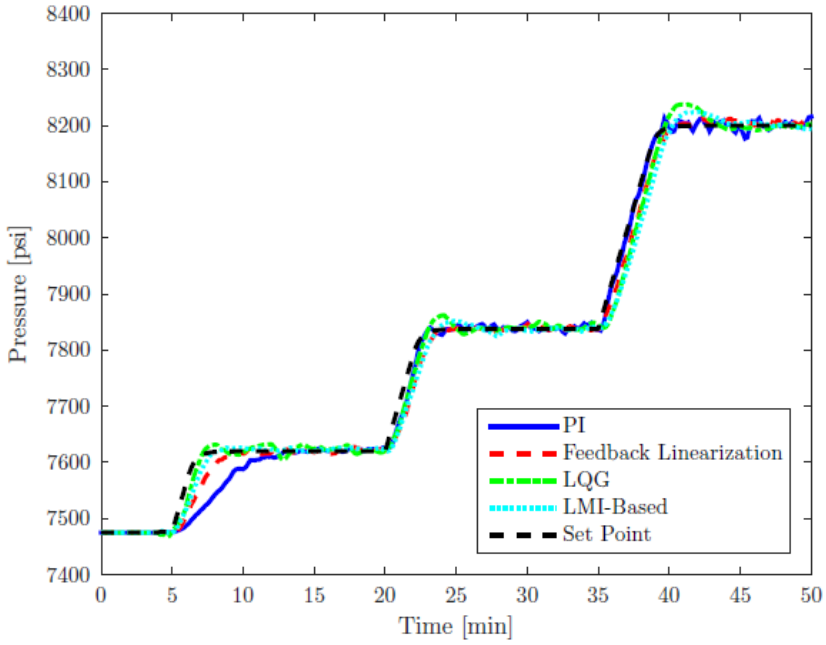

(a) BHP.

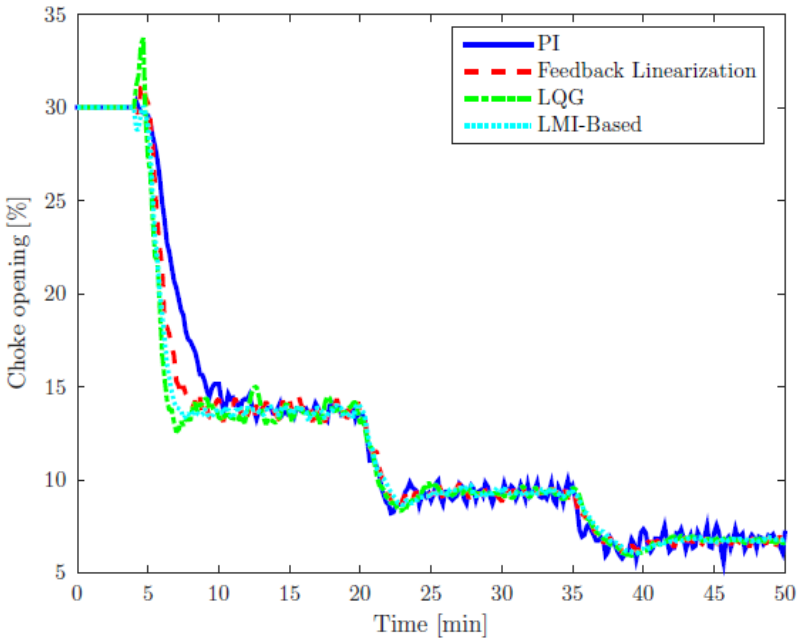

(b) Choke opening.

Figure 4.15: System response to step changes in pressure set point. Under ideal conditions, with no measurement delays, all controllers are stable for all set points.

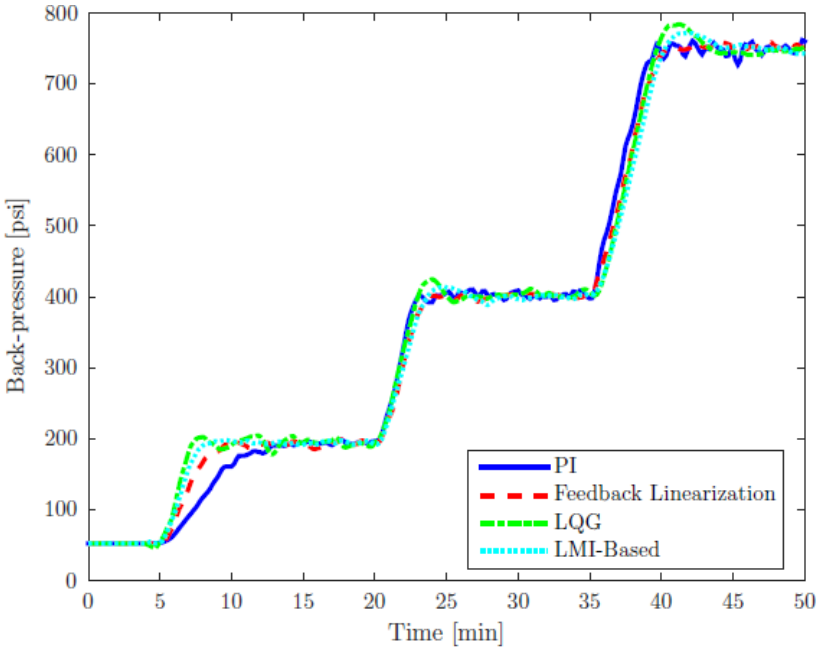

(a) Surface back-pressure.

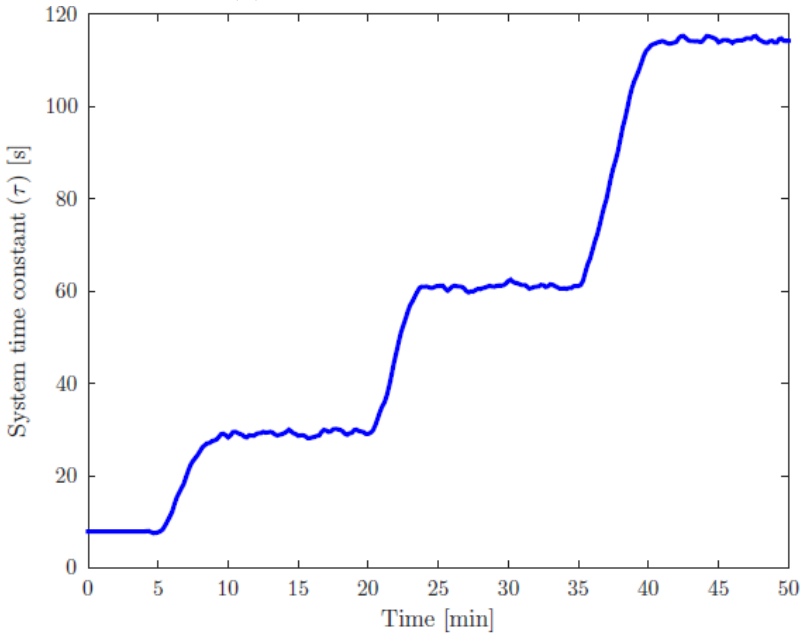

(b) System time constant $\tau(t)$.

Figure 4.16: Evolution of time constant during step changes in pressure set point. As the back-pressure increases, so does the system time constant.

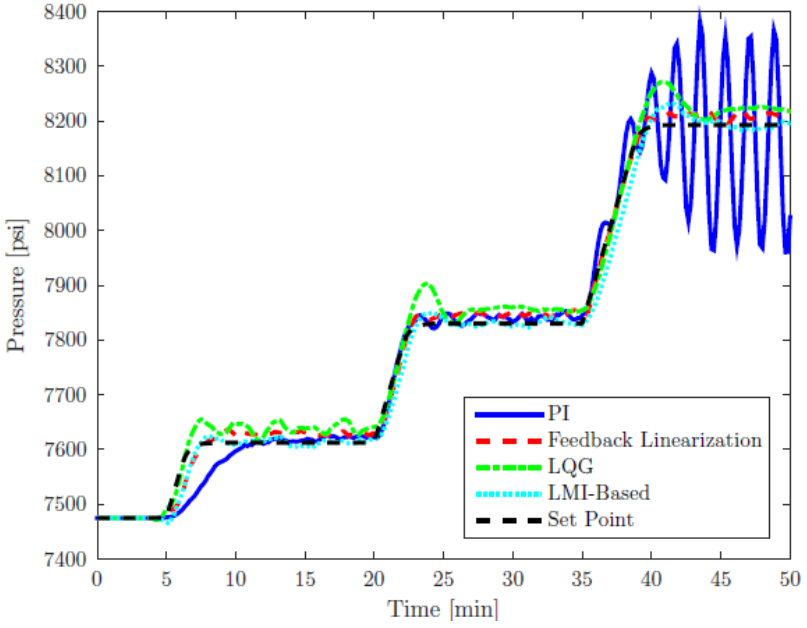

(a) BHP.

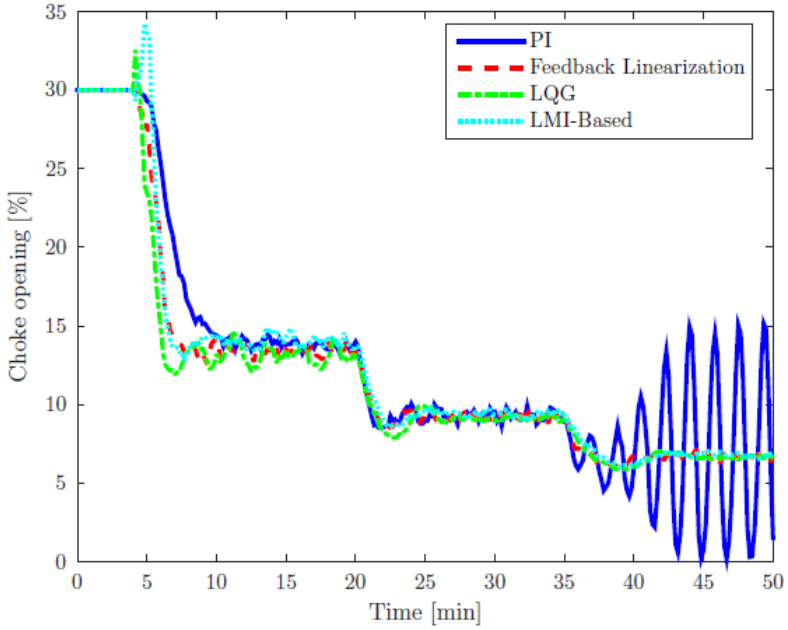

(b) Choke opening.

Figure 4.17: System response to step changes in pressure set point with 15 second delay in BHP. The PI controller becomes unstable at the third set point.

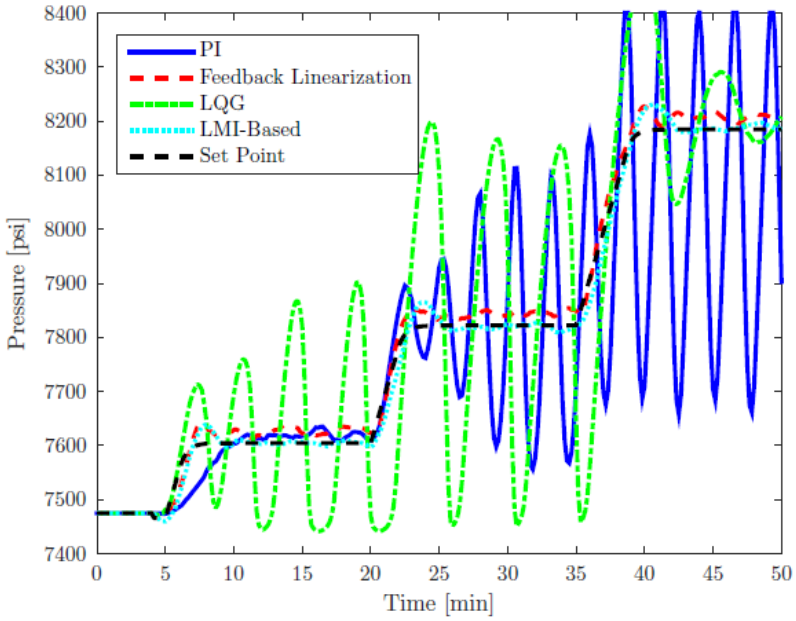

(a) BHP.

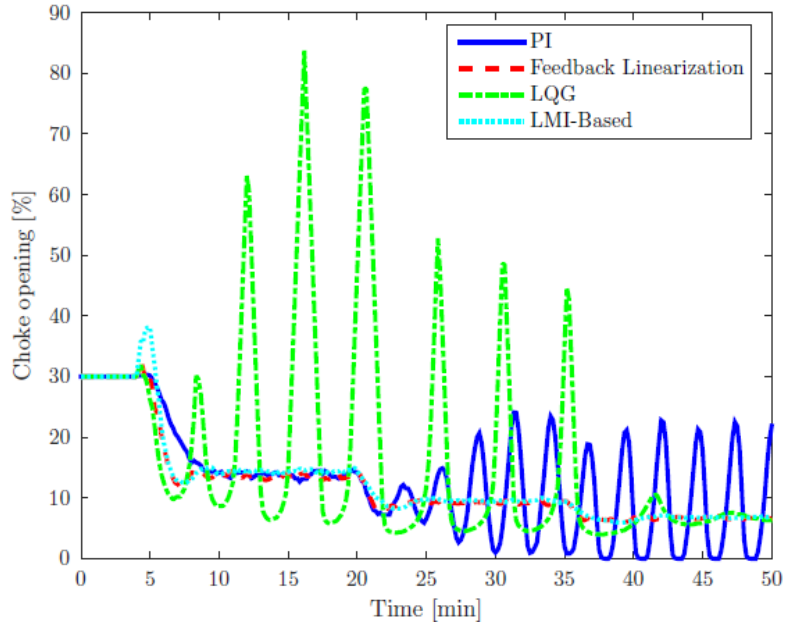

(b) Choke opening.

Figure 4.18: System response to step changes in pressure set point with 30 second delay in BHP. The PI and LQG controller become unstable (the latter regains stability at the highest set point).

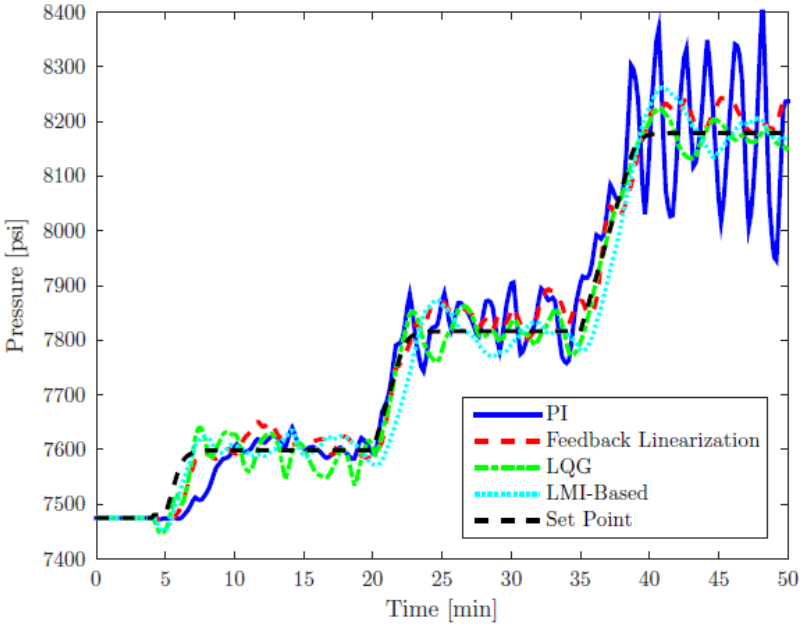

(a) BHP.

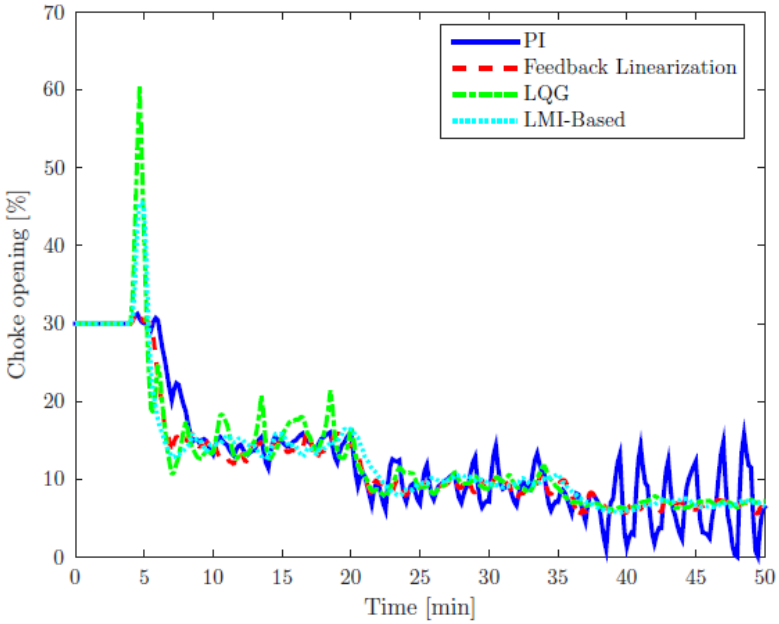

(b) Choke opening.

Figure 4.19: System response to step changes in pressure set point with BHP sampled every 30 seconds. Again, there is notable oscillation in the PI controller, and some oscillation in the LQG at the low set point.

To demonstrate control performance in response to pump rate changes, we start from a pump rate of 600 gpm, and gradually increase and then decrease the pump rate in 200 gpm increments. The commanded pump rate is passed through a low-pass filter with a 10 second time constant to simulate the pump actuation dynamics. The resulting flow rates through the choke are shown in the bottom plot of Figure 4.21. The BHP reference is kept constant at 7680 psi. The PI controller experiences overshoots of more than 100 psi and takes about 10 minutes to settle to the target pressure. The other controllers manage to keep these overshoots within 50 psi of the target, with the LMI controller showing the lowest settling time.

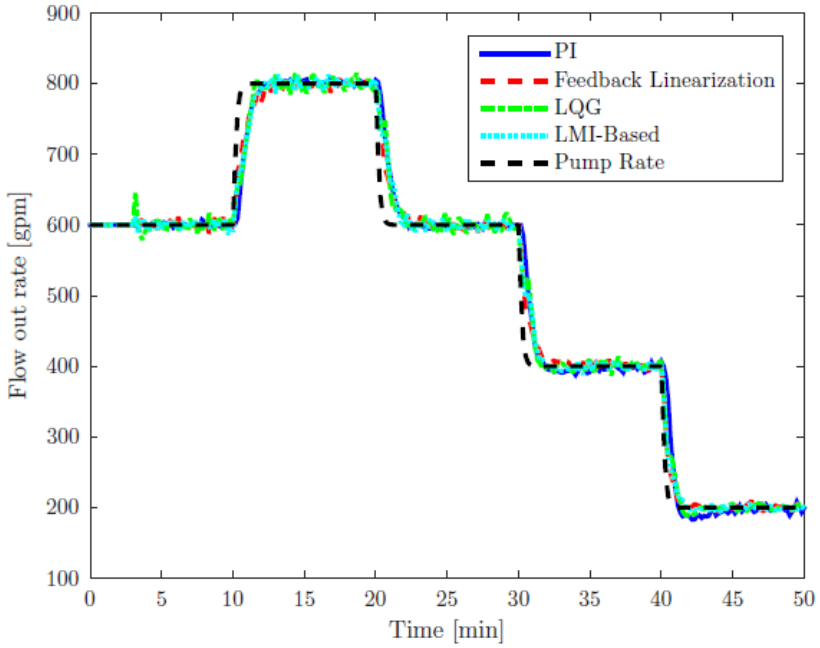

Figure 4.20: Step changes in pump rate and resulting flow out rates with different controllers.

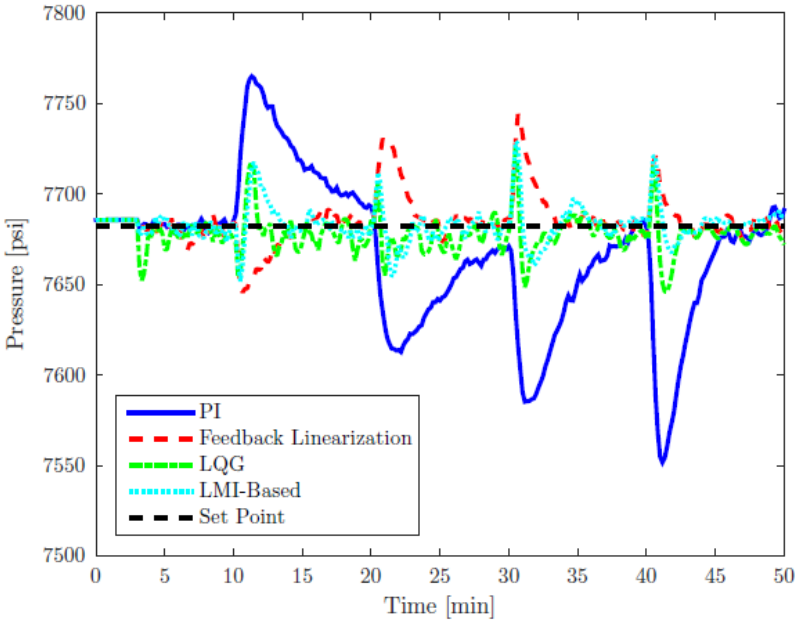

(a) BHP.

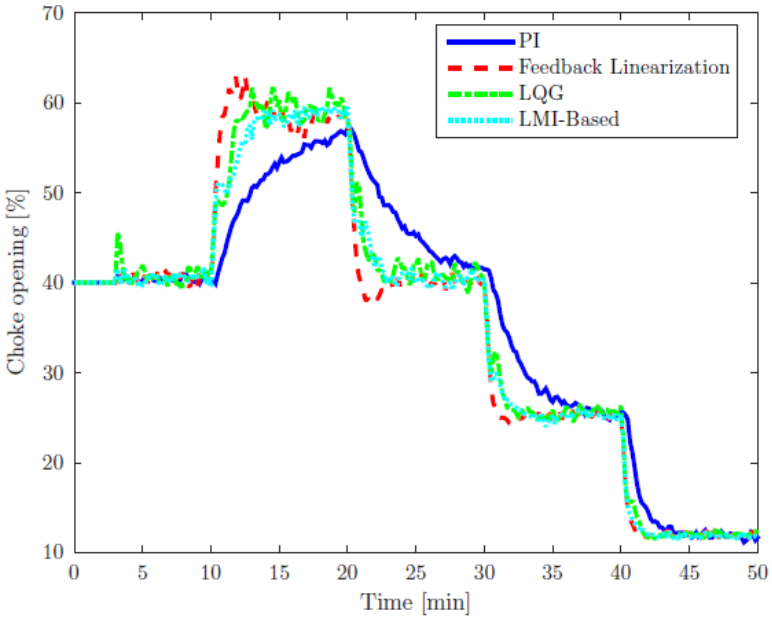

(b) Choke opening.

Figure 4.21: System response during pump rate step changes. The PI controller results in large overshoots and slow settling, while the other controllers achieve fast settling with low to moderate overshoots.

4.6.3 Gas Kick Tests

In this section we will evaluate the control performance when handling a natural gas kick taken in a 10-ppg WBM with YPL rheology (mud properties are same ones used in Table 3.1 in the Chapter 3 simulations). Later, we will also evaluate the control response for a similar kick intensity, but with an SBM. The well is initially overbalanced. A kick is introduced at 5 minutes by elevating the pore pressure to 85 psi above the bottom-hole circulating pressure. When the pit gain reaches 10 bbl, the flow control mode is initiated and the choke is closed until the BHP reaches a value equal to the reservoir pressure. The kick is attenuated within 5 minutes of detection, showing similar performance at this stage for all the controllers. Then, the pressure control mode is toggled, with a target set 150 psi above the reservoir pressure, in order to maintain a safety margin. The kick is then circulated out of the well while the pressure is being kept constant, as in the Driller's method of well control. We will investigate the control performance using BHP feedback, as well as feedback from SPP. Figures 4.22 and 4.23 show the BHP, choke actuation, back-pressure and pit gain trends with the four different control designs, for a kick taken in WBM using the setup described above. When gas starts to arrive at the choke at 50 minutes, the differences in performance become more noticeable. The PI controller experiences a large overshoot, while the other other controllers keep BHP close to the target, even as gas rapidly expands and the effective compressibility of the system changes. The feedback linearization design generates the smoothest actuation signal, while the LQG

and LMI controllers exhibit some fluctuations in the choke position as they mitigate the rapid gas migration out of the well. On the other hand, the LQG controller results in the lowest peak back-pressure, of 565 psi, and a maximum pit gain of 30 barrels.

It is noted that the LQG and LMI controller performance demonstrated in Figure 4.22 was for a gain-scheduled τ based on the real-time estimate of bulk modulus $\bar{\beta}$. Figure 4.24 compares the performance of two fixed-gain LQG controllers to the gain-scheduled one. The controller with $\tau = 20$ results in some low-frequency oscillations, while the $\tau = 100$ controller experiences large high-frequency oscillations in choke position, particularly when gas reaches the choke. The gain-scheduled controller yields the best performance overall, with low-amplitude oscillations while the kick is circulated out of the well. For an LMI-based controller with fixed $\tau = 20$, the actuation yields the least amount of oscillation, while the $\tau = 100$ case is comparable to the gain-scheduled one in terms of performance (Figure 4.25). If $\tau(t)$ can not be reliably estimated during the kick circulation, it is preferable to use a lower value of τ when designing the control gains.

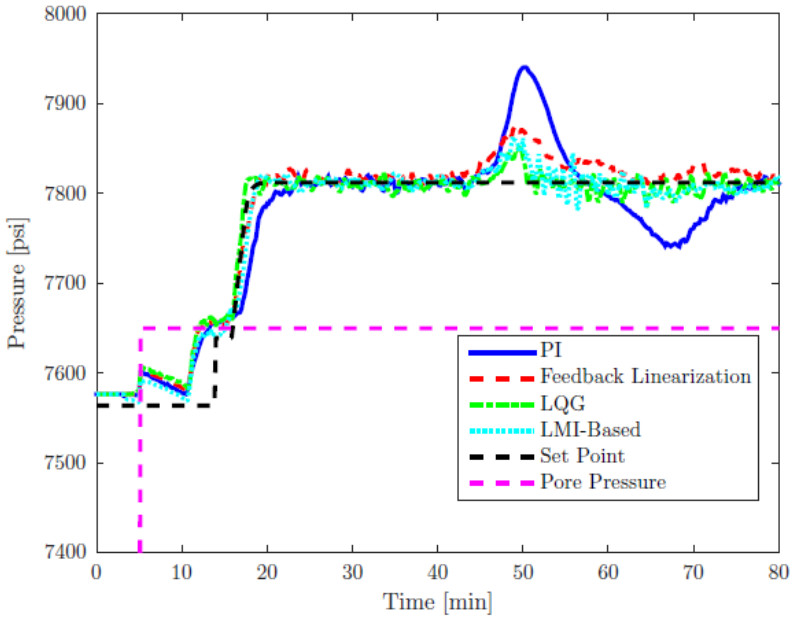

(a) BHP.

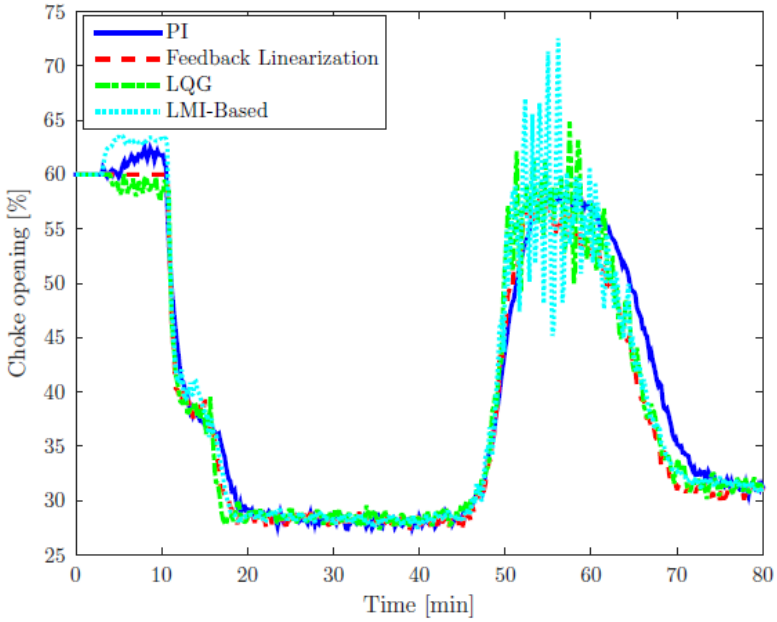

(b) Choke opening.

Figure 4.22: System response for a gas kick in WBM. LQG and LMI-based controllers result in lowest overshoots when gas reaches the choke at 50 minutes, at the expense of larger control effort.

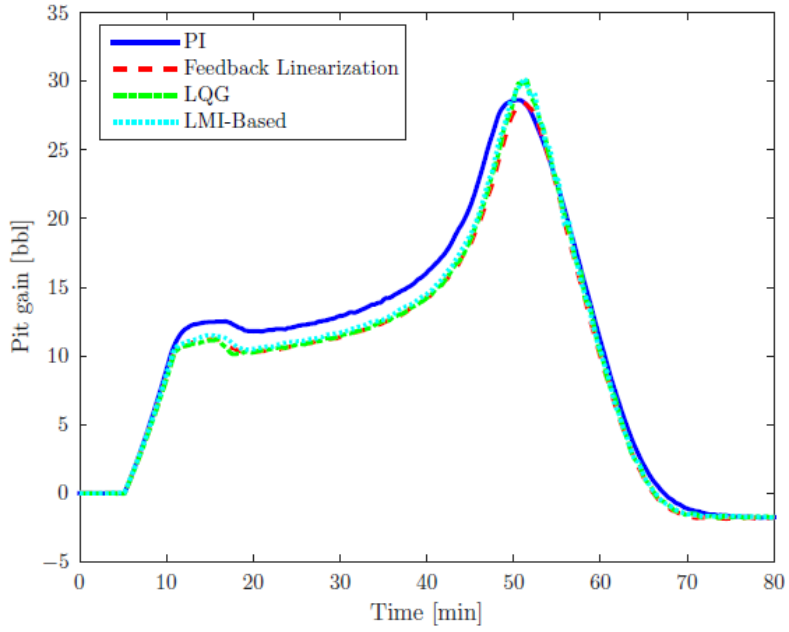

(a) Pit gain.

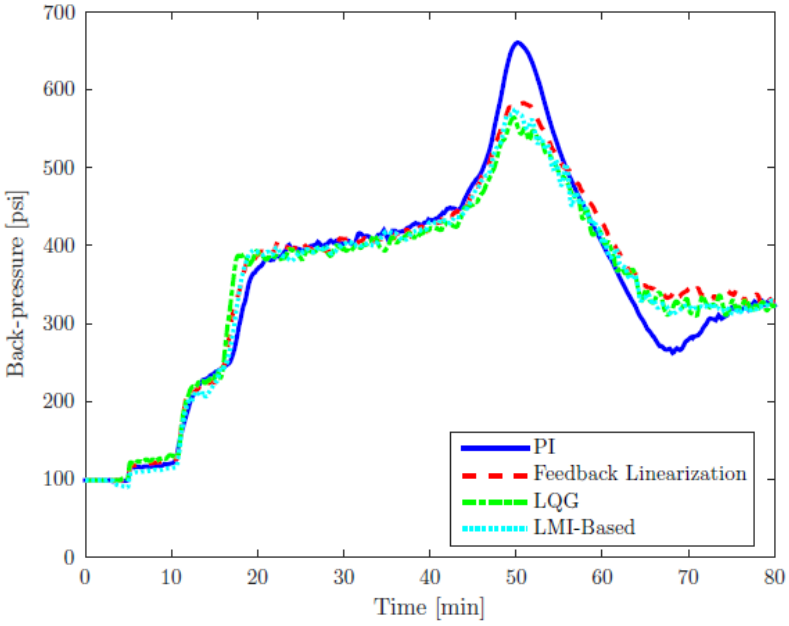

(b) Back-pressure.

Figure 4.23: Pit gain and back-pressure for a gas kick in WBM. Large back-pressures during the kick circulation may result in fracturing the formation. LQG and LMI-based controllers generate the lowest back-pressure peaks.

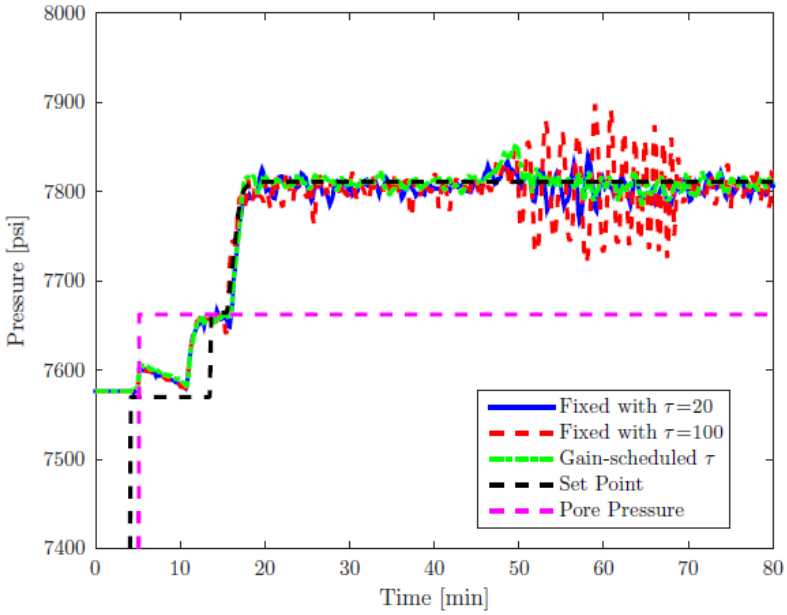

(a) BHP.

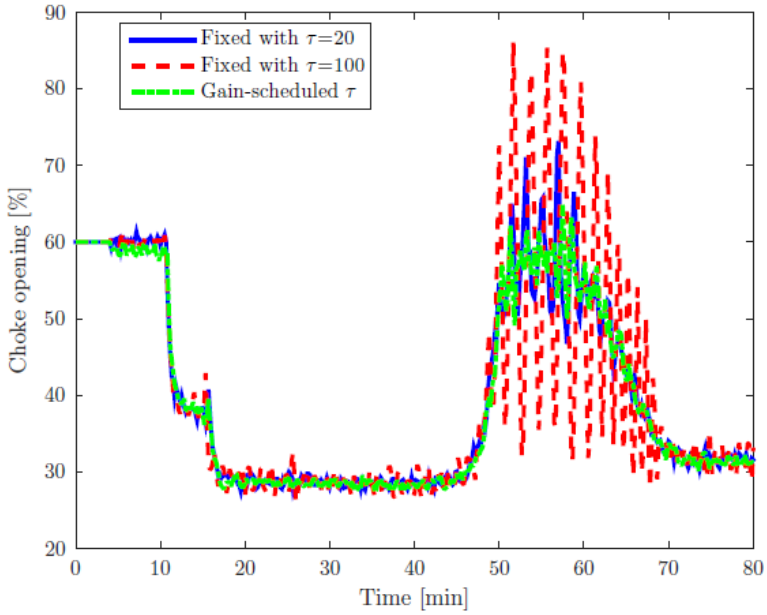

(b) Choke opening.

Figure 4.24: Response to gas kick in WBM for LQG controller with fixed and gain-scheduled $\tau(t)$. Gain scheduling helps improve the performance, particularly as gas reaches the choke.

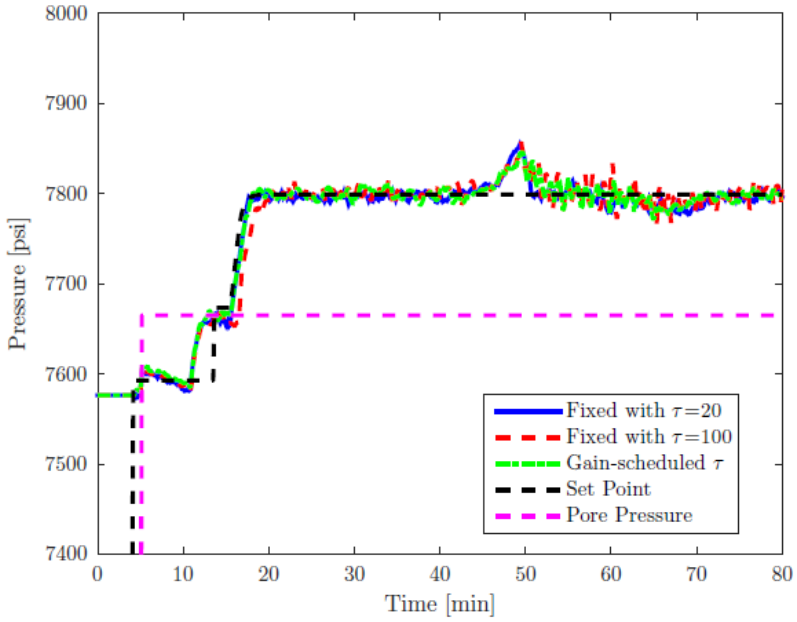

(a) BHP.

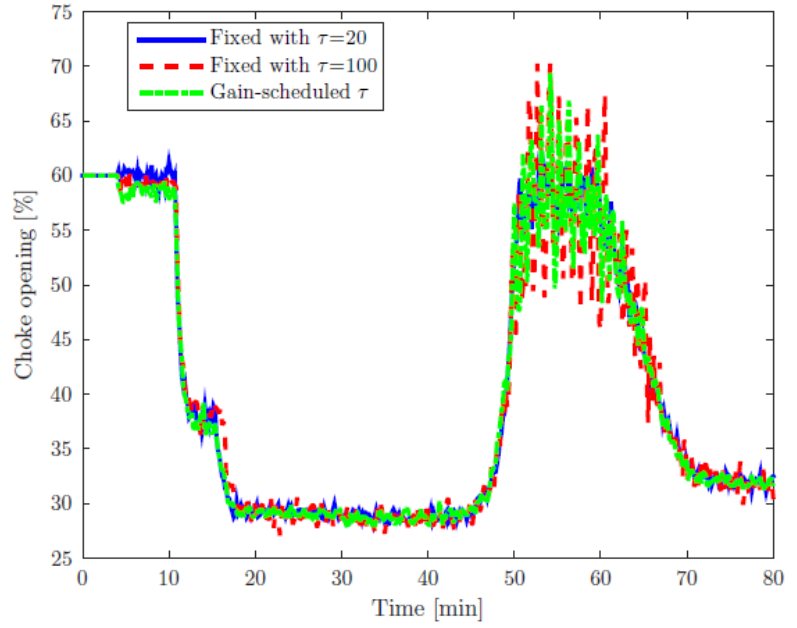

(b) Choke opening.

Figure 4.25: Response to gas kick in WBM for LMI-based controller with fixed and gain-scheduled $\tau(t)$. The difference in performance between gain-scheduled and fixed gain controllers is fairly small.

Next, consider the same setup, but with a 10-ppg SBM with an oil/water ratio of 70/30. The results are shown in Figures 4.26 and 4.27. The gas kick is fully dissolved in the mud as it enters the well, which explains the longer time elapsed until the 10 bbl pit gain threshold is reached, compared to the WBM case. It also takes about 8 minutes before the well and reservoir pressures are balanced. The previously dissolved gas starts to break out of the solution at 67 minutes, and quickly expands, requiring very fast choke adjustments to keep the BHP constant. The PI controller again results in a large overshoot (200 psi), while the LQG controller generates a very small BHP overshoot when gas reaches the choke. However, it does show fluctuations as gas starts to exit the well, as does the LMI controller (results shown here are for the case with gain-scheduled $\tau(t)$). Meanwhile, the feedback linearization design maintains a low overshoot and fairly smooth choke actuation, but a steady-state error is visible throughout this period, likely due to uncertainties in the parameters in the two-phase choke model.

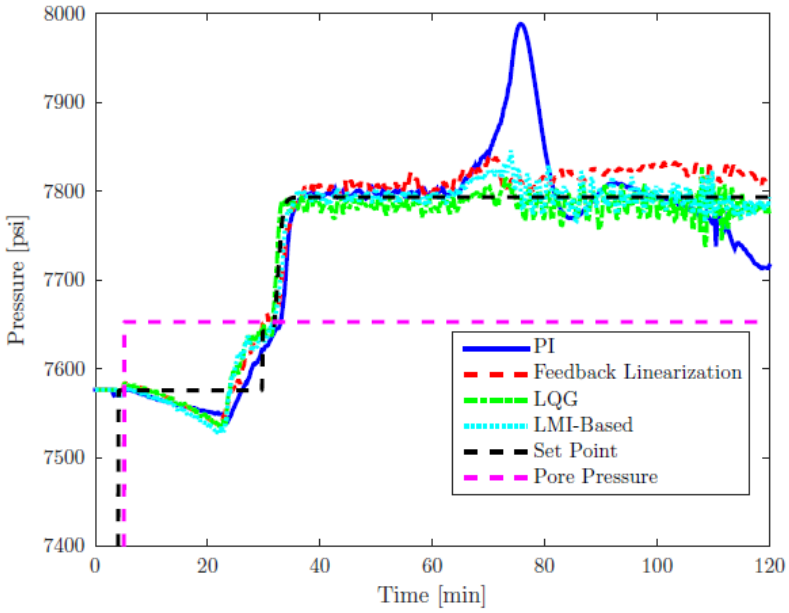

(a) BHP.

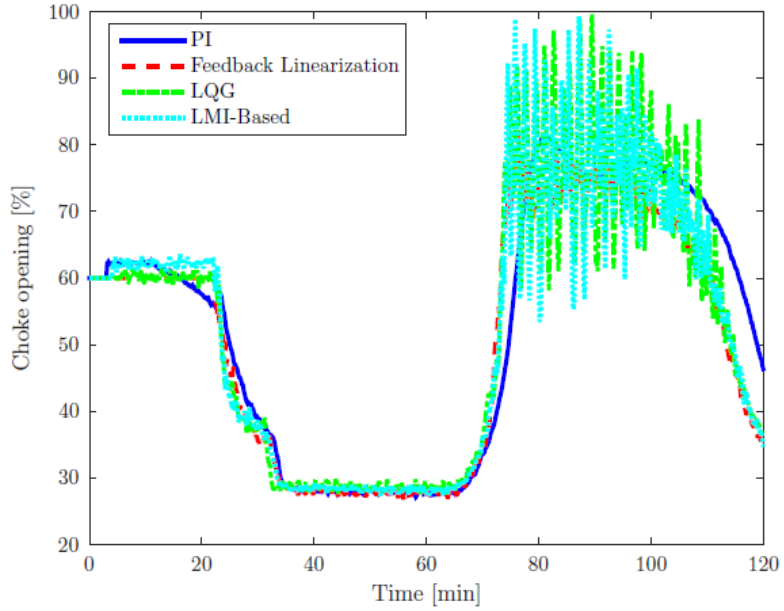

(b) Choke opening.

Figure 4.26: System response for a gas kick in SBM. The feedback linearization controller yields a visible steady-state error after the gas reaches the choke. LQG and LMI-based controllers maintain closer tracking at the expense of more control effort.

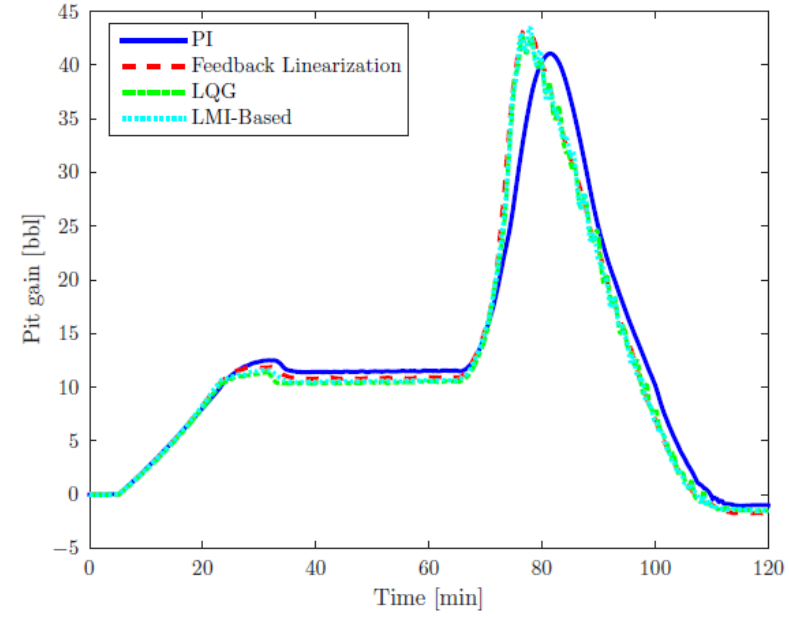

(a) Pit gain.

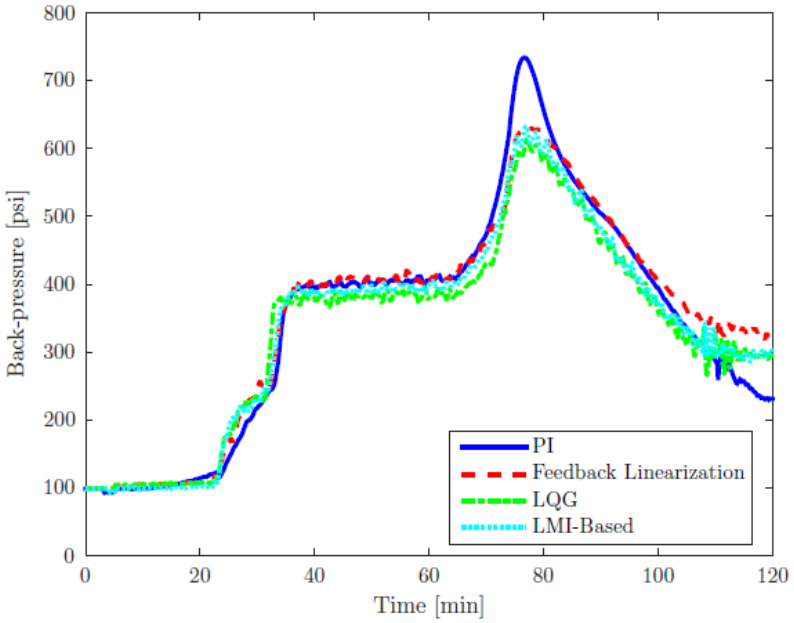

(b) Back-pressure.

Figure 4.27: Pit gain and back-pressure for a gas kick in SBM. A rapid increase in pit gain is observed as the dissolved gas breaks out of the mud after 65 minutes.

Finally, consider the WBM setup with SPP used in the control law instead of BHP. This results in similar behavior for the PI controller, and a slightly higher overshoot (compared with the BHP case) for the feedback linearization controller (Figure 4.28). The LMI-based controller also produces a larger overshoot and slight oscillations when gas arrives at the choke after 50 minutes. Finally, the LQG controller becomes unstable when gas reaches the choke. This behavior resembles that observed with BHP measurement delays in Section 4.6.2, even though the root causes are different (one is pure delay, while the other one is an effect of the pressure wave propagation, which takes longer to reach the standpipe compared to the well bottom). The large pressure oscillations with the LQG controller cause the well to become temporarily underbalanced and result in 4 bbl of additional kick being taken. Such situations require careful monitoring of the pressure response to avoid additional influx as the BHP drops below the pore pressure. If the instability persists, either the controller should be shut down, or its gains should be reduced.

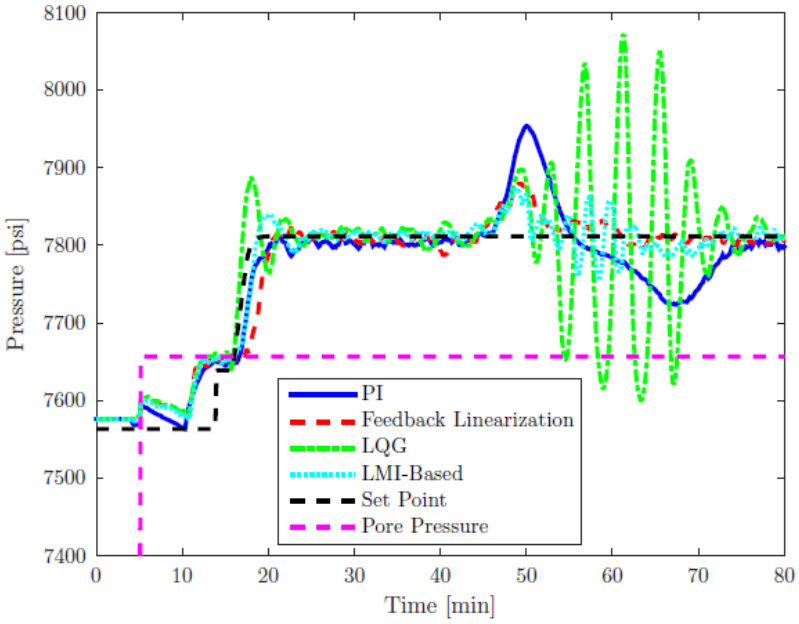

(a) BHP.

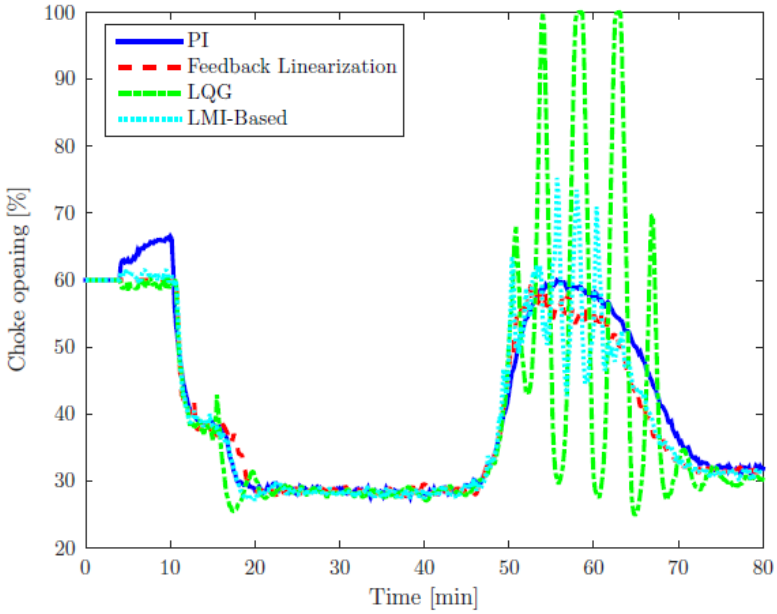

(b) Choke opening.

Figure 4.28: System response for a gas kick in WBM with SPP control. The LQG controller shows unstable behavior when gas reaches the choke, causing the well to become temporarily underbalanced during the pressure oscillations.

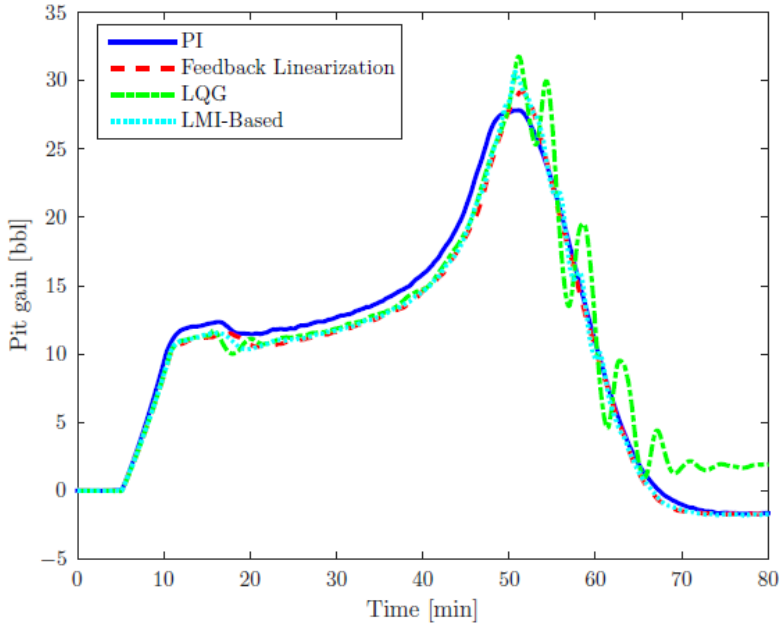

(a) Pit gain.

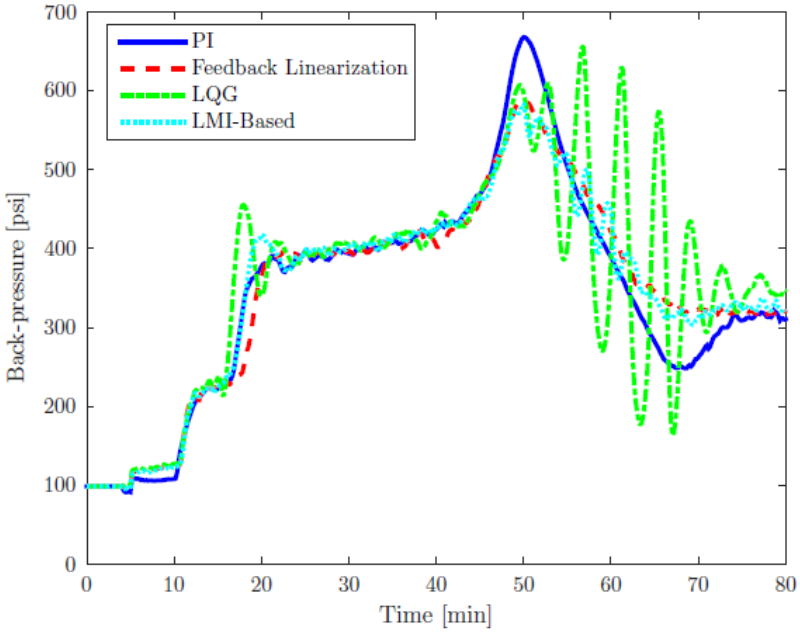

(b) Choke opening.

Figure 4.29: Pit gain and back-pressure for a gas kick in WBM with SPP control. The LQG controller results in a highly oscillatory back-pressure and 4 bbl of additional influx as a result of the instability.

Chapter 5

Automated Managed Pressure Drilling with Realistic Operational System Conditions

This chapter will focus on applying the choke control algorithms in a variety of scenarios representative of the challenges faced in an MPD operation, with a focus on system faults[1,2]. To achieve this goal, we will need to design several additional modules which will complement the control algorithms. We will first introduce a methodology for fault detection based on a type of probabilistic graphical model, the Bayesian network, and illustrate how it can be applied to MPD operations. Several simulation examples are provided. Once a fault is detected, the control logic needs to accommodate

[1]A large portion of this chapter is based on the conference paper: Adrian Ambrus, Ali Karimi Vajargah, Pradeepkumar Ashok and Eric van Oort. "Choke Controller Design for Automated Managed Pressure Drilling with Realistic Operational System Conditions". AADE National Technical Conference and Exhibition, April 2017. The dissertation author provided the theoretical development, simulations and discussion.

[2]The Recursive Least Squares estimation algorithm in Chapter 5.3.1 has also been featured in two other publications: Adrian Ambrus, Ulf Jakob F. Aarsnes, Ali Karimi Vajargah, Babak Akbari, Eric van Oort, and Ole Morten Aamo. "Real-time estimation of reservoir influx rate and pore pressure using a simplified transient two-phase flow model". Journal of Natural Gas Science and Engineering, Volume 32, May 2016, Pages 439-452; Ulf Jakob F. Aarsnes, Adrian Ambrus, Ali Karimi Vajargah, Ole Morten Aamo, and Eric van Oort. "A Simplified Gas-Liquid Flow Model for Kick Mitigation and Control During Drilling Operations". ASME Dynamic Systems and Control Conference, October 2015. The dissertation author contributed to these two papers through the development and implementation of the estimation algorithm, with input from Ulf Jakob Aarsnes and Ole Morten Aamo.

this, by switching the control mode or updating the set point, as well as the control model parameters. We will investigate several algorithms for modeling and estimation of system parameters related to faults, by making use of a transient hydraulics model coupled with linear and non-linear estimation algorithms, which will provide real-time updates of key parameters. In the final section, we will demonstrate the estimation and fault detection in conjunction with the control algorithms developed in the previous chapters for seven different test scenarios: kick, lost circulation, plugged choke, plugged bit nozzle, loss of pump efficiency, drill pipe washout, and BHP control during a drill pipe connection.

5.1 System Overview

We approach the control design problem through a modular structure, which performs several tasks concurrently at a system update rate of 1 Hz or better. Figure 5.1 shows a high-level block diagram of the system, with the relevant inputs and outputs for the different components. Real-time measurements (flow rates, pressures, mud volumes) are communicated to the controllers, observers and event detection algorithms. A Bayesian network model, detailed in the following section, is used for the event detection. The observers, presented in a later section, estimate key parameters which are subsequently fed to a hydraulics model, responsible for providing the control set points. The model is based on the reduced DFM developed in Chapter 3. The pressure and flow controllers, detailed in Chapter 4, are responsible for the choke ad-

justment to maintain a target pressure or flow rate, respectively. The control mode and set points are updated when certain events are detected.

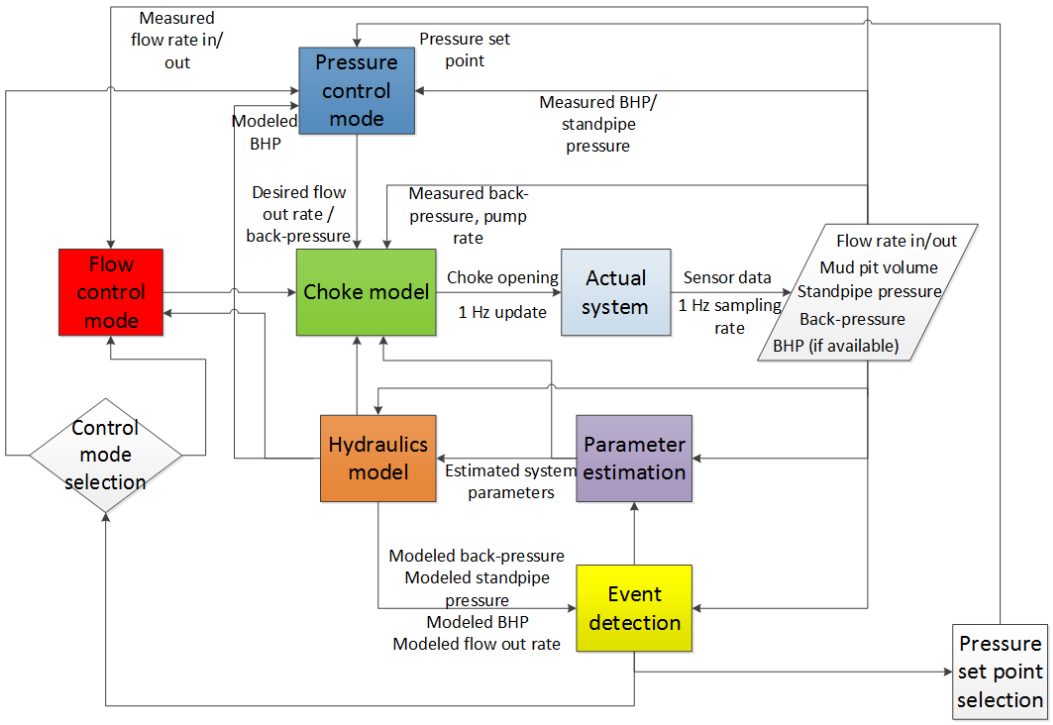

Figure 5.1: Block diagram for the proposed MPD control system. The control set points are computed using information from the hydraulics model and event detection algorithm. The controllers receive the set points and update the choke opening. Either the pressure or flow control mode is engaged depending on outputs from the event detection. The parameters of the hydraulics model are updated using available measurements and information about ongoing events. All calculations are performed at a rate of 1 Hz.

5.2 Event Detection using Bayesian Networks

5.2.1 Background

A Bayesian network is a directed acyclic graph representing a joint probability distribution over a set of random variables (Koller and Friedman, 2009). Letting $\mathcal{G}$ denote a Bayesian network defined over the random variables $X_1, ..., X_n$, then a factorization over $\mathcal{G}$ is

$$P(X_1, ..., X_n) = \prod_{i=1}^{n} (X_i | Pa_{X_i}) \tag{5.1}$$

where Pa_{X_i} represent the parent nodes of variable X_i.

Bayesian networks allow representation of dependence and conditional independence relations among the model variables. Two random variables, X and Y, are said to be conditionally independent given that a third random variable, Z, is observed[3], if and only if (Koller and Friedman, 2009)

$$P(X, Y|Z) = P(X|Z)P(Y|Z) \tag{5.2}$$

Due to their ability to combine conditional independence relationships, Bayesian networks are well-suited for exploiting relational redundancies among uncertain parameters in a physical system, and also for pattern classification problems. Bayesian networks for detecting sensor as well as process faults have been used in a variety of applications and industries (Bickmore (1994), Aradhye (1997), Mehranbod et al. (2005), Ibargengoytia et al. (2006), Mengshoel et al. (2008), Krishnamoorthy (2010), Ashok et al. (2011)).

[3] A shorthand notation for conditional independence between two random variables X, Y given a third one, Z is $X \perp Y|Z$.

When trying to predict a certain variable based on several observed variables (continuous or discrete-valued), a possible solution is to use a Naive Bayes classifier, where the feature variables are conditionally independent given the variable to be predicted, also known as the "class" variable (Koller and Friedman, 2009). An intrinsic advantage of the Naive Bayes model is that the number of independent parameters required to completely describe the distribution grows linearly with the number of variables, rather than exponentially, which reduces the storage and computational power requirement. The links between the nodes are mathematically represented by conditional probability tables (CPTs). Each CPT can be assigned, e.g. by a domain expert, or learned from labeled data sets. Furthermore, the Naive Bayes classifier can be used for predictions with incomplete or missing observations. Figure 5.2 shows a general Naive Bayes model with the class variable C and the feature variables $X_1, X_2, ..., X_n$. Let $c_1, c_2, ..., c_k$ denote the outcomes of C.

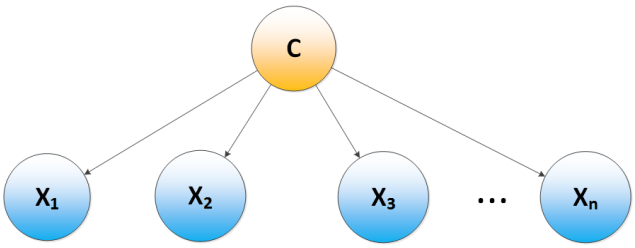

Figure 5.2: Generic Naive Bayes model. The outcome of the class variable C is predicted using evidence from the feature variables X_1, X_2,..., X_n.

The model can be factorized as:

$$P(C, X_1, ..., X_n) = P(C) \prod_{i=1}^{n} (X_i|C) \tag{5.3}$$

where we have used the fact that $(X_i \perp X_j|C)$ for all $i = 1, 2, .., n$ and $j \neq i$ (conditional independence assumption). Using Bayes' Theorem, we can compute the probability of outcome c_k based on the current evidence assigned to the features $X_1, X_2, ..., X_n$ (denote this evidence as $x_1, x_2, ..., x_n$):

$$P(C = c_k|x_1, ..., x_n) = \frac{P(C = c_k) \prod_{i=1}^{n} (X_i|C = c_k)}{P(x_1, ..., x_n)} \tag{5.4}$$

5.2.2 Bayesian Network for Event Detection

Figure 5.3 illustrates the detailed network constructed for MPD event detection. The class variable includes the following outcomes: kick, lost circulation, pump efficiency loss, plugged bit nozzle, plugged choke, drillstring washout, and a "no event" outcome. Each of these outcomes is described through a probability value.

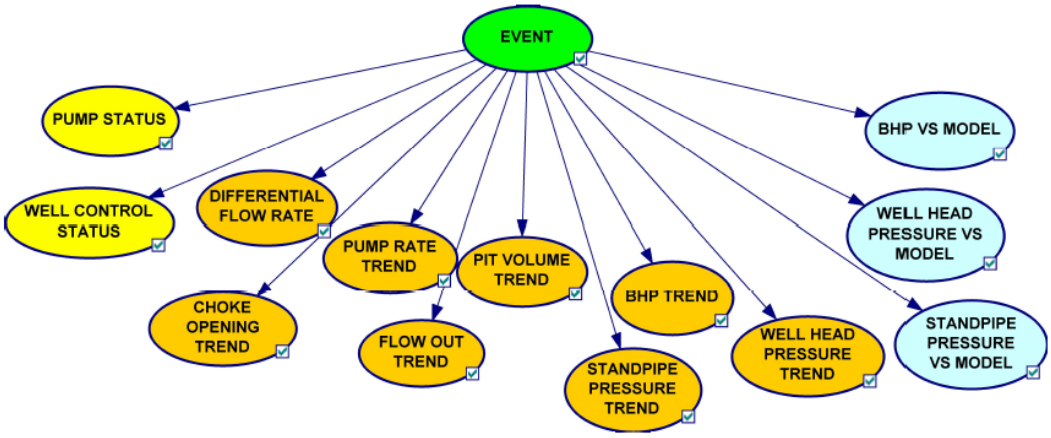

Figure 5.3: Naive Bayes model for MPD event detection. Blue nodes represent features relating a measurement to its model prediction, orange nodes are purely measurement-based, and yellow nodes are features derived using finite state machines. Each node is assigned a CPT in relation to the Event node.

The feature variables include sensor measurements and modeled variables, represented either as an instantaneous location relative to a threshold, or as trends extracted over a period of time, indicating a movement characteristic. Location-based features represent the degree (in a fuzzy sense) to which a variable (measured or modeled) is in a low, normal, or high state, or a negative/zero/positive state, when normalized around a threshold (see Figures 5.4a and 5.4b). Each of these states are designated as having values between 0 and 1, the larger the number, the stronger the membership to that particular category. Movement features indicate a statistical trend, for instance, increasing, constant, or decreasing. The trend is quantified by taking a linear least-squares regression of a variable over a time window and comparing the slope from the regression to a positive and negative threshold (Figure 5.5).

Location-based features for an MPD scenario may, for instance, include the differential flow rate (i.e. difference between flow out rate and circulation rate, an essential feature for kick and lost circulation detection). Another location-based feature is the difference between measured and modeled values for SPP, WHP and BHP (if a downhole sensor is used). Each of these parameters is run through a 60-second moving average before the features are calculated. For the movement features, we may include trends in pump rate, flow out rate, pit volume, WHP, SPP, BHP, and choke opening. A trend window size of 60 seconds is used. Table 5.1 indicates the thresholds used for the detection features, while Figures 5.6 and 5.7 illustrate simulated time series for different parameters (measured and modeled) and the extracted features.

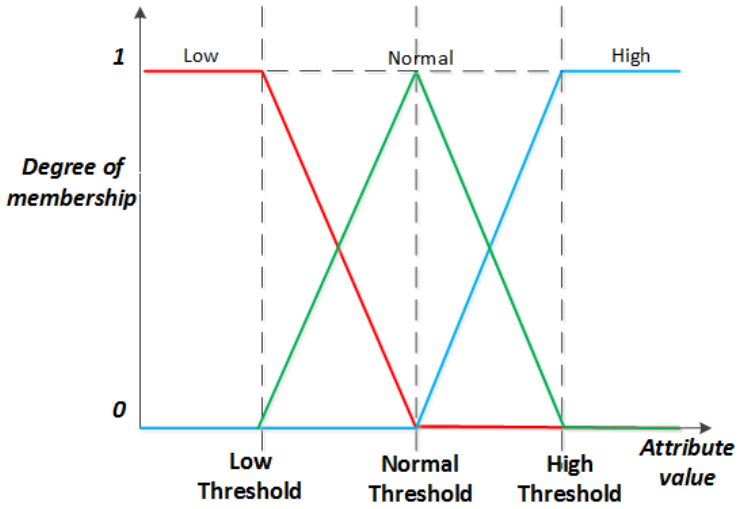

(a) Low/normal/high feature.

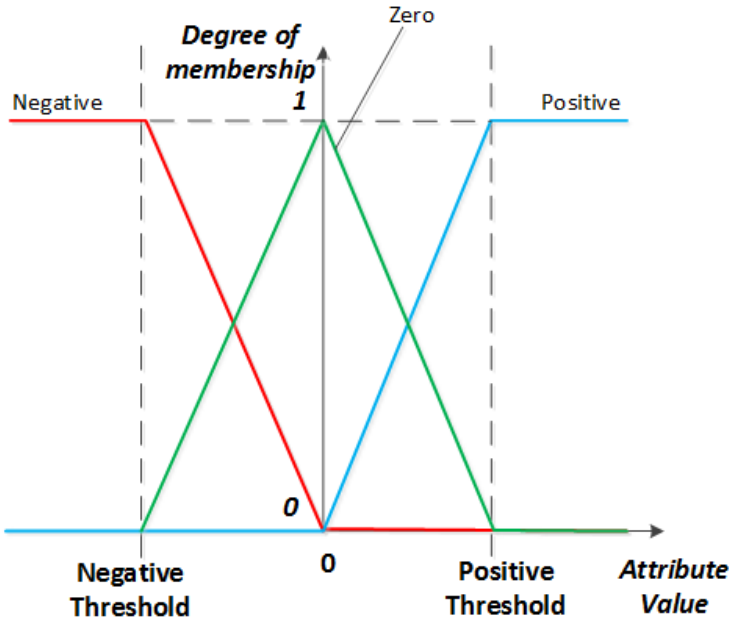

(b) Negative/zero/positive feature.

Figure 5.4: Graphical illustration of location features. Each feature is represented by the degree of membership to one or more categories based on a set of pre-defined thresholds. The membership degree is calculated using a normalized distance from the attribute value to the threshold value.

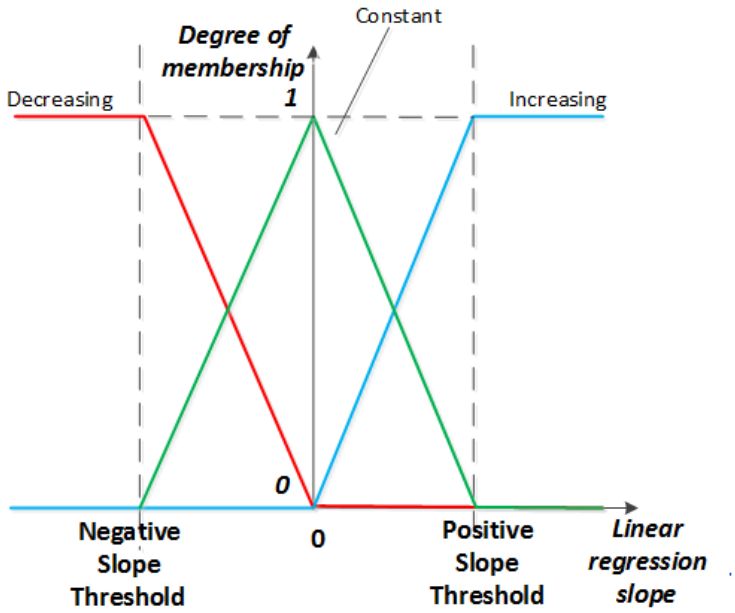

Figure 5.5: Graphical illustration of movement features representing constant, increasing or decreasing trends. These trends are evaluated with respect to the slope of a linear regression performed on a moving window of data samples.

Table 5.1: Thresholds for location and movement features.

Threshold	*Value*	*Unit*
Differential flow rate	10	gal/min
Difference between measured and model SPP	250	psi
Difference between measured and model WHP	75	psi
Difference between measured and model BHP	500	psi
Pump rate linear regression slope	1	gal/min/s
Flow out rate linear regression slope	0.2	gal/min/s
Pit volume linear regression slope	0.01	bbl/s
Pump pressure linear regression slope	0.5	psi/s
WHP linear regression slope	0.5	psi/s
BHP linear regression slope	0.5	psi/s
Choke opening linear regression slope	0.1	%/s

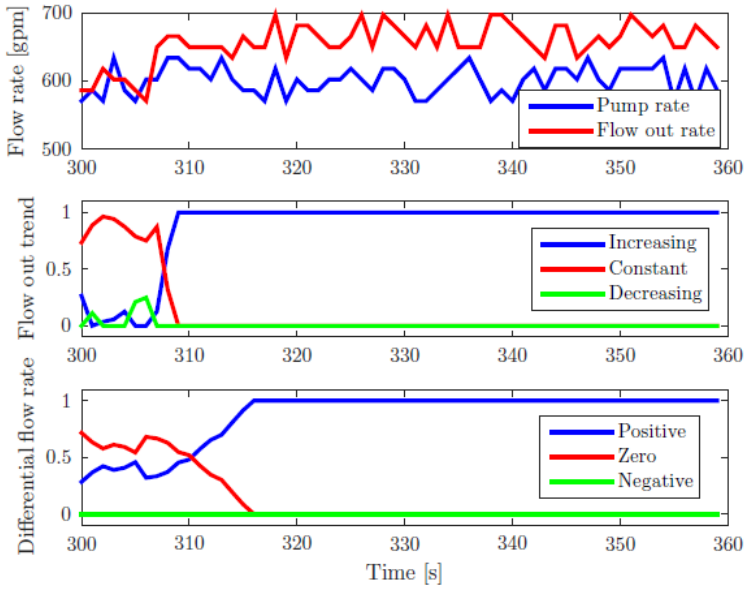

(a) Flow rate data (top) and extracted features (middle and bottom plots).

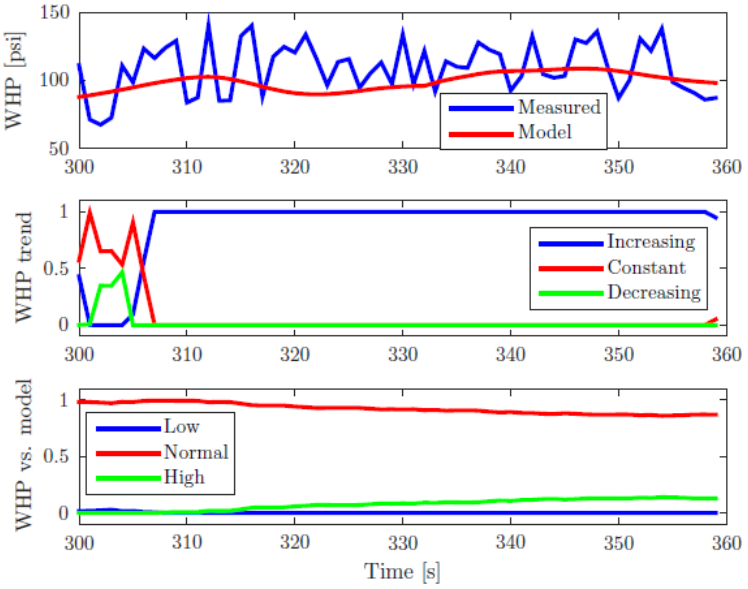

(b) WHP data (top) and extracted features (middle and bottom plots).

Figure 5.6: Location and movement features for flow rate and WHP during a gas kick. The kick starts at 305 seconds. Increasing flow out trend and positive differential flow are indicative of a kick.

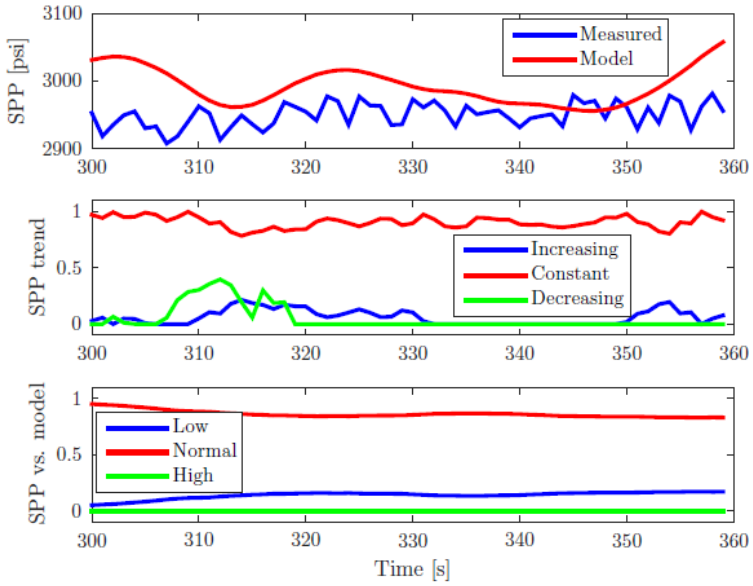

(a) SPP data (top) and extracted features (middle and bottom plots).

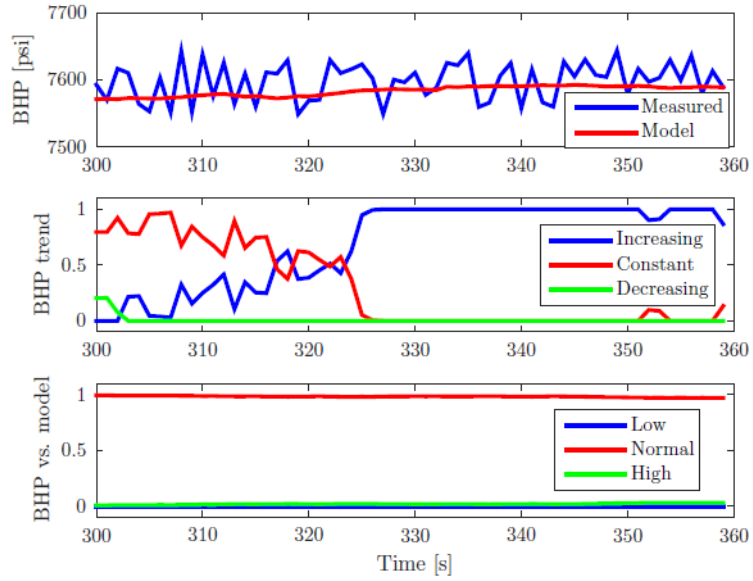

(b) BHP data (top plot) and extracted features (middle and bottom plots).

Figure 5.7: Location and movement features for SPP and BHP during a gas kick. A small increase in BHP is noted due to increased annular friction as gas initially enters the well.

Two special nodes designating the pump status (pumps off, pumps ramping up/down, or at steady state), and well control status (overbalanced or underbalanced) are also included to provide additional contextual information to the detection algorithm. When taking a gas kick, the well control status needs to be further detailed by taking into account gas migration, which allows differentiation between pit gain due to active influx and pit gain due to the expansion of the gas bubble as it is circulated out of the well. A finite state machine for determining the well control status is shown in Figure 5.8. In determining the state transition, the state machine relies on the predicted kick probability from the Bayesian Network, and also on model outputs such as gas distribution, BHP, and the projected reservoir pressure. The well control status, together with the pump status and the location and movement nodes, are continuously updated at every time instant when new information is available, and the event probabilities are computed using Bayesian inference.

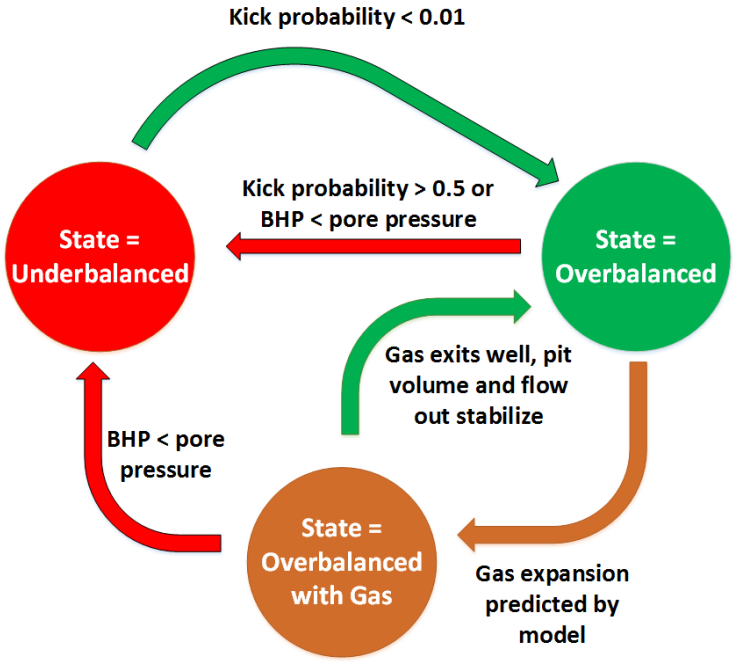

Figure 5.8: Well control finite state machine. The system can be in an underbalanced, overbalanced, or overbalanced with gas state. State transitions are determined from the probability of kick inferred by the Naive Bayes model, as well as from the estimated pore pressure and measured BHP (if available). The determination of overbalance with gas is based on the gas expansion predicted from the reduced DFM.

5.3 Fault Modeling and Parameter Estimation

In this section, we will develop algorithms for modeling various process faults and estimating relevant parameters. First, we will look at estimation and modeling of gas kicks, where we will use the reduced DFM described in Chapter 3 together with a Recursive Least Squares algorithm for pore pressure and influx rate (or reservoir productivity) estimation. Next, we will investigate a similar algorithm for fracture pressure and mud loss rate estimation during

a lost circulation event. Here, pore and fracture pressure estimation refers to real-time prediction based on flow and pressure readings, as opposed to traditional geo-mechanical correlations (Aadnøy et al., 2009). We will also explore real-time learning of system parameters, which may be affected by a process fault such as pump efficiency, bit nozzle flow area, and choke orifice area.

5.3.1 Reservoir Influx Rate and Pore Pressure Estimation

In this section, we present an approach for estimating the inflow rate and pore pressure of the flowing zone based on drilling parameters recorded during a kick. This requires a transient hydraulics model and a reservoir model, which correlates flow from the reservoir to the pressure draw-down, and also to a productivity index. The latter is a lumped parameter which is affected by the length of the exposed zone, reservoir permeability, porosity, skin factor, reservoir fluid viscosity and compressibility (Vefring et al., 2003). For this application, we are more interested in the qualitative relationship between inflow rate, productivity and pore pressure, thus we use a qualitatively correct, linear inflow relationship (Shayegi et al., 2012):

$$q_{res} = J(p_{res} - p_{bh}), \tag{5.5}$$

with p_{res} the reservoir pressure (for simplicity, it is assumed here that the influx occurs at the bottom, which is usually the case when drilling ahead in a new formation; however, the approach may be extended to any location in the uncased hole section), and J the productivity index. In the above, it is

assumed that $p_{res} > p_{bh}$ (i.e. the well is underbalanced), otherwise, q_{res} is set to zero. Eq. 5.17 can be recast in a form more amenable for parameter estimation:

$$q_{res} = \Phi^T X, \tag{5.6}$$

where $X = \begin{bmatrix} Jp_{res} \\ J \end{bmatrix}$ is the vector of unknown or uncertain parameters and $\Phi = \begin{bmatrix} 1 \\ -p_{bh} \end{bmatrix}$ is the regressor. Since q_{res} is not directly measured during a kick incident, we will instead use an estimate, $\hat{q}_{res}$. As a baseline, we can compute $\hat{q}_{res}$ from the instantaneous mud flow-out rate minus the mud injection rate. However, this is susceptible to measurement noise (particularly for flow out), and does not account for dynamics due to pressure changes and gas expansion as the kick is circulated. Therefore, we employ the first-order pressure dynamics from the reduced DFM, where we use $\hat{q}_{res}$ in place of the gas source term q_G, and we isolate all terms which explicitly depend on $\hat{q}_{res}$ (Note: in the following, all parameters which are estimated or derived from estimated quantities are denoted with a $\hat{}$ sign above their symbol):

$$\frac{dp_c}{dt} = \frac{\hat{\beta}}{V_a}\Big[q_L - q_c + \hat{q}_{res} + I_0 + 2(q_L + \hat{q}_{res})^2 I_1\Big], \tag{5.7}$$

with

$$I_0 = \int_0^L \frac{C_0 \hat{\alpha}_G}{\bar{\gamma}\hat{P}} \hat{v}_G \hat{\rho}_m g cos\theta A \mathrm{d}x \tag{5.8}$$

$$I_1 = \int_0^L \frac{C_0 \hat{\alpha}_G}{\bar{\gamma}\hat{P}} \hat{v}_G \hat{\rho}_m \frac{f}{AD} \mathrm{d}x \tag{5.9}$$

where I_0, I_1 account for gas expansion due to the hydrostatic and frictional pressure gradients, respectively. Note in the above that $\hat{\beta}$, $\hat{P}(x)$, $\hat{v}_G(x)$, $\hat{\alpha}_G(x)$

are also estimates of the true values as they all depend on $\hat{q}_{res}$. For MPD scenarios, where kick size is usually limited, we can assume $q_{res}^2 \ll q_L^2$, and thus neglect the quadratic $\hat{q}_{res}$ term in Eq. 5.7, which yields:

$$\frac{dp_c}{dt} = \frac{\hat{\beta}}{V_a}\Big[q_L - q_c + I_0 + 2q_L^2 I_1 + \hat{q}_{res}(1 + 4q_L I_1)\Big], \tag{5.10}$$

Eq. 5.10 above can be low-pass filtered to remove noise in the measurements, and also to allow a mathematical formulation which enables linear regression techniques. Using Laplace transform notation for the low-pass filter transfer function, $F(s) = \frac{1}{\tau s+1}$, we have:

$$\frac{s}{\tau s+1}p_c - \frac{1}{\tau s+1}\frac{\hat{\beta}}{V_a}\Big[q_L - q_c + I_0 + 2q_L^2 I_1\Big] \tag{5.11}$$

$$= \frac{1}{\tau s+1}\Big[\frac{\hat{\beta}(1 + 4q_L I_1)}{V_a}\Phi^T X\Big]. \tag{5.12}$$

Denoting the left-hand side of Eq. 5.12 by y and $\frac{1}{\tau s+1}\Big[\frac{\hat{\beta}(1+4q_L I_1)}{V_a}\Phi\Big]$ by Ψ allows us to write a linear equation of the form $y = \Psi^T X$, which can be solved using an on-line regression technique, such as recursive least squares (RLS). If we denote $\hat{X}(t)$ as the time-varying estimate of the vector of unknown parameters X, $\mathbf{P}(t)$ the covariance matrix and λ a forgetting factor between 0 and 1, we have the RLS scheme (Ljung, 1999):

$$\mathbf{P}(t) = \frac{1}{\lambda}[\mathbf{P}(t-1) - \epsilon(t)\Phi^T(t)\mathbf{P}(t-1)], \tag{5.13}$$

$$\hat{X}(t) = \hat{X}(t-1) + \epsilon(t)[y(t) - \Phi^T(t)\hat{X}(t-1)], \tag{5.14}$$

where we define

$$\epsilon(t) = \mathbf{P}(t-1)\Phi(t)[\lambda + \Phi^T(t)\mathbf{P}(t-1)\Phi(t)]^{-1}. \tag{5.15}$$

Alternately, an instantaneous influx rate may be computed as:

$$\hat{q}_{res}^{inst} = \frac{V_a y}{\hat{\beta}(1 + 4q_L I_1)}. \tag{5.16}$$

Figure 5.9 illustrates the steps in the estimation algorithm. The RLS algorithm starts as soon as flow from the formation is detected, i.e. using the Bayesian network outlined in Section 5.2.2. The term $\hat{q}_{res}$ is then updated, either from Eq. 5.6, or from Eq. 5.16, and subsequently fed as a source term to the reduced DFM, through either the q_G term in the boundary condition, or the Γ_G term, if the influx occurs at a location different from the well bottom (this may require prior knowledge of the potential influx zones based on lithological data). After all the reduced DFM states and parameters are updated, the algorithm proceeds to the next time step. Since the reservoir model (Eq. 5.17) is only valid while the well is underbalanced, the RLS algorithm can only be applied over the time window starting from the detection of the kick up to the point when the well reaches an overbalanced state. Thus, in order to ensure that the estimated parameters do not diverge, the RLS module needs to be stopped as soon as influx from the formation is no longer detected.

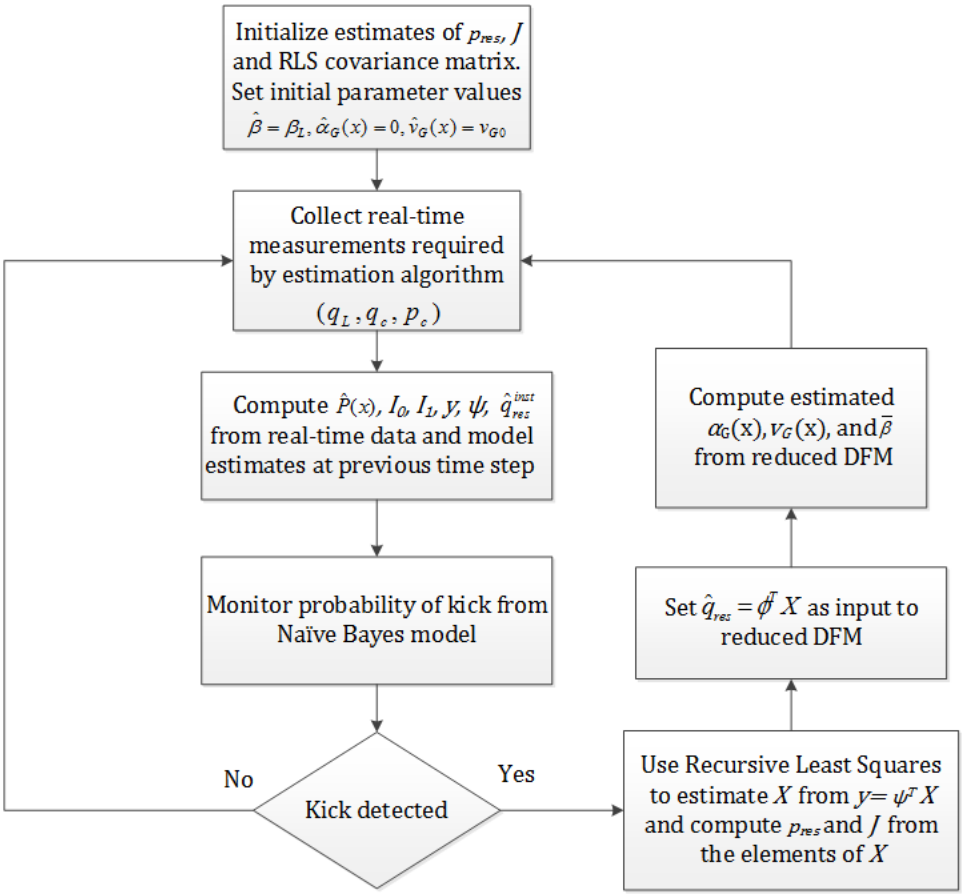

Figure 5.9: Flowchart for pore pressure and reservoir inflow estimation algorithm. The RLS algorithm iteratively computes the reservoir pressure p_{res} and reservoir production index J. The estimated reservoir inflow rate $\hat{q}_{res}$ is used as a source term in the reduced DFM, allowing the gas volume fraction $\alpha_G(x)$, gas velocity $v_G(x)$ and effective bulk modulus $\bar{\beta}$ to be updated. The sequence is repeated until no further influx is detected.

For simulations, τ= 20 seconds is used in Eq. 5.12. The RLS scheme uses the forgetting factor $\lambda = 0.5$, and is initialized with the estimated parameter vector $\hat{X} = \begin{bmatrix} 1 \\ 10^{-9} \end{bmatrix}$ and covariance matrix $\mathbf{P} = 2(\Phi\Phi^T + I)^{-1}$, with

$\Phi = \begin{bmatrix} 5 \times 10^7 \frac{\beta_L}{V_a} \\ \frac{\beta_L}{V_a} \end{bmatrix}$ and I the identity matrix.

5.3.2 Lost Circulation Rate and Fracture Pressure Estimation

For lost circulation estimation (assuming dynamic losses), we use the linear model

$$q_{frac} = k_{frac}[p(x_{loss}) - p_{frac}], p(x_{loss}) > p_{frac} \tag{5.17}$$

where k_{frac} is a constant dependent on the fracture size, p_{frac} is the fracture initiation pressure (or fracture propagation pressure, once a fracture has been created), p is the mud pressure and x_{loss} indicates any location between the casing shoe and the well bottom where mud losses may be experienced. We define the regressor $\Phi_{frac} = \begin{bmatrix} -1 \\ p(x_{loss}) \end{bmatrix}$, with the unknown parameter vector $X_{frac} = \begin{bmatrix} k_{frac}p_{frac} \\ k_{frac} \end{bmatrix}$. Then we proceed with the formulation similar to the procedure followed in Section 5.3.1, where we again use the RLS scheme to calculate k_{frac} and p_{frac}. For the lost circulation rate, we may also use the expression

$$\hat{q}_{frac} = -\frac{V_a y_{frac}}{\hat{\beta}}. \tag{5.18}$$

where

$$y_{frac} = \frac{s}{\tau s + 1} p_c - \frac{1}{\tau s + 1} \frac{\hat{\beta}}{V_a} (q_L - q_c). \tag{5.19}$$

The $\hat{q}_{frac}$ computed from Eq. 5.18 is then fed back to the reduced DFM, as the source term Γ_L at $x = x_{loss}$.

5.3.3 Estimation of Degrading System Parameters

Other parameters monitored include choke orifice area, bit nozzle area, and mud pump volumetric efficiency, which may be subject to degradation throughout the drilling process. To estimate these parameters, we will use a set of non-linear observers, formulated using a simplified version of the hydraulics model described in Section 3.1.1. We start by designing an observer for the choke area, which can change during a plugged (e.g. from debris or solid particles) or washed out choke incident. Since the choke is the primary actuator for the back-pressure MPD method, it is critical to monitor the effective choke area at all time, as the opening width of the choke is a function of the area that is available for flow.

First, recall the choke equation for single-phase flow:

$$q_c = C_v Z \frac{\sqrt{p_c - p_0}}{\sqrt{\rho_L}} \tag{5.20}$$

where $C_v = A_c\sqrt{2}$. For the observer, we will use the pressure dynamics, together with Eq. 5.20:

$$\frac{d\hat{p}_c}{dt} = \frac{\bar{\beta}}{V_a}\Big[q_p - \hat{A}_c Z \frac{\sqrt{2(\hat{p}_c - p_0)}}{\sqrt{\rho_L}}\Big] + \lambda_1(p_c - \hat{p}_c) \tag{5.21}$$

where p_c is the actual (measured) back-pressure and $\hat{p}_c$ is the observed back-pressure, with the observer gain $\lambda_1 > 0$. To estimate the choke area A_c, we need an additional dynamic equation ("update law"); we will denote this estimate as $\hat{A}_c$. An update law for an uncertain parameter is commonly obtained through Lyapunov analysis (Ioannou and Sun, 1996). This analysis

technique involves selecting a continuously differentiable, real-valued function of the states of a dynamic system, which is positive for every non-zero argument. This function is called a Lyapunov function, and may include system parameters that require estimation. Typically, the states and estimated parameters appear in the Lyapunov function as quadratic terms, such that the function is positive for any non-zero input. Lyapunov analysis applied to parameter estimation involves finding a parameter update law that will make the time derivative of the Lyapunov function negative for all non-zero inputs. This will guarantee system stability, which in the present case means that the observer state estimation will converge.

For choke area estimation, we select the following Lyapunov function:

$$\mathbf{V}(\tilde{p}_c, \tilde{A}_c) = \frac{1}{2}\tilde{p}_c^2 + \frac{\gamma_1}{2}\tilde{A}_c^2 \tag{5.22}$$

where we define the estimation errors $\tilde{p}_c = p_c - \hat{p}_c$,$\tilde{A}_c = A_c - \hat{A}_c$, and γ_1 is a positive constant. Next, we take the time derivative of $\mathbf{V}(\tilde{p}_c, \tilde{A}_c)$, and we evaluate the conditions under which $\frac{dV}{dt} < 0$, for all $t > 0$ and $\tilde{p}_c, \tilde{A}_c \neq 0$ (this is a condition to guarantee asymptotic stability of the error dynamics):

$$\frac{d\mathbf{V}}{dt} = \tilde{p}_c \frac{d\tilde{p}_c}{dt} + \gamma_1 \tilde{A}_c \frac{d\tilde{A}_c}{dt} \tag{5.23}$$

$$\frac{d\tilde{p}_c}{dt} = \frac{dp_c}{dt} - \frac{d\hat{p}_c}{dt} = \frac{\bar{\beta} Z \sqrt{2}}{V_a \sqrt{\rho_L}} \left(\hat{A}_c \sqrt{\hat{p}_c - p_0} - A_c \sqrt{p_c - p_0} \right) - \lambda_1 \tilde{p}_c \tag{5.24}$$

We assume that A_c, the true value of choke area, is constant or slowly varying, such that we can write $\frac{d\tilde{A}_c}{dt} = -\frac{d\hat{A}_c}{dt}$, which, together with Eq. 5.24,

and $\hat{A}_c = A_c - \tilde{A}_c$, result in:

$$\frac{d\mathbf{V}}{dt} = \frac{\bar{\beta} Z \sqrt{2}}{V_a \sqrt{\rho_L}} \big[- \tilde{A}_c \sqrt{\hat{p}_c - p_0} + A_c (\sqrt{\hat{p}_c - p_0} - \sqrt{p_c - p_0}) \big] \tilde{p}_c$$
$$- \lambda_1 \tilde{p}_c^2 - \gamma_1 \tilde{A}_c \frac{d\hat{A}_c}{dt} \tag{5.25}$$

Using the expression

$$\sqrt{\hat{p}_c - p_0} - \sqrt{p_c - p_0} = \frac{(\hat{p}_c - p_0) - (p_c - p_0)}{\sqrt{\hat{p}_c - p_0} + \sqrt{p_c - p_0}} = - \frac{\tilde{p}_c}{\sqrt{\hat{p}_c - p_0} + \sqrt{p_c - p_0}}, \tag{5.26}$$

and grouping together all the terms containing $\tilde{A}_c$ and $\tilde{p}_c^2$, we get:

$$\frac{d\mathbf{V}}{dt} = - \Big[\lambda_1 + \frac{\bar{\beta} Z A_c \sqrt{2}}{V_a \sqrt{\rho_L} (\sqrt{\hat{p}_c - p_0} + \sqrt{p_c - p_0})} \Big] \tilde{p}_c^2$$
$$- \Big[\gamma_1 \frac{d\hat{A}_c}{dt} + \frac{\bar{\beta} Z \sqrt{2(\hat{p}_c - p_0)}}{V_a \sqrt{\rho_L}} \Big] \tilde{A}_c \tag{5.27}$$

We can make the second square bracket in Eq. 5.27 equal to zero, by selecting the update law:

$$\frac{d\hat{A}_c}{dt} = - \frac{\bar{\beta} Z \sqrt{2(\hat{p}_c - p_0)}}{\gamma_1 V_a \sqrt{\rho_L}} (p_c - \hat{p}_c) \tag{5.28}$$

Substituting Eq. 5.28 into Eq. 5.27 will guarantee that $\frac{d\mathbf{V}}{dt} < 0$, for all $t > 0$ and $\tilde{p}_c \neq 0$, since the term in the first square bracket in Eq. 5.27 is always positive, hence the observer is asymptotically stable.

Next, we design an observer for the bit nozzle area A_b, which will change during a plugged or washed out nozzle scenario. For this purpose, we will use a dynamic equation describing the flow rate through the bit, together with the

equation for the bit pressure drop,

$$p_{bit} = \frac{\rho_L q_{bit}^2}{2A_b^2 C_d^2} \tag{5.29}$$

where q_{bit} is the volume flow rate through the bit, and C_d is the bit discharge coefficient. The observer is designed as:

$$\frac{d\hat{q}_{bit}}{dt} = \frac{1}{\int_0^L \frac{\rho_L}{A} \mathrm{d}x} \Big[p_p - p_c - p_f + \int_0^L \rho_L g cos\theta \mathrm{d}x - \frac{1}{2}\rho_L \hat{C}_b \hat{q}_{bit}^2 \Big] + \lambda_2 (q_p - \hat{q}_{bit}) \tag{5.30}$$

where $\lambda_2 > 0$ is a constant observer gain and $\hat{C}_b = \frac{1}{\hat{A}_{bit}^2 C_d^2}$. It is assumed that we have measurements for p_p, p_c, and that the p_f term (frictional pressure drop) can be calculated using the YPL correlations in Appendix C. We use the following notation: $\tilde{q}_{bit} = q_{bit} - \hat{q}_{bit} \approx q_p - \hat{q}_{bit}$ and $\tilde{C}_b = C_b - \hat{C}_b$, with $\frac{dC_b}{dt} = 0$. We can again use Lyapunov analysis to derive a law for estimating $\hat{C}_b$, using the Lyapunov function:

$$\mathbf{V}(\tilde{q}_{bit}, \tilde{C}_b) = \frac{\tilde{q}_{bit}^2}{2} + \frac{\gamma_2 \tilde{C}_b^2}{2} \tag{5.31}$$

with $\gamma_2 > 0$. Its derivative is given by:

$$\frac{d\mathbf{V}}{dt} = \tilde{q}_{bit} \Big[\frac{\rho_L}{2\int_0^L \frac{\rho_L}{A} \mathrm{d}x} (\hat{C}_b \hat{q}_{bit}^2 - C_b q_{bit}^2) - \lambda_2 \tilde{q}_{bit} \Big] + \gamma_2 \tilde{C}_b \frac{d\tilde{C}_b}{dt} \tag{5.32}$$

$$\frac{d\mathbf{V}}{dt} = \tilde{q}_{bit} \frac{\rho_L}{2\int_0^L \frac{\rho_L}{A} \mathrm{d}x} \Big[- \tilde{C}_b \hat{q}_{bit}^2 + C_b (\hat{q}_{bit}^2 - q_{bit}^2) \Big] - \lambda_2 \tilde{q}_{bit}^2 - \gamma_2 \tilde{C}_b \frac{d\hat{C}_b}{dt} \tag{5.33}$$

Using the difference of squares formula,

$$\hat{q}_{bit}^2 - q_{bit}^2 = (\hat{q}_{bit} - q_{bit})(\hat{q}_{bit} + q_{bit}), \tag{5.34}$$

we can write:

$$\frac{d\mathbf{V}}{dt} = -\Big[\lambda_2 + \frac{\rho_L C_b(\hat{q}_{bit} + q_{bit})}{2\int_0^L \frac{\rho_L}{A}\mathrm{d}x}\Big]\tilde{q}_{bit}^2 - \Big[\gamma_2\frac{d\hat{C}_b}{dt} + \frac{\rho_L \hat{q}_{bit}^2\tilde{q}_{bit}}{2\int_0^L \frac{\rho_L}{A}\mathrm{d}x}\Big]\tilde{C}_b \tag{5.35}$$

We can cancel out the second square bracket by selecting the update law:

$$\frac{d\hat{C}_b}{dt} = -\frac{\rho_L \hat{q}_{bit}^2\tilde{q}_{bit}}{2\gamma_2\int_0^L \frac{\rho_L}{A}\mathrm{d}x}(q_p - \hat{q}_{bit}) \tag{5.36}$$

which makes $\frac{d\mathbf{V}}{dt} < 0$, for all $t > 0$ and $\tilde{q}_{bit} \neq 0$. Note that this holds as long as $q_p \equiv q_{bit}$, which is a reasonable assumption except during pump rate transients.

Similarly, we can design an observer for the volumetric pump efficiency η. For this case, we will use a slightly modified formulation for the annular pressure dynamics:

$$\frac{dp_c}{dt} = \frac{\bar{\beta}}{V_a}(\eta q_p - q_c) \tag{5.37}$$

where q_p is the commanded pump rate. It is assumed that the actual pump output, ηq_p, is not readily available from measurements (i.e. no direct measurement of η). For this estimation task, we will design the observer:

$$\frac{d\hat{p}_c}{dt} = \frac{\bar{\beta}}{V_a}(\hat{\eta} q_p - q_c) + \lambda_3(p_c - \hat{p}_c) \tag{5.38}$$

We define $\tilde{p}_c = p_c - \hat{p}_c, \tilde{\eta} = \eta - \hat{\eta}$, and select a Lyapunov function:

$$\mathbf{V}(\tilde{p}_c, \tilde{\eta}) = \frac{\tilde{p}_c^2}{2} + \frac{\gamma_3\tilde{\eta}^2}{2} \tag{5.39}$$

and follow the same procedure as before, i.e. take the derivative $\frac{d\mathbf{V}}{dt}$, and group the common terms, which gives:

$$\frac{d\mathbf{V}}{dt} = -\lambda_3\tilde{p}_c^2 + \Big[\frac{\bar{\beta} q_p\tilde{p}_c}{V_a} - \gamma_3\frac{d\hat{\eta}}{dt}\Big]\tilde{\eta} \tag{5.40}$$

from which we get the update law:

$$\frac{d\hat{\eta}}{dt} = \frac{1}{\gamma_3}\frac{\bar{\beta}}{V_a}q_p(p_c - \hat{p}_c) \tag{5.41}$$

The observers defined in this section are implemented with $\lambda_1 = 1, \gamma_1 = 5 \times 10^{16}$, $\lambda_2 = 1, \gamma_2 = 2 \times 10^{-17}$, $\lambda_3 = 1$, and $\gamma_3 = 10^{12}$. These values were selected to achieve fast convergence of the estimates.

5.4 Test Scenarios

All scenarios are generated with the high-fidelity hydraulics simulator (Ma et al., 2016) modeling the actual physical process. The test setup is that of a 15,850-ft MD well with the deviated trajectory shown in Figure 3.2, with 9.76-in (inner diameter) casing set at 13,000 ft and a 9.5-inch open-hole diameter. The drill string consists of 5-in drill pipe and a 1285-ft BHA comprising 6.5-in drill collars. An SBM with oil/water ratio of 70/30 is used. Mud is circulated at a rate of 600 gpm, unless otherwise indicated. The mud properties and other parameters are given in Table 5.2, while Figure 5.10 shows the pressure window in the well. For the kick simulation, it will be assumed that the gas reservoir is at the well bottom, and its pore pressure varies from 7000 psi to 7870 psi. For all other scenarios, pore pressure is fixed at 7000 psi. For the lost circulation case, the fracture is generated at the casing shoe, with a fracture initiation pressure of 7200 psi, and a fracture propagation pressure of 7000 psi. In all other scenarios, the fracture initiation pressure at the casing shoe is set at 7300 psi to allow a larger pressure window.

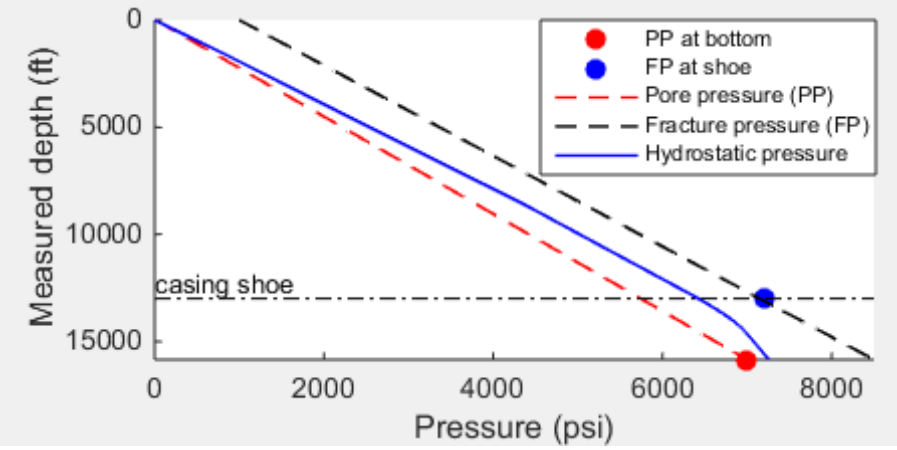

Figure 5.10: Pressure window for simulation scenarios. The default values (unless otherwise indicated) for pore pressure at bottom, and fracture initiation pressure at casing shoe, are 7000 psi, and 7300 psi, respectively.

Table 5.2: Input parameters for simulation scenarios.

Parameter	*Value*	*Unit*
Mud density	10	lbm/gal
Mud consistency index	20	cP
Mud power-law index	1	
Mud yield stress	10	lbs/(100ft^2)
Sound velocity in mud	3400	ft/s
Number of size of bit nozzles	3× 0.5	in
Nozzle total flow area	0.6	in^2
Circulation rate	600	gpm
Choke line ID	2	in
Gas viscosity	0.005	cP
Gas specific gravity	0.65	-
Gas adiabatic index	1.32	-
Reservoir productivity index	0.146	ft^3/min/psi
Mud loss index	0.0146	ft^3/min/psi
Surface temperature	60	°F
Bottom-hole temperature	135	°F

The measurements available in the simulations include SPP, WHP, pump rate, flow rate out, and pit volume. The BHP sensor is assumed to be unavailable, and thus the system needs to rely on SPP feedback, or on modeled BHP. Random noise with a standard deviation of 30 psi is added to the pressure readings, while flow rate and pit volume are injected with noise equal to 5% of the reading for flow rate, and 1% for pit volume. An event detection threshold of 50% is used throughout the simulations.

The LMI-based pressure controller from Chapter 4.3 is used for the kick scenario, due to its superior performance in handling two-phase flow. In all the other scenarios, the feedback linearization controller in Chapter 4.1 is used; this is motivated by its high gain and phase margins under single-phase conditions, as per the analysis in Chapter 4.6.1. The controller parameters are the same as the ones defined in Chapter 4.6.

5.4.1 Kick Scenario

The scenario starts with the well at overbalance. After 5 minutes, an over-pressured dry gas reservoir with a pore pressure of 7870 psi is drilled through, resulting in an underbalance of 300 psi at the well bottom. The system manages to detect the kick after a pit gain of less than 1 bbl, as the kick event probability reaches close to 100% (Figure 5.11). The controller immediately proceeds to close the choke in flow control mode, until the influx stops, about 8 minutes later. During this process, an additional 1 bbl of pit gain is observed; at this point, the gas is fully dissolved in the mud.

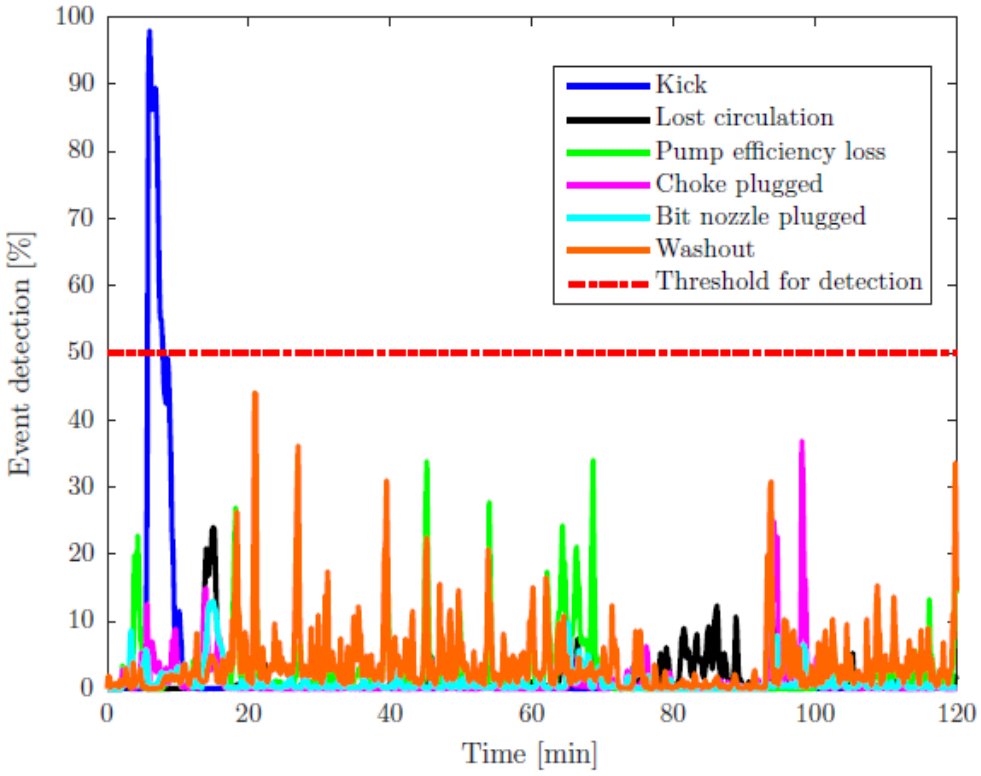

Figure 5.11: Event detection outputs for a kick scenario. The kick starts at 5 minutes and is detected with a very high probability within 1 minute from its start.

While the kick is being attenuated by rapidly closing the choke, the system also accurately estimates the reservoir pressure and the influx rate (Figure 5.12). The RLS algorithm determined a value of 7884 psi for pore pressure and 0.058 ft^3/min/psi for the productivity index. The kick response time can be reduced by adjusting the controller aggressiveness, but this may affect the estimation of reservoir pressure as it may not have sufficient data samples to learn from. Depending on the kick size and detection volume,

however, it may be preferred to minimize response times for kick tolerance purposes.

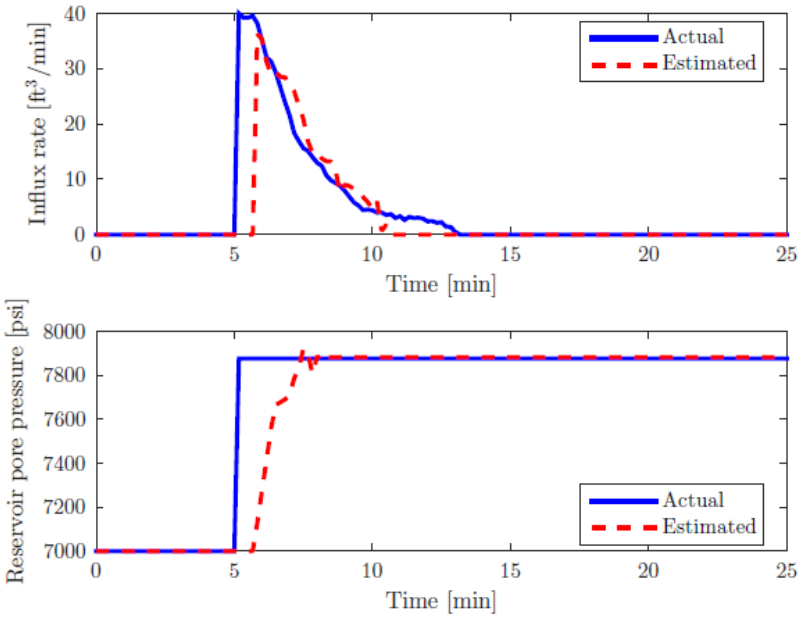

Figure 5.12: Influx rate and pore pressure estimation for a kick scenario. Once the kick is detected, the system tracks the influx rate (upper) and pore pressure (lower). After 10 minutes, the influx rate is below the flow sensor noise threshold, so the estimated influx rate is set to zero.

Once no further influx is detected, the system switches to pressure control with a set point equal to the estimated reservoir pressure plus a safety margin of 150 psi. The controller manages to keep BHP within 50 psi of the target, even when gas breaks out of the solution, as seen by the increased pit gain and flow out at 70 minutes (see Figures 5.13a and 5.13b). As the free gas expands, the choke opening is quickly updated, resulting in a noisy flow out signature. However, BHP remains smooth throughout this phase.

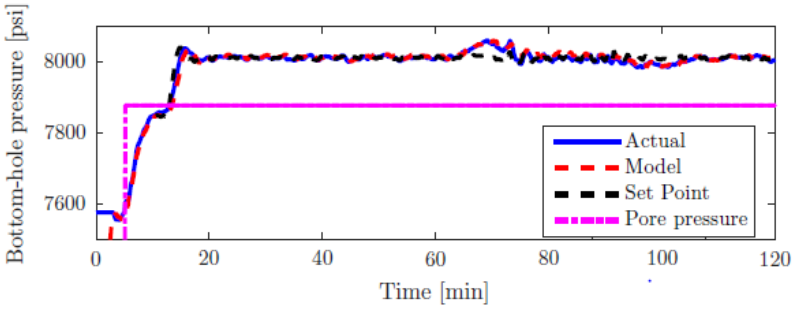

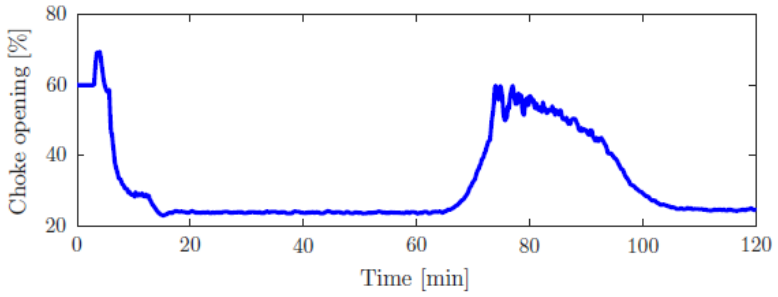

(a) BHP (upper) and choke opening (lower).

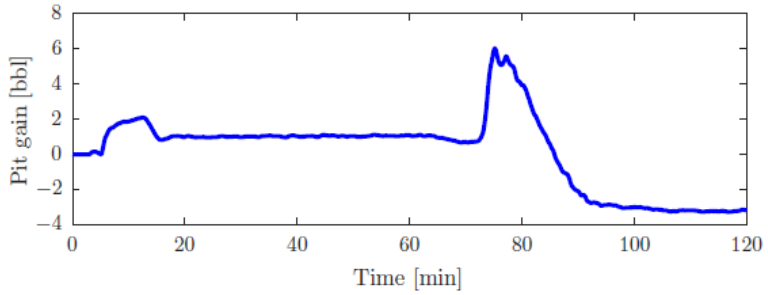

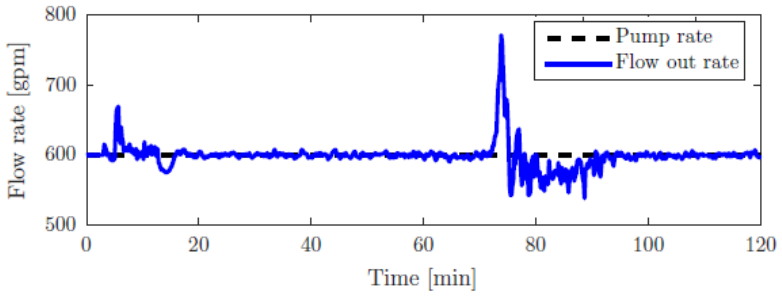

(b) Pit gain/loss (upper) and flow rate (lower).

Figure 5.13: System response for a kick scenario. The influx is stopped within 8 minutes from detection, and then it is circulated out while BHP is kept close to its target.

The close agreement between the BHP predicted by the model and the actual value should also be noted. The model is also correct in tracking the amount of gas once it starts breaking out of the mud. Indeed, for both dissolved gas and free gas, the agreement between the estimated profiles (obtained from the reduced DFM) and the actual ones is very good, as Figures 5.14 and 5.15 show. Compared to results in Chapter 3.3.1, it should be noted that the amount of gas was significantly lower here due to the early detection, and thus the BHP prediction error was smaller.

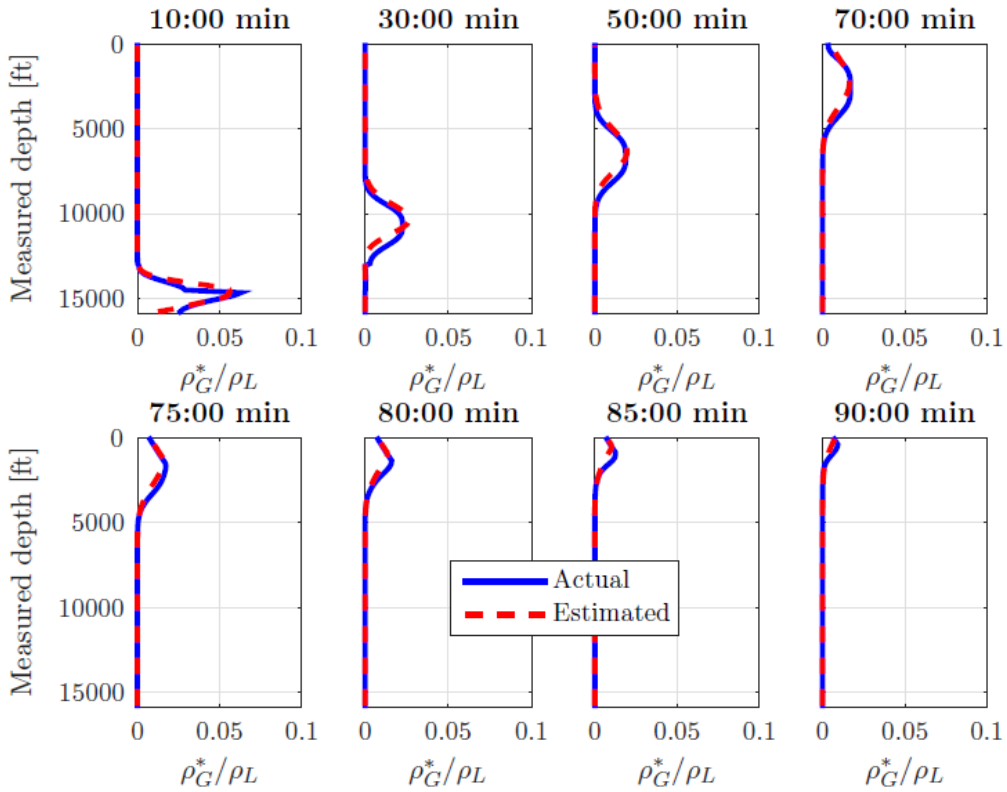

Figure 5.14: Estimation of dissolved gas profile for a kick scenario. The actual (from the high-fidelity simulator) and estimated profiles (from the reduced DFM) are in close agreement throughout the simulation.

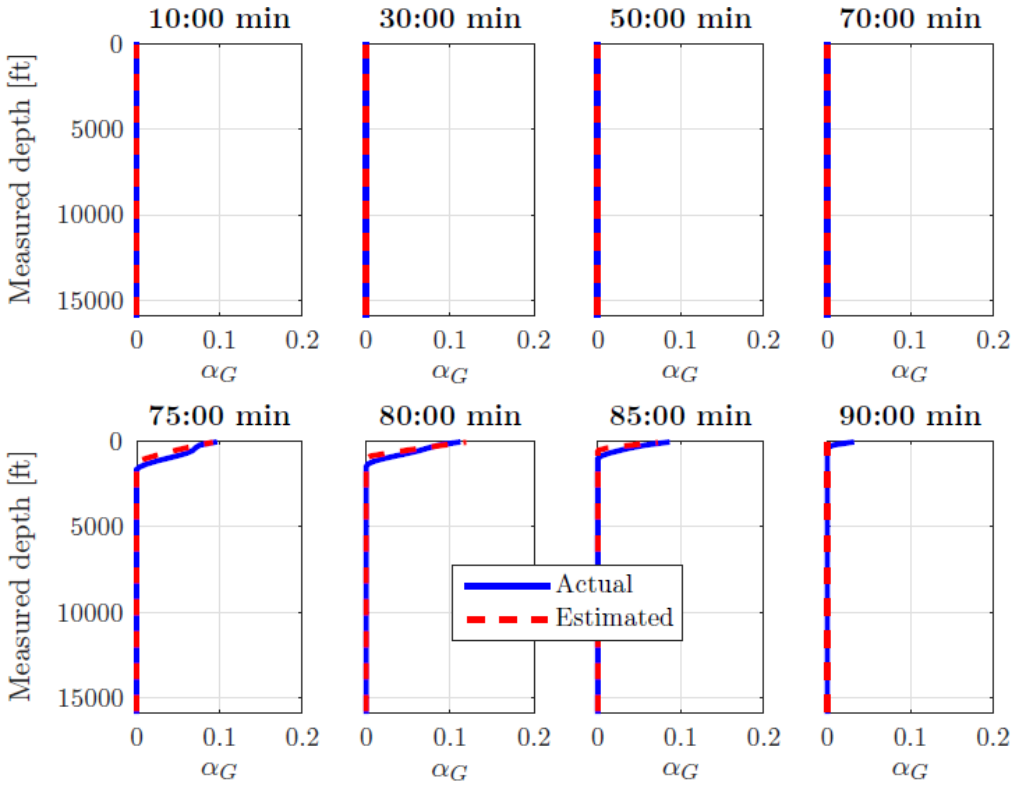

Figure 5.15: Estimation of free gas profile for a kick scenario. The actual (from the high-fidelity simulator) and estimated profiles (from the reduced DFM) are in close agreement throughout the simulation.

5.4.2 Lost Circulation

The simulation begins with a circulation rate of 400 gpm, which results in a casing shoe pressure well below the fracture initiation pressure. At 5 minutes, the pump is ramped up to 600 gpm, resulting in the circulating pressure to exceed the limit for fracture initiation. As the fracture is opened, mud starts flowing into the formation, and less than 1 bbl of mud is lost before the system detects the loss event with a probability of 70% (Figure 5.16).

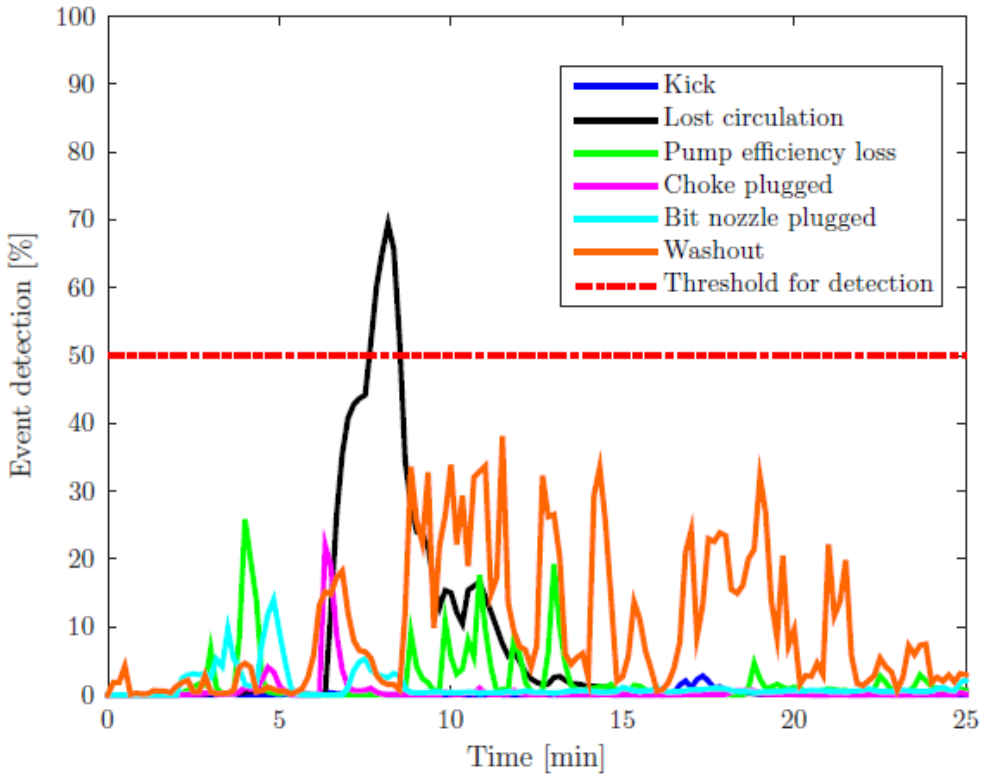

Figure 5.16: Event detection outputs for a lost circulation scenario. The lost circulation starts at 6.5 minutes and is detected with a probability of 70% within 1 minute from its onset.

Note that the total loss at this point is 5 bbl. However, this includes any temporary losses caused by increasing the pump rate, as the flow rate out lags behind the pump rate (due to the time it takes for mud to travel from the pump to the return line). Upon detection, the system immediately goes into flow control, which results in opening the choke to release back-pressure. It takes about 7 minutes to stop the loss, during which time the system keeps track of the loss rate and estimates the fracture pressure. The estimate falls between

the fracture initiation and propagation pressure, as shown in Figure 5.17. The system then applies a new pressure set point below the fracture propagation pressure (which, in this case, was assumed to be below the initiation pressure) to ensure that no further mud losses occur.

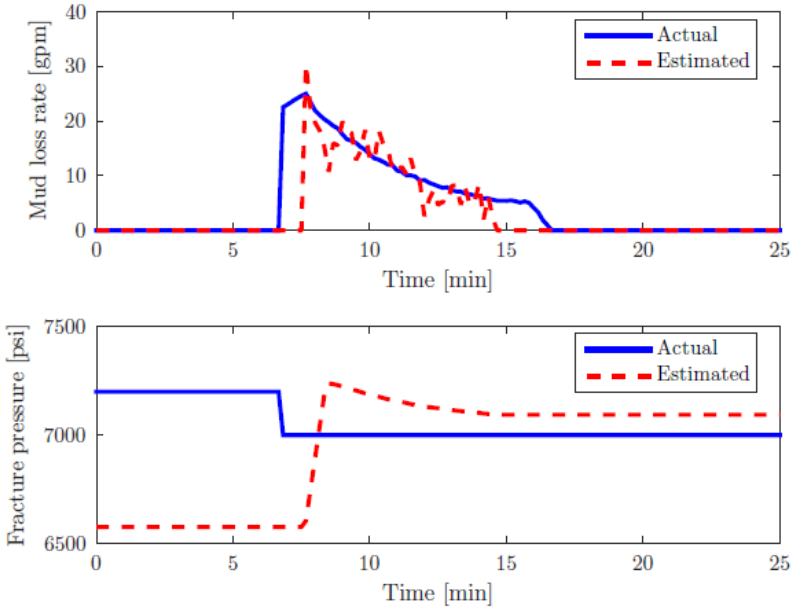

Figure 5.17: Estimation of mud loss rate and fracture pressure for a lost circulation scenario. Once the loss incident is detected, the system tracks the lost circulation rate (upper) and fracture pressure (lower) close to their actual values. After 15 minutes, the loss rate is below the flow sensor noise threshold, so the estimated loss rate is set to zero.

The pressure and flow trends throughout the incident are shown in Figures 5.18a and 5.18b. The increased flow out after 15 minutes is a result of some of the mud flowing back to the well as the fracture is closed. Figure 5.18b still indicates a net loss of pit volume at the end of the simulation, which is due to the aforementioned loss of drilling fluid during the pump rate increase.

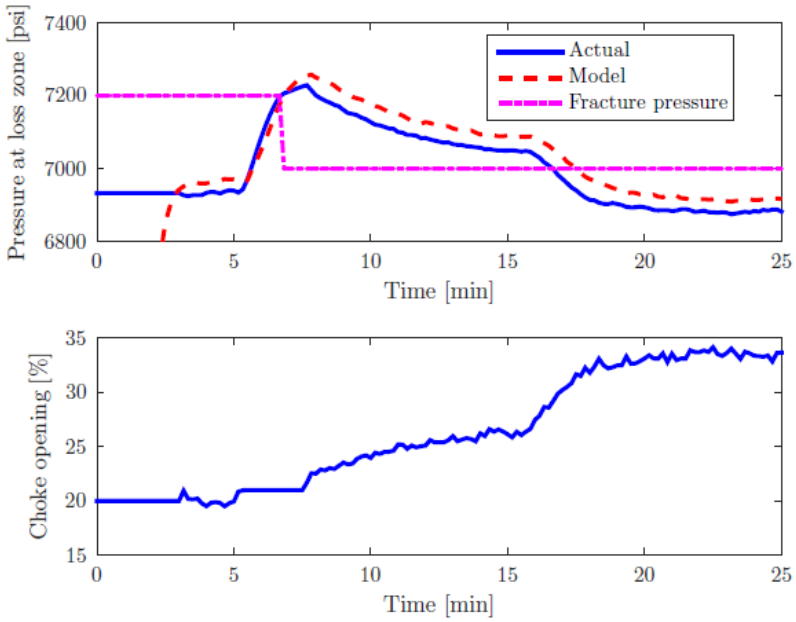

(a) Casing shoe pressure (upper) and choke opening (lower).

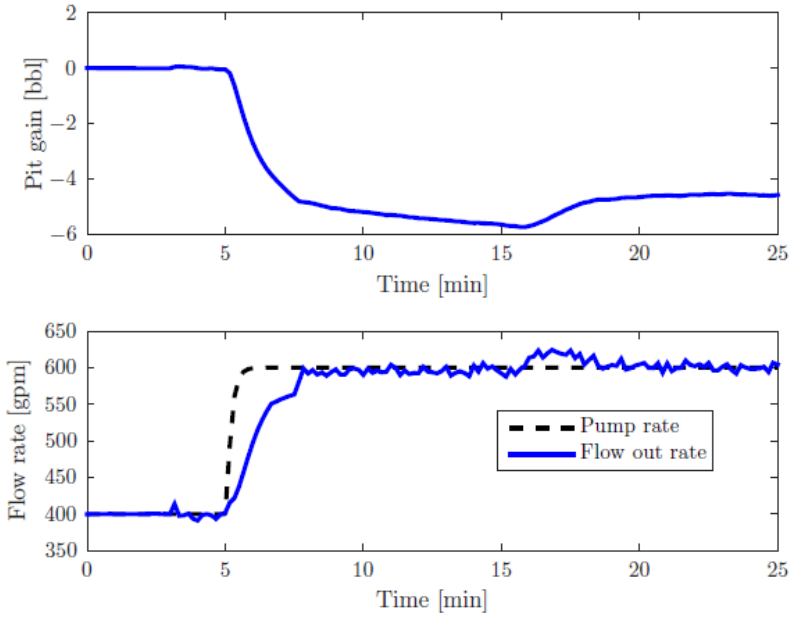

(b) Pit gain/loss (upper) and flow rate (lower).

Figure 5.18: System response for a lost circulation scenario. The losses are stopped after 7 minutes from detection, and the pressure set point is then reduced to a value below the estimated fracture pressure.

5.4.3 Plugged Choke Valve

A partially plugged choke (e.g. due to solids in the mud such as cuttings, cavings, lost circulation materials, etc.) is simulated by reducing its effective flow area by 30%. While the choke plugging may happen gradually, the reduction is assumed to be instantaneous here, to test the controller robustness when dealing with a sudden fault. The plugging starts at 15 minutes and is quickly detected with a 90% probability after less than 30 seconds, as shown in Figure 5.19.

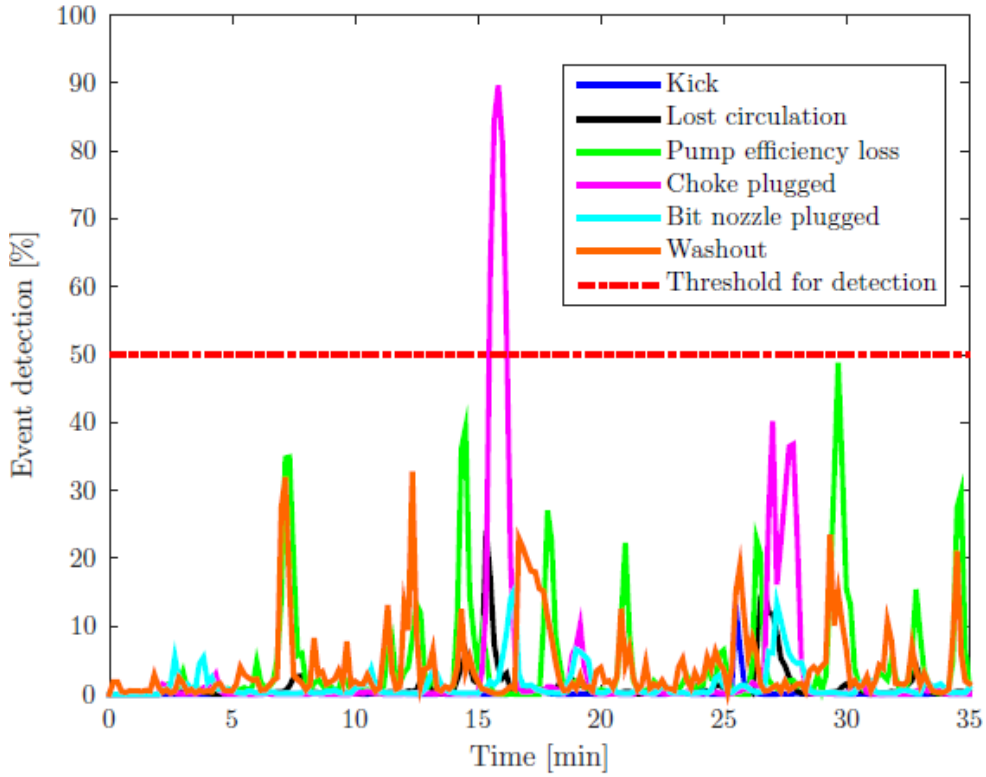

Figure 5.19: Event detection outputs for a plugged choke scenario. The choke becomes plugged at 15 minutes and is detected within 30 seconds with a peak probability of 90%.

As soon as the choke gets plugged, the choke needs to open quickly to counter the increase in back-pressure. The system is able to quickly learn the change in choke area due to the plug, and apply a larger choke opening until the pressure stabilizes (see Figures 5.20 and 5.21). When the plug is removed (again, assuming an instantaneous change), 10 minutes later, the choke needs to be again closed to restore the BHP to the value prior to the incident. It should be noted that failure to update the choke area used in the control model quickly enough would have resulted in too much or too little back-pressure being applied, causing potential fracturing or underbalanced situations, respectively.

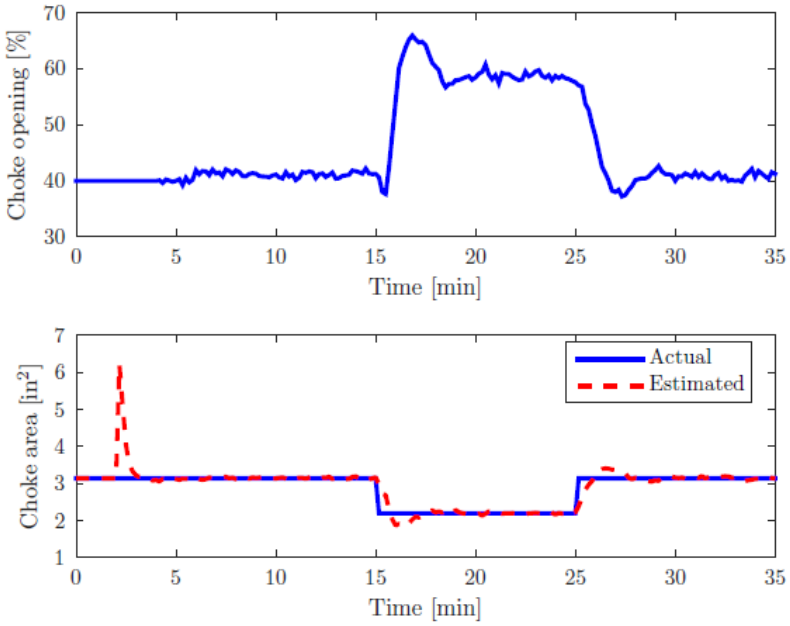

Figure 5.20: Choke opening (upper) and choke orifice area (lower) during a plugged choke scenario. The system correctly estimates the new choke area after the plugging starts, and also as the plug is later removed at 25 minutes.

Even though the plugging conditions persist for some time, the detection probability is quickly reduced following the initial detection. This is because the model is now updated with the correct choke area. There is another spike in detection once the choke plug is removed, which is quickly damped as soon as the choke area communicated to the model is once again correctly updated.

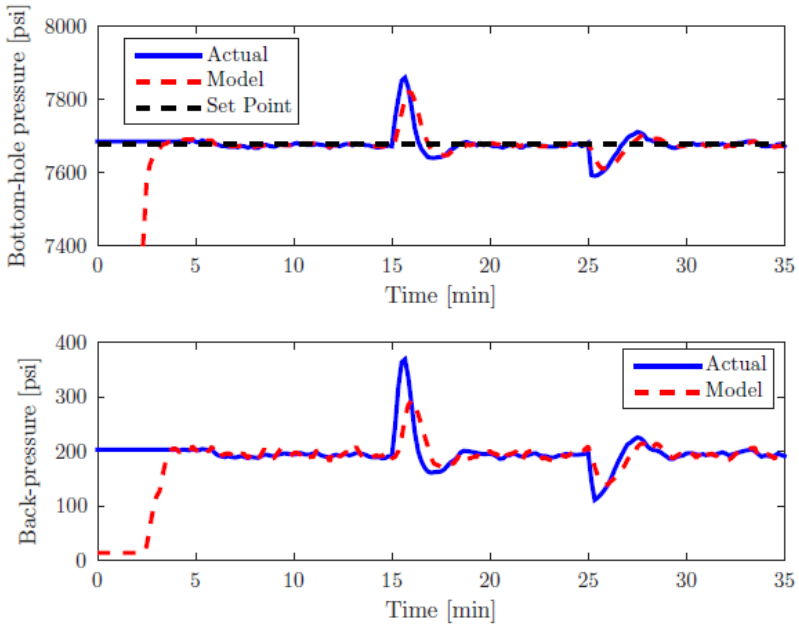

Figure 5.21: BHP (upper) and back-pressure (lower) for a plugged choke scenario. The initial spike in back-pressure occurs before the plugged choke is detected. After detection, the controller reduces the back-pressure and stability is regained.

5.4.4 Plugged Bit Nozzle

In this simulation, one of the three 0.5-in bit nozzles becomes suddenly plugged at 15 minutes. This is almost immediately caught by the event detec-

tion with a probability close to 80%, as indicated by Figure 5.22. This presents a challenge to the pressure controller, because it is initially configured to use SPP feedback. Once the nozzle is plugged, the higher bit pressure drop increases the SPP significantly (lower plot of 5.24). In response, the controller, unless instructed otherwise, will open the choke to offset that increase in pump pressure.

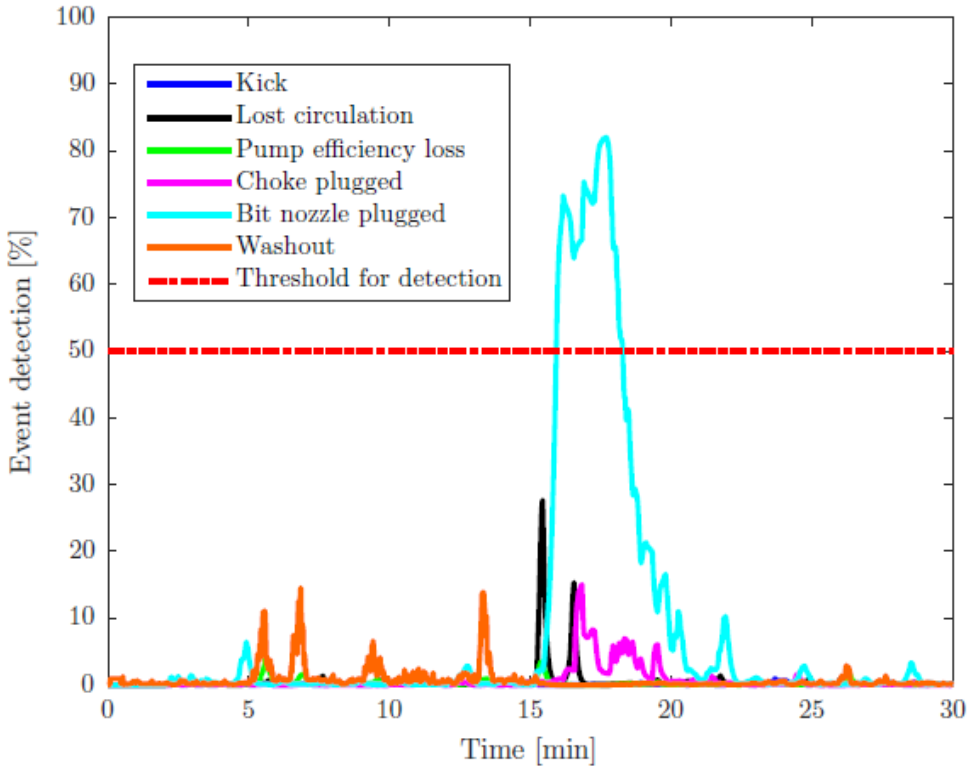

Figure 5.22: Event detection outputs for a plugged bit nozzle scenario. The bit nozzles becomes plugged at 15 minutes and is detected with a high probability within one minute from its start.

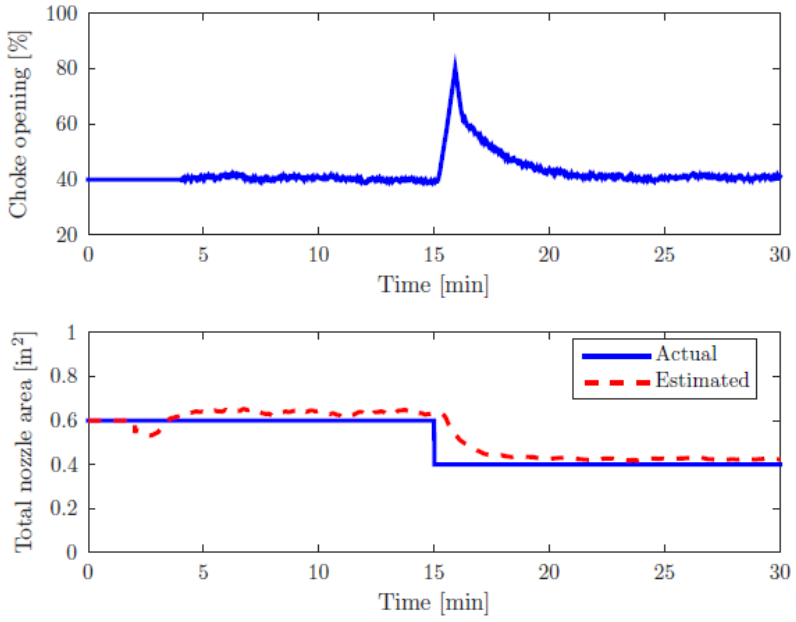

Figure 5.23: Choke opening (upper) and bit nozzle area (lower) during a plugged bit nozzle scenario. The system correctly estimates the new bit nozzle area after the plugging starts.

Opening the choke causes a drop in BHP, which could jeopardize well control if the margins are very tight (upper plot of Figure 5.24. The system acts upon this by switching the pressure control set point from standpipe to BHP as soon as the plug is detected. In the absence of a downhole sensor, the controller will rely on the value from the hydraulics model, which stays close to the actual value throughout the incident. Here it was assumed that the nozzle plug does not cause a change in flow rate or ECD which would also affect the BHP.

In addition, the system successfully estimates the new bit nozzle area and proceeds to close the choke, restoring the BHP to its value prior to the

incident (Figure 5.23). If downhole pressure data were available, BHP could have been used throughout to avoid this issue. However, this simulation shows that the system is capable of handling such a scenario just with surface data and a properly calibrated hydraulics model.

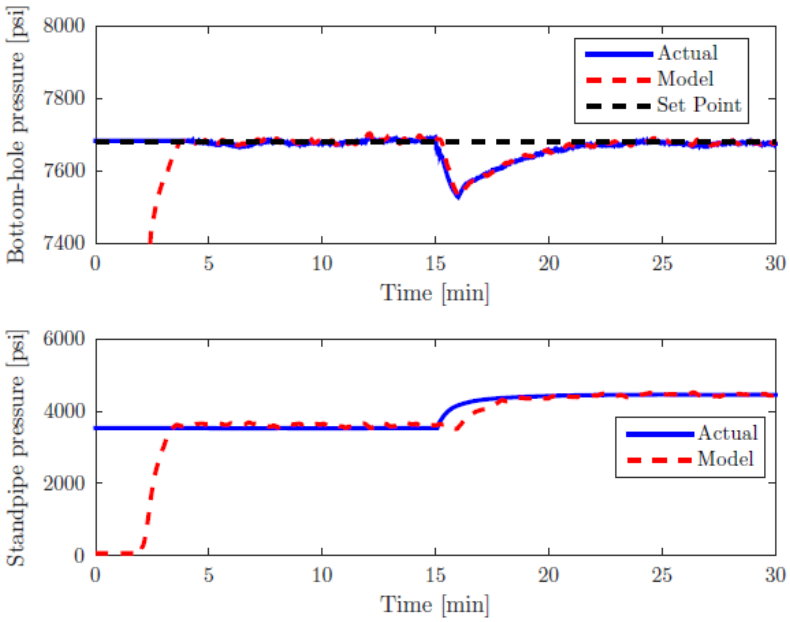

Figure 5.24: BHP (upper) and SPP (lower) for a plugged bit nozzle scenario. The BHP initially drops before the plugged nozzle is detected. After detection, the system adds back-pressure to bring the BHP back to the target.

5.4.5 Pump Efficiency Loss

The pump efficiency loss is simulated through a gradual drop (see bottom plot of Figure 5.25) over a 15-minute period, reaching as low as 70% before it stabilizes. The system detects this within 2 minutes of the onset of pump degradation, and the event probability peaks at 74% (Figure 5.26).

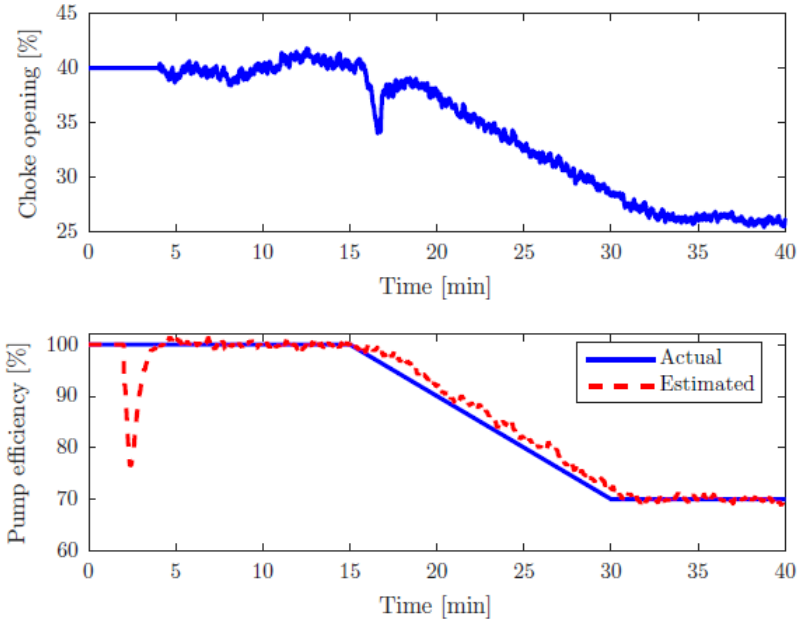

Figure 5.25: Choke opening (upper) and pump efficiency (lower) during a pump efficiency loss scenario. The system correctly tracks the degrading pump efficiency.

As the pump produces lower volumes per stroke, the SPP also drops (lower plot of Figure 5.27) as a result of the lower effective flow rate into the well. Since SPP control is used, this causes the automatic closing of the choke in order to keep the pressure close to the target by adding back-pressure. The initial choke adjustment is too drastic, which results in a pressure spike seen at the bottom-hole (upper plot of Figure 5.27). Upon detection of the pump efficiency loss, the controller switches to the BHP set point. The system opens the choke slightly to relieve the extra back-pressure and then gradually closes it in synchronization with the pump efficiency reduction. This allows the system to maintain the BHP close to the target value of 7680 psi.

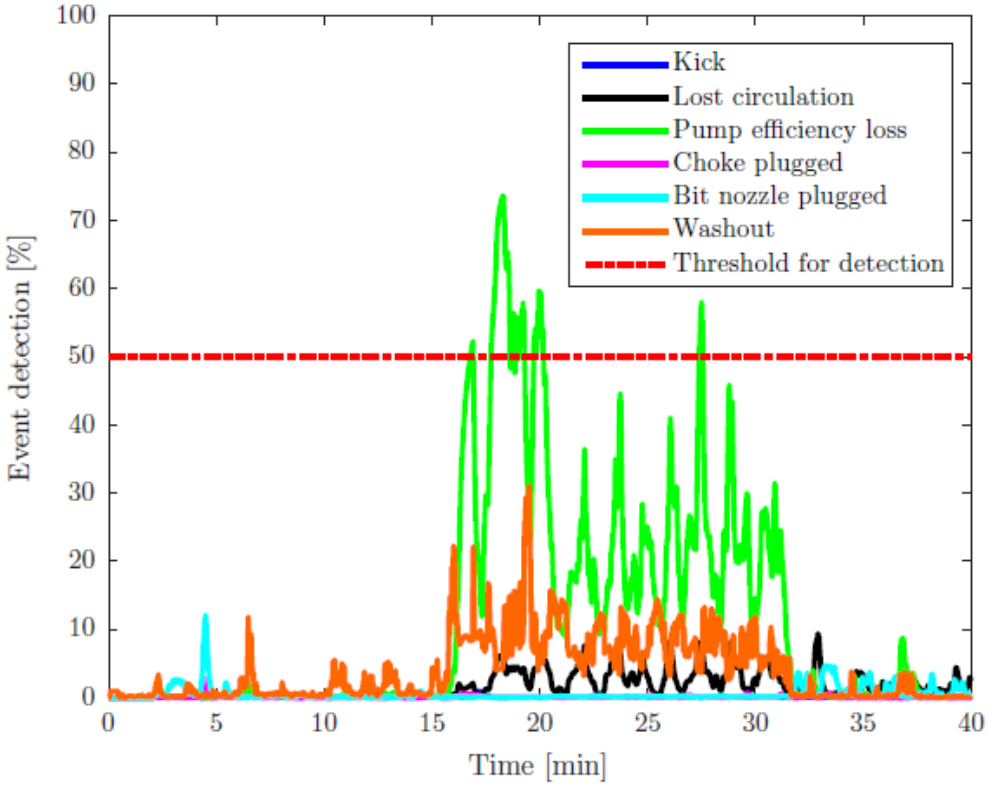

Figure 5.26: Event detection outputs for a pump efficiency loss scenario. The pump efficiency loss starts at 15 minutes and is detected within 2 minutes from its onset.

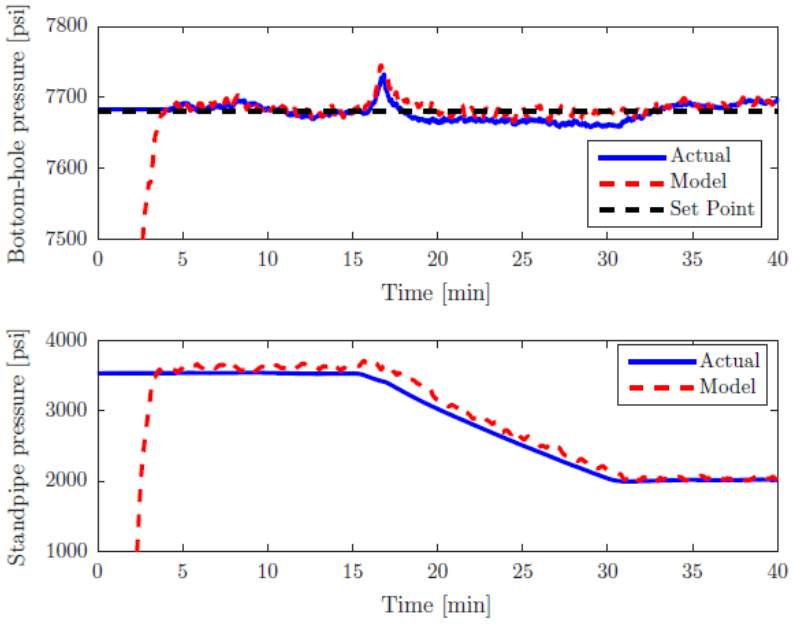

Figure 5.27: BHP (upper) and SPP (lower) for a pump efficiency loss scenario. There is a small spike in BHP before the pump efficiency loss is detected. After detection, the BHP is reduced back to the target value.

5.4.6 Drill Pipe Washout

For this scenario, we simulate a leak inside the drill pipe at 3000 ft MD, its size increasing linearly over a 15-minute period. The washout is detected after 3 minutes, with a probability peaking at 68% (Figure 5.28). The initial spike in pump efficiency detection is a result of the similar signatures shared by the two events (decrease in SPP and flow out). Eventually, the system is capable of distinguishing the washout as flow out stabilizes after the transient (bottom plot of Figure 5.29). Also, the initial signature of decreasing SPP (lower plot of Figure 5.30) is masked by the increase in back-pressure, as the

choke is closed to maintain the SPP target.

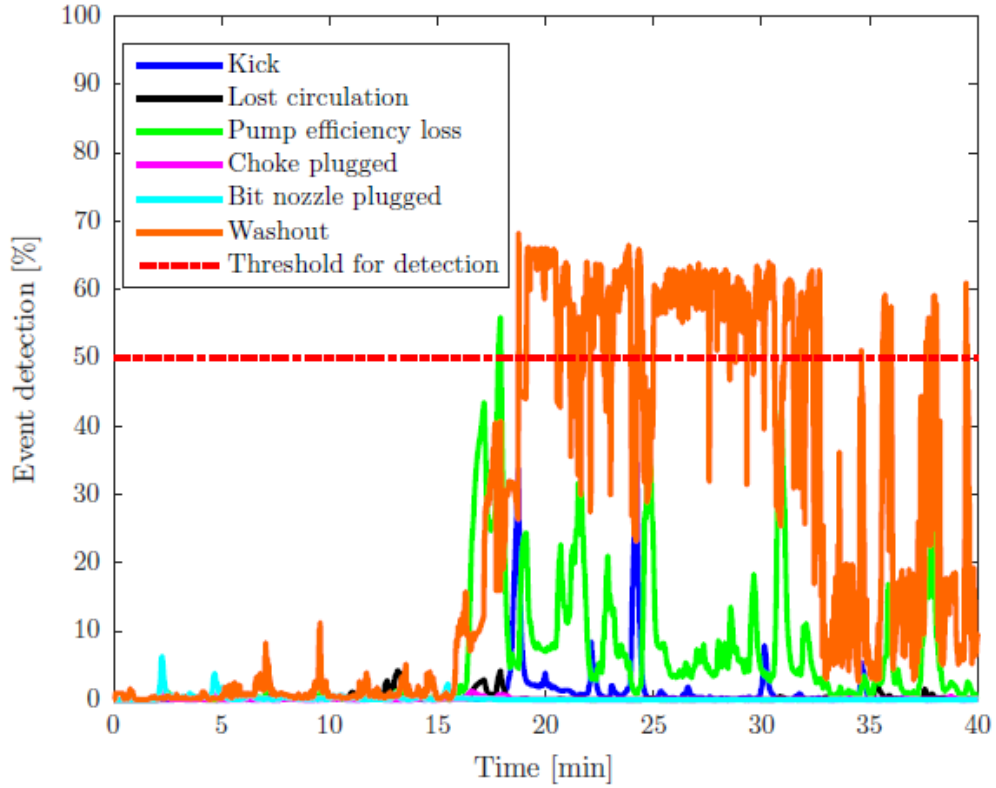

Figure 5.28: Event detection outputs for a drill pipe washout scenario. The drill pipe washout starts to develop at 15 minutes and is detected 3 minutes later.

As in the previous scenarios, the control set point is switched to BHP, and the choke opens again to restore the correct amount of back-pressure required to maintain the BHP target. The washout magnitude reaches 160 gpm at its peak, as seen from the difference between pump rate and flow rate through the bit (Figure 5.29). Since the hydraulics model is not re-calibrated to account for the washout, a large discrepancy remains between the model

and actual pump pressure measurement. One possible solution to address this discrepancy is to use an observer for the bit flow rate, similar the one in Eq. 5.30. The estimated bit flow rate can be used to re-compute the frictional pressure losses. However, estimating the exact location of the washout would require additional sensors. This model discrepancy does not affect the model-predicted BHP, as Figure 5.30 indicates. The effective drop in BHP due to the washout is less than 30 psi, which accounts for the reduction in annular friction losses.

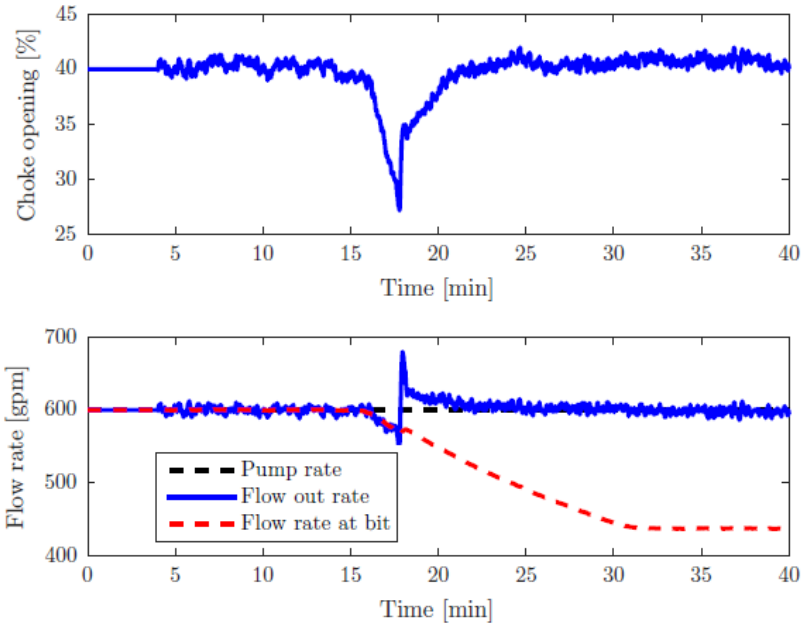

Figure 5.29: Choke opening (upper) and flow rate (lower) for a drill pipe washout scenario. The flow rate at the bit is notably reduced during the washout.

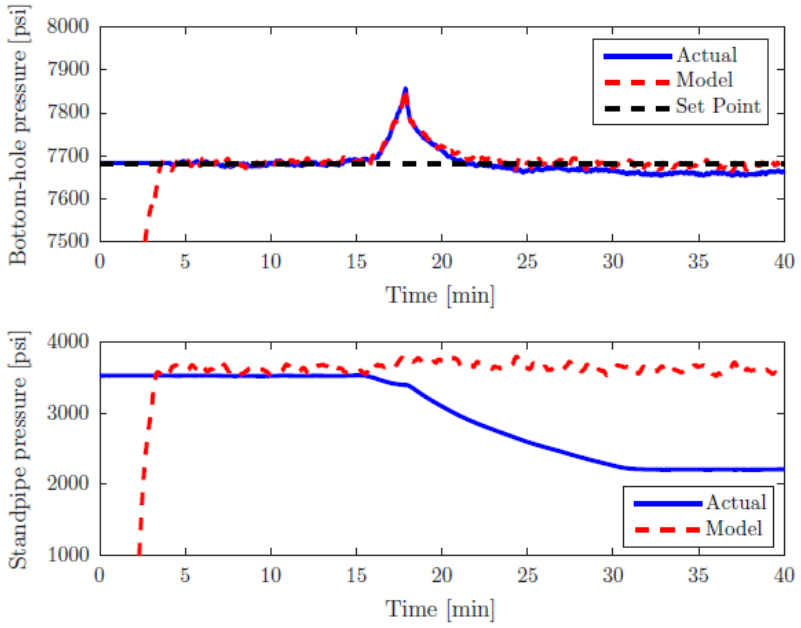

Figure 5.30: BHP (upper) and SPP (lower) for a drill pipe washout scenario. The initial spike in BHP occurs before the washout is detected. The discrepancy in SPP prediction due to the washout does not affect the control performance as the system begins to use the modeled BHP for feedback.

5.4.7 Drill Pipe Connection

The final scenario investigates the controller performance during a drill pipe connection, aiming to keep a constant BHP target of 7580 psi. To simulate the connection, the pump rate is brought from 600 gpm down to zero in 5 minutes, kept at zero for 7 minutes, and then ramped back to 600 gpm, as per the lower plot of Figure 5.31. The choke is allowed to close completely during the connection, using the trapped back-pressure to compensate for the annular friction once circulation stops. For this task, the modeled BHP value will be used throughout for the pressure controller, as SPP varies significantly

during the pump shut-down and start-up.

As Figure 5.32 shows, the BHP stays within a 50 psi range of the target during the entire process, with minimal overshoot during pump shut-down and start-up. In practice, due to the choke size and geometry, it may not be possible for the choke to close completely and therefore it may not be possible to trap sufficient back-pressure with zero flow through the choke. A back-pressure pump with a dedicated controller may be used to maintain continuous flow through the choke, and further smoothen out the pressure transients. This approach will require precise coordination between the choke and pump controller and is beyond the scope of this work.

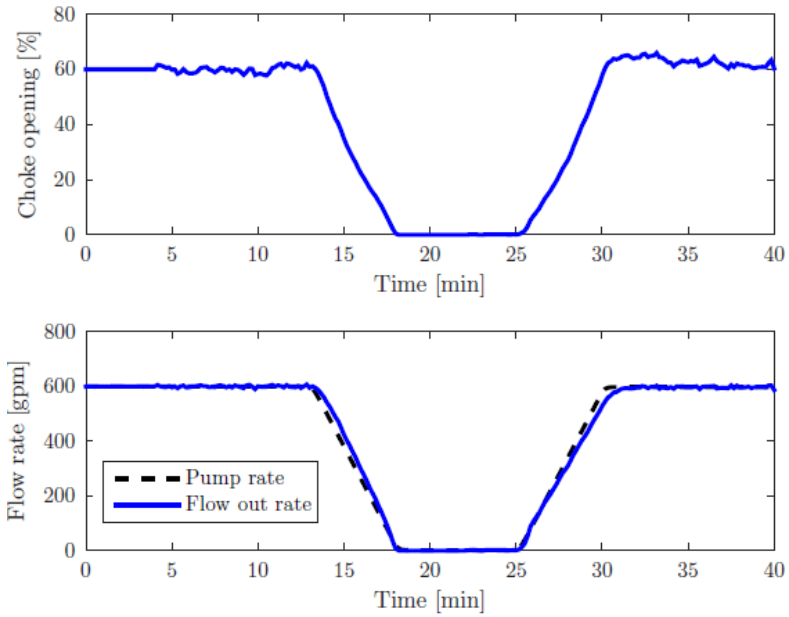

Figure 5.31: Choke opening (upper) and flow rate (lower) for a drill pipe connection scenario. The pump rate is gradually brought down to zero for the connection. Pumping is resumed once the connection is completed. The choke opening is adjusted in synchronization with the change in pump rate.

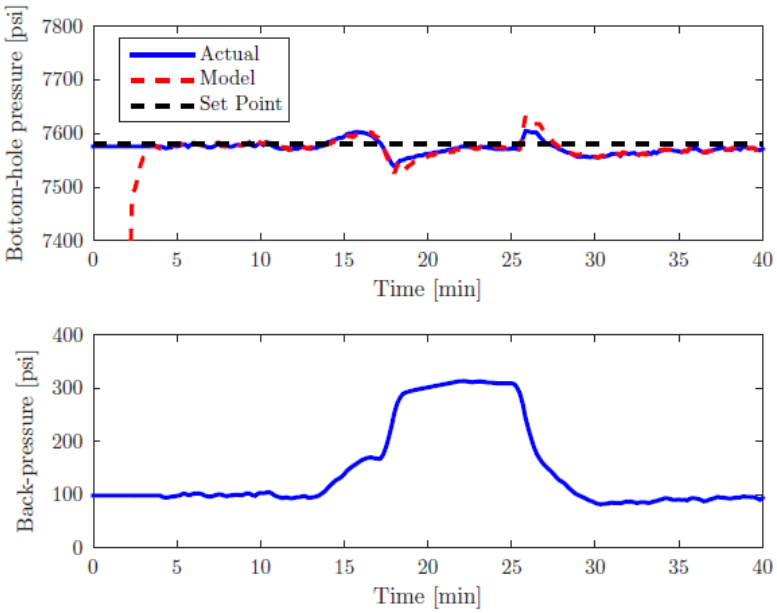

Figure 5.32: BHP (upper) and back-pressure (lower) for a drill pipe connection scenario. The additional back-pressure replaces the annular friction lost as the pump is shut down. The system is capable of maintaining BHP close to the set point throughout the connection procedure.

5.5 Sensitivity of Event Detection System

The previous sections demonstrated the event detection capabilities for scenarios where measurements were only corrupted by noise. It is also important to evaluate how the system performs with poorly calibrated sensors. Simulations for the scenarios in Chapter 5.4.1-5.4.6 with a constant bias of $\pm 10\%$ in the sensors used for the event detection features (standpipe pressure, well head pressure, pump rate, flow out rate, and pit volume) were performed. In each case, the events were considered to be detected when their corresponding probability exceeded the 50 % threshold within a 20-minute window from

the start of the event. The detection times for each of the six events for the different sensor bias cases (assuming one biased sensor at a time) are summarized in Table 5.3. For kick and lost circulation incidents, the gain or loss volumes before detection are also provided in Table 5.4.

The results indicate that the event detection algorithms are the most sensitive to bias in pump rate and flow out rate. For the lost circulation scenario, in particular, a 10% negative bias in pump rate or a 10% positive bias in flow out rate resulted in failure to detect the loss within the 20-minute. Also, for the gas kick, a 10% positive bias in pump rate resulted in 3.5 bbl of pit gain before detection, while a 10% negative bias in flow out yielded a 9.6 bbl pit gain. Since early kick detection is crucial for wells with low kick tolerance, it is important to have properly calibrated flow rate measurements at all times. From Table 5.3 it can be seen that a biased pump rate reading also led to delayed detection of pump efficiency loss and washout incidents. The consequence of this delayed detection may be an increased overshoot in BHP since the controller will now take longer to respond to the event.

In a few scenarios, the event was detected much earlier with a biased sensor than in the baseline case, such as a washout in the case of negative SPP bias. In such circumstances, it may be desirable to wait several minutes before confirming the event, as the bias may lead to difficulties in distinguishing events with similar signatures (such as washout and pump efficiency loss). It may also be possible to utilize a larger threshold for detection in order to avoid potential false alarms.

Table 5.3: Detection times (in minutes) for different events with biased sensor readings. GK = Gas kick, LC = Lost circulation, PC = Plugged choke, PN = Plugged bit nozzle, PE = pump efficiency loss, WO = drill pipe washout. N/A indicates a missed detection instance.

	GK	*LC*	*PC*	*PN*	*PE*	*WO*
Base case (no bias)	0.62	1.38	0.46	0.83	1.04	2.28
SPP -10% bias	0.59	1.73	0.46	1.96	0.87	0.22
SPP +10% bias	0.74	3.51	0.59	0.65	1.91	2.33
WHP -10% bias	0.66	1.54	0.59	0.87	1.15	2.28
WHP +10% bias	0.64	1.61	0.59	0.89	0.9	0.62
Pump rate -10% bias	0.59	N/A	0.59	0.61	6.53	4.1
Pump rate +10% bias	2.25	1.55	0.59	0.61	0.61	0.66
Flow out rate -10% bias	5.63	1.38	0.59	1.30	1.44	2.28
Flow out rate +10% bias	0.65	N/A	0.59	0.8	0.61	1.94
Pit volume -10% bias	0.74	1.65	0.59	0.86	0.9	2.44
Pit volume +10% bias	0.59	1.68	0.59	0.83	0.93	2.24

Table 5.4: Detection volumes (in bbl) for gas kick and lost circulation events with biased sensor readings. N/A indicates a missed detection instance.

	Gas kick	*Lost circulation*
Base case (no bias)	0.73	1.27
SPP -10% bias	0.65	1.62
SPP +10% bias	0.9	2.78
WHP -10% bias	0.78	1.4
WHP +10% bias	0.74	1.54
Pump rate -10% bias	0.65	N/A
Pump rate +10% bias	3.45	1.42
Flow out rate -10% bias	9.57	1.28
Flow out rate +10% bias	0.76	N/A
Pit volume -10% bias	0.91	1.49
Pit volume +10% bias	0.65	1.51

Chapter 6

Conclusions and Recommendations

6.1 Summary and Conclusions

This dissertation presented a novel approach to modeling and control system design for back-pressure MPD operations. To assist with the control design and analysis, a powerful yet simple-to-implement hydraulics model was developed from first principles such as the conservation of mass and momentum for one-dimensional flow in a wellbore. This model, essentially a "reduced" Drift-Flux model, consists of a set of partial and ordinary differential equations governing the gas dynamics and the pressure dynamics in the well during MPD operations. The model captures essential two-phase dynamics during a gas kick with less numerical complexity compared to high-fidelity simulators. It allows for a fast, explicit numerical solution scheme, which is suitable for real-time implementation in automatic control and estimation applications. The model can handle gas solubility in drilling fluids, real gas behavior, non-Newtonian (Yield-Power Law) fluid properties, and wellbore deviation. Variables predicted by the model include real-time annular pressure profiles, liquid and gas (free and dissolved) hold-up, effective mud compressibility, gas rise velocities, liquid and gas flow out rates and total mud volume.

The reduced DFM was successfully validated on a couple of MPD kick scenarios generated with a high-fidelity multi-phase hydraulics simulator, yielding close agreement for pressure and flow out predictions compared to the simulator results, and also for predictions of the gas volume fractions at different instants following the kick. The model was also applied to an experimental data set from a test well, where a kick was simulated through controlled gas injection. Very good agreement was observed between the measured and the modeled surface back-pressure and pit gain, as well as between the BHP predicted by the model and the value derived from the SPP measurements.

Several approaches to MPD choke control were explored in this dissertation, utilizing elements of model-based control design and robustness considerations. One of them used the feedback linearization technique to cancel the non-linearity in the choke model, which determines how the actuation enters the system. The feedback linearizing control law was expanded to include two-phase flow through the choke. It also included feedforward terms relating to the gas expansion in a two-phase scenario. Two separate control modes were designed: pressure control, aimed at tracking a pressure set point, and flow control, designed to balance flow into the well with flow out of the well during a kick or lost circulation incident. It was shown through theoretical analysis and simulations that the flow controller was able to halt influxes and losses. One of the disadvantages of the feedback linearization approach is the uncertainty at low frequencies, particularly when actuation and measurement dynamics come into play, and also its dependency on high quality

back-pressure measurements.

A different control design approach used a linearized first-order model of the pressure dynamics in the annulus, where the choke actuation was mapped to the control input in a manner that simplifies algebraic manipulation. The time constant of this approximated model was found to depend on the equilibrium back-pressure state, and also on the compressibility (bulk modulus) of the drilling fluid, which varies with the amount of free gas in the well. An attempt was also made to characterize the modeling error resulting from the high-frequency dynamics, which were discarded by the first-order approximation. It was determined that a multiplicative norm-bounded uncertainty can adequately capture the high-frequency effects, and an appropriate error bound was selected.

Using the approximated first-order model, two gain-scheduled, second-order state feedback controllers were designed. The first one used Linear Quadratic Gaussian design, with the control and estimation gains explicitly dependent on the first-order system time constant. Estimation of the time constant for the two-phase case was performed using the effective bulk modulus predicted by the reduced DFM. The other design used LMIs to minimize the L_2 gain from a disturbance to the integrated tracking error. For this purpose, the state space was cast as a polytope defined by lower and upper bounds on the time constant and uncertainty in its estimation. A time-varying gain expressed as a function of the time constant was also added to the LMI-based controller to improve performance.

The three different control designs were tested in a variety of single-phase and two-phase (gas kick) scenarios, showing improved robustness compared to a conventional PI design with a fixed tuning. The LMI-based design proved to be the most effective at handling both single and two-phase flow, even in the presence of measurement delays, low sampling rates, sudden changes in pump rate, or rapid gas expansion at the choke, as demonstrated in a series of simulations conducted with a high-fidelity hydraulics simulator to which the different control algorithms were applied. It should be noted that feedback linearization and LQG controllers for MPD choke control were proposed before. However, these techniques had not been coupled with a two-phase model providing real-time estimates of fluid compressibility, which allows for adaptive gain scheduling. Meanwhile, the LMI-based controller represents a novel application for choke control in MPD.

The last portion of this dissertation augmented the MPD choke control system with event detection and observers for parameter estimation during a variety of degrading system conditions. The event detection system, capable of identifying kick, lost circulation, plugged choke or bit nozzle, mud pump degradation and drillstring washout incidents, consists of a Bayesian Network model, which fuses real-time data and predictions from the hydraulics model while encompassing process and measurement uncertainty through Conditional Probability Tables. The probabilistic representation ensures that the event detection method is robust to sensor noise and biased measurements, which is an improvement over the event detection methods currently used in

the industry. A sensitivity study with biased sensor readings revealed that pump rate and flow out rate had the largest impact on the detection times for the incidents investigated in this study.

The observers, designed using Recursive Least Squares and Lyapunov analysis techniques, allow for real-time estimation of pore pressure, fracture pressure, influx and lost circulation rates, reservoir productivity index, mud pump efficiency, choke flow area, and bit nozzle area. The full system was tested in different simulated cases with induced system faults. For each scenario, the system was able to hold the BHP close to the specified target, and correctly detect and respond to any adverse conditions in a timely manner.

6.2 Recommendations

6.2.1 Field Implementation

The control algorithms designed as part of this dissertation have so far been validated only using high-fidelity simulation software. The next step in this research project is to evaluate the feasibility for field implementation and integrate the system on an actual drilling rig with ongoing MPD operations. Figure 6.1 illustrates a possible system architecture. The algorithms will be programmed into a multi-threaded software platform. The software will connect to real-time data streams (e.g using the Wellsite Information Transfer Specification (WITS) or Wellsite Information Transfer Standard Markup Language (WITSML) formats), and also to other contextual data sources (e.g. daily reporting and well planning software) through separate reader threads.

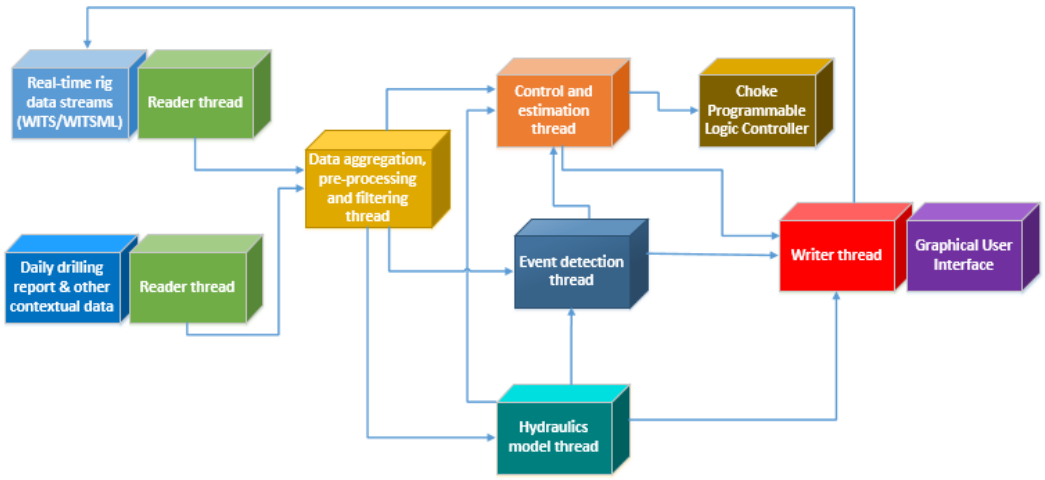

Figure 6.1: Proposed software architecture for field implementation. A multi-threaded application reads real-time drilling data and daily report data. The data channels are pre-processed before being sent to the controller, event detection and hydraulics model threads at a common sampling rate (1 Hz or higher). The controller thread sends the choke position command to the rig site programmable logic controllers. The outputs of the controller, event detection and modeling threads are supplied to the real-time rig data streams and also to a graphical user interface.

Since drilling rig data arrives at different frequencies (real-time data every 1, 5 or 10 seconds, drilling report data once or twice day, typically), a data aggregation thread needs to merge all this data and apply pre-processing (e.g. outlier removal, quality check, bias/drift correction etc.) and filtering algorithms. From there, the processed inputs are sent to the control and estimation, event detection and modeling threads at a common sampling rate (1 Hz or better). Each of these threads should communicate with each other. The outputs are then sent to a common writer thread which organizes them in a standardized format (e.g. WITS/WITSML) and then sends them back

into the real-time data stream. It also sends the information to a graphical user interface or other visualization software. The choke position command computed by the controller thread at every time instant should be sent to the low-level choke controllers, using the available data communication protocols.

6.2.2 Tuning and Validation

Once integrated in a field or experimental rig setting, the system should be run in open-loop mode first to ensure all parameters are calibrated. The plant transfer function can be identified using a series of step response and impulse response tests, or using the approximated first-order model detailed in Chapter 4. Any communication delays and lags due to low-pass filtering should be quantified in this phase, to ensure that these delays do not reduce the phase margins too much. Next, the control gains may be tuned off-line, based on the plant model, to give a first pass control design. A set of experiments should be conducted with the closed-loop system, and the performance evaluated, using similar scenarios to those proposed in Chapters 4 and 5. If deployed on an offshore rig, additional testing should be done under heave conditions, to ensure that the control response remains stable.

The hydraulics model outputs should be recorded and compared with actual measurements. A BHP sensor and suitable telemetry systems (e.g. wired drill pipe) should be used, if available, to ensure that the pressure profile reported by the model is consistent with actual data. Finally, the event detection design parameters (Bayesian network CPT) and thresholds should

also be tuned to ensure quick detection and minimal false and missed alarms. Ideally, the CPTs could be learned from actual data, provided that data from faulty conditions is sufficiently well represented versus normal operation data, in order to prevent over-fitting the model.

6.3 Further Work

Aside from field implementation of the control algorithms and further model validation, handling of additional fault scenarios (annular pack-off, borehole enlargement, RCD failure, sensor drift or bias, etc.) may be possible, as well as simulating multiple faults occurring simultaneously (e.g. loss of pump efficiency during a kick or lost circulation event). Implementing additional control laws for main pump and/or back-pressure pump control, and ensuring smooth coordination with the choke controller may be another area of further work.

On the modeling front, additional research can be done to extend the reduced DFM applicability to underbalanced drilling, Pressurized Mud Cap Drilling, or Managed Pressure Cementing operations. The formulation should be expanded to include multiple gas and liquid phases, solid phases (e.g. drill cuttings), and more detailed PVT data representations. Also, heat transfer and thermal modeling could be added by including the energy balance. Other applications, such as modeling of heave effects, or swab/surge pressure prediction during drill pipe hoisting and lowering could also be pursued.

Appendices

Appendix A

List of Symbols and Abbreviations

A.1 Symbols

Symbol	Description	Unit
A	Wellbore cross-sectional area	m^2
A_d	Drill pipe cross-sectional area	m^2
A_b	Total bit nozzle flow area	m^2
A_c	Choke orifice area	m^2
B_o	Oil formation volume factor	
c_G	Speed of sound in gas	m/s
c_L	Speed of sound in liquid	m/s
C_0	Slip law profile parameter	
C_b	Bit nozzle flow area coefficient	m^{-4}
C_d	Bit discharge coefficient	
C_K	Factor in choke model linearization	
C_v	Choke area coefficient	m^2
$C(s)$	Controller transfer function	
D	Wellbore diameter	m
D_d	Drill pipe inner diameter	m
D_h	Hydraulic diameter	m
D_i	Annulus inner diameter	m
D_o	Annulus outer diameter	m
e_p	Pressure tracking error	Pa
$E_G(x,t)$	Free gas expansion term	$1/s$
f	Friction factor	
g	Gravitational acceleration	m/s^2
$G(s)$	Transfer function	
h	True vertical depth	m
I_0, I_1	Convenience variables in influx observer	

Symbol	Description	Unit
I_v	Integral in gas velocity equation	
J	Reservoir productivity index	$m^3/s/Pa$
k_{frac}	Fracture fluid loss index	$m^3/s/Pa$
k_i	Integral gain	
k_p	Proportional gain	
K	Drilling fluid consistency index	$Pa \cdot s^m$
K_p,K_u	Choke model linearization coefficients	
L	Well measured depth	m
m	Drilling fluid power-law index	
M	Fluid inertia	kg/m^4
N	Generalized fluid behavior index	
$P(s)$	Plant transfer function	
$P_n(s)$	Nominal plant transfer function	
$P(x,t)$	Annular pressure	Pa
p_0	Choke downstream pressure	Pa
p_{bit}	Bit pressure drop	Pa
p_{bh}	Bottom-hole pressure	Pa
p_{bh}^{ref}	Bottom-hole pressure set point	Pa
p_c	Surface back-pressure	Pa
p_{dd}	Pressure draw-down	Pa
p_f	Frictional pressure drop	Pa
p_{frac}	Formation fracture pressure	Pa
p_g	Hydrostatic pressure	Pa
p_p	Standpipe pressure	Pa
p_{res}	Reservoir pressure	Pa
q_{bit}	Bit volumetric flow rate	m^3/s
q_c	Choke volumetric flow rate	m^3/s
q_{frac}	Reservoir volumetric flow rate	m^3/s
q_G	Gas volumetric flow rate	m^3/s
$q_{G,c}$	Gas volumetric flow rate at choke	m^3/s
q_L	Liquid volumetric flow rate	m^3/s
$q_{L,c}$	Liquid volumetric flow rate at choke	m^3/s
q_{res}	Reservoir volumetric flow rate	m^3/s
q_p	Mud pump volumetric flow rate	m^3/s
R_G	Ideal gas constant	$J/(kg \cdot K)$

Symbol	Description	Unit
R_s	Gas/oil solubility ratio	
S	Source term in momentum balance equation	Pa/m
s	Laplace variable	
t	Time	s
T	Wellbore temperature	K
T_{ex}	Total gas expansion rate	m^3/s
T_{E_G}	Integral of gas velocity gradient	m^3/s
u	Control input	
u_d	Derivative of control input	
$v_G(x,t)$	Gas velocity	m/s
$v_m(x,t)$	Mixture velocity	m/s
$v_L(x,t)$	Liquid velocity	m/s
v_∞	Slip velocity	m/s
$\mathbf{V}$	Lyapunov function	
V_a	Annulus volume	m^3
V_d	Drillstring volume	m^3
V_G	Total gas volume	m^3
w	Process disturbance	
w_c	Choke mass flow rate	kg/s
x	Position along well measured depth	m
Y	Choke gas expansion factor	
Z	Choke opening	
$Z_c(s)$	Characteristic line impedance	
Z_G	Gas compressibility factor	
α_G	Gas volume fraction	
α_L	Liquid volume fraction	
α_L^*	Alternate notation for slip law profile parameter	
$\bar{\beta}$	Effective drilling fluid bulk modulus	Pa
β_L	Liquid bulk modulus	Pa
γ	Gas adiabatic constant	
$\bar{\gamma}$	Correction factor for gas compressibility	
$\Gamma(s)$	Propagation operator in transmission line model	
Γ_D	Mass transfer between gas and liquid	$kg/m^3/s$
Γ_G	Gas mass source term per unit volume	$kg/m^3/s$

Symbol	Description	Unit
Γ_L	Liquid mass source term per unit volume	$kg/m^3/s$
Γ_G^*	Normalized gas mass source term	$1/s$
Γ_L^*	Normalized liquid mass source term	$1/s$
η	Mud pump volumetric efficiency	
θ	Well inclination (measured from vertical)	rad
ρ_G	Density of free gas	kg/m^3
ρ_G^*	Density of dissolved gas	kg/m^3
$\rho_{G,sat}^*$	Dissolved gas saturation threshold	kg/m^3
$\rho_{G,sc}$	Gas density at standard conditions	kg/m^3
ρ_m	Mixture density	kg/m^3
ρ_L	Liquid density	kg/m^3
τ	Time constant	s
τ_w	Shear stress at pipe wall	Pa
τ_y	Drilling fluid yield stress	Pa
ν	Measurement noise	
χ_G	Gas mass fraction	
χ_L	Liquid mass fraction	

A.2 Abbreviations

BHA	Bottom-Hole Assembly
BHP	Bottom-Hole Pressure
BLUT	Base Look-Up Table
BOP	Blow-Out Preventer
CBHP	Constant Bottom-Hole Pressure
CCS	Confined Compressive Strength
CPD	Conditional Probability Distribution
CPT	Conditional Probability Table
DAPC	Dynamic Annular Pressure Control
DFM	Drift-Flux Model
DLUT	Derived Look-Up Table
DSATS	Drilling Systems Automation Technical Section
ECD	Equivalent Circulating Density
ERD	Extended Reach Drilling
HPHT	High-Pressure High-Temperature
HSI	Hydraulic Horsepower per Square Inch
HWDP	Heavy Weight Drill Pipe
IADC	International Association of Drilling Contractors
ID	Inner Diameter
LDI	Linear Differential Inclusion
LMI	Linear Matrix Inequality
LTI	Linear Time-Invariant
LQG	Linear Quadratic Gaussian
LUT	Look-Up Table
MD	Measured Depth
MPC	Model Predictive Control
MPD	Managed Pressure Drilling
MSE	Mechanical Specific Energy
MWD	Measurement While Drilling
NM	Non-Magnetic
OBM	Oil-Based Mud
OD	Outer Diameter
ODE	Ordinary Differential Equation
PDC	Polycrystalline Diamond Compact

PDE	Partial Differential Equation
PI	Proportional-Integral
PID	Proportional-Integral-Derivative
PVT	Pressure-Volume-Temperature
PWD	Pressure While Drilling
RCD	Rotating Control Device
RLS	Recursive Least Squares
ROP	Rate of Penetration
RPM	Revolutions Per Minute
SBM	Synthetic-Based Mud
SPE	Society of Petroleum Engineers
SPM	Strokes Per Minute
SPP	Standpipe Pressure
STRS	Soft Torque Rotary System
TVD	True Vertical Depth
UBD	Underbalanced Drilling
UCS	Unconfined Compressive Strength
WBM	Water-Based Mud
WDP	Wired Drill Pipe
WHP	Well Head Pressure
WOB	Weight on Bit
WITS	Wellsite Information Transfer Specification
WITSML	Wellsite Information Transfer Standard Markup Language
XO	Cross-Over
YPL	Yield Power Law

Appendix B

Numerical Scheme for Reduced Drift-Flux Model

The reduced DFM equations are discretized using an explicit algorithm consisting of a first-order upwind scheme in space and the forward Euler method in time. We will denote the cell index $i = 1, 2, .., N$ and the time index $k = 1, 2, ..$ For free gas, we have:

$$\frac{\alpha_G(i,k+1) - \alpha_G(i,k)}{\Delta t} + max(v_G(i,k),0)\frac{\alpha_G(i,k) - \alpha_G(i-1,k)}{\Delta x} + min(v_G(i,k),0)\frac{\alpha_G(i+1,k) - \alpha_G(i,k)}{\Delta x} = E_G(i,k) + \frac{c_G^2(i,k)(1 - C_0\alpha_G(i,k))(\Gamma_G(i,k) - \Gamma_D(i,k))}{\bar{\gamma}P(i,k)} - \frac{C_0\alpha_G(i,k)(\Gamma_L(i,k) + \Gamma_D(i,k))}{\rho_L} \tag{B.1}$$

where

$$E_G(i,k) = -\frac{\alpha_G(i,k)(1 - C_0\alpha_G(i,k))}{\bar{\gamma}(i,k)P(i,k)}\Big(\frac{\Delta p_c(k)}{\Delta t} + v_G(i,k)S(i,k)\Big), \tag{B.2}$$

$$S(i,k) = -\Big(\rho_L\alpha_L(i,k) + \frac{P(i,k-1)}{Z_G(i,k-1)R_GT(i)}\alpha_G(i,k)\Big)\Big[gcos(\theta(i)) + \frac{2f(q_G(k) + q_L(k))^2}{A^2D}\Big], \tag{B.3}$$

$$\bar{\gamma}(i,k) = \gamma\Big[1 - \rho_G(i,k)R_GT(i)\Big(\frac{\Delta Z_G(i,k)}{\Delta P(i,k)}\Big)\Big]^{-1}, \tag{B.4}$$

$$\Gamma_D(i,k) = \begin{cases} \Gamma_{D0}(i,k) & \rho_G^*(i,k) \geq \rho_{G,sat}^*(i,k) \\ 0 & \rho_G^*(i,k) < \rho_{G,sat}^*(i,k) \end{cases} \tag{B.5}$$

with

$$\Gamma_{D0}(i,k) = \frac{\rho_L}{\rho_L - \rho^*_{G,sat}(i,k)}\Big[\alpha_L(i,k)\Big(\frac{\partial \rho^*_{G,sat}(i,k)}{\partial t} + v_L(i,k)\frac{\partial \rho^*_{G,sat}(i,k)}{\partial x}\Big) + \frac{\rho^*_{G,sat}(i,k)\Gamma_L(i,k)}{\rho_L}\Big] \tag{B.6}$$

Note that in Eq. B.4 we have use the gas equation of state evaluated using pressure P and the compressibility factor $Z_G(P)$ at the previous time point to calculate the gas density ρ_G. This is done in order to avoid having to implicitly solve for pressure, which requires an iterative scheme, such as the Newton-Raphson method. The gas velocity profile is calculated using

$$v_G(i,k) = e^{-I_v(i,k)}\Big(v_G(1,k) + C_0\sum_{\xi=1}^{i}\Big[\frac{c_G^2(\xi,k)}{\bar{\gamma}(\xi,k)P(\xi,k)}(\Gamma_G(\xi,k) - \Gamma_D(\xi,k)) + \frac{\Gamma_L(\xi,k) + \Gamma_D(\xi,k)}{\rho_L}\Big]e^{I_v(\xi,k)}\Delta x\Big), \tag{B.7}$$

$$I_v(i,k) = \sum_{\xi=1}^{i}\frac{C_0\alpha_G(\xi,k)}{\bar{\gamma}(\xi,k)P(\xi,k)}S(\xi,k)\Delta x \tag{B.8}$$

$$v_G(1,k) = \frac{C_0}{A}\Big(q_G(k) + q_L(k)\Big) + v_\infty, \tag{B.9}$$

and the annular pressure profile is given by:

$$P(i,k) = p_c(k) - \sum_{\xi=i}^{N} S(\xi,k)\Delta x \tag{B.10}$$

For dissolved gas below the saturation limit ($\rho^*_G(i,k) < \rho^*_{G,sat}(i,k)$), we have:

$$\frac{\rho^*_G(i,k+1) - \rho^*_G(i,k)}{\Delta t} + max(v_L(i,k),0)\frac{\rho^*_G(i,k) - \rho^*_G(i-1,k)}{\Delta x} + min(v_L(i,k),0)\frac{\rho^*_G(i+1,k) - \rho^*_G(i,k)}{\Delta x} = \Gamma_G(i,k) - \frac{\rho^*_G(i,k)}{\rho_L}(\Gamma_L(i,k) + \Gamma_G(i,k)) \tag{B.11}$$

where

$$v_L(i,k) = v_L(1,k) + \sum_{\xi=1}^{i} \frac{\Gamma_L(\xi,k) + \Gamma_G(\xi,k)}{\rho_L} \Delta x \tag{B.12}$$

The boundary conditions for Eqs. B.1 and B.11 are:

$$\alpha_G(1,k) = \frac{q_G(k)}{A v_G(1,k)}, \tag{B.13}$$

$$\rho_G^*(1,k) = \frac{\rho_L q_L(k) q_G(k)}{q_L(k) + q_G(k)} \tag{B.14}$$

We solve for α_G and ρ_G^* at each grid cell using Eqs. B.1 and B.11, then update $\rho_{G,sat}^*(i,k) = \rho_{G,sc} \frac{R_s(i,k)}{B_o(i,k)}$ and set $\rho_G^*(i,k) = min(\rho_G^*(i,k), \rho_{G,sat}^*(i,k))$ and $\alpha_G(i,k) = 0$ for all cells that have $\rho_G^*(i,k) < \rho_{G,sat}^*(i,k)$. To update the back-pressure p_c we use the explicit Euler method:

$$\frac{p_c(k+1) - p_c(k)}{\Delta t} = \frac{\bar{\beta}(k)}{V_a} \Big[q_L(k) + q_G(k) - q_c(k) + T_{ex}(k) \Big] \tag{B.15}$$

where

$$\bar{\beta}(k) = \frac{\beta_L}{1 + \frac{\beta_L}{V_a} \sum_{\xi=1}^{N} \frac{C_0 \alpha_G(\xi,k)}{\bar{\gamma}(\xi,k) P(\xi,k)} A \Delta x}, \tag{B.16}$$

$$T_{ex}(k) = \sum_{\xi=1}^{N} \Big[- \frac{C_0 \alpha_G(i,k)}{\bar{\gamma}(i,k) P(i,k)} v_G(i,k) S(i,k) + \frac{c_G^2(i,k) (\Gamma_G(i,k) - \Gamma_D(i,k))}{\bar{\gamma}(i,k) P(i,k)} + \frac{\Gamma_L(i,k) + \Gamma_D(i,k)}{\rho_L} \Big] A \Delta x. \tag{B.17}$$

Appendix C

Frictional Pressure Loss Calculations for Yield-Power Law Fluids

A Yield-Power Law (YPL) fluid is characterized by the following relationship between shear stress (τ) and shear rate ($\dot{\gamma}$) (Kelessidis et al., 2011):

$$\tau = \tau_y + K\dot{\gamma}^m \tag{C.1}$$

where τ_y is the yield stress, K is the consistency index and m is the power-law index (fluid behavior index). For a Bingham plastic fluid ($m = 1$), K is typically referred to as the plastic viscosity. The apparent viscosity of a YPL fluid is given by:

$$\mu_a = \frac{\tau_w}{\left(\frac{\tau_w - \tau_y}{K}\right)^{1/m}} \tag{C.2}$$

with τ_w denoting shear stress at the pipe wall. For flow inside the pipe, τ_w can be computed from (Vajargah and van Oort, 2015):

$$\frac{8v_m}{D_d} = \frac{(\tau_w - \tau_y)^{\frac{1+m}{m}}}{K^{1/m}\tau_w^3}\frac{4m}{3m+1}\left(\tau_w^2 + \frac{2m\tau_y\tau_w}{1+2m} + \frac{2m^2\tau_y^2}{(1+m)(1+2m)}\right) \tag{C.3}$$

where D_d is the drill pipe inner diameter. For annular flow, we get τ_w by solving (Kelessidis et al., 2011):

$$\frac{12v_m}{D_o - D_i} = \frac{(\tau_w - \tau_y)^{\frac{1+m}{m}}}{K^{1/m}\tau_w^2}\frac{3m}{2m+1}\left(\tau_w + \frac{m\tau_y}{1+m}\right) \tag{C.4}$$

with D_o and D_i being the annulus outer and inner diameters, respectively. Next, we compute the Reynolds number:

$$Re = \frac{\rho_m v_m D_h}{\mu_a} \tag{C.5}$$

where D_h is the hydraulic diameter. For pipe flow, we have:

$$D_h = \frac{4N}{1+3N} D_d \tag{C.6}$$

$$\frac{4N}{1+3N} = \frac{4m}{3m+1}\Big(1 - \frac{\tau_y}{\tau_w}\Big)\Big(1 + \frac{2m}{1+2m}\frac{\tau_y}{\tau_w} + \frac{2m^2}{(1+m)(1+2m)}\frac{\tau_y^2}{\tau_w^2}\Big) \tag{C.7}$$

For flow in the annulus, the hydraulic diameter is given by:

$$D_h = \frac{3N}{1+2N}(D_o - D_i) \tag{C.8}$$

$$\frac{3N}{1+2N} = \frac{3m}{2m+1}\Big(1 - \frac{\tau_y}{\tau_w}\Big)\Big(1 + \frac{m}{1+m}\frac{\tau_y}{\tau_w}\Big) \tag{C.9}$$

Finally, we can calculate the friction factor f, based on the flow regime (laminar or turbulent). For laminar flow, we have:

$$f = \begin{cases} \frac{16}{Re}, & pipeflow \\ \frac{24}{Re}, & annularflow \end{cases}, \tag{C.10}$$

while for turbulent flow, we can compute f by solving the equation (Dodge and Metzner, 1959):

$$\frac{1}{f^{0.5}} = \frac{4}{N^{0.75}} log_{10}[f^{1-N/2} Re] - \frac{0.395}{N^{1.2}}. \tag{C.11}$$

Laminar flow occurs up to $Re = 3250 - 1150N$, while turbulent flow happens above $Re = 4150 - 1150N$. For Reynolds numbers between the two values, we can interpolate between the laminar and turbulent friction factors.

Once f is determined, the frictional pressure loss per unit length of pipe (or annulus) can be calculated as

$$\frac{\partial p_f}{\partial x} = \begin{cases} \frac{2f\rho_m v_m^2}{D_d}, & pipeflow \\ \frac{2f\rho_m v_m^2}{D_o - D_i}, & annularflow \end{cases} \tag{C.12}$$

and the total frictional pressure loss is given by

$$p_f = \int_0^L \frac{\partial p_f}{\partial x} \mathrm{d}x. \tag{C.13}$$

Appendix D

Derivation of Linear Matrix Inequality in Chapter 4

We start by defining the $\mathbf{L}_2$ gain: $\gamma \equiv \sup_{\|w\|_2 \neq 0} \frac{\|z\|_2}{\|w\|_2}$ and the Lyapunov function $V(x) = x^T P x$ with $P > 0$ satisfying (Boyd et al., 1994):

$$\dot{V}(x) + z^T z - \gamma^2 w^T w \leq 0 \tag{D.1}$$

For the norm-bound LDI with the state feedback $u = Kx$:

$$\dot{x} = (A + B_u K)x + B_w w + B_p p, \tag{D.2}$$

$$q = (C_q + D_{qu} K)x + D_{qp} p, \tag{D.3}$$

$$z = C_z x \tag{D.4}$$

$$p = \Delta(t) q, \quad |\Delta(t)| \leq 1, \tag{D.5}$$

we have:

$$\begin{aligned} \dot{V}(x) = x^T[(A^T + K^T B_u^T)P + P(A + B_u K)]x + x^T P B_w w \\ + w^T B_w^T P x + x^T P B_p p + p^T B_p^T P x \end{aligned} \tag{D.6}$$

which, substituted in D.1, together with $z^T z = x^T C_z^T C_z x$, gives:

$$\begin{aligned} x^T[(A^T + K^T B_u^T)P + P(A + B_u K) + C_z^T C_z]x + x^T P B_w w \\ + w^T B_w^T P x + x^T P B_p p + p^T B_p^T P x - \gamma^2 w^T w \leq 0 \end{aligned} \tag{D.7}$$

Setting $w = 0$ in D.7 gives:

$$\begin{bmatrix} x \\ p \end{bmatrix}^T \begin{bmatrix} (A^T + K^T B_u^T)P + P(A + B_u K) + C_z^T C_z & PB_p \\ B_p^T P & 0 \end{bmatrix} \begin{bmatrix} x \\ p \end{bmatrix} \leq 0 \qquad \text{(D.8)}$$

The condition $p = \Delta(t)q, |\Delta(t)| \leq 1$ implies that

$$p^T p \leq q^T q \qquad \text{(D.9)}$$

$$\begin{aligned} \implies p^T(1 - D_{qp}^T D_{qp})p &\leq x^T(C_q + D_{qu}K)^T(C_q + D_{qu}K)x \\ &+ x^T(C_q + D_{qu}K)^T D_{qp}p + p^T D_{qp}^T(C_q + D_{qu}K)x \end{aligned} \qquad \text{(D.10)}$$

or, in matrix notation,

$$\begin{bmatrix} x \\ p \end{bmatrix}^T \begin{bmatrix} -(C_q + D_{qu}K)^T(C_q + D_{qu}K) & -(C_q + D_{qu}K)^T D_{qp} \\ -D_{qp}^T(C_q + D_{qu}K) & I - D_{qp}^T D_{qp} \end{bmatrix} \begin{bmatrix} x \\ p \end{bmatrix} \leq 0. \qquad \text{(D.11)}$$

Using the S-procedure (Boyd et al., 1994) gives the LMI, with $\lambda > 0$:

$$\begin{bmatrix} \begin{pmatrix} (A^T + K^T B_u^T)P + P(A + B_u K) + C_z^T C_z \\ +\lambda(C_q + D_{qu}K)^T(C_q + D_{qu}K) \end{pmatrix} & PB_p + \lambda(C_q + D_{qu}K)^T D_{qp} \\ B_p^T P + \lambda D_{qp}^T(C_q + D_{qu}K) & -\lambda(I - D_{qp}^T D_{qp}) \end{bmatrix} \leq 0, \qquad \text{(D.12)}$$

or, equivalently, using $Q = P^{-1}$, $Y = KQ$, and $\mu = 1/\lambda$

$$\begin{bmatrix} QA^T + AQ + Y^T B_u^T + B_u Y + C_z^T C_z + \mu B_p B_p^T & \mu B_p D_{qp}^T + QC_q^T + Y^T D_{qu}^T \\ \mu D_{qp} B_p^T + C_q Q + D_{qu} Y & -\mu(I - D_{qp} D_{qp}^T) \end{bmatrix} \leq 0. \qquad \text{(D.13)}$$

Augmenting D.13 with the inequalities involving w in D.7 yields the LMI:

$$\begin{bmatrix} \begin{pmatrix} AQ + QA^T \\ +B_u Y + Y^T B_u^T \\ +B_w B_w^T + \mu B_p B_p^T \end{pmatrix} & QC_z^T & \mu B_p D_{qp}^T + QC_q^T + Y^T D_{qu}^T \\ C_z Q & -\gamma^2 I & 0 \\ \mu D_{qp} B_p^T + C_q Q + D_{qu} Y & 0 & -\mu(I - D_{qp} D_{qp}^T) \end{bmatrix} \leq 0 \qquad \text{(D.14)}$$

Appendix E

Publications

E.1 Journal Publications

1. E. Cayeux, R. Shor, A. Ambrus, P. Pournazari, P. Ashok, and E. van Oort. **From Laboratory Scale Drilling to ERD Wells: How Scale affects Drillability and the Management of Drilling Incidents**. Journal of Petroleum Science and Engineering, *In Review*.

2. U.J.F. Aarsnes, B. Açikmeşe, A. Ambrus, O.M. Aamo. **Robust controller design for automated kick handling in managed pressure drilling**. Journal of Process Control, Volume 47, November 2016, Pages 46-57.

3. U.J.F. Aarsnes, A. Ambrus, F. Di Meglio, A. Karimi Vajargah, O.M. Aamo, and E. van Oort. **A simplified two-phase flow model using a quasi-equilibrium momentum balance**. International Journal of Multiphase Flow, Volume 83, July 2016, Pages 77-85.

4. A. Ambrus, U.J.F. Aarsnes, A. Karimi Vajargah, B. Akbari, E. van Oort, and O.M. Aamo. **Real-time estimation of reservoir influx rate and pore pressure using a simplified transient two-phase**

flow model. Journal of Natural Gas Science and Engineering, Volume 32, May 2016, Pages 439-452.

E.2 Conference Publications

1. A. Ambrus, A. Karimi Vajargah, P. Ashok and E. van Oort. **Choke Controller Design for Automated Managed Pressure Drilling with Realistic Operational System Conditions**. AADE National Technical Conference and Exhibition, April 2017.

2. Z. Ma, A. Karimi Vajargah, A. Ambrus, P. Ashok, D. Chen, E. van Oort, R. May, D. Curry, J. Macpherson, and G. Becker. **A Comprehensive Hydraulic Software Package for Drilling Operations**. AADE National Technical Conference and Exhibition, April 2017.

3. Z. Ma, A. Karimi Vajargah, A. Ambrus, P. Ashok, D. Chen, E. van Oort, R. May, J. Macpherson, G. Becker, and D. Curry. **Multi-Phase Well Control Analysis During Managed Pressure Drilling Operations**. SPE Annual Technical Conference and Exhibition, September 2016.

4. A. Ambrus, U.J.F. Aarsnes, A. Karimi Vajargah, B. Akbari and E. van Oort. **A Simplified Transient Multi-Phase Model for Automated Well Control Applications**. International Petroleum Technology Conference, December 2015.

5. U.J.F. Aarsnes, A. Ambrus, A. Karimi Vajargah, O.M. Aamo, and E. van Oort. **A Simplified Gas-Liquid Flow Model for Kick Mitigation and Control During Drilling Operations**. ASME Dynamic Systems and Control Conference, October 2015.

6. A. Ambrus, P. Pournazari, P. Ashok, R. Shor, and E. van Oort. **Overcoming Barriers to Adoption of Drilling Automation: Moving Towards Automated Well Manufacturing**. SPE/IADC Drilling Conference and Exhibition, March 2015.

7. A. Ambrus, P. Ashok, and E. van Oort. **Drilling Rig Sensor Data Validation in the Presence of Real-Time Process Variations**. SPE Annual Technical Conference and Exhibition, October 2013.

8. P. Ashok, A. Ambrus, and E. van Oort. **Automatic Sensor Data Validation: Improving the Quality and Reliability of Rig Data**. SPE Digital Energy Conference, March 2013.

Appendix F

Paper SPE/IADC 173164-MS[1]

[1]This appendix contains the publication: Adrian Ambrus, Parham Pournazari, Pradeepkumar Ashok, Roman Shor, and Eric van Oort. "Overcoming Barriers to Adoption of Drilling Automation: Moving Towards Automated Well Manufacturing". SPE/IADC Drilling Conference and Exhibition, March 2015. The author of this dissertation made substantial contributions, particularly on the theoretical development, compilation of data for the look-up tables required for the control algorithms, and their implementation on simulated Managed Pressure Drilling scenarios.


SPE/IADC-173164-MS

Overcoming Barriers to Adoption of Drilling Automation: Moving Towards Automated Well Manufacturing

Adrian Ambrus, Parham Pournazari, Pradeepkumar Ashok, Roman Shor, Eric van Oort, The University of Texas at Austin

This paper was prepared for presentation at the SPE/IADC Drilling Conference and Exhibition held in London, United Kingdom, 17–19 March 2015.

Abstract

There has been a growing interest in automated drilling in the recent decade, motivated primarily by increased well construction efficiency, enhanced safety and well quality requirements. Many drilling tasks have been successfully automated and pilot technologies have been deployed, but broader adoption has remained slow. This can be attributed to some key factors. First, no two wells or rigs are the same. So the concept of "developing one algorithm applicable to all scenarios" is difficult except in the simplest of cases where only a limited set of tightly integrated sensors and actuators are involved. Secondly, full automation requires cohesive data and information integration between multiple stakeholders: the operator, the service provider, the drilling contractor and the equipment manufacturer. No efficient mathematical construct has been adopted for integrating data / information from these different stakeholders. Thirdly, any drilling automation task requires the full buy-in of the drilling crew, which is often difficult when these algorithms are presented as black-box solutions and it is unclear how to bring the rig to a safe condition when automation fails.

A mathematical construct, and the methodology / architecture is presented that would enable one to combine information and data from multiple sources in a meaningful way and the rapid development of intuitive control algorithms that can be easily understood without advanced degrees or training is demonstrated. The algorithm development process is purposefully simplified, allowing for well engineers to easily develop their

own control strategies while enabling rig- and site-specific customization. Additionally, the visual nature of the methodology enables easy monitoring by the rig crew for troubleshooting purposes. Automation scenarios are presented for tripping and Managed Pressure Drilling operations that demonstrate the ease of use. Multiple control strategies are developed for each task, and compared against criteria that include easy comprehension of the algorithm and optimality. This automation approach can help reduce some of the current barriers to broad scale adoption of automation.

Introduction

Oil and gas extraction is becoming increasingly difficult and automation of drilling is being explored as a means to improve economics and safety. Past automation attempts have achieved varying degrees of success, and a few are now deployed in the field:

- Jansen et al. (1992; 1995) developed a methodology to control torsional vibrations in drill strings using feedback from motor current and speed. Their method, called Soft Torque Rotary System (STRS), has been commercially available for many years (Dwars et al., 2013).
- Santos et al. (2003) presented the Micro-Flux Control system, which can detect formation influxes by monitoring return flow rate signatures and automatically adjusts the choke valve setting until the influx is attenuated. This system was tested with different mud systems and commercialized thereafter.
- van Riet et al. (2003) described Dynamic Annular Pressure Control, a fully automatic MPD system which manipulates the choke opening and back pressure pump flow rate to maintain constant bottom-hole pressure. This system was successfully implemented on several challenging deepwater operations.
- Kyllingstad and Nessjøen (2009) described another methodology for reducing torsional vibrations which requires only speed input. This has also been field tested and is now commercially available.
- Florence et al. (2009) described an auto-drilling system that provides steady state WOB and differential pressure across the motor to achieve faster ROP and a better quality wellbore. The methodology demonstrated increased ROP and improved drill bit life on several fields tested.
- Matheus and Naganathan (2010) showcased a trajectory control system that can automatically control inclination and azimuth while maintaining the trajectory within a tight tolerance.
- Godhavn and Knudsen (2010) presented another automatic choke control system for MPD, which was used to successfully drill North Sea wells in narrow pressure windows. A continuous circulation system was used to provide mud circulation during connections. The system was enhanced with capabilities to handle influxes, rig power failures and choke plugging.

- Dunlop et al. (2011) described an automated ROP optimization methodology that automatically adjusts the WOB and RPM to achieve optimal drilling. This was tested successfully on 13 different fields.
- Cayeux et al. (2011a) described an automated mud pump management system that aims to minimize formation fracture possibility during pump startup and mud circulation. Their paper described the experiences with the system in the North Sea. Another paper by the same authors (2011b) described automation of the drawworks and the top drive to minimize swab and surge effects. These algorithms were also tested in the North Sea. Many of these are now commercially available.

These recent developments are very encouraging. However, there still remain significant challenges that need to be overcome before broader adoption of automation in the industry is achieved:

1) Each well that is drilled is unique and sensors, actuators, and other rig equipment vary in type, number, performance and quality from one rig to the next. This implies that automation and control algorithms (especially ones that can have safety and high cost ramifications on failure) have to be reviewed and signed off, for each well drilled. Current algorithms (except for the simplest ones) require tight control on the hardware for execution, and require significant expertise for adaptation from one rig to another.

2) A well drilled today generally has four primary stakeholders: the operator, the service provider(s), the drilling contractor, and the equipment manufacturer(s). An automation solution usually requires input from all these parties. Each of them holds data critical to a complete automation solution. More often than not, these stake holders are hesitant to share data due to fear and competing business interests. The SPE DSATS sessions (Florence et al, 2013) indicate a general consensus that the operator is the stakeholder who holds most authority in this scenario, and is best suited to play the role of a data integrator / automation supervisor. But integrating all the data together (when the operator does get access) and devising a control algorithm in a short time period is a challenge.

3) Drilling contractors are often very cautious when it comes to automated algorithms. There are several reasons for this. A first concern is safety: control algorithms provided by service providers and operators are often black box / proprietary, and rig contractors are hesitant to hook them up to their rig systems because of potentially harmful (to people, equipment etc.) unintended consequences / failures. Secondly, it is often unclear what the value-proposition is for the rig contractor: whereas the potential benefits to an operator or service provider may be evident, the rig contractor may see only downside risks by adopting automated routines. Both of these concerns need to be addressed to

achieve the buy-in of the rig contractor; making the control algorithm transparent and intuitive for the driller goes a long way to addressing the black box concern.

4) Data quality in this industry is generally not good enough to reliably implement automated control algorithms. Many who have implemented automation solutions in the past recommend improving rig instrumentation (Cayeux et al., 2013). While this is a desirable goal, it is not an economically feasible solution on a broad level. The current generation of automation algorithms is not capable of independently handling uncertainties in sensed data.

In this paper, we propose a data and controller architecture intended to address many of the above challenges. The architecture requires data to be stored as conditional probability distributions or tables. It enables control algorithms to be rapidly developed and implemented on a well by well basis. The ultimate goal is a control algorithm development methodology that results in "driller friendly" control algorithms and can be developed quickly by people without advanced science and engineering background. We describe how the architecture and methodology suggested here can be applied to the automation of a few operations, such as tripping and managed pressure drilling.

Control Architecture

The automation control architecture suggested (Figure F.1) may be split into four broad categories: system hardware, software modules, unified database and data source. An option is provided within the architecture for the operator to plug in a third party proprietary controller. This would be very desirable option, where such controllers are proven to be reliable both in performance and consistency, and therefore acceptable as a black box unit. In such cases, there needs to be a mechanism for non-conflicting operation of the operators' controller, and the third party controller.

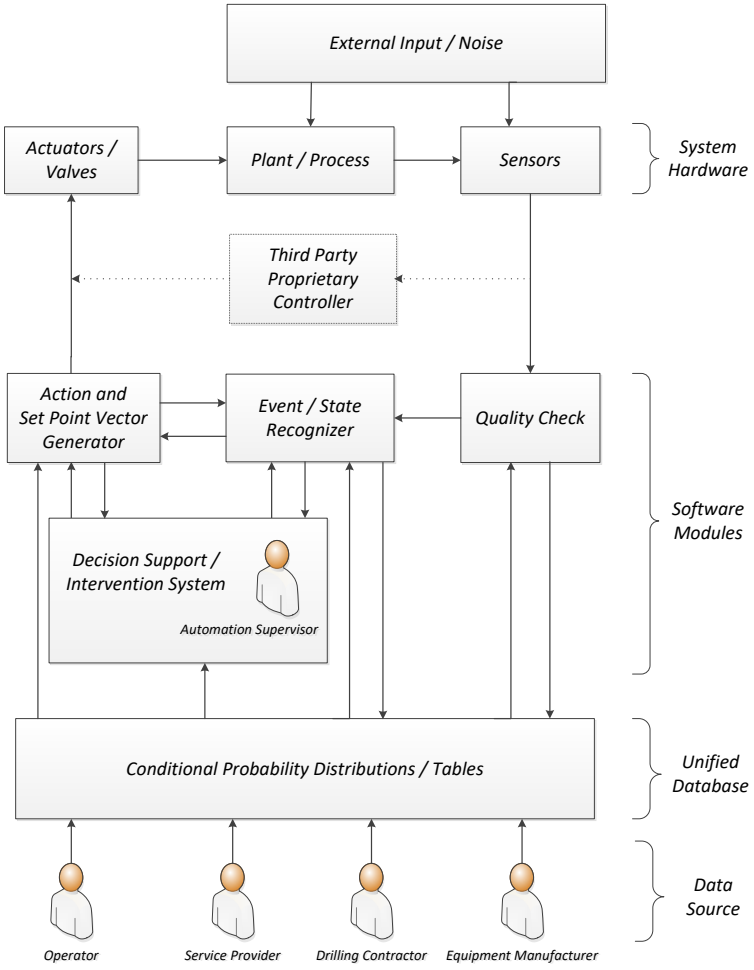

Figure F.1: Control architecture.

System Hardware

These include the actuators, valves, etc., that can be controlled to modify the plants' (drilling rigs') response to external inputs and noise. These also include the sensors attached to the plant to measure all the response characteristics that are essential for closed loop control. In some instances, the sensors may be offline and manual human input of the sensed data will be required to complete the loop.

Software Modules

There are four software modules that may be considered essential to this control architecture. They are:

1. **Quality Check.** Due to the harsh environment on a drilling rig, the sensors generally have a high failure rate. Therefore it is essential that there exists a module within this architecture to ensure that the data can be trusted for the purposes of automatic control. No data validation module can deterministically predict sensor failure at all times, and a probabilistic framework is therefore desired (Ambrus et al., 2013). Control algorithms have to be designed to account for sensor failure in a probabilistic sense. This quality check module can be a black box as far as the driller is concerned, since the outputs coming from this module can be easily checked with actual sensor conditions for module troubleshooting purposes.
2. **Event / State Recognizer.** Once the data has been checked for quality, one needs to apply algorithms to detect the current drilling operation state or event automatically. Various techniques are available to do this (Ringer et al., 2013; Arnaout et al., 2012). Here also, as in the quality check module, a probabilistic estimate is desired, since no algorithm can detect events to 100% accuracy. Control actions need to be tied to probabilistic estimates of events or states. This module can also be a black box as far the driller is concerned, since the output from this module can be easily validated, and the software module held accountable for errors.

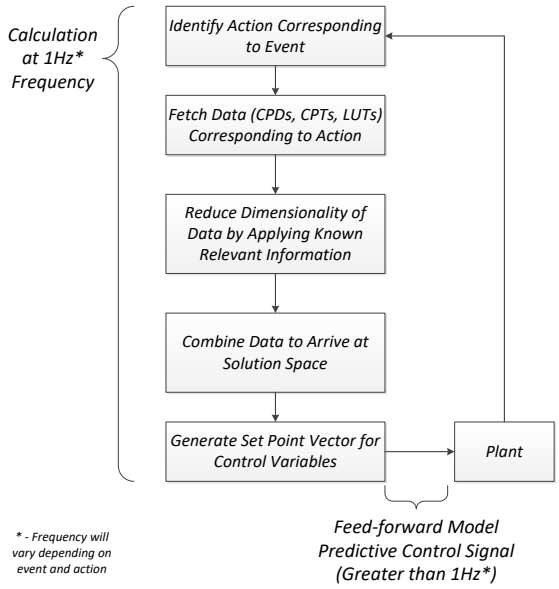

Figure F.2: Flow chart for generation of set point vector.

3. **Action and Set Point Vector Generator.** This is the module that takes all the real-time data gathered from sensors, the model data from the database, information from the event / state recognizer, and all other relevant known information to arrive at set point vector for the control variables. The set point vector is generated through a combination of both feedback and feedforward control**.** Figure F.1 is a high level flowchart detailing the steps. This architecture allows for control at different time scales. While the set point vector itself is calculated generally once every second (or at another pre-determined frequency), the control signals may be sent to the actuators at a higher frequency. For example, a set point vector for a certain variable, with a length 'n' essentially implies 'n' separate set point value changes to the controlled variable within the one second.

   Also, in arriving at the set point vector, a finite response horizon (greater than the one second feedback loop) may be taken into consideration for robust control. One primary objective with the approach suggested in this paper is to enable the development of control laws that are intuitive, does not involve direct use of differential equations and can be generally understood by the driller. This has two implications. First, the control laws may be heuristical in nature and therefore there will be many different control solutions. Second, these control laws may not be optimal, although they may be close to optimal. The control laws will however be transparent, allow automated operation, and will be more efficient and safer than manual drilling (which involves manual interpretation of the data followed by manual setting of the control set points).

   The control laws should also account for the fact that there could be errors in the event / state recognizer and quality check module. The control laws should ideally be developed during the well planning phase. Further, effort should be expended on educating the drilling crew so they understand how the set point vectors are generated.

4. **Decision Support / Intervention System.** Currently, automation solutions tend to drastically increase the workload on a drilling crew when something does not work as expected. This is generally due to the black box nature of present-day automatic control implementations. Even when the drilling crew is aware of the logic underlying the generation of control signals, a decision support module would be valuable in enabling the drillers to visualize what is happening and consequently increasing their confidence in the system. Further, the module should allow the driller to intervene when necessary, and take manual control of the rig if the situation demands it. This module would be the primary interface into the automated system for the "Automation Supervisor" (Figure F.1). Such a module should incorporate human factor engineering in the design of the visual display unit, and prevent data / alarm overload.

Unified Database

This is a central database that is a repository for all the models, all information about the rig equipment, and the data collected from the sensors. The architecture suggested in this paper requires all the data to be stored in the form of Conditional Probability Tables (CPT) or Conditional Probability Distributions (CPD). Statistically, a CPT is a table or a matrix probabilistically relating one output random variable to one or more random variables. CPDs are the continuous variants of CPTs, and in this paper both are used interchangeably.

Data Source

The data that is stored in the database generally comes from one of the following sources.

1. **Operator.** The operator generally has information with regards to the well, its geology, trajectory, casing program, etc. They are also the primary owners of the well drilling plan and therefore have access to the models used to predict well behavior.
2. **Service Provider.** Data from surface sensors, MWD tools and other specialized sensors and services may be provided by the service provider in a WITSML or other industry standard format, and used to update the stored CPD/CPT models. The real time data may also be stored in a tabular format.
3. **Drilling Contractor.** Data with regards to working condition of rig equipment as well as surface sensors is required information for the control system, and this data is usually available from the drilling contractor, and the maintenance crew.
4. **Equipment Manufacturer.** Data with regards to equipment performance characteristics may be obtained directly from the equipment manufacturers in a tabular format.

Conditional Probability Tables / Distributions for Model Representation and Data Storage

The key feature of the architecture suggested in this paper is a model representation and data storage mechanism, namely the Conditional Probability Table (CPT) or the Conditional Probability Distribution (CPD). CPTs are matrixes that represent probabilistic relationship between various drilling parameters. By requiring all parties involved in a drilling operation to adhere to this format, one can achieve efficient data aggregation eliminating the complications involved in linking complex mathematical models from different sources. The model CPTs may be generated through the offline solving of algebraic or differential equations derived from first principles, through experimentation or even data from offset wells. These CPTs can be updated in real time as new sensor data is obtained and can be visually presented in a manner that is intuitive

and readily understandable by the drill crew. One main premise of this paper is that, if a concerted effort is made to represent all information in a format that enables rapid visualization, there exists the possibility for creating quicker, driller-friendly control algorithms. Visual data in the form of Look-Up Tables (LUTs) have been used in control algorithms and in the decision making process for some time now. Ashok and Tesar (2013) offer examples of their uses in the recent past. LUTs may be considered to be specific instances of CPTs or CPDs, and can be constructed in real-time from the same. Figure F.3 presents an overview of suggested data architecture.

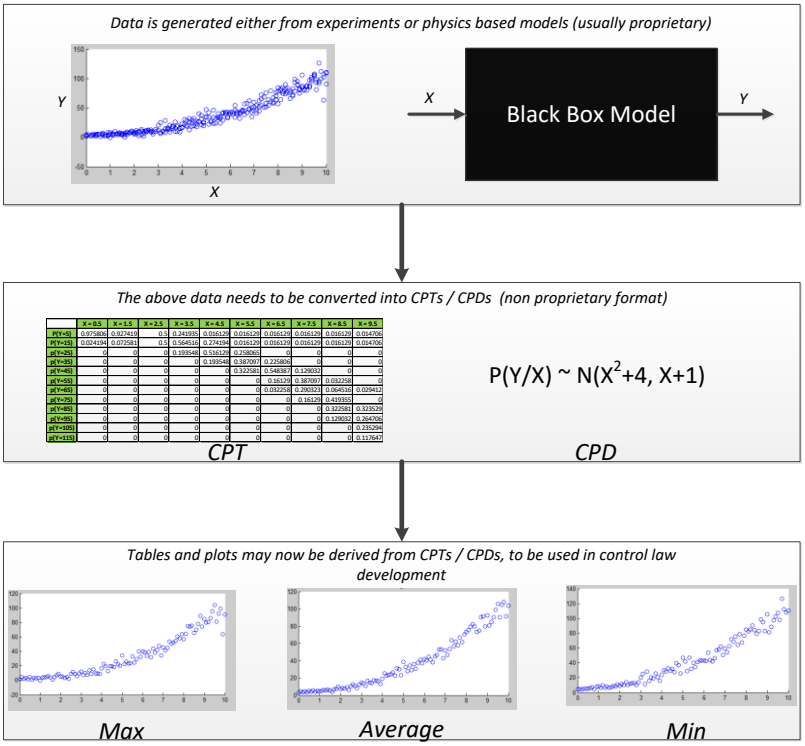

Figure F.3: Different stages of data collection, storage and usage.

In the following sections, we will detail some key features of the suggested data architecture and describe how they tie in to the control architecture presented.

Incorporating Uncertainty Handling Mechanism

The world we will live in is not deterministic. Decisions we make are always based on probabilistic information (though we may not be conscious of the process we follow). Similarly, very little about drilling is deterministic. So control algorithms should be written to take uncertainty into account. This in turn requires one to account for the uncertainty in the models, the uncertainty in the empirical data, the uncertainty in the operational capacities of the rig equipment etc. The CPDs / CPTs are therefore an ideal

construct for data storage from which to build the different software modules (quality check, event recognizer, etc.). The various parts of the controller software have access to information with regards to system uncertainty.

Storing Conditional Probability Tables

Storing information and data in CPTs can require large data storage capacities, depending on the granularity / accuracy of the desired model representation. Recent advances in high-volume data storage and retrieval technology has made it possible to now store and retrieve huge multi-dimensional data sets with ease (Feuerlicht, 2010). Data storage is also continuing to be cheaper by the day. CPDs are more efficient than CPTs when it comes to representing models, require very few parameters to be stored, and are preferred when the model is generally monotonic in nature. Additional techniques such as the use of a graphical model (Bayesian network or undirected graphical models) can offer efficient means of storing data, by exploiting conditional independence relations.

Separating Modeling from Control Algorithm Design

Drilling is a multi-disciplinary operation. Efficient and safe drilling requires good models from diverse domains such as fluid hydraulics, drill bit / rock interactions, torque and drag modeling, vibration modeling, drilling machinery operation, etc. Building good models require significant expertise in the individual domains. One of the goals of this architecture is to enable a separation of modeling expertise from control algorithm design. In this architecture, the domain expert team provides models in a CPT/CPD format to the control algorithm designers. The control algorithm designer bases controller design on CPT/CPD data that can be easily reviewed visually for correctness.

Visualization of Data Used to Develop Control Law

As noted in the previous section, the control law designer does not have to be an expert in all the domains relevant to drilling. However, he / she should have a mechanism to check the data received from the different parties to ensure there are no gross errors. Here it is often beneficial to convert CPTs / CPDs into Look-up Tables (LUT) and plotting them as 2D/3D plots. One of the advantages of using CPDS/CPTs to store data is that they allow representations of uncertain information. From these, one may extract one or multiple LUTs (used interchangeable with plots) relating the parameters of interest for a given confidence requirement. The top plot (a) in Figure F.4 shows what a CPT looks like when plotted. There are multiple values of Y for each X, and there is an upper and lower bound on Y for each value of X. This plot represents the process relating Y and X and the uncertainties associated with the process. The three plots (b), (c) and (d) are extracted from (a). Plot (b) represents the upper bound limit of Y given an X (i.e. the probability that Y will be above the value shown in this plot is probabilistically very low). Plot (c) represents the expected value of Y given X and plot (d) represents the lower limit. These plots allow the control algorithm designer to better understand how the process is expected to behave and the limits and uncertainties. It thereby enables a quick validation

of the model, placing the control law designer in a position to choose an upper or lower bound depending on the overall goal.

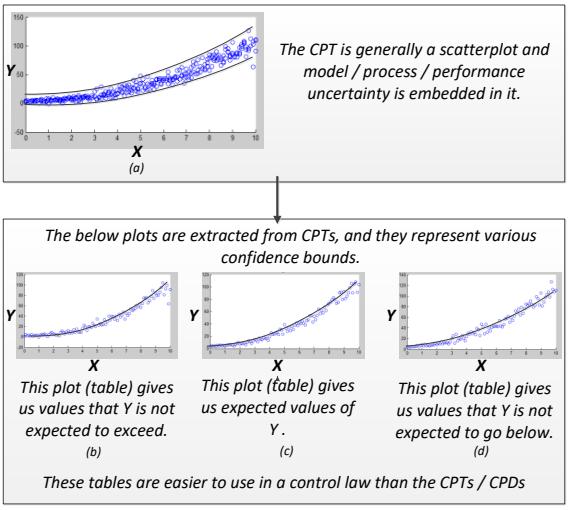

Figure F.4: Appropriate LUTs are extracted from CPDs/CPTs for the development of the control laws.

Representing System Dynamics Using CPDs/CPTs/LUTs

System dynamics in the form of ordinary or partial differential equations are very difficult to integrate into an already existing control algorithm. Also, unlike the visual plots shows above, these equations provide little intuitive meaning to the control algorithm designers, especially if they are themselves not experts in the domain. Converting these equations into CPTs can help capture the important information that a controller designer would need to build the controller. Techniques exist for representing dynamics in easily interpretable CPT/LUT formats (Alpigini, 2004; Coffey, 2012).

As an example of how one might convert a partial differential equation representation of system dynamics to a CPT/LUT representation, consider the operation of a drillstring tripping out of a borehole (see Figure F.5). As the pipe is pulled out, pressure transients are generated in the annulus, and not accounting for the associated dynamics can lead to a kick or a lost circulation scenario. A physics-based model can be built to understand these transients and this involves taking into account the principles of continuity, conservation of momentum, etc. This, in turn, translates to a set of partial differential equations and the solution is often numerically obtained. Figure F.6 is illustrative of the bottom-hole pressure variations as the bit is tripped out, at first accelerating to a certain speed, then maintaining that speed and finally decelerating to a full stop. Accurate calculations of such transients are very difficult in real time.

However, it is quite possible that such models can be solved offline for various input conditions and pertinent information can be extracted from these simulations and

condensed into CPTs/LUTs. For example, in the tripping-out operation, it is important that the maximum and minimum bottom-hole pressures that result during the transients not exceed the fracture pressure and pore pressure respectively.

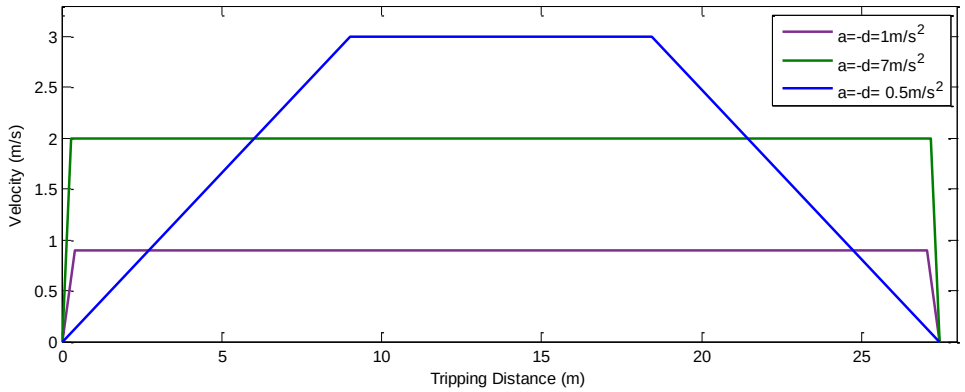

Figure F.5: Three possible trajectories during a tripping operation.

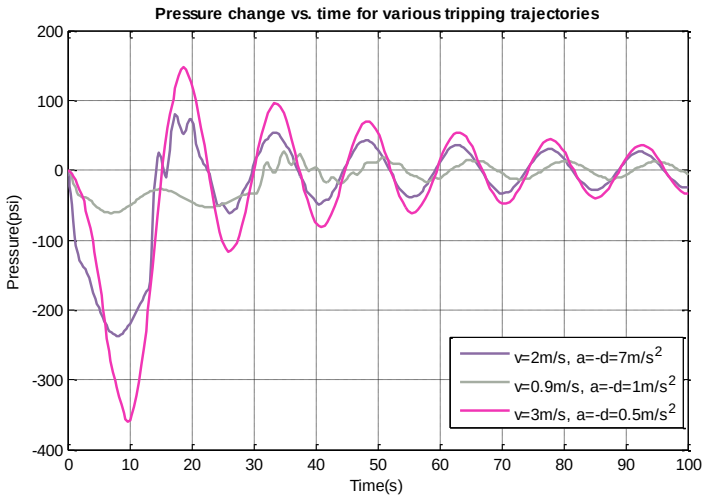

Figure F.6: Bottom-hole pressure variation for trajectories in Figure F.5.

Simulations such as the ones shown in Figure F.6 may be repeated for various velocities and accelerations such as the ones in Figure F.5, the trends may be recorded and then summarized into a CPT/LUT. Figure F.7 is an example of one such exercise. Here, the maximum transient swabbing pressure is shown for different tripping velocities, for a certain constant acceleration. This chart is intuitive, easy to interpret and ultimately useful in the design of the control algorithm. The control algorithm designer does not have to deal with complex partial differential equations and their solution methodologies.

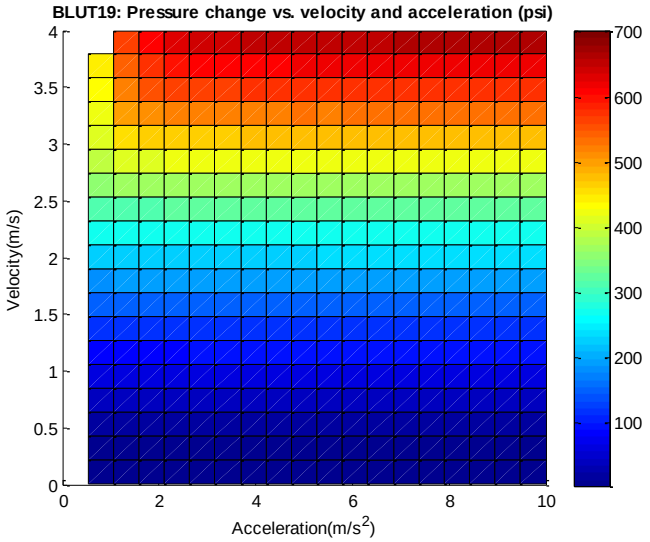

Figure F.7: Look-up tables or charts such as the above summarize system dynamics and can be extremely useful in controller design.

This whole process is summarized in Figure F.8. Comprehension of the system dynamics is greatly increased as one moves from left to right in Figure F.8 Note that, in this process, no pertinent information is lost. Depending on how confident the domain expert feels about the model, he / she may assign an upper and lower bound for such plots using CPTs.

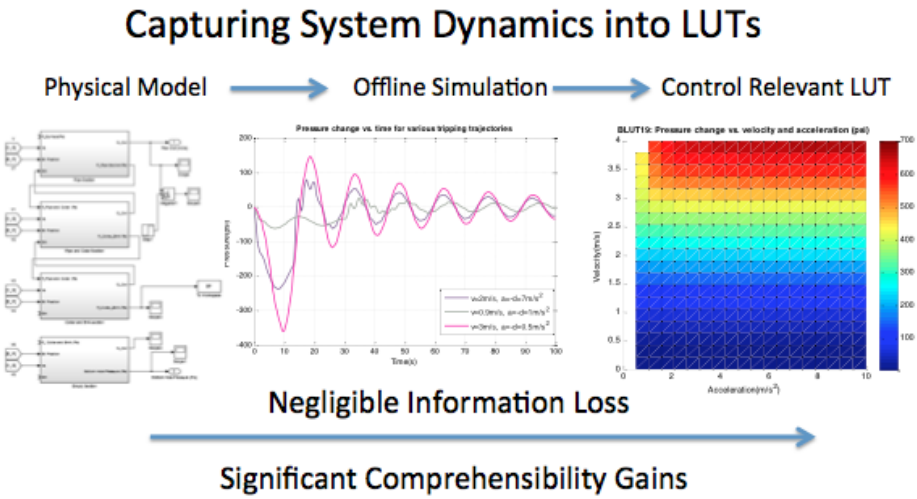

Figure F.8: The transition from differential equations representing fluid dynamics to look-up tables representing the fluid dynamics.

A similar approach can be taken to represent the mechanical dynamics of the drillstring in a LUT. As shown in Figure F.9, a mechanical model of the drillstring can be simulated for various input forces and the obtained steady state velocities can be stored in a LUT for real-time use.

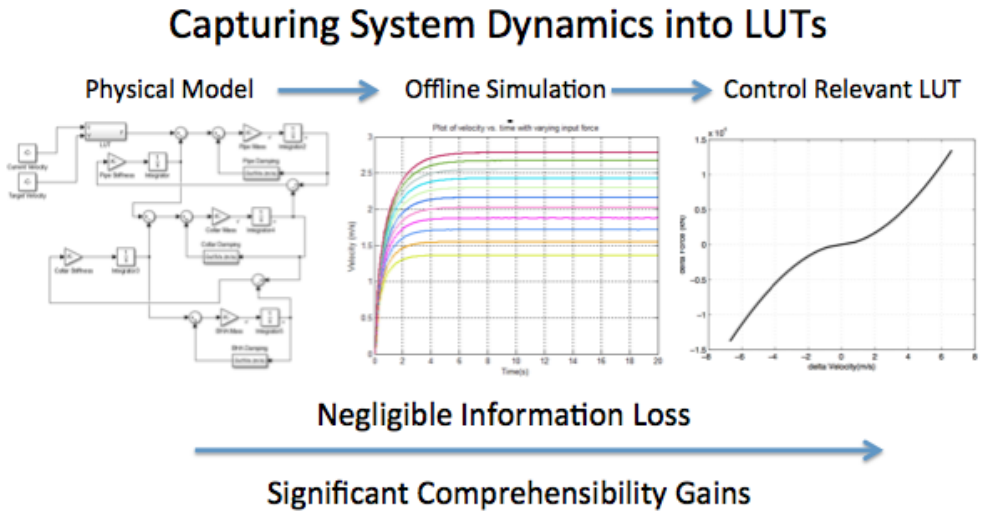

Figure F.9: The transition from differential equations representing mechanical dynamics to look-up tables representing the dynamics.

CPT / LUT Combination Math

Often the tables that would be most relevant for a particular control algorithm may not be readily available. This would necessitate the combinations of various LUTs to arrive at the desired table. Various techniques to do this are already available in literature. The approach was formalized in (Ashok, 2008), and the interested reader is referred to that paper for more details. It is stressed here that the look-up table math is in general no more difficult than high school level math, and we consider this simplicity essential for building driller-friendly control systems.

Modularity and Re-Usability

CPDs / CPTs / LUTs are self-contained units of information. New tables can be added to the database or deleted easily based on availability and relevance. Also when vendors or service providers change, the operator may request data in the same tabular format as before, and this could potentially mean no change whatsoever to the control algorithm. Also this allows for the operator to continue to build the model database and add new automation algorithms over a period of time. In the next two sections we show how a controller architecture based on LUTs allows rapid development of control algorithms.

Drilling Scenario

The scenario utilized below covers operations on an example well. The operations will entail the drilling of a 12 ¼" vertical intermediate hole using a six-blade PDC bit with 6 × 14" nozzles. 13.375" surface casing is set at 1000 feet and the target depth of the intermediate section is 4700 feet. The bottom-hole assembly is detailed in Table F.1 and is used throughout for hydraulics and dynamics calculations.

Table F.1: Bottom-hole assembly specification.

Joints	*Component*	*OD (in)*	*ID (in)*
	Drill Pipe	5	4.276
10	HWDP	5	3
1	XO Sub	6 ½	2 ¼
7	Drill Collar	6 ½	2 ¾
1	XO Sub	8	2.375
3	Drill Collar	8	2.375
2	NM Drill Collar	8	2 ¾
1	MWD	8	
1	Stabilizer	8	2 ¾
1	Bit	12 ¼	

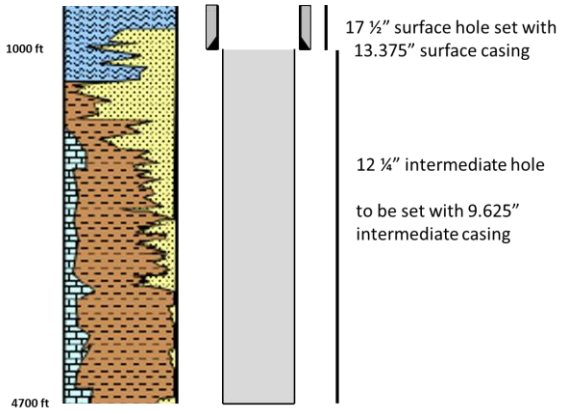

Figure F.10: Lithology expected in the intermediate section.

The lithology is primarily shale behind the surface casing, followed by a section of interbedded shale and sandstone. At 1800 feet, mudstones appear and become the dominant lithology for the remainder of the section, as is seen in Figure F.10. A 9 ppg mud is used during the simulated MPD operation and 10 ppg mud is used during the tripping operation.

Application to Managed Pressure Drilling

A potential use for the control methodology presented in the previous sections is for Managed Pressure Drilling (MPD). The goal of back-pressure MPD is to maintain a constant bottom hole fluid pressure so as to avoid influxes, wellbore instability or lost circulation events while drilling formations with narrow pressure windows. This is accomplished with additional equipment, such as a rotating control device (RCD) mounted at the wellhead, a drillstring float valve, a dedicated choke manifold and a back-pressure pump or rig pump diverter (Saeed et al., 2012). In its most basic form, the operator has to manually adjust the choke opening, allowing pressure to be trapped or released from the top side of the annulus. This requires considerable fine tuning and swift

reaction time to deal with pressure transients such as the ones caused by swab and surge effects, or by ramping the rig pumps up and down during connections. Several commercial control systems (Santos et al., 2003; van Riet et al., 2003; Godhavn and Knudsen, 2010) have been developed to automate this process, but they suffer from bandwidth limitations and lack of robustness as they are typically tuned for a particular operating point, requiring recalibration once the wellbore environment changes significantly. This process relies upon precise measurement of surface and downhole pressures, flow rates in and out of the well and density of the drilling mud. Moreover, a dynamic hydraulics model has to compute the required pressure set points in real-time, which may require trading off the model complexity with run-time capabilities. More importantly, these controllers require considerable domain expertise to understand. Using the principles outlined in the previous sections, a LUT-based controller can be designed for the MPD case without the need for advanced hydraulics knowledge.

We start by introducing the control variables, task relevant known information, and the set of look-up tables required for automating this task and outline their integration to arrive at LUTs needed to design the control algorithm. A high level outline of this process is illustrated in Figure F.11. We then show how these LUTs enable the design of a control algorithm.

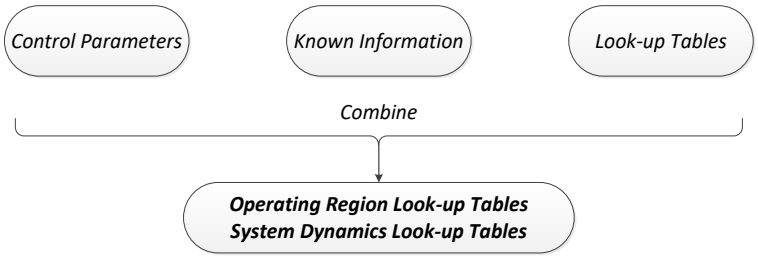

Figure F.11: Data integration to arrive at look-up tables needed to design control algorithm.

Control Variables

The variables that can be controlled in a MPD operation are the main rig pump rate, choke opening and back pressure pump rate, on the pressure management side, in addition to Weight on Bit (WOB) and top drive RPM/torque. The methodology presented herein will assume only the main pump and choke are available for control, and will additionally use WOB and surface RPM. For the choke control, a set-point backpressure value is specified, which translates to an actuation of the choke opening. This will allow easier adaptation of the control laws to MPD systems having various choke orifice sizes.

Known Information

The automation system would require real-time and offline information to safely perform a tripping operation. Known information reduces dimensionality of the LUTs that are

needed for the task. For this scenario, the variables below are assumed to be known information:

Real-time depth position of the drillstring

- BHA / drillstring configuration details
- Wellbore geometry
- Depth of last casing shoe
- Mud properties
- Choke geometry
- Mud pump, RCD and top drive specifications
- Lithology

Set of Required Look-Up Tables

Below is a list of look-up tables required for an automated MPD operation. Note that some of these are shared with the database for the tripping operation. Plots of these look-up tables after reducing their dimensionality are given in Appendix A.

- BLUT 1: Hydrostatic pressure vs. mud weight, depth, annular cuttings concentration and cuttings density. The hydrostatic pressure increases linearly with true vertical depth, mud weight and annular cuttings loading. A plot of hydrostatic pressure varying with well depth and cuttings concentration is shown in Figure F.34.
- BLUT 2: Annular frictional pressure vs. flow rate, mud weight, depth, drillstring RPM, mud plastic viscosity, mud yield point, hole diameter, pipe outer diameter, annular cuttings concentration and cuttings density. To calculate frictional pressure drop, we need to first determine whether the flow is laminar or turbulent, and then apply the appropriate friction factor correlations for the mud rheology (Guo and Liu, 2011). Since the annulus is made up of sections with different internal and outer diameters (drill pipe vs. casing, drill pipe vs. open hole, drill collar vs. open hole etc.), the frictional pressure drop is calculated separately for each section and the final result is a summation of all the individual sections. The effect of drillstring rotation is also applied (Ahmed et al., 2010). A plot of annular pressure loss vs. flow rate and RPM is shown in Figure F.34.
- BLUT 3: Drillstring frictional pressure vs. flow rate, mud weight, depth, mud plastic viscosity, mud yield point and pipe inner diameter. This table is constructed similarly to BLUT 2, however the effect of drillstring rotation is not considered here. Drillstring pressure loss is plotted against flow rate in Figure F.34.
- BLUT 4: Bit pressure drop vs. flow rate, mud weight, nozzle size, discharge coefficient. The bit pressure drop is important in evaluating the hydraulic horsepower generated at the bit. A plot of bit pressure drop versus flow rate is displayed in Figure F.34.

- BLUT 5: Flow rate vs. pump strokes/minute, pump volume/stroke, pump volumetric efficiency. The volume/stroke factor is a function of pump geometry, specifically the liner size and stroke length of the pump. The pump configuration (duplex, triplex, single-acting or double-acting) also impacts the effective flow rate generated (Guo and Liu, 2011). In the current scenario, single-acting triplex pumps are used. A plot of flow rate vs. pump strokes/minute is shown in Figure F.34.
- BLUT 6: Pore pressure vs. depth. This data is usually obtained prior to drilling from offset wells and seismic tests. The operator usually owns this information. During the well construction process, pore pressure can be measured using the repeat formation tester, or computed using empirical correlations to sonic, density and resistivity logs (Aadnoy et al., 2009). The pore pressure curve for the current scenario is plotted in Figure F.34.
- BLUT 7: Fracture pressure vs. depth. This data is also obtained from offset wells. Formation integrity tests are often used to update this table. The fracture pressure curve for the current scenario is plotted in Figure F.34.
- BLUT 8: Minimum flow rate for bit cleaning vs. bit diameter. A general rule of thumb for PDC bits (Lapeyrouse, 2002) is used to generate the plot in Figure F.34.
- BLUT 9: Pump capability (yes/no) vs. pump pressure, flow rate, maximum working pressure, pump horsepower rating. At high flow rates, the maximum allowable pump pressure is limited by the pump horsepower, resulting in a curve such as the one shown in Figure F.35. This table can be obtained from the equipment manufacturer.
- BLUT 10: Minimum flow rate for hole cleaning vs. mud weight, hole diameter, pipe outer diameter, mud yield point, mud plastic viscosity, cuttings density, cutting diameter, cutting sphericity, porosity, Rate of Penetration. This table uses the cuttings transport model in (Clark and Bickham, 1994) to calculate the flow rate required to maintain the cuttings concentration in the annulus at a value below 5%. The average cuttings concentration in the annulus depends on the Rate of Penetration and formation porosity. The cuttings transport model also requires computing the slip velocity, which is calculated using a model for irregularly shaped particles in a Bingham Plastic mud (Chien, 1994). A plot of the minimum allowable flow rate vs. Rate of Penetration is shown in Figure F.35.
- BLUT 11: Choke opening vs. mud weight, cuttings concentration, cuttings density, backpressure, flow rate. This table uses a nonlinear valve model commonly cited in the MPD literature (Saeed et al., 2012). Since mud in the annulus might contain dispersed cuttings, it uses the mixture density in the valve equation. Choke opening is plotted for different combinations of flow rate and backpressure in Figure F.35.
- BLUT 12: Drill bit dullness / foot vs. depth, Weight on Bit, bit RPM. The bit dullness characteristic is highly dependent on the lithology drilled (Warren and Armagost, 1988). Figure F.36 shows a plot of drill bit dullness / foot vs. depth generated for the

described drilling scenario. The drill bit dullness /foot decreases as the lithology transitions from harder rocks (sandstone and shale) to softer ones (mudstone). Note that this is an instantaneous characteristic (i.e. how much dullness the bit would experience if the bit run started at a given depth). The effective dullness that the bit would experience over a drilling interval can be obtained from the area under the dullness / foot curve, with an appropriate normalization factor.

- BLUT 13: Top drive capability (yes/no) vs. bit RPM, Weight on Bit, depth, drill bit dullness. To obtain this LUT, the load torque is related to the Weight-on-Bit through the bit-rock interaction (function of drill-bit dullness and depth). Then, the load torque is translated to the top drive torque to verify whether this combination is physically feasible based on the top drive torque-speed operational envelope. This table can be obtained from the equipment manufacturer. A plot of top drive capability vs. bit RPM and WOB is shown in Figure F.36.
- BLUT 14: Whirl (yes/no) vs. bit RPM, Weight on Bit, depth, drill bit dullness. This table requires a lateral vibration model to be run offline and return the ranges of RPM and WOB where the onset of whirl is avoided (Dunayevsky and Abbassian, 1998). Figure F.36 shows one such plot.
- BLUT 15: Torsional Vibration (Yes/No) vs. Bit RPM, Weight on Bit, Depth, Drill Bit Dullness. This table requires a torsional vibration model to be run offline and return the ranges of RPM and WOB where stick-slip is avoided (Dunayevsky and Abbassian, 1998). Figure F.36 shows an example plot.
- BLUT 16: Bit Torque vs. Bit RPM, Weight on Bit, Drill Bit Dullness. This table is generated using a velocity-weakening frictional characteristic caused by the bit-rock interaction (Dunayevsky and Abbassian, 1998). A plot of bit torque vs. bit RPM and WOB is given in Figure F.36.
- BLUT 17: Rate of Penetration (ROP) vs. Unconfined Compressive Strength (UCS), friction angle, bit RPM, Weight on Bit, bit torque, drill bit dullness, bit diameter, Equivalent Circulating Density, pore pressure, depth. Rate of Penetration is predicted using the model from (Caicedo et al., 2005), which uses Confined Compressive Strength (CCS) as an indicator of the rock strength. To calculate CCS, knowledge of UCS, friction angle, as well as pressure overbalance is required. Plots of ROP for different RPM and WOB combinations are shown in Figure F.16 and Figure F.36.

While not detailed in this paper, additional look-up tables can be constructed to handle well control in MPD operations where influxes of formation fluids may occur. Those look-up table values can be calibrated off-line after running multi-phase flow models consisting of partial differential equations. For the scenario presented in this paper, it is assumed only liquid and solid phases (cuttings) are present in the mud at all times.

Combining Base LUTs to Obtain Control Relevant Derived LUTs

The look-up tables described in the previous section are now linked together. A flow chart is presented in Figure F.12 that outlines how the BLUTs may be combined. Each of the boxes in Figure F.12 contain 5 pieces of information: the serial number of the LUT in the database, the number of parameters before the known parameters are applied, the known parameters, the number and names of parameters passed on to the next stage. Figure F.12 and Figure F.13 highlight the steps in this sequence, while Figure F.14 through Figure F.17 show possible look-up tables that can be generated using the sequence outlined above.

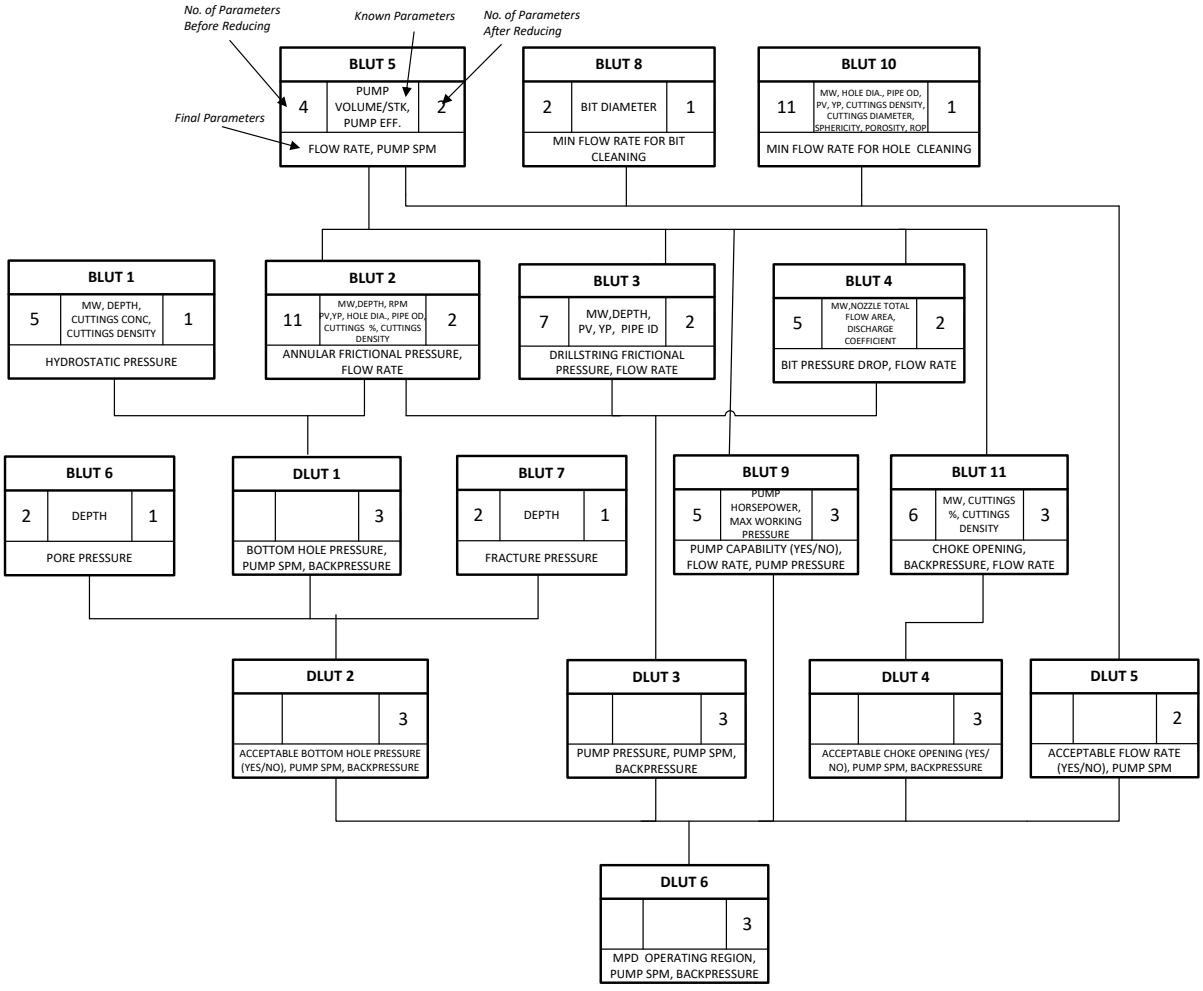

Figure F.12: High-level diagram showing how data is combined to arrive at pump rate and backpressure constraints.

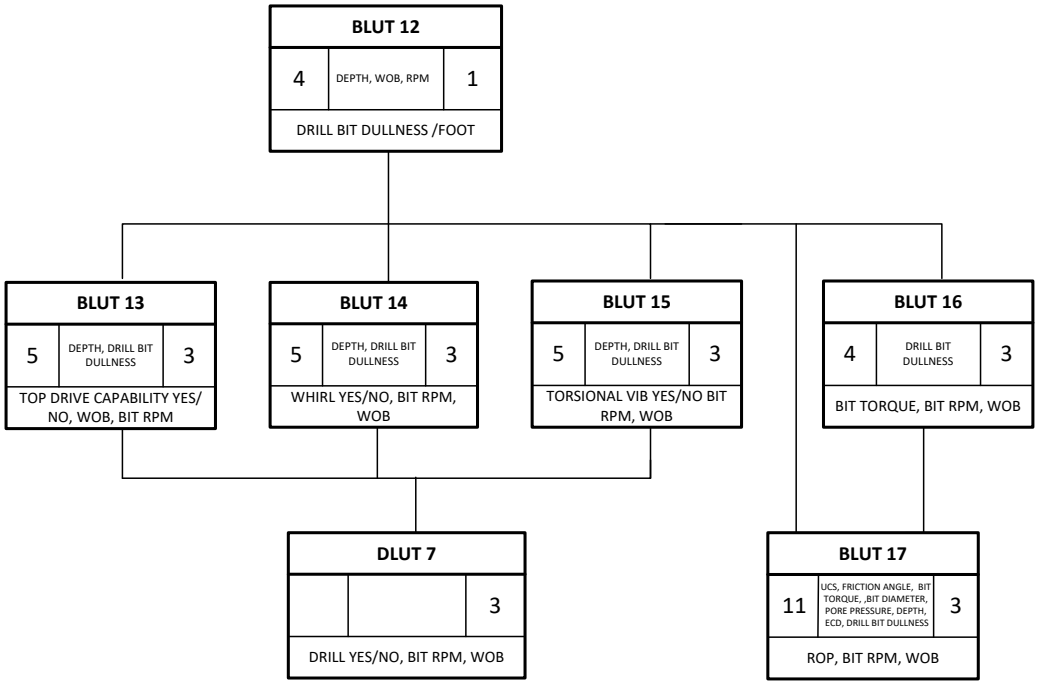

Figure F.13: High-level diagram showing how data is combined to arrive at bit rpm and weight on bit constraints.

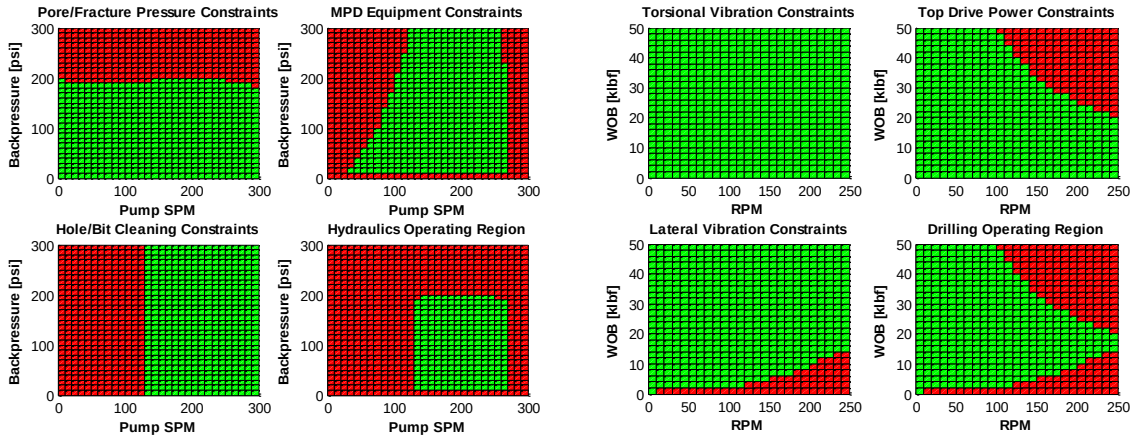

Figure F.14: Constraints for controller design at 1000 ft measured depth. Green regions represent allowable combinations of parameters.

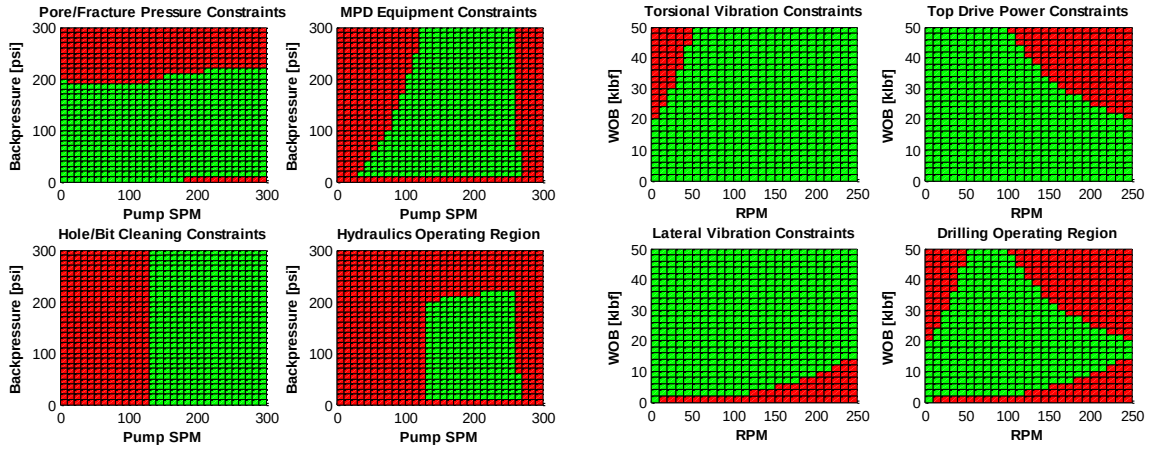

Figure F.15: Constraints for controller design at 2000 ft measured depth. Green regions represent allowable combinations of parameters.

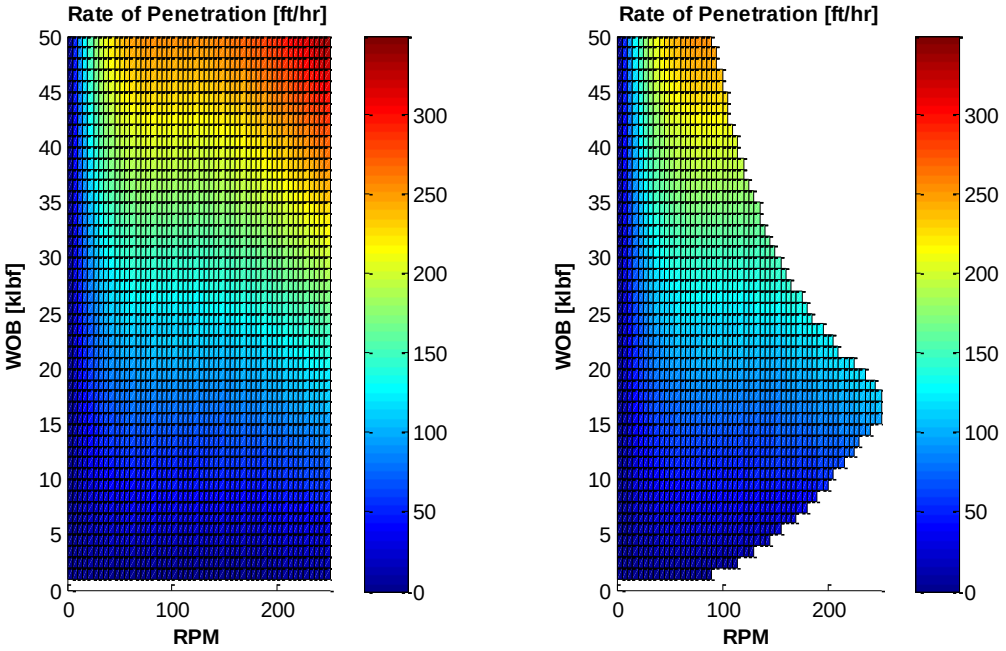

Figure F.16: Rate of penetration look-up table at 1000 ft. Left plot is before constraints are enforced, right plot is with constraints.

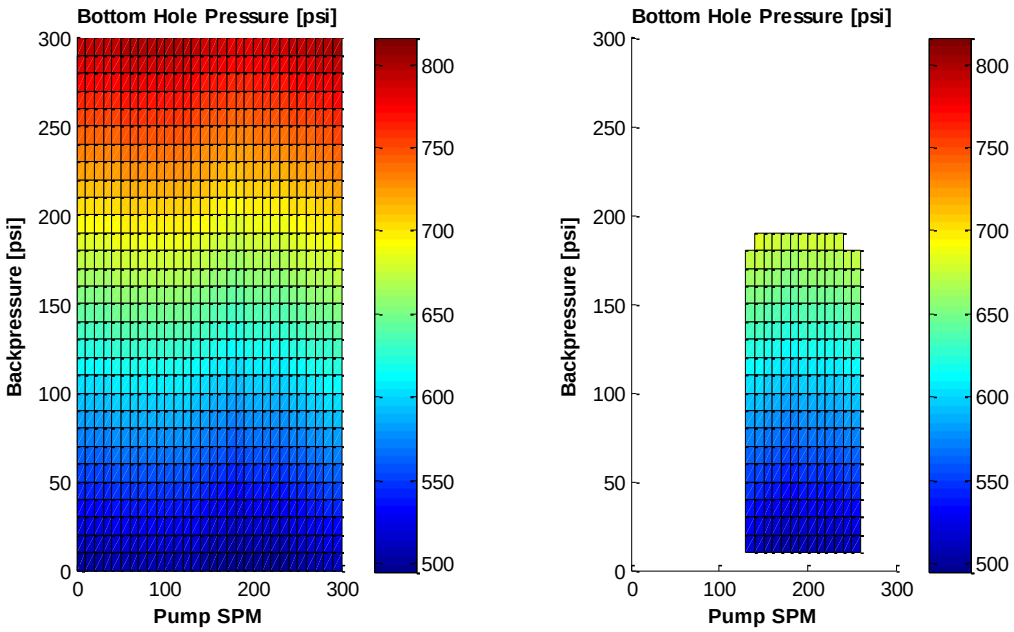

Figure F.17: Bottom-hole pressure look-up table at 1000 ft. Left plot is before constraints are enforced, right plot is with constraints.

Control Algorithm Design and Simulation Results

The plant on which the controllers are tested consists of ordinary differential equation models of hydraulics and drillstring torsional vibration. The dynamics are based on the models developed in (Dunayevsky and Abbassian, 1998) and (Kaasa et al., 2012), coupled with steady-state Non-Newtonian fluid frictional pressure loss models (Guo and Liu, 2011), drillstring rotation effects on annular pressure (Ahmed et al. 2010) and cuttings transport (Clark and Bickham, 1994). The model in (Caicedo et al. 2005) is used for calculating the Rate of Penetration. Proportional-Integral (PI) control is used to track the set point values for back pressure and surface RPM. The initial setpoint values are ramped from zero over a period of one minute to simulate equipment start-up procedures. Weight on Bit is added after 30 seconds from the start of the simulation and then ramped to the setpoint value. All simulations start at a measured depth of 1000 feet. The mud weight used in all the simulations in this section is 9 ppg while the desired Equivalent Circulating Density (ECD) is 10.5 ppg.

Controller 1

The first controller designed will be a naïve controller, which will compute the constraints and generate the allowable region for a given depth, then pick control

variables in or close to the centroid of the allowable ranges. This will guarantee that even with unexpected transients, the operational constraints will not be exceeded.

Controller 2

The second controller will resort to optimization to achieve the desired performance while staying within the constraints. To generate the control setpoints, at every time instant, a set of performance metrics are evaluated for the following 90 feet drilled. These metrics can include one or more of the following: Rate of Penetration (ROP), Mechanical Specific Energy (MSE), Hydraulic Horsepower per Square Inch (HSI) and variation in bottom hole ECD After scaling the metrics to yield similar order of magnitude, the resulting values can be combined into the following cost function, which can be minimized in order to find an optimal combination of control variables (note that some of the quantities, such as ROP, will be inverted, since maximizing them is equivalent to minimizing their reciprocal):

$$J(u) = \sum_{0}^{90\ ft} [W_1 y_1 + W_2 y_2 + W_3 y_3 + W_4 y_4 + \Delta u^T V \Delta u]$$

where:

$$y_1 = \frac{ROP_{max}}{ROP}, \qquad y_2 = \frac{MSE}{MSE_{max}}, \qquad y_3 = \frac{HSI_{max}}{HSI}, \qquad y_4 = \left[\frac{\Delta ECD}{(\Delta ECD)_{max}}\right]^2,$$

$$u^T = [\text{Top Drive RPM},\ \text{Weight on Bit},\ \text{Pump Rate},\ \text{Backpressure}],$$

V is a matrix containing penalties for excessive variations in the control inputs (Δu) across the 90-feet interval, and W_1, W_2, W_3, W_4 are weights assigned to each of them to denote the relative importance of each metric at a particular point in the operation. For instance, a control law aimed at maximizing ROP irrespective of MSE and HSI will use a high value of W_1, while a controller aimed at keeping ECD at a constant value at all times will use a large W_4 while keeping the other weights small. These weights can be manually assigned by the driller or automatically adjusted by the system when instances of inefficient drilling are detected.

The cost function can be minimized through a numerical optimization technique or through a heuristic search in the solution space. The optimization problem can be mathematically formulated as:

$$\min_{u \in U} J(u) \text{ such that}$$
$$f_i(u) = 0, \quad i = 1, \ldots, m$$
$$g_j(u) \leq 0, \quad j = 1, \ldots, n$$

where $f_i(u)$ and $g_j(u)$ are constraints imposed to the control variables and U represents the set of possible values that the control variables can take. Since the cost function and constraints are nonlinear, solving the problem formulated requires nonlinear programming tools (Bertsekas, 1999). The constrained minimization problem was solved using the MATLAB™ Optimization Toolbox (MathWorks, 2011). Simulation results are presented for three different controllers, which differ in the optimization objective and the selection of weights.

Controller 1 Simulation Results

The naïve controller is simulated with the following setpoints: surface rotation rate of 125 rev/min, Weight on Bit of 25 klbs, pump rate of 200 strokes/min (782 gal/min) and 100 psi backpressure. The initial values were ramped from zero to the reference value over one minute.

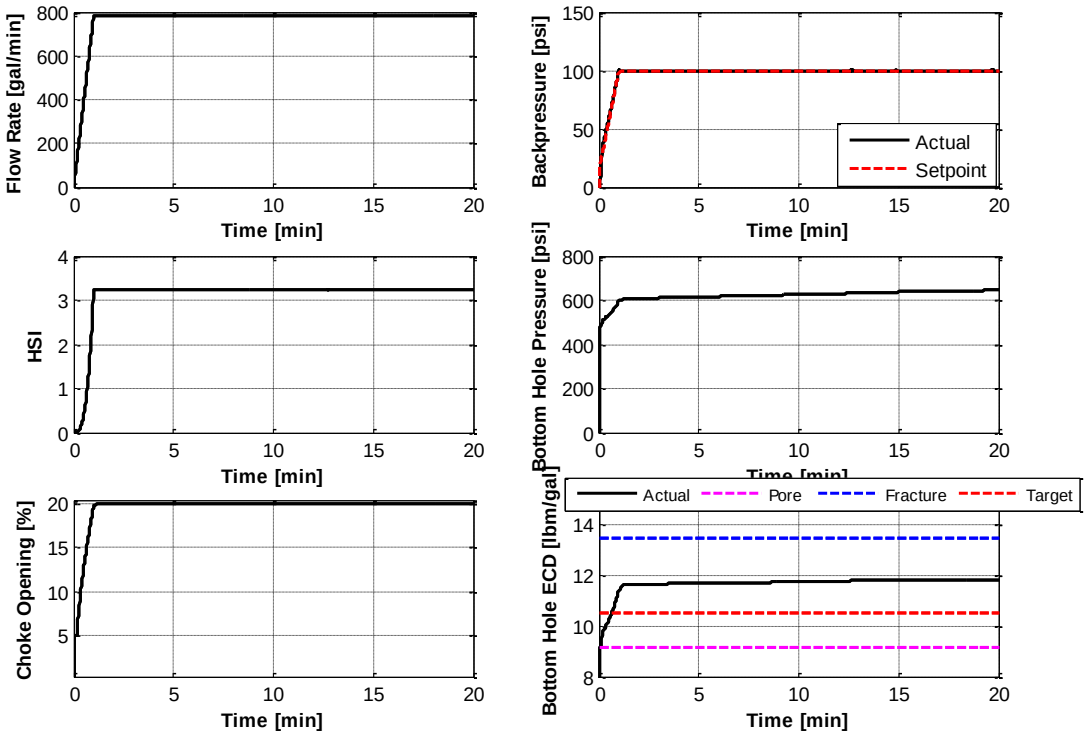

Figure F.18: Hydraulics inputs and outputs for Controller 1.

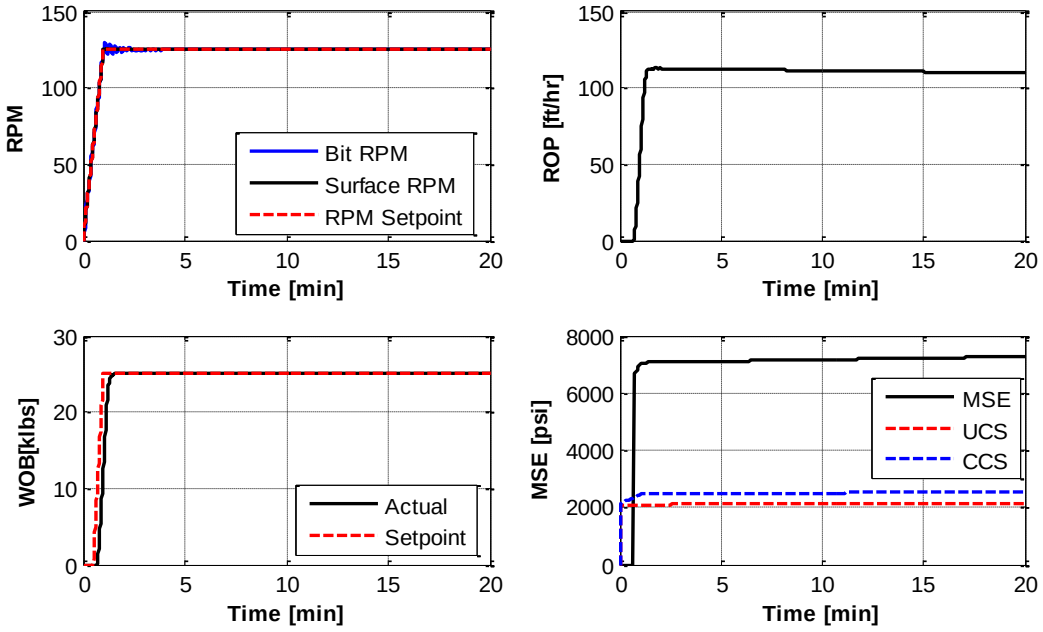

Figure F.19: Drilling inputs and outputs for Controller 1.

Controller 2A Simulation Results

The objective of this controller is to maximize ROP and HSI while keeping WOB to a constant setpoint and varying the RPM and pump rate. The backpressure is kept at atmospheric conditions. The cost function uses the following weights:

$$W_1 = 0.9, \qquad W_3 = 0.1, \qquad W_2 = W_4 = 0, \qquad V = \begin{bmatrix} 10^{-3} & 0 & 0 & 0 \\ 0 & 0 & 0 & 0 \\ 0 & 0 & 10^{-3} & 0 \\ 0 & 0 & 0 & 0 \end{bmatrix}$$

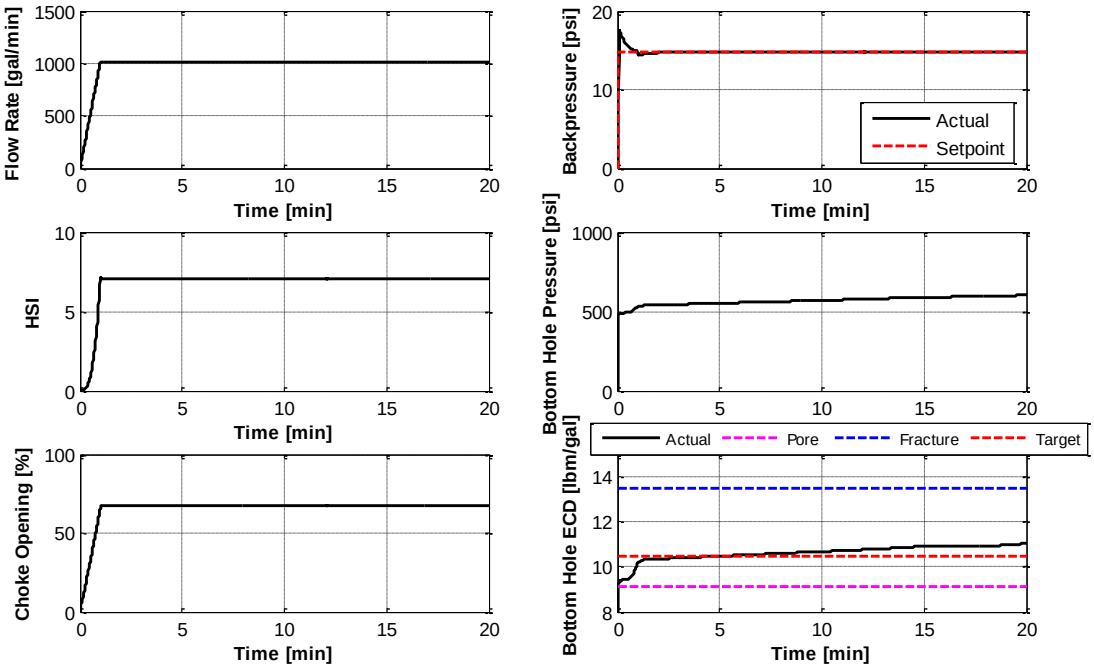

Figure F.20: Hydraulics inputs and outputs for Controller 2A.

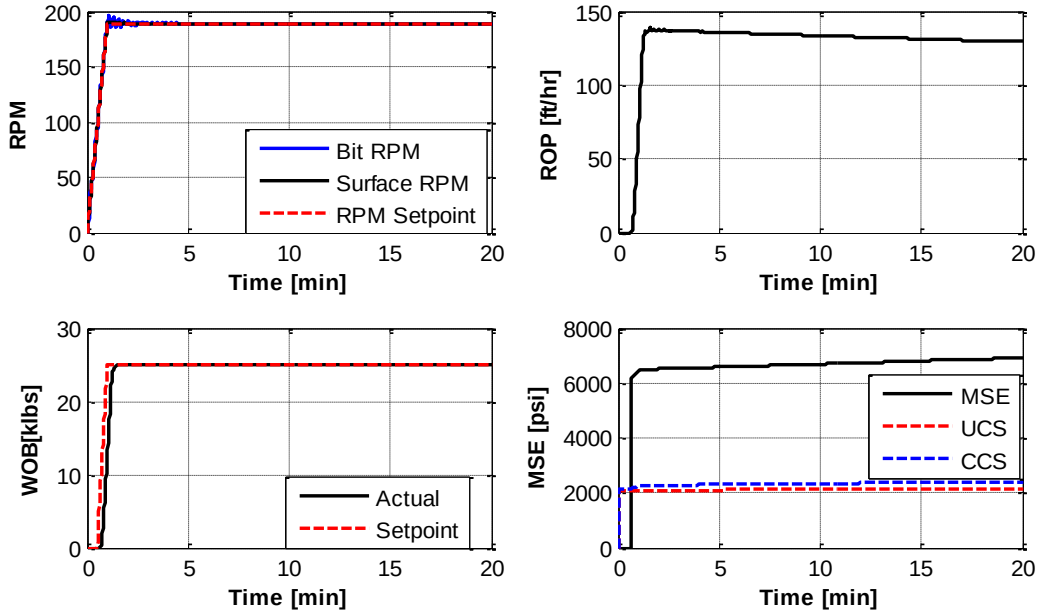

Figure F.21: Drilling inputs and outputs for Controller 2A.

Controller 2B Simulation Results

The objective of this controller is to minimize MSE and maximize HSI for a setpoint ROP value. RPM, WOB and pump SPM are allowed to vary, while the backpressure is again kept at atmospheric conditions. The cost function weights are:

$$W_1 = W_4 = 0, \qquad W_2 = 0.9, \qquad W_3 = 0.1; \; V = \begin{bmatrix} 10^{-2} & 0 & 0 & 0 \\ 0 & 10^{-6} & 0 & 0 \\ 0 & 0 & 10^{-4} & 0 \\ 0 & 0 & 0 & 0 \end{bmatrix}$$

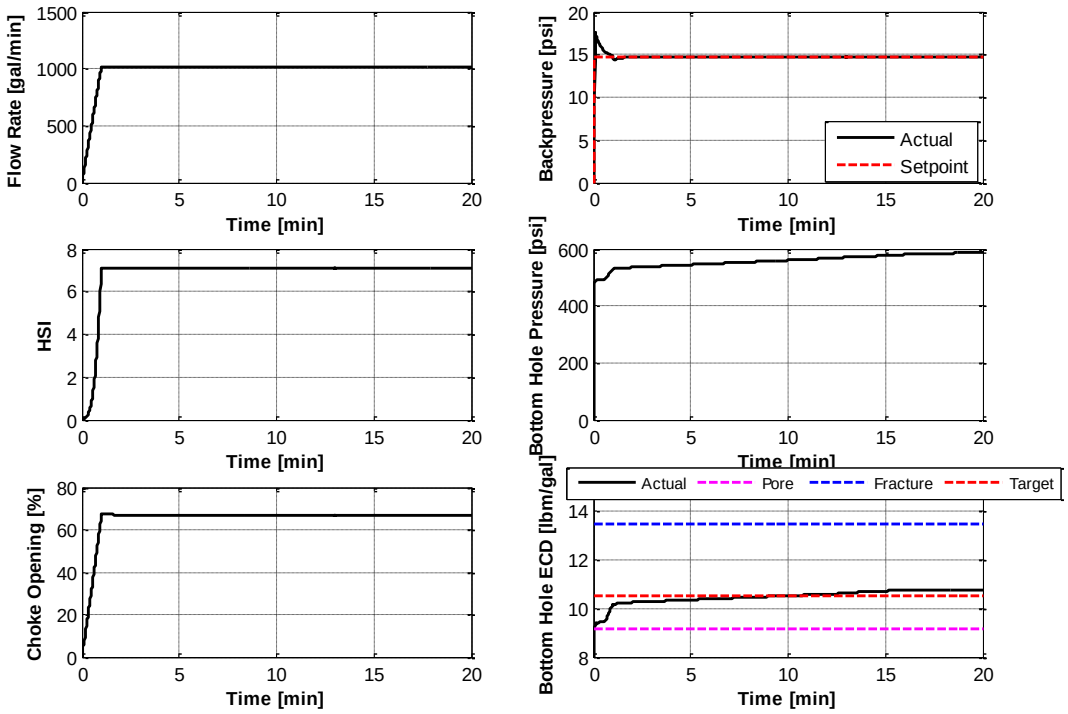

Figure F.22: Hydraulics inputs and outputs for Controller 2B.

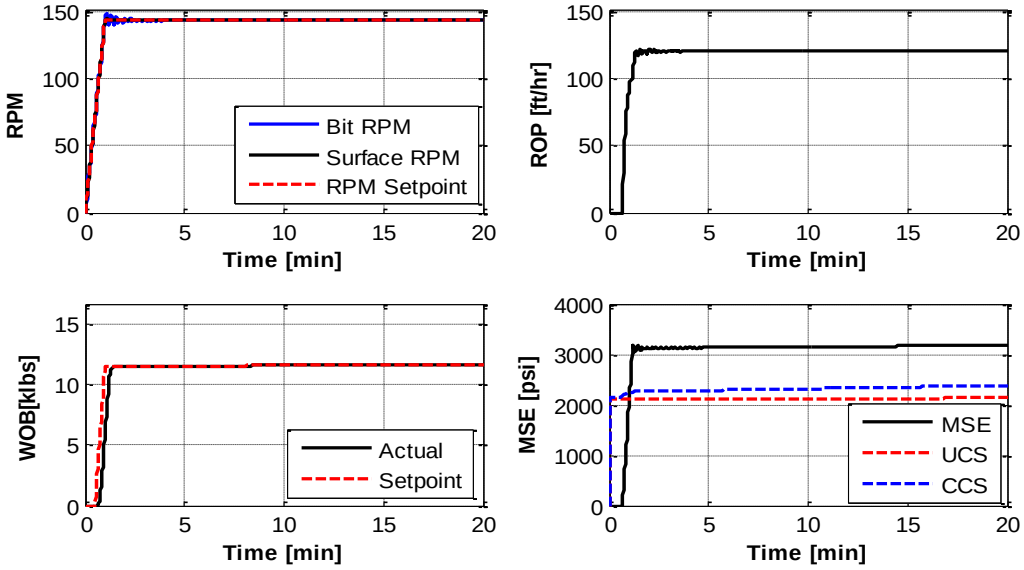

Figure F.23: Drilling inputs and outputs for Controller 2B.

Controller 2C Simulation Results

The objective of this controller is to maximize ROP and HSI, and keep the ECD as close to the target value as possible using both the pump rate and backpressure. RPM is allowed to vary while WOB is kept constant. The cost function weights are:

$$W_1 = 0.5, \qquad W_2 = 0, \qquad W_3 = 0.2, \qquad W_4 = 0.3,$$

$$V = \begin{bmatrix} 10^{-3} & 0 & 0 & 0 \\ 0 & 0 & 0 & 0 \\ 0 & 0 & 10^{-3} & 0 \\ 0 & 0 & 0 & 10^{-4} \end{bmatrix}$$

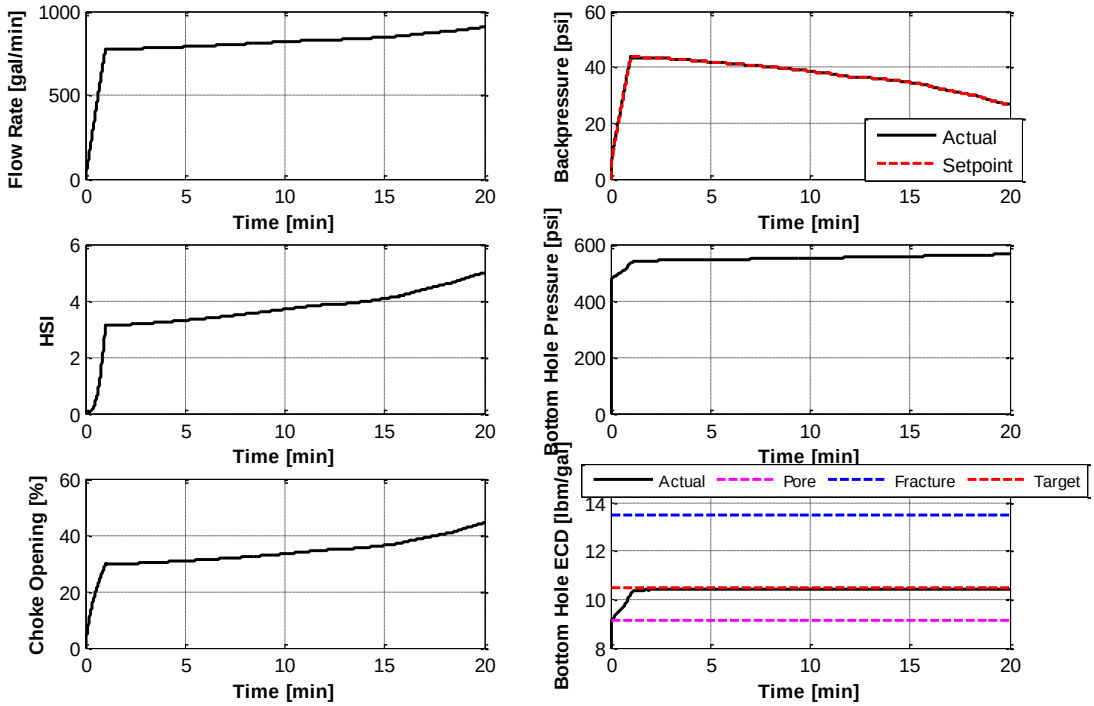

Figure F.24: Hydraulics inputs and outputs for Controller 2C.

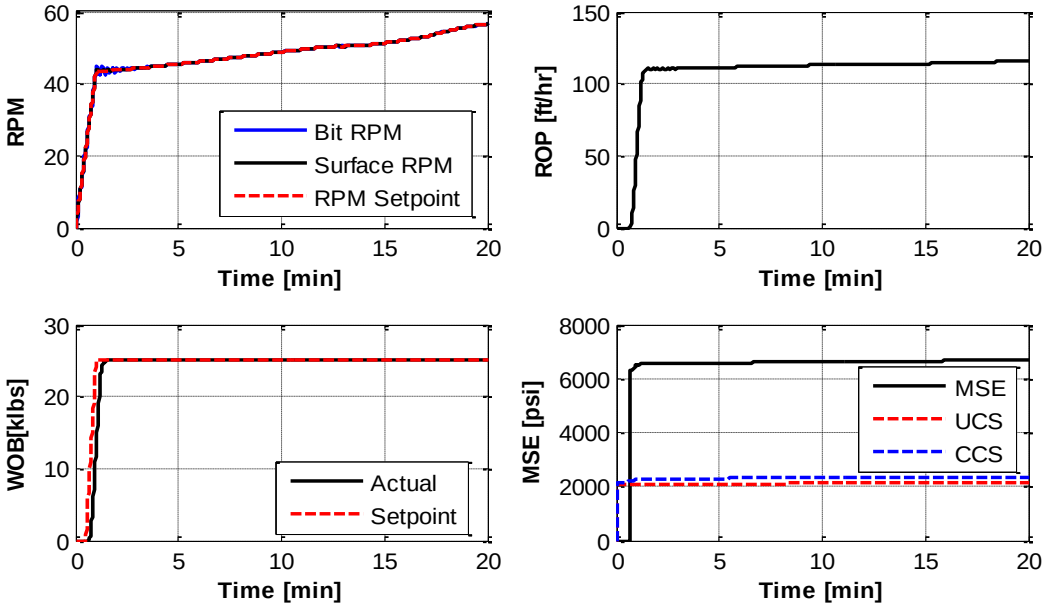

Figure F.25: Drilling inputs and outputs for Controller 2C.

Discussion of Results

The naïve controller achieved a high ROP value, but the other performance metrics were far from optimal. The optimal controllers show good performance with respect to the objective they were tasked with, and were overall superior to the naïve controller. Controller 2A achieved the highest ROP, at the expense of a larger MSE value which can be detrimental in the long term. Controller 2A and 2B performed better in terms of HSI maximization than controller 2C, since the latter had to trade-off hydraulics optimization for downhole pressure management. Controller 2B minimized the MSE while still keeping an optimal HSI value of 7 for most of the run. In assessing MSE optimization, values of Unconfined Compressive Strength (UCS) and Confined Compressive Strength (CCS) are also observed, with the latter derived using the principles outlined in (Caicedo et al., 2005). Since CCS depends on the overbalance, drilling with downhole ECD closer to the pore pressure gradient will lead to lower MSE values, and consequently, higher ROP.

All controllers managed to avoid the onset of stick-slip and bit RPM closely followed the RPM prescribed on surface. As the drillstring is being extended, the operational envelope for stick-slip avoidance will reduce, and the system will adjust the setpoints accordingly. It is also worth noting that, while controller 2A and 2B yielded acceptable ECD values with a choke setpoint on the order of atmospheric pressure, this value will not be enough at higher depths. Since pump rate is limited by pump performance and hole cleaning considerations, the change in backpressure needs to be coordinated with the change in pump rate. For the setpoint generator to effectively achieve this, higher weight must be placed on the pressure management term of the objective function, and the operation will have to carry on with ROP, MSE or HSI values that might be deemed sub-optimal in a different context. Visualization of the control input trajectories overlaid on the constraints plots (Figure F.14 and Figure F.15) may serve to reassure the driller or the system operator that valid parameter combinations are being selected at all times.

Application to Pipe Tripping

Many of the problems that account for major downtimes during the drilling process occur when the drillstring is being tripped in/out of the hole. These issues are typically arise from the BHA / drill pipe getting stuck inside the hole or kick or lost circulation due to surge and swab effects. Therefore, a tripping operation requires careful attention of the driller to avoid costly down time. Another important issue is the effective detection of such occurrences. Not only is it difficult to prevent the occurrence of such events, but also it is equally difficult to detect a kick or a loss after it has started and delay in taking appropriate actions can result in disastrous consequences. Hence, an automated tripping system is potentially beneficial if it can eliminate the chance of such events happening while also optimizing for maximum tripping speeds to complete the drilling process as effectively as possible.

Control Variables
During a tripping operation, the main variables that are controlled are the acceleration/deceleration and the velocity of the drill string. The acceleration will primarily depend on the torque applied by the drawworks and the velocity depends on the duration of the applied torque.

Known Information
For this scenario, the variables below are assumed to be known information:

- Real-time depth position of the drillstring
- BHA / drillstring configuration details
- Mud properties
- Drawworks performance specifications

Set of Base Look-up Tables (BLUTs) Required
Before the controller can be designed, one needs to collect all the LUTs required to build it. The following is a list of LUTS that are needed to build a controller for a tripping out operation.

- BLUT 6: LUT relating pore pressure to depth. This data is usually obtained from offset wells and seismic tests. The operator usually owns this information.
- BLUT 7: LUT of fracture pressure vs. depth. This data is also obtained from offset wells. Formation integrity tests are often used to update this table.
- BLUT 1: LUT of hydrostatic pressure as function of depth. This data is calculated from the mud weight being used at a certain depth. A plot of hydrostatic pressure, pore pressure and fracture pressure vs. depth is available in Figure F.37.
- BLUT 19: LUT of change in pressure vs drillstring velocity and drillstring acceleration. This BLUT is obtained by performing simulations for a range of velocity/accelerations using a transient hydraulics model. This plot is available in Figure F.37.
- BLUT 20: LUT of drawworks force capability versus drillstring velocity. This information is obtained from the drawworks manufacturer. A performance plot of a typical drawworks is available in Figure F.37.
- BLUT 21: LUT of drill string velocity as a function of initial drill string velocity and force. This LUT is obtained by performing simulations using a mechanical model of the tripping operation. The results are available in Figure F.37.

Combining Base LUTs to Obtain Control Relevant Derived LUTs

The BLUTs described in the previous sections need to be combined to obtain LUTs that may be readily used by the control algorithm designer. A flow chart is presented in Figure F.26 that outlines how the BLUTs may be combined. First, BLUTs 6, 7, 18 and 19 are combined in order to define an operating region for drillstring velocity and acceleration only in terms of pressure constraints. Next, the drawworks limits are converted into an operating region in terms of velocity and acceleration using the mechanical model and then enforced on the pressure operating region. Combining these LUTs in the order presented lead to the operating region LUTs that are visually represented in Figure F.27. The operating region on the left represents the allowable combinations of velocity and acceleration that will stay within the pressure limits only and the plot on the right of Figure F.27 demonstrates the allowable velocity/acceleration combinations that will satisfy both the pressure constraints as well as the drawworks limits.

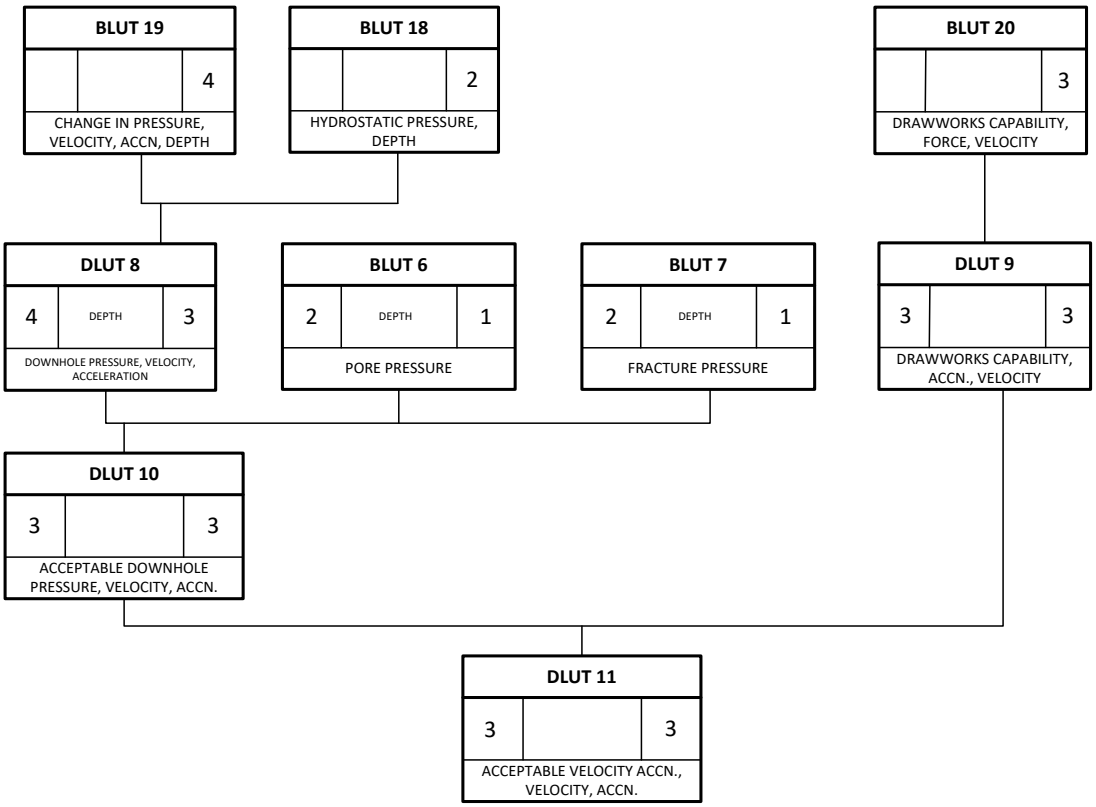

Figure F.26: A flowchart showing how data is combined to arrive at pipe tripping operating region look-up table.

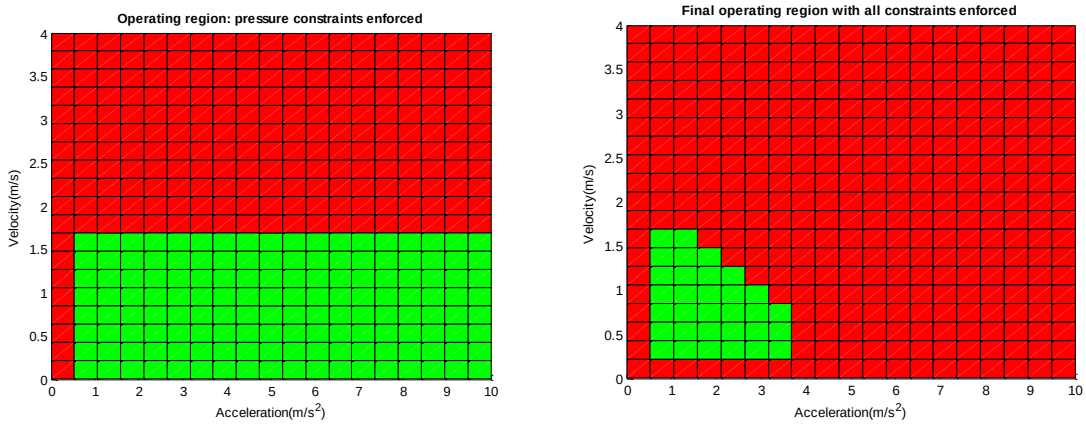

Figure F.27: Operating region look-up tables for pipe tripping operation.

Control Algorithm Design and Simulation Results

There are two critical pieces of information that will be provided to the control system designers so that they may proceed to design the controller: the operating region LUT and the system dynamics LUT. The following section briefly outlines how a potential controller can be designed using such information. To begin with, the operating region obtained in Figure F.27 is evaluated in terms of three different controller objectives: tripping time, operation safety with regards to swabbing pressure and operation safety with regards to drawworks limits. Using the three regions presented in Figure F.28, the controller can define an optimization objective and select the appropriate velocity/acceleration combination for the 90ft tripping operation. To achieve the optimization task, the controller assigns a weight to each of the objectives and then searches for the optimum combination in the combined solution space. The objective weights are defined as follows:

$$W_P = Swabbing\ Pressure\ Safety$$

$$W_V = Minimum\ Tripping\ Time$$

$$W_D = Drawworks\ Power\ Safety$$

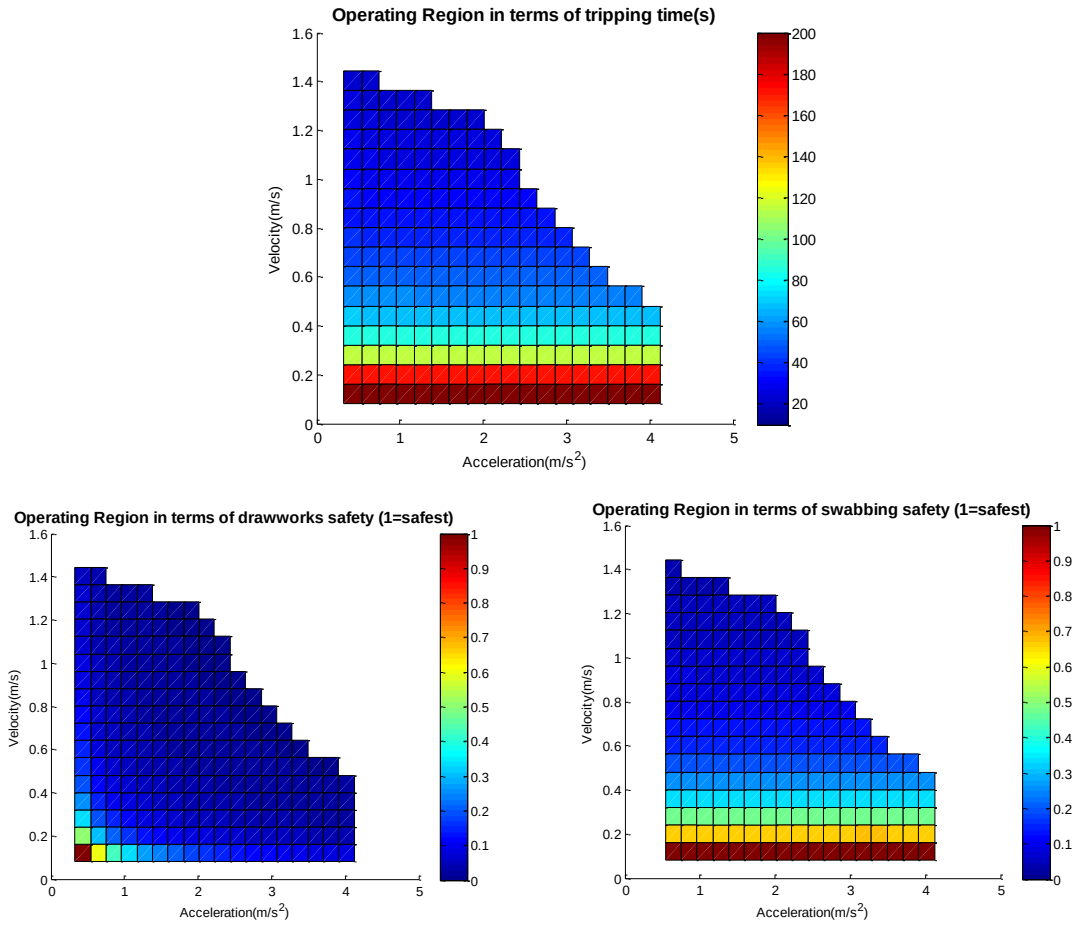

Figure F.28: Tripping operating region for various controller objectives.

During the real-time operation, the controller uses BLUT 21 in Figure F.37 in order to determine the input to the drawworks. The controller refines this input and the planned trajectory every second based on the real-time feedback of drillstring velocity and position.

Controller 1

This naive controller does not perform any optimization. It simply selects the centroid of the operating region to perform the tripping operation.

$$v = 0.7\frac{m}{s}\,, a = 1.5\frac{m}{s^2}$$

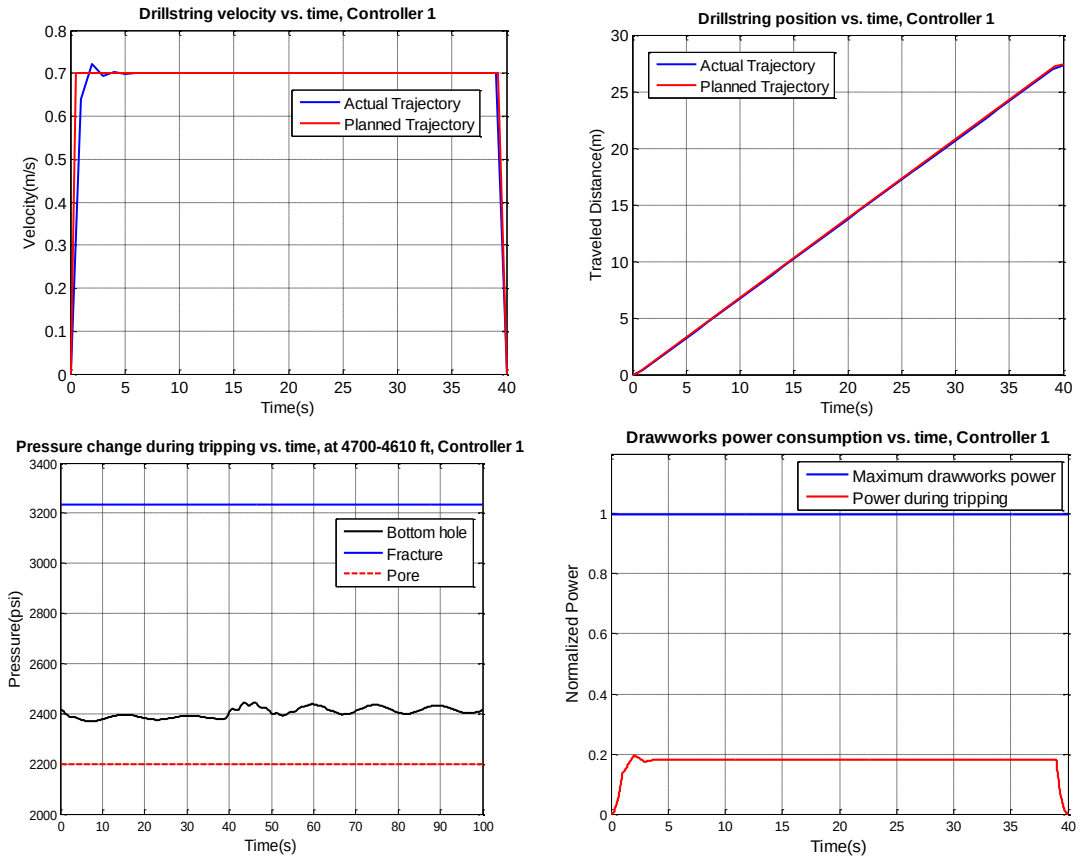

Figure F.29: Simulation results for Controller 1 with no optimization objective.

Controller 2

The goal of this controller is to optimize for both swabbing pressure safety and drawworks power safety. The selected objective weights in this case are:

$$W_P = 0.3,\ W_V = 0.1, W_D = 0.6$$

The refined operating region for this controller objective is shown in Figure F.30. The selected velocity/acceleration combination based on this objective becomes:

$$v = 0.16\frac{m}{s}\ , a = 0.75\frac{m}{s^2}$$

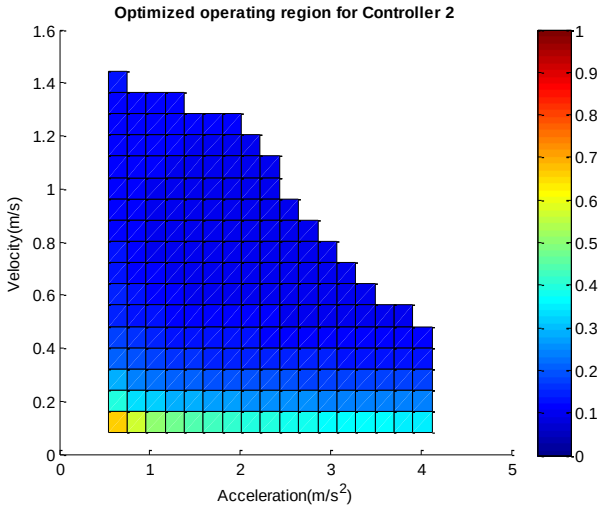

Figure F.30: Refined solution space for Controller 2 objective.

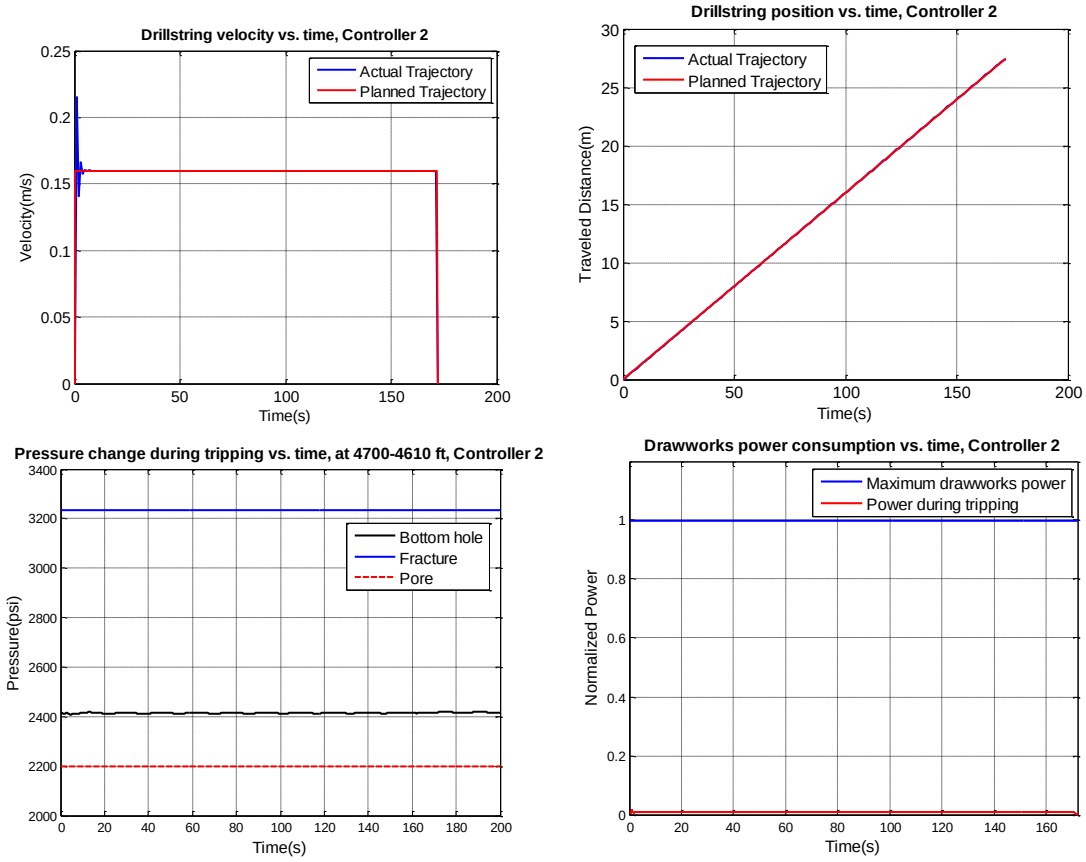

Figure F.31: Simulation results for Controller 2 with the goal of optimizing for swabbing pressure safety and drawworks performance safety.

Controller 3

The goal of this controller is to optimize for a fast tripping operation while staying within the constraints. Swabbing pressure safety and drawworks power safety are not the main objectives of this controller. The selected objective weights in this case are:

$$W_P = 0.3\,, W_V = 0.7, W_D = 0$$

The refined operating region for this controller objective is shown in Figure F.32. The selected velocity/acceleration combination based on this objective becomes:

$$v = 1.17\frac{m}{s}\,, a = 1.28\frac{m}{s^2}$$

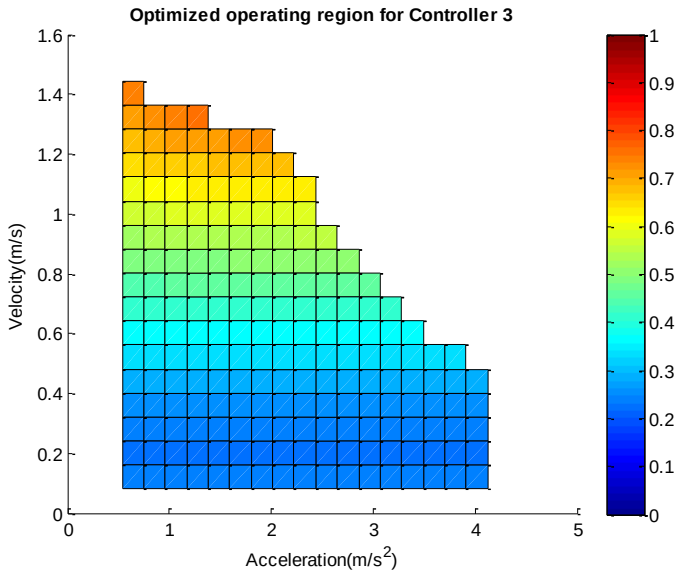

Figure F.32: Refined solution space for Controller 3 objective.

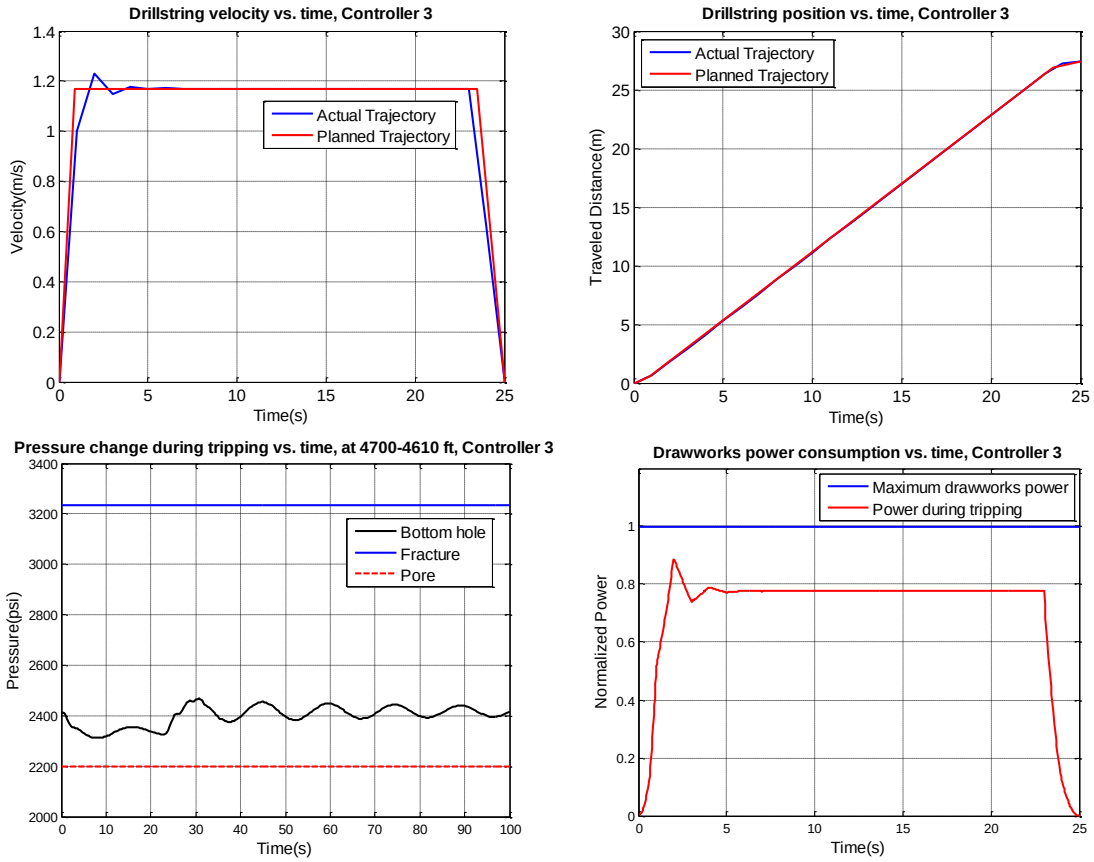

Figure F.33. Simulation results for Controller 3 with the goal of optimizing for shortest tripping time while staying within the constraints.

Discussion of Results

The simulation results presented in Figure F.29, Figure F.31 and Figure F.33 conform well to each controller's main objective. In the case of the naïve controller, the operation occurs without any specific objective while staying within the main operating region. Controller 2 aimed at minimizing swabbing pressures and staying away from the drawworks' maximum power curve. As shown in Figure F.31 this controller takes 175 seconds to complete the 90ft tripping distance. In the case of Controller 3, the main optimization objective was to minimize tripping time while remaining within the main constraints. As seen in Figure F.33, the controller is capable of completing the tripping distance of 90 ft in 25 seconds. As expected, the controller gets relatively close to the drawworks maximum available power and causes higher swabbing pressures than Controller 2.

Conclusions

Automation has long promised increased efficiency and safety, and it certainly shows the potential to deliver these. However, industry progress and results have often been isolated and disconnected. In this paper, we identified some of the main barriers to the broad adoption of automation, and detail a data sharing construct (CPDs/CPTs) and control architecture that would potentially make automating drilling tasks more amenable. Some key features of the methodology are:

- The person in charge of working with the automated system (typically, the driller) needs to be able to understand how the computer chooses the set points. Until such time that automated systems are reliable to a very high degree, this is a necessity for this person to be able to trust the automated system. Hence simpler "close to optimal" solutions that the driller understands should be preferred over complex, truly optimal solutions. The methodology presented here enables this approach.
- The methodology described here is very amenable to integrating complex data from various sources. LUTs are universal, easy to display, interpret, validate and troubleshoot. When uncertainty-related information is available, it can be stored as CPDs/CPTs, from which the relevant LUTs can be extracted easily in real-time. The methodology was demonstrated on two distinct automation tasks. These two tasks shared some of the BLUTs. This demonstrated the modular nature of this architecture wherein BLUTs once added to the database can be used in multiple tasks.
- Data-aggregation is key to automation, and CPD's/CPTs provide an elegant and practical means to that end.
- The architecture presented in this paper does not require replacing existing sensors with sophisticated sensors (although in the end this may be highly desirable). It is understood that such replacement may not be practical in the vast majority of the land-based rigs for economic reasons. There is a built-in mechanism within this architecture to handle uncertainty. This makes the approach more amenable to rapid and widespread use, even for the existing set of rig sensors.
- The authors envision the automation algorithms to eventually become the responsibility of the operator (much like a well plan), built with support from the service providers and the rig contractors, on whose equipment the controller will run. These algorithms should be built during the well planning process by an integrated automation team with the active involvement of all stakeholders. This is enabled here by the separation of domain expertise from control algorithm design.
- The operator may require the service providers, the contractors, the equipment manufactures and other to share data in a CPD/CPT/LUT format. The data providers do not compromise their proprietary know-how by disclosing information in this format, and this helps them maintain their competitive edge. There will, however,

need to be accountability for data quality and reliability. The probabilistic approach suggested in this paper enables this. The control architecture is implementable in a software platform that allows the engineers in the operator company to use visual programming techniques to implement and simulate their control law. Such software may be made available by the service providers for the operator.

Acknowledgments

The authors gratefully acknowledge the feedback and input from the Drilling Rig Automation Group at the University of Texas at Austin, in the preparation of this manuscript.

References

Aadnoy, B.S., Cooper, I., Miska, S.Z., Mitchell, R.F., and Payne, M.L (2009). Advanced Drilling and Well Technology. Society of Petroleum Engineers.

Ahmed, R., Enfis, M., Miftah-El-Kheir, H., Laget, M. & Saasen, A. (2010, September 19). The Effect of Drillstring Rotation on Equivalent Circulation Density: Modeling and Analysis of Field Measurements. SPE Annual Technical Conference and Exhibition, Florence, Italy. doi: 10.2118/135587-MS

Alpigini, J. J. (2004). Dynamical system visualization and analysis via performance maps. Information Visualization, 3(4), 271-287.

Ambrus, A., Ashok, P., & van Oort, E. (2013, September). Drilling Rig Sensor Data Validation in the Presence of Real-Time Process Variations. Society of Petroleum Engineers. doi:10.2118/166387-MS

Arnaout, A., Thonhauser, G., Esmael, B., & Fruhwirth, R. K. (2012, January 1). Intelligent Real-time Drilling Operations Classification Using Trend Analysis of Drilling Rig Sensors Data. Society of Petroleum Engineers. doi:10.2118/163302-MS

Ashok, P., & Tesar, D. (2008). A visualization framework for real time decision making in a multi-input multi-output system. Systems Journal, IEEE, 2(1), 129-145.

Ashok, P., & Tesar, D. (2013). The Need for a Performance Map Based Decision Process. Systems Journal, IEEE, 7(4), 616-631.

Bertsekas, D. P. (1999). Nonlinear Programming: 2nd Edition. Athena Scientific

Caicedo, H.U., Calhoun, W.M., & Ewy, R.T (2005, February 23). Unique ROP Predictor using Bit-Specific Coefficient of Sliding Friction and Mechanical Efficiency as a Function of Confined Compressive Strength Impacts Drilling Performance. SPE IADC Drilling Conference, Amsterdam, The Netherlands. doi:10.2118/92576-MS

Cayeux, E., Daireaux, B., & Dvergsnes, E. (2011, December 1). Automation of Drawworks and Topdrive Management To Minimize Swab/Surge and Poor-Downhole-Condition Effect. Society of Petroleum Engineers. doi:10.2118/128286-PA

Cayeux, E., Daireaux, B., & Dvergsnes, E. (2011, March 1). Automation of Mud-Pump Management: Application to Drilling Operations in the North Sea. Society of Petroleum Engineers. doi:10.2118/128285-PA

Cayeux, E., Daireaux, B., Dvergsnes, E. W., & Florence, F. (2013, March 5). Toward Drilling Automation: On the Necessity of Using Sensors That Relate to Physical Models. Society of Petroleum Engineers. doi:10.2118/163440-MS

Chien, S.-F. (1994, December 1). Settling Velocity of Irregularly Shaped Particles. Society of Petroleum Engineers. doi:10.2118/26121-PA

Clark, R.K., & Bickham, K.L. (1994, September 25). A Mechanistic Model for Cuttings Transport. SPE Annual Technical Conference and Exhibition, New Orleans, LA. doi: 10.2118/28306-MS

Coffey, Brian. (2012). Using Building Simulation and Optimization to Calculate Lookup Tables for Control. UC Berkeley: Center for the Built Environment. Retrieved from: https://escholarship.org/uc/item/1202p562.

Dunayevsky, V. A., & Abbassian, F. (1998, June 1). Application of Stability Approach to Bit Dynamics. Society of Petroleum Engineers. doi:10.2118/30478-PA

Dunlop, J., Isangulov, R., Aldred, W. D., Sanchez, H. A., Flores, J. L. S., Herdoiza, J. A., Luppens, C. (2011, January 1). Increased Rate of Penetration Through Automation. Society of Petroleum Engineers. doi:10.2118/139897-MS

Dwars, S., Stulemeijer, I., & Runia, J. J. (2013, March 5). A brief history of the Shell "Soft Torque Rotary System" and some recent case studies. Society of Petroleum Engineers. doi:10.2118/163548-MS

Feuerlicht, G. (2010, April). Database Trends and Directions: Current Challenges and Opportunities. In DATESO (pp. 163-174).

Florence, F., Iversen, F. P., Macpherson, J. D., Zamora, M., Chapman, C. D., Laing, M. L., & de Wardt, J. P. (2013, September 30). Drilling Systems Automation: Current State, Initiatives and Potential Impact. Society of Petroleum Engineers. doi:10.2118/166263-MS

Florence, F., Porche, M., Thomas, R., & Fox, R. (2009, January 1). Multi-Parameter Autodrilling Capabilities Provide Drilling, Economic Benefits. Society of Petroleum Engineers. doi:10.2118/119965-MS

Godhavn, J., & Knudsen, K. A. (2010, January 1). High Performance and Reliability for MPD Control System Ensured by Extensive Testing. Society of Petroleum Engineers. doi:10.2118/128222-MS

Guo, B. and Liu, G. (2011). Applied Drilling Circulation Systems: Hydraulics, Calculations and Models. Gulf Professional Publishing,

Jansen, J. D., & Van den Steen, L. (1995). Active damping of self-excited torsional vibrations in oil well drillstrings. Journal of sound and vibration, 179(4), 647-668.

Jansen, J. D., Stulemeijer, I. P., Van Walstijn, B. G., & Worrall, R. N. (1992). U.S. Patent No. 5,117,926. Washington, DC: U.S. Patent and Trademark Office.

Kaasa, G.-O., Stamnes, Ø. N., Aamo, O. M., & Imsland, L. S. (2012, March 1). Simplified Hydraulics Model Used for Intelligent Estimation of Downhole Pressure for a Managed-Pressure-Drilling Control System. Society of Petroleum Engineers. doi:10.2118/143097-PA

Kyllingstad, A., & Nessjøen, P. J. (2009, January 1). A New Stick-Slip Prevention System. Society of Petroleum Engineers. doi:10.2118/119660-MS

Lapeyrouse, N. J. (2002). Formulas and Calculations for Drilling, Production and Workover. Second Edition. Gulf Professional Publishing,

Matheus, J., & Naganathan, S. (2010, January 1). Automation of Directional Drilling--Novel Trajectory Control Algorithms for RSS. Society of Petroleum Engineers. doi:10.2118/127925-MS

MATLAB Optimization Toolbox User's Guide - Version 6.0, (2011), The MathWorks, Inc., Natick, MA, USA.

Ringer, M., Luppens, J. C. (Chris., Chapman, C. D., Dunlop, J., Yu, H., Wong, R., & Liu, Q. (2013, March 5). Advances in Real-Time Event Detection While Drilling. Society of Petroleum Engineers. doi:10.2118/163515-MS

Saeed, S., Lovorn, R. & Knudsen, K.A. (2012, March 6). Automated Drilling Systems for MPD – The Reality. Society of Petroleum Engineers. doi:10.2118/151416-MS

Santos, H., Leuchtenberg, C. & Shayegi, S. (2003, April 27). Micro-Flux Control: The Next Generation in Drilling Process. Society of Petroleum Engineers. doi:10.2118/81183-MS

van Riet, E.J., Reitsma, D. & Vandecraen, B. (2003, October 20). Development and Testing of a Fully Automated System to Accurately Control Downhole Pressure During Drilling Operations. Society of Petroleum Engineers. doi:10.2118/85310-MS

Warren, T. M., & Armagost, W. K. (1988, June 1). Laboratory Drilling Performance of PDC Bits. Society of Petroleum Engineers. doi:10.2118/15617-PA

Appendix A. Base look-up tables used in this paper

The base look-up tables are plotted in Figure F.34, Figure F.35, Figure F.36, and Figure F.37**.** The plots were generated for a measured depth of 2000 feet, unless depth was specified as an input, in which case the entire range (1000 to 4700 ft) was used to generate the plot.

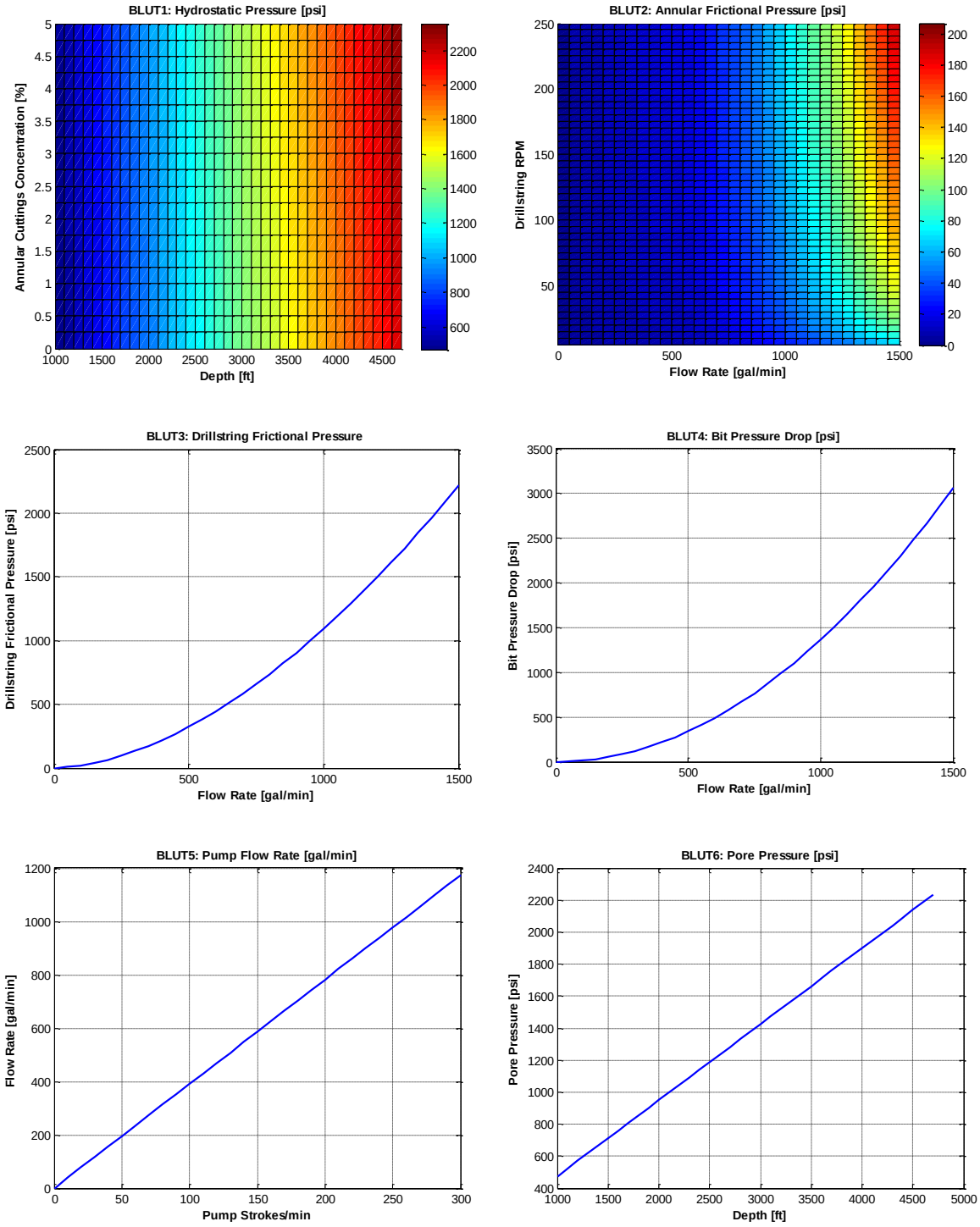

Figure F.34: Base look-up tables 1 through 6.

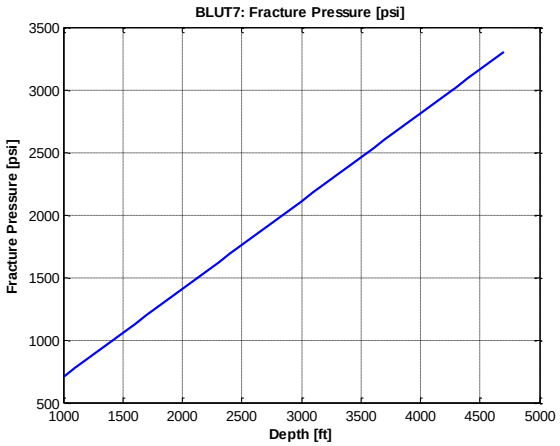

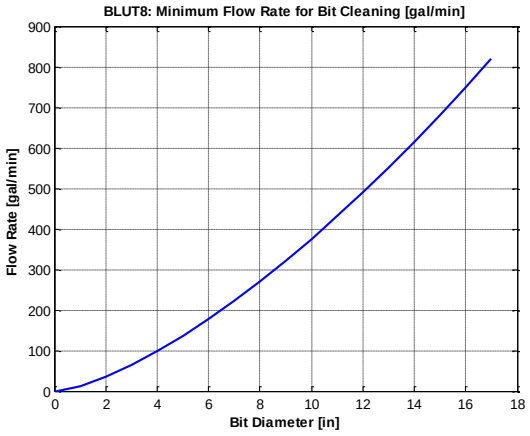

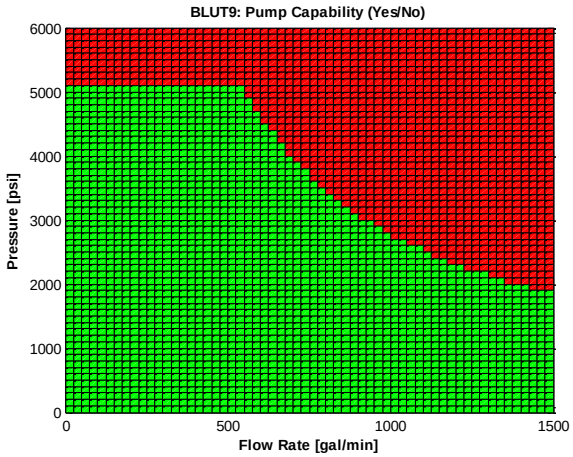

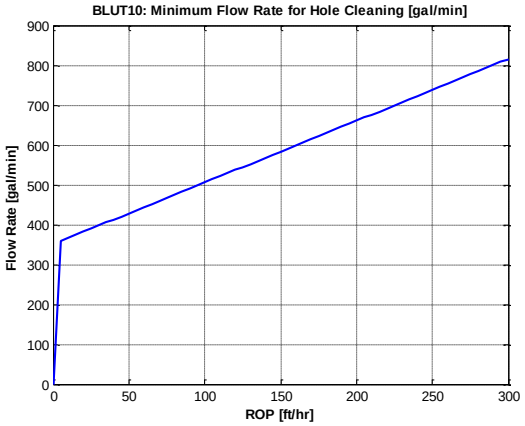

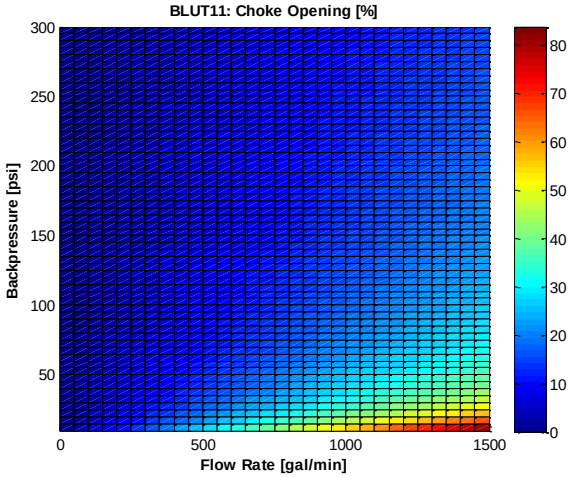

Figure F.35: Base look-up tables 7 through 11.

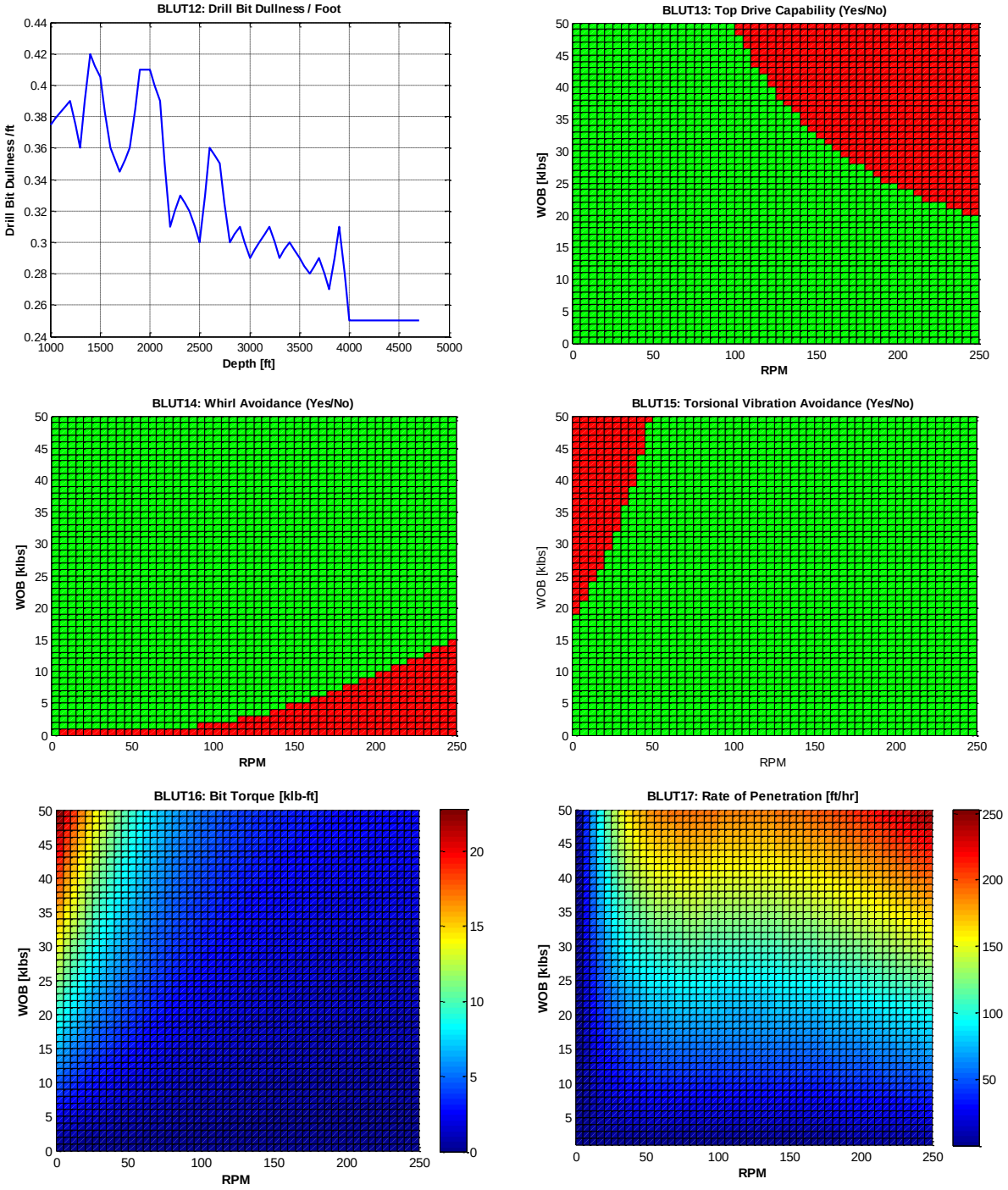

Figure F.36: Base look-up tables 12 through 17.

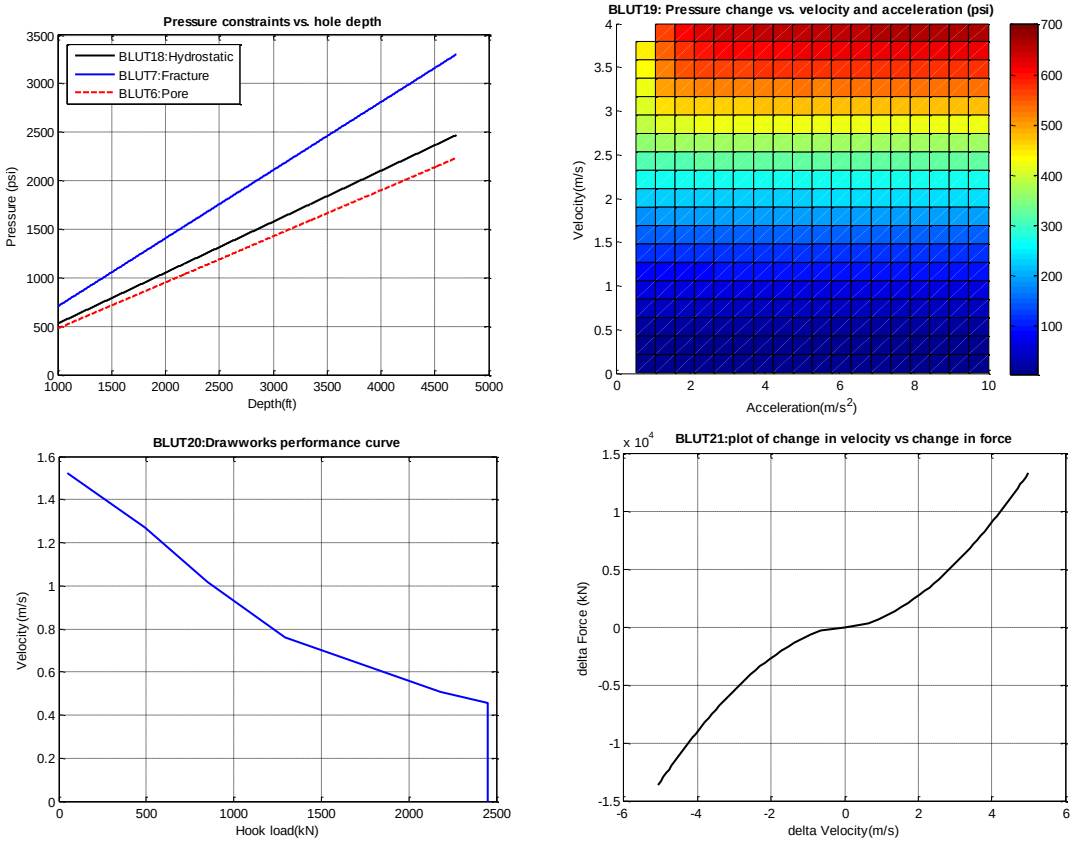

Figure F.37: Base look-up tables 18 through 21.

Bibliography

B. S. Aadnøy, I. Cooper, S. Z. Miska, R. Mitchell, and M. Payne. *Advanced drilling and well technology*. Society of Petroleum Engineers, 2009.

O. M. Aamo. Disturbance rejection in 2 x 2 linear hyperbolic systems. *IEEE Trans. Automat. Contr.*, 58(5):1095–1106, May 2013. ISSN 0018-9286. doi: 10.1109/TAC.2012.2228035. URL `http://ieeexplore.ieee.org/lpdocs/epic03/wrapper.htm?arnumber=6355616`.

U. J. F. Aarsnes, O. M. Aamo, and A. Pavlov. Quantifying Error Introduced by Finite Order Discretization of a Hydraulic Well Model. In *Australian Control Conference*, pages 54–59, Sydney, Australia, 2012.

U. J. F. Aarsnes, A. Ambrus, A. K. Vajargah, O. M. Aamo, and E. van Oort. A simplified gas-liquid flow model for kick mitigation and control during drilling operations. In *ASME 2015 Dynamic Systems and Control Conference*, pages V002T20A002–V002T20A002. American Society of Mechanical Engineers, 2015.

U. J. F. Aarsnes, B. Açıkmeşe, A. Ambrus, and O. M. Aamo. Robust controller design for automated kick handling in managed pressure drilling. *Journal of Process Control*, 47:46–57, 2016a.

U. J. F. Aarsnes, A. Ambrus, F. Di Meglio, A. K. Vajargah, O. M. Aamo, and E. van Oort. A simplified two-phase flow model using a quasi-equilibrium momentum balance. *International Journal of Multiphase Flow*, 83:77–85, 2016b.

U. J. F. Aarsnes, T. Flåtten, and O. M. Aamo. Review of two-phase flow models for control and estimation. *Annual Reviews in Control*, 42:50–62, 2016c.

T. Ahmed. *Reservoir Engineering Handbook*. Gulf Professional Publishing, 2006.

W. Aldred, R. Hutin, J. C. Luppens, and G. Ritchie. SPE/IADC 111757 Development and Testing of a Rig-Based Quick Event Detection System to Mitigate Drilling Risks. In *SPE/IADC Drilling Conference*, Orlando, Florida, USA, 2008.

A. Ambrus, U. J. F. Aarsnes, A. K. Vajargah, B. Akbari, and E. van Oort. A simplified transient multi-phase model for automated well control applications. In *International Petroleum Technology Conference*. International Petroleum Technology Conference, 2015a.

A. Ambrus, P. Pournazari, P. Ashok, R. Shor, and E. van Oort. SPE/IADC 173164 Overcoming Barriers to Adoption of Drilling Automation: Moving Towards Automated Well Manufacturing. In *SPE/IADC Drilling Conference and Exhibition*, London, United Kingdom, 2015b.

A. Ambrus, U. J. F. Aarsnes, A. K. Vajargah, B. Akbari, E. van Oort, and O. M. Aamo. Real-time estimation of reservoir influx rate and pore pressure using a simplified transient two-phase flow model. *Journal of Natural Gas Science and Engineering*, 32:439–452, 2016.

A. Ambrus, A. K. Vajargah, P. Ashok, and E. van Oort. Choke controller design for automated managed pressure drilling with realistic operational system conditions. In *AADE National Technical Conference and Exhibition*. American, 2017.

B. D. Anderson and J. B. Moore. *Optimal Control Linear quadratic methods*. Courier Corporation, 1990. ISBN 0-486-45766-4.

H. B. Aradhye. Sensor fault detection, isolation, and accommodation using neural networks, fuzzy logic, and bayesian belief networks. Master's thesis, 1997.

A. Arnaout, R. Fruhwirth, B. Esmael, and G. Thonhauser. SPE 163302 Intelligent Real-time Drilling Operations Classification Using Trend Analysis of Drilling Rig Sensors Data. In *SPE Kuwait International Petroleum Conference and Exhibition*, Kuwait City, Kuwait, 2012.

A. Arnaout, P. Zoellner, G. Thonhauser, and N. Johnstone. SPE 167437 Intelligent Data Quality Control of Real-time Rig Data. In *SPE Middle East Intelligent Energy Conference and Exhibition*, Manama, Bahrain, 2013.

P. Ashok, G. Krishnamoorthy, and D. Tesar. Guidelines for managing sensors in cyber physical systems with multiple sensors. *Journal of Sensors*, 2011.

K. J. Åström and R. M. Murray. *Feedback systems: an introduction for scientists and engineers*. Princeton university press, 2010. ISBN 9780691135762. URL `http://books.google.com/books?hl=en\&lr=\&id=cdG9fNqTDS8C\&oi=fnd\&pg=PP2\&dq=Feedback+Systems:+An+Introduction+for+Scientists+and+Engineers\&ots=K4FHawqkgU\&sig=7JXrh4cOEW-ymc1NWM8HvtZa4e8`.

D. H. Beggs and J. P. Brill. A study of two-phase flow in inclined pipes. *Journal of Petroleum technology*, 25(05):607–617, 1973.

K. H. Bendiksen, D. Maines, M. Randi, and S. Nuland. The Dynamic Two-Fluid Model OLGA: Theory and Application. *SPE Production Engineering*, 6(4):171–180, May 1991. ISSN 08859221.

T. W. Bickmore. Real-time sensor data validation. Technical Report NASA Contractor Report No. 195295, Gencorp Aerojet Propulsion Division, 1994.

K. S. Bjørkevoll, D. O. Molde, R. Rommetveit, and S. Syltøy. SPE/IADC 112739 MPD Operation Solved Drilling Challenges in a Severely Depleted HP/HT Reservoir. In *SPE/IADC Drilling Conference and Exhibition*, Orlando, Florida, USA, 2008.

S. P. Boyd, L. El Ghaoui, E. Feron, and V. Balakrishnan. *Linear matrix inequalities in system and control theory*, volume 15. SIAM, 1994.

O. Breyholtz, G. Nygaard, and M. Nikolaou. Automatic control of managed pressure drilling. In *American Control Conference (ACC), 2010*, pages 442–447, June 2010a. doi: 10.1109/ACC.2010.5531008.

Ø. Breyholtz, G. Nygaard, H. Siahaan, and M. Nikolaou. Managed Pressure Drilling: A multi-level control approach. In *SPE Intelligent Energy Conference and Exhibition*, Utrecht, The Netherlands, 2010b.

A. Calderoni, A. Chiura, P. Valente, F. Soliman, E. Squintani, R. Vogel, and J. Jenner. SPE 102859 Balanced Pressure Drilling With Continuous Circulation Using Jointed Drillpipe - Case History, Port Fouad Marine Deep 1, Exploration Well Offshore Egypt. In *SPE Annual Technical Conference and Exhibition*, San Antonio, Texas, USA, 2006.

L. A. Carlsen, G. Nygaard, J. E. Gravdal, I. Petroleum, M. Nikolaou, J. Schubert, and A. Texas. SPE / IADC 113693 Performing the Dynamic Shut-In Procedure Because of a Kick Incident When Using Automatic Coordinated Control of Pump Rates and Choke- Valve Opening. 2008.

L. A. Carlsen, G. Nygaard, and M. Nikolaou. Evaluation of control methods for drilling operations with unexpected gas influx. *Journal of Process Control*, 23(3):306 – 316, 2013. ISSN 0959-1524. doi: http://dx.doi.org/10.1016/j.jprocont.2012.12.003. URL `http://www.sciencedirect.com/science/article/pii/S0959152412002685`.

E. Cayeux and B. Daireaux. Precise Gain and Loss Detection Using a Transient

Hydraulic Model of the Return Flow to the Pit. In *SPE/IADC Middle East Drilling Technology Conference and Exhibition*, Dubai, UAE, 2013.

E. Cayeux, B. Daireaux, E. W. Dvergsnes, and F. Florence. SPE / IADC 163440 Toward Drilling Automation : On the Necessity of Using Sensors That Relate to Physical Models. In *SPE/IADC Drilling Conference and Exhibition*, Amsterdam, The Netherlands, 2013.

E. Cayeux, B. Daireaux, M. Karimi Balov, S. Haavardstein, L. Magne Stokland, and A. Saasen. Automatic performance analysis and estimation of risk level embedded in drilling operation plans. In *SPE Intelligent Energy International Conference and Exhibition*. Society of Petroleum Engineers, 2016.

N. Cheremisinoff and A. Davletshin. *Emergency Response Management of Offshore Oil Spills: Guidelines for Emergency Responders*. Wiley, 2010. ISBN 9781118011713. URL `http://books.google.com/books?id=v2hgPGwYNvoC`.

J. E. Chirinos, J. R. Smith, and D. A. Bourgoyne. A simplified method to estimate peak casing pressure during mpd well control. In *SPE Annual Technical Conference and Exhibition*. Society of Petroleum Engineers, 2011.

J. Choi, E. Pereyra, C. Sarica, H. Lee, I. S. Jang, and J. Kang. Development of a fast transient simulator for gas–liquid two-phase flow in pipes. *Journal of Petroleum science and engineering*, 102:27–35, 2013.

M. J. Chustz, J. May, C. Wallace, D. Reitsma, F. Paul, D. Scott, and L. D. Smith. SPE/IADC 108348 Managed-Pressure Drilling With Dynamic Annular Pressure-Control System Proves Successful in Redevelopment Program on Auger TLP in Deepwater Gulf of Mexico. In *SPE/IADC Managed Pressure Drilling and Underbalanced Operations Conference and Exhibition*, Galveston, Texas, USA, 2007.

M. J. Chustz, L. D. Smith, and D. M. Dell. Managed pressure drilling success continues on auger tlp. In *IADC/SPE Drilling Conference*. Society of Petroleum Engineers, 2008.

A. Craig, T. Jackson, D. Ramnarace, R. Schulze, and M. Briscoe. SPE/IADC 163416 The Evolution of Wired Drilling Tools: A Background, History and Learnings from the Development of a Suite of Drilling Tools for Wired Drillstrings. In *SPE/IADC Drilling Conference and Exhibition*, Amsterdam, The Netherlands, 2013.

F. Di Meglio and U. Aarsnes. A distributed parameter systems view of control problems in drilling. In *2nd IFAC Workshop on Automatic Control in Offshore Oil and Gas Production, Florianópolis, Brazil*, 2015.

D. Dodge and A. Metzner. Turbulent flow of non-newtonian systems. *AIChE Journal*, 5(2):189–204, 1959.

J. Dunlop, W. Lesso, W. Aldred, R. Meehan, M. Orton, and W. Fitzgerald. System and method for rig state detection, Oct. 31 2006. URL `https://www.google.com/patents/US7128167`. US Patent 7,128,167.

A. Eaton, L. Beal, S. Thorpe, E. Janis, C. Hubbell, J. Hedengren, R. Nybø, M. Aghito, K. Bjrkevoll, R. Boubsi, J. Braaksma, and G. van Og. Ensemble model predictive control for robust automated managed pressure drilling. In *SPE Annual Technical Conference and Exhibition*, Houston,Texas, 2015.

B. A. Eaton, C. R. Knowles, and I. Silberberg. The prediction of flow patterns, liquid holdup and pressure losses occurring during continuous two-phase flow in horizontal pipelines. *Journal of Petroleum technology*, 19(06):815–828, 1967.

S. Evje and K. K. Fjelde. Hybrid Flux-Splitting Schemes for a Two-Phase Flow Model. *Journal of Computational Physics*, 175(2):674–701, Jan. 2002. ISSN 00219991. doi: 10.1006/jcph.2001.6962. URL `http://www.sciencedirect.com/science/article/pii/S0021999101969621http://linkinghub.elsevier.com/retrieve/pii/S0021999101969621`.

K. Fjalestad, A. Mjaavatten, A. Aasheim, and R. Schüller. Simple equation for two-phase flow rate prediction through chokes. 2010.

P. Fredericks, G. Garcia, and O. Sehsah. SPE/IADC 130316 Managed Pressure Drilling Avoids Losses while Improving Drilling and ECD Management in the Gulf of Thailand. In *SPE/IADC Managed Pressure Drilling and Underbalanced Operations Conference and Exhibition*, Kuala Lumpur, Malaysia, 2010.

P. D. Fredericks, L. Smith, and K. J. Moreau. SPE/IADC 140289 ECD Management and Pore Pressure Determination with MPD Improves Efficiency in

GOM Well. In *SPE/IADC Drilling Conference and Exhibition*, Amsterdam, The Netherlands, 2011.

S. Gavrilyuk and J. Fabre. Lagrangian coordinates for a drift-flux model of a gas-liquid mixture. *International Journal of Multiphase Flow*, 22(3):453 – 460, 1996. ISSN 0301-9322. doi: http://dx.doi.org/10.1016/0301-9322(95)00085-2. URL http://www.sciencedirect.com/science/article/pii/0301932295000852.

J.-M. Godhavn. Control Requirements for Automatic Managed Pressure Drilling System. *SPE Drilling & Completion*, 25(3):17–19, Sept. 2010. ISSN 1064-6671. doi: 10.2118/119442-PA. URL https://www.onepetro.org/journal-paper/SPE-119442-PA.

J.-M. Godhavn and K. A. Knudsen. SPE/IADC 128222 High Performance and Reliability for MPD Control System Ensured by Extensive Testing. In *SPE/IADC Drilling Conference and Exhibition*, New Orleans, Louisiana, USA, 2010.

J.-M. Godhavn, A. Pavlov, G.-O. Kaasa, and N. L. Rolland. Drilling Seeking Automatic Control Solutions. In B. Sergio, editor, *18th IFAC World Congr. Milano*, pages 10842–10850, Milano, Italy, Aug. 2011. doi: 10.3182/20110828-6-IT-1002.00551. URL http://www.nt.ntnu.no/users/skoge/prost/proceedings/ifac11-proceedings/data/html/papers/0551.pdfhttp://www.ifac-papersonline.net/Detailed/51035.html.

R. E. Goodson and R. G. Leonard. A Survey of Modeling Techniques for Fluid Line Transients. *Journal of Basic Engineering*, 94(2):474, 1972. ISSN 00219223. doi: 10.1115/1.3425453. URL `http://fluidsengineering.asmedigitalcollection.asme.org/article.aspx?articleid=1436306`.

J. Gradishar, G. Ugueto, and E. van Oort. Setting Free the Bear: The Challenges and Lessons of the Ursa A-10 Deepwater Extended-Reach Well. *SPE Drilling & Completion*, 29(2):182–193, 2014. doi: 10.2118/163525-PA.

J. E. Gravdal, R. Lorentzen, K.-K. Fjelde, and E. H. Vefring. Tuning of computer model parameters in managed pressure drilling applications using an unscented kalman filter technique. In *SPE Annual Technical Conference and Exhibition*, number September, Dallas, Texas, 2005. doi: 10.2118/97028-MS. URL `http://www.onepetro.org/mslib/servlet/onepetropreview?id=SPE-97028-MS`.

J. E. Gravdal, M. Nikolaou, Ø. Breyholtz, and L. A. Carlsen. Improved kick management during mpd by real-time pore-pressure estimation. *SPE Drilling & Completion*, 25(04):577–584, 2010.

J. E. Gravdal, H. Siahaan, and K. S. Bjørkevoll. SPE 169211 Back-Pressure MPD in Extended-Reach Wells - Limiting Factors for the Ability to Achieve Accurate Pressure Control. In *SPE Bergen One Day Seminar*, Bergen, Norway, 2014.

B. Guo and G. Liu. *Applied Drilling Circulation Systems*. Gulf Professional Publishing, Boston, 2011. ISBN 978-0-12-381957-4. doi: http://dx.doi.org/

10.1016/B978-0-12-381957-4.00017-6. URL http://www.sciencedirect.com/science/article/pii/B9780123819574000176.

D. Hargreaves, S. Jardine, and B. Jeffryes. SPE 71369 Early Kick Detection for Deepwater Drilling: New Probabilistic Methods Applied in the Field. In *SPE Annular Technical Conference and Exhibition*, New Orleans, Louisiana, USA, 2001.

E. Hauge, O. M. Aamo, and J.-M. Godhavn. Model-based estimation and control of in/out-flux during drilling. In *2012 American Control Conference*, pages 4909–4914. IEEE, June 2012a. ISBN 978-1-4577-1096-4. doi: 10.1109/ACC.2012.6315027. URL http://ieeexplore.ieee.org/lpdocs/epic03/wrapper.htm?arnumber=6315027.

E. Hauge, O. M. Aamo, and J.-M. Godhavn. Tracking of Choke Pressure during Managed Pressure Drilling. In *Modelling, Identification and Control / 770: Advances in Computer Science and Engineering*, Phuket, Thailand, 2012b.

E. Hauge, Ø. N. Stamnes, O.-M. Aamo, and J.-M. Godhavn. A Dynamic Model of Percolating Gas in a Wellbore. *SPE Drilling and Completion*, Feb. 2012c. URL http://www.onepetro.org/mslib/servlet/onepetropreview?id=SPE-160481-PA.

E. Hauge, O. Aamo, and J.-M. Godhavn. Application of an infinite-dimensional observer for drilling systems incorporating kick and loss de-

tection. In *Control Conference (ECC), 2013 European*, pages 1065–1070, July 2013.

P. H. Ibargengoytia, S. Vadera, and L. E. Sucar. A probabilistic model for information and sensor validation. *The Computer Journal*, 49:113–126, 2006.

P. Ioannou and J. Sun. *Robust Adaptive Control*. Number v. 1 in Control theory. PTR Prentice-Hall, 1996. ISBN 9780134391007. URL `https://books.google.com/books?id=TIYqAQAAMAAJ`.

M. Ishii. One-dimensional drift-flux model and constitutive equations for relative motion between phases in various two-phase flow regimes. Technical report, Argonne National Laboratory (ANL), Argonne, IL (United States), Oct. 1977. URL `http://www.osti.gov/servlets/purl/6871478-ToP1T3/`.

F. Iversen, J. Gravdal, E. Dvergsnes, G. Nygaard, H. Gjeraldstveit, L. Carlsen, E. Low, M. C., and S. Torvund. SPE 102842 Feasibility Study of Managed-Pressure Drilling With Automatic Choke Control in Depleted HP/HT Field. In *SPE Annual Technical Conference and Exhibition*, San Antonio, Texas, USA, 2006.

G.-O. Kaasa, Ø. N. Stamnes, L. S. Imsland, and O. M. Aamo. Simplified hydraulics model used for intelligent estimation of downhole pressure for a managed-pressure-drilling control system. *SPE Drilling & Completion*, 27(March):127—-138, 2012. URL `http://www.onepetro.org/mslib/servlet/onepetropreview?id=SPE-143097-PA`.

A. Karimi Vajargah. *Pressure Signature of Gas Influx*. PhD thesis, U. of Tulsa, Sept. 2013.

A. Karimi Vajargah, B. B. Hoxha, and E. van Oort. Automated Well Control Decision-Making during Managed Pressure Drilling Operations. In *SPE Deepwater Drilling and Completions Conference*, Galveston, Texas, USA, Sept. 2014. Society of Petroleum Engineers. doi: 10.2118/170324-MS. URL `http://www.onepetro.org/doi/10.2118/170324-MS`.

V. C. Kelessidis, P. Dalamarinis, and R. Maglione. Experimental study and predictions of pressure losses of fluids modeled as herschel–bulkley in concentric and eccentric annuli in laminar, transitional and turbulent flows. *Journal of Petroleum Science and Engineering*, 77(3):305–312, 2011.

D. Koller and N. Friedman. *Probabilistic graphical models: principles and techniques*. MIT press, 2009.

G. Krishnamoorthy. *A Framework for Utilizing Data from Multiple Sensors in Intelligent Mechanical Systems*. PhD thesis, 2010.

I. S. Landet. Modeling and Control for Managed Pressure Drilling from Floaters. Master's thesis, Norwegian University of Science and Technology, June 2011. URL `http://ntnu.diva-portal.org/smash/get/diva2:434337/FULLTEXT01`.

I. S. Landet, H. Mahdianfar, A. Pavlov, and O. M. Aamo. Modeling for MPD Operations With Experimental Validation. In *IADC/SPE Drilling*

Conference and Exhibition, San Diego, California, USA, 2012a. doi: 10.2118/150461-MS. URL http://www.onepetro.org/mslib/servlet/onepetropreview?id=SPE-150461-MS.

I. S. Landet, A. Pavlov, O. M. Aamo, and H. Mahdianfar. Control of heave-induced pressure fluctuations in managed pressure drilling. In *American Control Conference*, pages 2270–2275, Montreal, Canada, 2012b. ISBN 9781457710964. URL http://ieeexplore.ieee.org/xpls/abs_all.jsp?arnumber=6314622.

C. Leuchtenberg. Drilling system and method, May 6 2008. URL https://www.google.com/patents/US7367411. US Patent 7,367,411.

Z. Li, N. Hovakimyan, and G.-O. Kaasa. Fast estimation and l1 adaptive control for bottomhole pressure in managed pressure drilling. In *Intelligent Control (ISIC), 2011 IEEE International Symposium on*, pages 996–1001, Sept 2011. doi: 10.1109/ISIC.2011.6045426.

G. Linga, P. Aursand, and T. Flåtten. Two-phase nozzle flow and the subcharacteristic condition. *Journal of Mathematical Analysis and Applications*, 426 (2):917–934, 2015.

L. Ljung. *System identification : theory for the user*. Prentice Hall, Upper Saddle River, 2nd edition, 1999. ISBN 0136566952.

J. Lovorn, C. Bruder, N. Skinner, and J. Karigan. Pressure and flow control in

drilling operations, Oct. 9 2012. URL https://www.google.com/patents/US8281875. US Patent 8,281,875.

Z. Ma, A. K. Vajargah, A. Ambrus, P. Ashok, D. Chen, E. van Oort, R. May, J. Macpherson, G. Becker, and D. Curry. Multi-phase well control analysis during managed pressure drilling operations. In *SPE Annual Technical Conference and Exhibition*. Society of Petroleum Engineers, 2016.

H. Mahdianfar, O. Aamo, and A. Pavlov. Attenuation of heave-induced pressure oscillations in offshore drilling systems. In *American Control Conference (ACC), 2012*, pages 4915–4920, June 2012. doi: 10.1109/ACC.2012.6315166.

K. Malloy, R. Stone, G. Medley, D. Hannegan, O. Coker, D. Reitsma, H. Santos, J. Kinder, J. Eck-Olsen, J. McCaskill, J. May, K. Smith, and P. Sonnemann. SPE/IADC 122281 Managed-Pressure Drilling: What It Is and What It Is Not. In *SPE / IADC Managed Pressure Drilling and Underbalanced Operations Conference and Exhibition*, San Antonio, Texas, 2009.

J. Masella, Q. Tran, D. Ferre, and C. Pauchon. Transient simulation of two-phase flows in pipes. *Int. J. Multiph. Flow*, 24(5):739–755, Aug. 1998. ISSN 03019322. doi: 10.1016/S0301-9322(98)00004-4.

W. Mathis and G. Thonhauser. SPE/IADC 107567 Mastering Real-Time Data Quality Control - How to Measure and Manage the Quality of (Rig) Sensor Data. In *SPE/IADC Middle East Drilling and Technology Conference*, Cairo, Egypt, 2007.

G. H. Medley, D. Moore, and S. Nauduri. SPE/IADC 113689 Simplifying MPD - Lessons Learned. In *SPE/IADC Managed Pressure Drilling and Underbalanced Operations Conference and Exhibition*, Abu Dhabi, UAE, 2008.

N. Mehranbod, M. Soroush, and C. Panjapornpon. A method of sensor fault detection and identification. *Journal of Process Control*, 15(3):321 – 339, 2005. ISSN 0959-1524. doi: http://dx.doi.org/10.1016/j.jprocont.2004.06.009. URL `http://www.sciencedirect.com/science/article/pii/S0959152404000812`.

O. J. Mengshoel, A. Darwiche, and S. Uckun. Sensor validation using bayesian networks. In *9th Intl. Symp. on Artificial Intelligence, Robotics and Automation in Space (iSAIRAS-08)*, Los Angeles, California, USA, 2008.

E. N. Monteiro, P. R. Ribeiro, and R. F. Lomba. Study of the pvt properties of gas–synthetic-drilling-fluid mixtures applied to well control. *SPE Drilling & Completion*, 25(01):45–52, 2010.

S.-Y. Moon, J.-R. Shin, and J.-Y. Choi. Speed of sound and real gas solution algorithm for supercritical flows. In *49th AIAA Aerospace Sciences Meeting including the New Horizons Forum and Aerospace Exposition*, page 471, 2011.

H. Mukherjee and J. P. Brill. Liquid holdup correlations for inclined two-phase flow. *Journal of Petroleum Technology*, 35(05):1–003, 1983.

H. Nickens. A dynamic computer model of a kicking well. *SPE Drilling Engineering*, 2(02):159–173, 1987.

M. Niedermayr, M. Pinckard, G. Glaser, and J. de Sousa. Automated method and system for recognizing well control events, Nov. 23 2004. URL `https://www.google.com/patents/US6820702`. US Patent 6,820,702.

R. Nybø. *Efficient Drilling Problem Detection - Early fault detection by the combination of physical models and artificial intelligence*. PhD thesis, 2009.

R. Nybø and D. Sui. SPE 167864 Closing the Integration Gap for the Next Generation of Drilling Decision Support Systems. In *SPE Intelligent Energy Conference and Exhibition*, Utrecht, the Netherlands, 2014.

R. Nybø, K. S. Bjørkevoll, and R. Rommetveit. SPE 112212 Spotting A False Alarm. Integrating Experience And Real-Time Analysis With Artificial Intelligence. In *SPE Intelligent Energy Conference and Exhibition*, Amsterdam,The Netherlands, 2008.

R. Nybø, J. Frøyen, A. D. Lauvsnes, T. Korsvold, and M. Choate. SPE 150306 The Overlooked Drilling Hazard: Decision Making From Bad Data. In *SPE Intelligent Energy International*, Utrecht, The Netherlands, 2012.

P. L. O'Bryan and A. T. Bourgoyne Jr. Swelling of oil-based drilling fluids resulting from dissolved gas. *SPE drilling engineering*, 5(02):149–155, 1990.

J. Orkiszewski. Predicting two-phase pressure drops in vertical pipe. *Journal of Petroleum Technology*, 19(06):829–838, 1967.

J. Petersen, R. Rommetveit, K. S. Bjørkevoll, and J. Frøyen. SPE/IADC 114688 A General Dynamic Model for Single and Multi-phase Flow Operations during Drilling, Completion, Well Control and Intervention. In *SPE/IADC Asia Pacific Drilling Technology Conference and Exhibition*, Jakarta, Indonesia, 2008.

D. Pixton, R. A. Shishavan, C. Hubbell, H. D. Perez, J. D. Hedengren, and A. Craig. Addressing UBO and MPD Challenges with Wired Drill Pipe Telemetry. In *SPE/IADC Managed Pressure Drilling and Underbalanced Operations Conference and Exhibition*, Madrid, Spain, 2014.

A. Podio and A.-P. Yang. Well Control Simulator for IBM Personal Computer. In *SPE/IADC Drilling Conference*, number June, pages 159–173. Society of Petroleum Engineers, apr 1986. doi: 10.2118/14737-MS. URL `http://www.onepetro.org/doi/10.2118/14737-MS`.

C. Pool, N. Davis, F. Urias, and N. Skinner. Pressure and flow control in drilling operations, Mar. 19 2013. URL `https://www.google.com/patents/US8397836`. US Patent 8,397,836.

D. Reitsma and Y. Couturier. New Choke Controller for Managed Pressure Drilling. In *2012 IFAC Workshop on Automatic Control in Offshore Oil and Gas Production*, Trondheim, Norway, 2012. URL `http://www.nt.ntnu.no/users/skoge/prost/proceedings/offshore-control-2012/papers/0049.pdf`.

V. Roes, D. Reitsma, L. Smith, M. J., and H. F. SPE/IADC 98077 First Deepwater Application of Dynamic Annular Pressure Control Succeeds. In *SPE/IADC Drilling Conference*, Miami, Florida, USA, 2006.

R. Rommetveit and E. Vefring. Comparison of Results From an Advanced Gas Kick Simulator With Surface and Downhole Data From Full Scale Gas Kick Experiments in an Inclined Well. In *SPE Annual Technical Conference and Exhibition*. Society of Petroleum Engineers, apr 1991. ISBN 9781555635220. doi: 10.2118/22558-MS. URL `http://www.onepetro.org/mslib/servlet/onepetropreview?id=00022558{\&}soc=SPEhttp://www.onepetro.org/doi/10.2118/22558-MS`.

S. A. Rostami, K. Kinik, F. Gumus, and M. Kirchhoff. Dynamic calibration of the empirical pore pressure estimation methods using mpd data. In *Offshore Technology Conference*, Houston,Texas, 2015.

S. Saeed, C. Pool, F. Urias, J. Lovorn, and E. Bakri. Well drilling methods with event detection, Feb. 3 2011. URL `https://www.google.com/patents/US20110024189`. US Patent App. 12/831,716.

S. Saeed, R. Lovorn, and K. A. Knudsen. SPE/IADC 151416 Automated Drilling Systems for MPD - The Reality. In *SPE/IADC Drilling Conference and Exhibition*, San Diego, CA, USA, 2012.

H. Santos, C. Leuchtenberg, and S. Shayegi. SPE 81183 Micro-Flux Control: The Next Generation in Drilling Process. In *SPE Latin American*

and Caribbean Petroleum Engineering Conference, Port-of-Spain, Trinidad, 2003.

A. B. Serapiao, J. R. Mendes, and K. Miura. Artificial immune systems for classification of petroleum well drilling operations. In L. de Castro, F. Von Zuben, and H. Knidel, editors, *Artificial Immune Systems*, volume 4628 of *Lecture Notes in Computer Science*, pages 47–58. Springer Berlin Heidelberg, 2007. ISBN 978-3-540-73921-0. doi: 10.1007/978-3-540-73922-7_5. URL `http://dx.doi.org/10.1007/978-3-540-73922-7_5`.

S. Shayegi, C. S. Kabir, S. Christensen, K. Ken, J. Casasus-Bribian, A. Hasan, and D. Moos. Reservoir characterization begins at first contact with the drill bit. *SPE Drilling & Completion*, 27(01):11–21, 2012.

H. Shi, J. A. Holmes, L. J. Durlofsky, K. Aziz, L. Diaz, B. Alkaya, and G. Oddie. Drift-flux modeling of two-phase flow in wellbores. *SPE Journal*, 10(01):24–33, 2005.

M. Shirdel and K. Sepehrnoori. Development of a Transient Mechanistic Two-Phase Flow Model for Wellbores. *SPE Journal*, 17(03), 2012. doi: 10.2118/142224-PA. URL `http://www.onepetro.org/doi/10.2118/143101-PA`.

R. A. Shishavan, C. Hubbell, H. D. Perez, J. D. Hedengren, and D. S. Pixton. Combined rate of penetration and pressure regulation for drilling optimization using high speed telemetry. In *SPE Deepwater Drilling and Completions Conference*, Galveston, Texas, USA, 2014.

H. Siahaan, E. Vefring, M. Nikolaou, and J. E. Gravdal. SPE 169205 Evaluation of Coordinated Control During Back Pressure MPD Operations. In *SPE Bergen One Day Seminar*, Bergen, Norway, 2014.

J. Stakvik, C. Berg, G.-O. Kaasa, O. M. Aamo, and U. Lehner. Adaptive model based choke control system for mpd operations. In *SPE/IADC Managed Pressure Drilling and Underbalanced Operations Conference and Exhibition*, Galveston,Texas, 2016.

O. Stamnes, J. Zhou, G.-O. Kaasa, and O. Aamo. Adaptive observer design for the bottomhole pressure of a managed pressure drilling system. In *Decision and Control, 2008. CDC 2008. 47th IEEE Conference on*, pages 2961–2966, Dec 2008. doi: 10.1109/CDC.2008.4738845.

Ø. N. Stamnes. *Nonlinear Estimation with Applications to Drilling*. PhD thesis, Norwegian University of Science and Technology, April 2011.

Ø. N. Stamnes, O. M. Aamo, and G.-O. Kaasa. Adaptive Redesign of Nonlinear Observers. *IEEE Transactions on Automatic Control*, 56(5): 1152–1157, May 2011. ISSN 0018-9286. doi: 10.1109/TAC.2011.2107090. URL `http://ieeexplore.ieee.org/xpls/abs\_all.jsp?arnumber=5692818http://ieeexplore.ieee.org/lpdocs/epic03/wrapper.htm?arnumber=5692818`.

S. Syltoy, S. Eide, S. Torvund, B. P.C., L. T., F. H., K. Bjørkevoll, J. McCaskill, O. Prebensen, and E. Low. SPE/IADC 114184 Highly Advanced

Multitechnical MPD Concept Extends Achievable HP/HT Targets in the North Sea. In *SPE/IADC Managed Pressure Drilling and Underbalanced Operations Conference and Exhibition*, Abu Dhabi, UAE, 2008.

Y. Taitel, O. Shoham, and J. Brill. Simplified transient solution and simulation of two-phase flow in pipelines, 1989. ISSN 00092509.

A. Torsvoll, P. Horsrud, and N. Reimers. SPE/IADC 98947 Continuous Circulation During Drilling Utilizing a Drillstring Integrated Valve-The Continuous Circulation Valve. In *SPE/IADC Drilling Conference*, Miami, Florida, USA, 2006.

J. E. Udegbunam, K. K. r. Fjelde, S. Evje, and G. Nygaard. A Simple Transient Flow Model for MPD and UBD Applications. In *SPE/IADC Managed Pressure Drilling and Underbalanced Operations Conference and Exhibition*, number April, pages 8–9. Society of Petroleum Engineers, Apr. 2014. doi: 10.2118/168960-MS. URL `http://www.onepetro.org/doi/10.2118/168960-MS`.

U.S. National Research Council. *Macondo Well Deepwater Horizon Blowout: Lessons for Improving Offshore Drilling Safety*. National Academies Press, 2012. ISBN 9780309221382. URL `http://books.google.com/books?id=v553tgAACAAJ`.

A. K. Vajargah and E. van Oort. Determination of drilling fluid rheology under downhole conditions by using real-time distributed pressure data. *Journal of Natural Gas Science and Engineering*, 24:400–411, 2015.

E. van Oort. PGE 383 - Advanced Well Construction Lecture Notes, 2013.

E. van Riet. Dynamic annular pressure control apparatus and method, June 14 2005. URL https://www.google.com/patents/US6904981. US Patent 6,904,981.

E. van Riet, D. Reitsma, and B. Vandecraen. SPE/IADC 85310 Development and Testing of a Fully Automated System to Accurately Control Downhole Pressure During Drilling Operations. In *SPE/IADC Middle East Drilling Technology Conference and Exhibition*, Abu Dhabi, UAE, 2003.

E. H. Vefring, G. Nygaard, R. J. Lorentzen, G. Nævdal, and K. K. Fjelde. Reservoir characterization during ubd: Methodology and active tests. In *IADC/SPE Underbalanced Technology Conference and Exhibition*. Society of Petroleum Engineers, 2003.

M. Wiggins, J. Russell, and J. Jennings. Analytical Development Of Vogel-Type Inflow Performance Relationships. *SPE Journal*, 1(4): 355–362, Dec. 1996. ISSN 1086-055X. doi: 10.2118/23580-PA. URL http://www.onepetro.org/mslib/servlet/onepetropreview?id=00023580http://www.onepetro.org/mslib/servlet/onepetropreview?id=00023580\&soc=SPE.

A. Willersrud, L. Imsland, A. Pavlov, and G.-O. Kaasa. A Framework for Fault Diagnosis in Managed Pressure Drilling Applied to Flow-Loop Data. In *10th IFAC International Symposium on Dynamics and Control of Process Systems*, Mumbai, India, 2013.

M. Yilmaz, N. R. Dhansria, and S. Mujeeb. An Intelligent Control Approach for Oil Drilling Processes. *Procedia Computer Science*, 6(0):106 – 111, 2011. ISSN 1877-0509. doi: http://dx.doi.org/10.1016/j.procs.2011.08.021. URL `http://www.sciencedirect.com/science/article/pii/S1877050911004868`. Complex adaptive sysytems.

M. Yilmaz, S. Mujeeb, and N. R. Dhansri. A H-infinity Control Approach for Oil Drilling Processes . *Procedia Computer Science*, 20(0):134 – 139, 2013. ISSN 1877-0509. doi: http://dx.doi.org/10.1016/j.procs.2013.09.251. URL `http://www.sciencedirect.com/science/article/pii/S187705091301051X`. Complex Adaptive Systems.

H. Yuan and D. Zhou. Evaluation of twophase flow correlations and mechanistic models for pipelines at horizontal and inclined upward flow. In *SPE Production and Operations Symposium*. Society of Petroleum Engineers, 2009.

J. Zhou, O. Stamnes, O. Aamo, and G.-O. Kaasa. Adaptive output feedback control of a managed pressure drilling system. In *Decision and Control, 2008. CDC 2008. 47th IEEE Conference on*, pages 3008–3013, Dec 2008. doi: 10.1109/CDC.2008.4738844.

J. Zhou, O. Stamnes, O. Aamo, and G.-O. Kaasa. Switched Control for Pressure Regulation and Kick Attenuation in a Managed Pressure Drilling System. *Control Systems Technology, IEEE Transactions on*, 19(2):337–350, March 2011. ISSN 1063-6536. doi: 10.1109/TCST.2010.2046517.

Vita

Adrian Marius Ambruș graduated from Elena Ghiba Birta National College in Arad, Romania, in 2007, and then went to Drexel University in Philadelphia to pursue an accelerated Bachelor's/Master's degree program in Mechanical Engineering. He received his Bachelor of Science and Master of Science degrees in 2012, and was subsequently admitted to the University of Texas at Austin in the fall of 2012, to pursue a Doctor of Philosophy degree in Mechanical Engineering.

Permanent address: aambrus@utexas.edu

This dissertation was typeset with LaTeX[†] by the author.

[†]LaTeX is a document preparation system developed by Leslie Lamport as a special version of Donald Knuth's TeX Program.